

Supplementary Materials for

Decoding the Multi-Dimensional Complexity of Glycosylation

Reaction via Machine Learning

Authors: Fizza Sabbor^{1,2,3}, Po-Wei Lu^{3,4}, Shang-Yi Chen^{2,3,5}, Sung-Chi Lin³, Sefunmi Peace Akinseye^{3,5,6}, Rapelly Venkatesh³, Tiow-Gan Ong^{1,3*}, Cheng-Chung Wang^{3,5*}

Affiliations:

¹Molecular Science and Technology (MST), Taiwan International Graduate Program (TIGP), Academia Sinica; Taipei 115, Taiwan.

²Department of Chemistry, National Tsing Hua University; Hsinchu, 300, Taiwan.

³Institute of Chemistry, Academia Sinica; Taipei, 115, Taiwan.

⁴Institute of Biochemistry and Molecular Biology, National Yang Ming Chiao Tung University; Taipei, Taiwan.

⁵Chemical Biology and Molecular Biophysics (CBMB), Taiwan International Graduate Program (TIGP), Academia Sinica; Taipei, 115, Taiwan.

⁶Institute of Biological Sciences, National Taiwan University; Taipei, 10617, Taiwan.

*Email(s): wangcc@chem.sinica.edu.tw; tgong@gate.sinica.edu.tw

Table of Contents

1	Materials and Methods	3
2	Results and Programming Details	5
2.1	Environmental Factor Impact index (EFI)	5
2.2	Screening of temperature parameter	6
2.3	Screening of solvent parameter	9
2.4	Screening of concentration parameter	12
2.5	Screening of stoichiometry parameter	15
2.6	Comparative performance analysis of ML models in predicting data-driven glycosylation outcomes	16
2.7	Core ML model schematics	28
2.8	Model performance evaluation on train and validation sets for target prediction	31
2.9	Empirical analysis of ML models	46
2.10	Performance Metrics	50
2.11	Mechanistic mapping of reaction space	54
2.12	Programming details	55
3	Experimental Section for Synthesis	58
4	NMR Spectra	77

1 Materials and Methods

1.1 General information

All reactions were conducted in flame-dried glassware, under nitrogen atmosphere, unless otherwise noted. All solvents were purified and dried from a safe purification system containing activated Al_2O_3 . All reagents obtained from commercial sources were used without purification. Air/moisture-sensitive liquids were transferred with the gas-tight syringes fitted with stainless-steel needles. Liquid reagents were added via Hamilton gas-tight microliter syringes. Thin-layer chromatography (TLC) was performed on pre-coated glass plates and aluminum sheets of Silica Gel 60 F₂₅₄ (0.25 mm, E. Merck); detection was executed by spraying with a solution of $\text{Ce}(\text{SO}_4)_2$, $(\text{NH}_4)_6\text{Mo}_7\text{O}_{21}$, and H_2SO_4 in water and subsequently heating on a hot plate. UV light for TLC analysis was UVGL-25 compact UV lamp (4 watt/ 254 nm), UVP. Flash column chromatography was carried out by Silica Gel Geduran® Si 60 (0.040-0.063 mm, E. Merck). Stir plate: MR Hei-Standard.

1.2 Material and reagents

All commercially available reagents were purchased from Sigma-Aldrich, Alfa Aesar, Strem, Oakwood, Acros Organics, Matrix Scientific, TCI, Chem-Impex, Carbosynth, or Ambeed and were used without purification unless otherwise indicated. Solvents for chromatography and extraction were purchased from Sigma Aldrich as ACS grade or above and used without additional purification. Solvents for HPLC were purchased from Sigma Aldrich or Fisher as HPLC grade and used without additional purification. Anhydrous reaction solvents were passed through aluminum oxide on a solvent purification system (LC Technology Solutions) and sparged with Argon for 1 hour before use. Deuterated solvents were purchased from Cambridge Isotope Laboratories and used without prior purification.

1.3 Instrumentation

Nuclear magnetic resonance (NMR) spectra such as ^1H , ^{13}C NMR, DEPT, ^1H - ^1H COSY, ^1H - ^{13}C COSY, and NOESY spectra were recorded by Bruker AV400, and AV500 MHz instruments. Chemical shifts are in ppm from Me_4Si , generated from the CDCl_3 lock signal at $\delta 7.26$. Multiplicities are reports by using the following abbreviations: s = singlet, d = doublet, t = triplet, q = quartet, m = multiplet, br = broad, ABq = AB quartets. bd = broad doublet; J = coupling constant values in Hertz. IR spectra were taken by a Bruker alpha FT-IR spectrometer using ZnSe plates. Mass spectra were analyzed by a Waters Premier XE instrument with ESI source. Optical rotations were measured with a JASCO P-2000 polarimeter at 25-30 °C, and using a 100 mm cell at 589 nm (Na).

1.4 Standard procedure for glycosylation

A flame-dried round-bottom flask was charged with a magnetic bar, glycosylating agent (1 equiv.), anhydrous DCM (0.167 M), and activated 3 Å molecular sieves. The nucleophile (1.5 equiv.) was added to a reaction solution at -40 °C, and the resulting mixture was stirred for 1 h. Subsequently, NIS (1.0 equiv.) and TfOH (0.4 equiv.) were added sequentially at -40 °C and the reaction mixture was stirred overnight at -40 °C. Upon completion, the reaction was quenched by the addition of TEA at same temperature. The mixture was then filtered through a Celite, washing with DCM. The filtrates were concentrated under reduced pressure, and the crude product was

purified by silica gel column chromatography (8:1 hexanes-/EtOAc) to afford the desired glycosylated product.

1.5 General procedure for temperature screening

A suspension of glycosylating agent **A-E** (100 mg), molecular sieves (4 Å, 100 mg), and alcohol **51-56** (1.5 equiv.) in DCM (0.167M) was stirred at varied temperature (-40 °C, -20 °C, 0 °C, 25 °C) under a nitrogen atmosphere for 1 hour. NIS (1.0 equiv.) and TfOH (0.4 equiv.) was then added to the reaction mixture, which was stirred for 12 hours at the same temperature, with progress monitored by TLC (*n*-Hexane/EtOAc, 8:1). The reaction mixture was filtered through Celite, washed with DCM, and the filtrate was concentrated under reduced pressure. The resulting crude product was purified by flash chromatography to afford the desired product.

1.6 General procedure for solvent screening

A suspension of glycosylating agent **A-E** (100 mg), molecular sieves (4 Å, 100 mg), and alcohol **51-56** (1.5 equiv.) in varied solvent systems DCM, or THF, or Toluene, DCM/ACN (*v/v* = 1/2), DCM/DMF (*v/v* = 1/2), DCM/*p*-dioxane (*v/v* = 2/1), of which solvent concentration is 0.167M, was stirred at -40 °C under a nitrogen atmosphere for 1 hour. NIS (1.0 equiv.) and TfOH (0.4 equiv.) was then added to the reaction mixture, which was stirred for 12 hours at the same temperature, with progress monitored by TLC (*n*-Hexane/EtOAc, 8:1). The reaction mixture was filtered through Celite, washed with DCM, and the filtrate was concentrated under reduced pressure. The resulting crude product was purified by flash chromatography to afford the desired product.

1.7 General procedure for concentration screening

A suspension of glycosylating agent **A-E** (100 mg), molecular sieves (4 Å, 100 mg), and alcohol **51-56** (1.5 equiv.) in DCM with varied concentration (0.308M, 0.167M, 0.051M, 0.038M, 0.018M) was stirred at -40 °C under a nitrogen atmosphere for 1 hour. NIS (1.0 equiv.) and TfOH (0.4 equiv.) was then added to the reaction mixture, which was stirred for 12 hours at the same temperature, with progress monitored by TLC (*n*-Hexane/EtOAc, 8:1). The reaction mixture was filtered through Celite, washed with DCM, and the filtrate was concentrated under reduced pressure. The resulting crude product was purified by flash chromatography to afford the desired product.

1.8 General procedure for stoichiometry screening

A suspension of glycosylating agent **A-E** (100 mg), molecular sieves (4 Å, 100 mg), and alcohol **51-56** at varied equivalents (1.5 equiv., and 0.66 equiv.) in DCM (0.167 M) was stirred at -40 °C under a nitrogen atmosphere for 1 hour. NIS (1.0 equiv.) and TfOH (0.4 equiv.) was then added to the reaction mixture, which was stirred for 12 hours at the same temperature, with progress monitored by TLC (*n*-Hexane/EtOAc, 8:1). The reaction mixture was filtered through Celite, washed with DCM, and the filtrate was concentrated under reduced pressure. The resulting crude product was purified by flash chromatography to afford the desired product.

2 Results and Programming Details

2.1 Environmental Factor Impact index (EFI)

EFI quantifies the overall efficiency of glycosylation under given environmental conditions, capturing both mechanistic favorability (α -ratio) and practical productivity (yield) while penalizing unfavorable reactivity, nucleophilicity, and temperature conditions.

- Higher EFI = efficient, selective, practical glycosylation
- Lower EFI = poor selectivity, low yield, or harsh conditions

$$EFI_{General} = \frac{\text{Outcome Metrics } (\alpha\text{-ratio \& yield})}{\prod_{i=1}^n f_i(\text{parameter}_i)} \quad (S1)$$

Where;

Outcome Metrics= α -ratio, yield, or another measurable reaction outcome that reflects stereochemical efficiency.

parameter_i= represents each parameter, such as solvent $P_{solvent}$ (table S3), reactivity of glycosylating agent (RRV), alcohol nucleophilicity (Aka), Temperature (T), or concentration (C).

$f_i(\text{parameter}_i)$ = Function to quantify the influence of parameter_i on the reaction. These could be linear or non-linear functions derived from experimental conditions or empirical data.

$$\prod_{i=1}^n f_i(\text{parameter}_i) = f_1(\text{parameter}_1) \times f_2(\text{parameter}_2) \times \dots \times f_n(n)$$

$\prod_{i=1}^n$ multiplies all the f_i values for the individual parameters

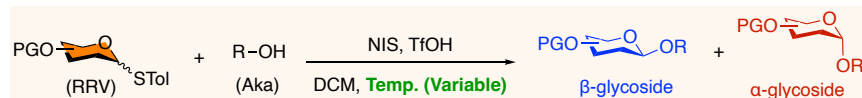
EFI for Temperature:

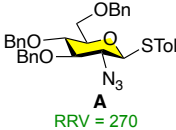
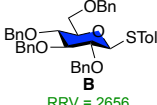
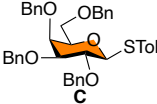
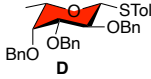
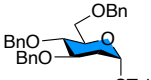
$$EFI_{Temp.} = \frac{\alpha\text{-ratio} \times \text{yield}}{RRV \times Aka \times T_{normalized}} \quad (S2)$$

Where, $T_{normalized} = T_{\text{C}} + 273.15$

An example for $EFI_{Temp.}$							
Temp (°C)	Solvent	RRV	Aka	α -ratio	Yield	EFI	Efficiency
-40	DCM	2656	1.36	71	90	0.0068	Good α -selectivity under mild conditions

Supplementary Table 1. Screening of temperature effects on glycosylation selectivity across matching partners varying RRV and Aka scale.

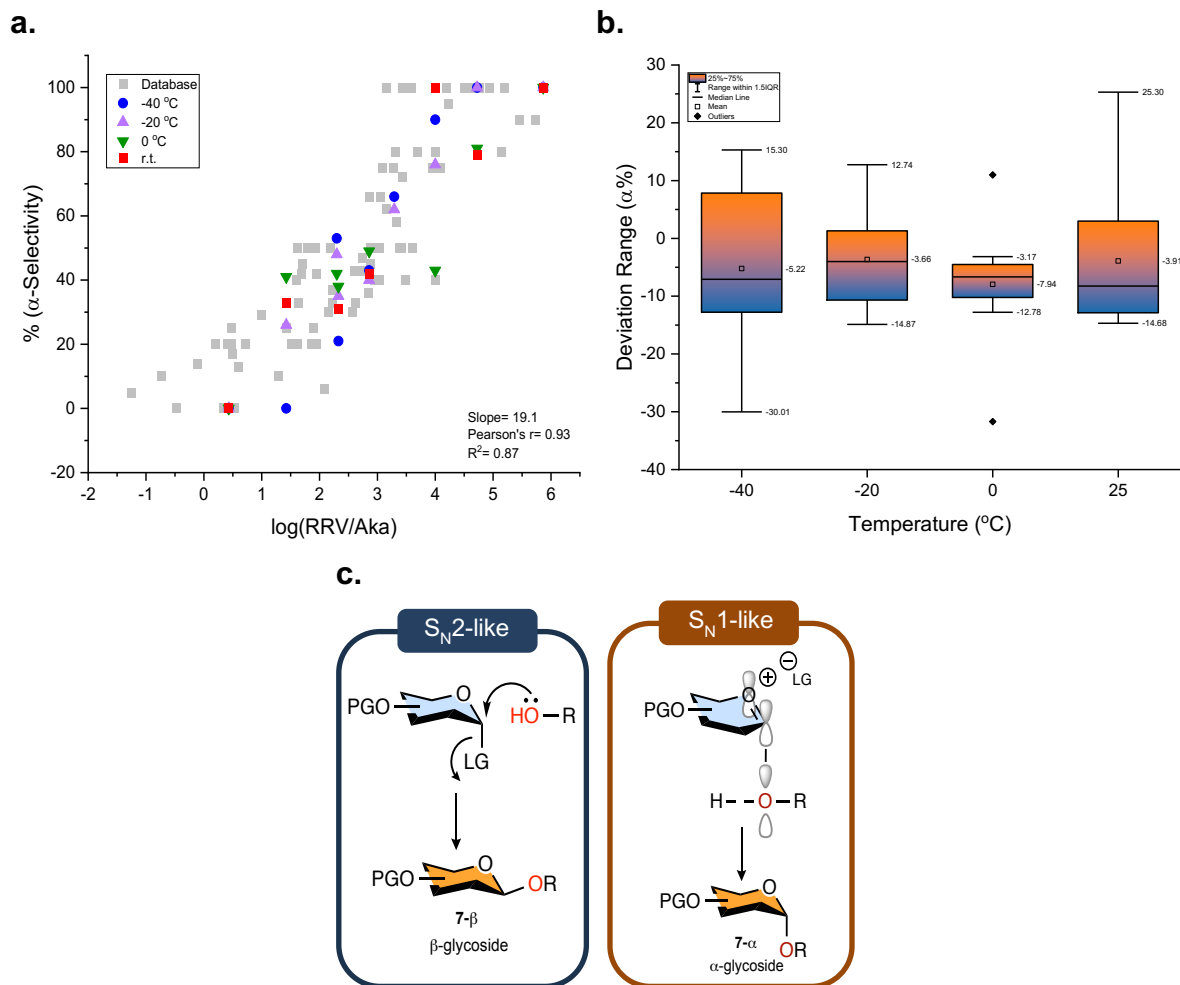


Glycosylating agent	Temp. Alcohol	-40 °C α-ratio(%) (yield)	-20 °C α-ratio(%) (yield)	0 °C α-ratio(%) (yield)	25 °C α-ratio(%) (yield)
 <p>A RRV = 270</p>	MeOH 51	0% (62%)	0% (38%)	0% (7%)	Trace
	6-OH-Glc 53	80% (78%)	77% (85%)	70% (80%)	65% (49%)
	Ph 55	47% (69%)	47% (67%)	43% (57%)	Trace
	4-OH-Gal 56	68% 62%	56% (90%)	53% (74%)	61% (50%)
 <p>B RRV = 2656</p>	MeOH 51	0% (82%)	27% (69%)	40% (70%)	32% (97%)
	6-OH-Glc 53	31% (86%)	30% (85%)	50% (80%)	54% (51%)
	Ph 55	66% (84%)	62% (86%)	Trace	Trace
	4-OH-Gal 56	72% 52%	71% (78%)	70% (84%)	73% (58%)
 <p>C RRV = 17000</p>	1-adm 52	40% (87%)	36% (78%)	38% (80%)	31% (92%)
 <p>D RRV = 72000</p>	MeOH 51	62% (93%)	40% (91%)	50% (80%)	35% (92%)
	6-OH-Glc 53	73% (91%)	64% (87%)	52% (68%)	58% (48%)
	Ph 55	100% (72%)	100% (92%)	100% (55%)	100% (46%)
	4-OH-Gal 56	66% 87%	77% (89%)	73% (83%)	77% (48%)
 <p>E RRV = 10⁶</p>	MeOH 51	83% (38%)	77% (24%)	50% (19%)	100% Trace
	6-OH-Glc 53	78% (74%)	77% (71%)	72% (60%)	82% (57%)
	Ph 55	100% (64%)	100% (53%)	100% (52%)	100% (20%)
	4-OH-Gal 56	86% (65%)	89% (68%)	84% (48%)	87% (43%)

100	+80	+60	+50	$\alpha(\%)$	-40	-60	-80	100
-----	-----	-----	-----	--------------	-----	-----	-----	-----

Reactions were performed in dichloromethane (DCM) under NIS/TfOH activation. At cryogenic temperatures, glycosylation operates predominantly under kinetic control, favoring β -selectivity. This behavior is particularly evident for low RRV glycosylating agents like glucosamine **A** and **B**, where α -ratios remain negligible (<5%), with EFI nearly 0, reflecting insufficient thermal energy to overcome steric and electronic barriers, where $T_{normalized}$ is $^{\circ}\text{C} + 273.15$. Temperature critically shapes both selectivity and efficiency in glycosylation. As the temperature increases to 0 $^{\circ}\text{C}$, the system enters a transitional zone. Partial dissociation of glycosyl intermediates promotes rotational freedom, resulting in an increase in α -selectivity. Glucose **A** shows an α -ratio improvement of +40% with stable yield, indicating balanced kinetic and thermodynamic influences. High RRV glycosylating agents like fucose **D** exhibit enhanced α -selectivity (+35%) with an EFI of 0.00235, reflecting improved efficiency as the system transitions toward thermodynamic control. At higher temperatures, glycosylation shifts to $\text{S}_{\text{N}}1$ -like pathways, with free rotation of dissociated oxocarbenium ion intermediates favoring the thermodynamically stable α -product, specially the high RRV glycosylating agents, such as fucose **D** and 2-deoxy-glucopyranoside **E**, predominates α -selectivity showcasing the dominance of thermodynamic control, yet EFI values remain modest—largely due to declining yields, particularly for agent **E**, highlighting the increased competition from side reactions and thermal decomposition.

2.2.1 System analysis of quantification of temperature parameter



Supplementary Figure 1. Temperature dependence of glycosylation selectivity and mechanism. (a) Correlation between $\log(\text{RRV}/\text{Aka})$ and α -ratio (%) for glycosylation reactions at different temperatures (-40 °C, -20 °C, 0 °C, 25 °C). (b) Box plot showing deviation range in selectivity across temperatures. (c) Proposed mechanistic pathways for β - ($\text{S}_{\text{N}}2$ -like) and α -glycoside ($\text{S}_{\text{N}}1$ -like) formation. RRV, relative reactivity value; LG, leaving group; PGO, protecting group; OR, glycoside product.

2.3 Screening of solvent parameter

Supplementary Table 2. Screening of solvent effects on glycosylation selectivity across matching partners varying RRV and Aka scale.

PGO--STol (RRV) + R-OH (Aka) $\xrightarrow[\text{Solvent (Variable), -40 } ^\circ\text{C}]{\text{NIS, TfOH}}$ PGO--OR (β -glycoside) + PGO--OR (α -glycoside)

Glycosylating agent	Solvent Alcohol	DCM α -ratio(%) (yield)	THF α -ratio(%) (yield)	Toluene α -ratio(%) (yield)	DCM/ACN ^a α -ratio(%) (yield)	DCM/DMF ^a α -ratio(%) (yield)	DCM/ <i>p</i> -Dioxane ^b α -ratio(%) (yield)
<p>A RRV = 270</p>	MeOH 51	0% (62%)	0% (44%)	0% (54%)	0% (58%)	N.R. ^c	N.R. ^c
	6-OH-Glc 53	20% (78%)	63% (28%)	75% (22%)	100% (94%)	40% (23%)	60% (52%)
	Ph 55	47% (69%)	78% (18%)	85% (36%)	62% (21%)	N.R. ^c	78% (39%)
	4-OH-Gal 56	68% 62%	44% (33%)	58% (23%)	55% (87%)	50% (38%)	62% (55%)
<p>B RRV = 2656</p>	MeOH 51	0% (82%)	23% (92%)	47% (82%)	18% (85%)	Trace	33% (30%)
	6-OH-Glc 53	31% (86%)	30% (55%)	80% (85%)	90% (85%)	50% (40%)	54% (63%)
	Ph 55	66% (84%)	N.R. ^c	70% (73%)	69% (80%)	N.R. ^c	47% (80%)
	4-OH-Gal 56	72% 52%	68% (49%)	61% (47%)	32% (96%)	70% (63%)	78% (68%)
<p>C RRV = 17000</p>	1-adm 52	40% (93%)	52% (89%)	38% (90%)	40% (93%)	N.R. ^c	45% (72%)
	<p>D RRV = 72000</p>	MeOH 51	63% (90%)	45% (41%)	20% (75%)	26% (84%)	76% (70%)
6-OH-Glc 53		73% (91%)	64% (87%)	71% (60%)	79% (87%)	72% (56%)	89% (77%)
Ph 55		100% (72%)	100% (68%)	100% (78%)	100% (59%)	N.R. ^c	100% (67%)
4-OH-Gal 56		66% 87%	77% (89%)	63% (80%)	64% (91%)	66% (50%)	73% (82%)
<p>E RRV = 10⁶</p>	MeOH 51	83% (43%)	47% (39%)	41% (21%)	45% (33%)	73% (58%)	38% (46%)
	6-OH-Glc 53	78% (74%)	77% (58%)	72% (60%)	75% (68%)	72% (56%)	90% (55%)
	Ph 55	100% (64%)	100% (18%)	100% (48%)	100% (31%)	N.R. ^c	N.R. ^c
	4-OH-Gal 56	86% (65%)	89% (68%)	83% (43%)	79% (45%)	84% (38%)	92% (32%)

100
+80
+60
+50
 α (%)
-40
-60
-80
100

α -ratio(%)= 100- β -ratio (%), a= 1:2 (v/v), b= 2:1 (v/v), c= No Reaction

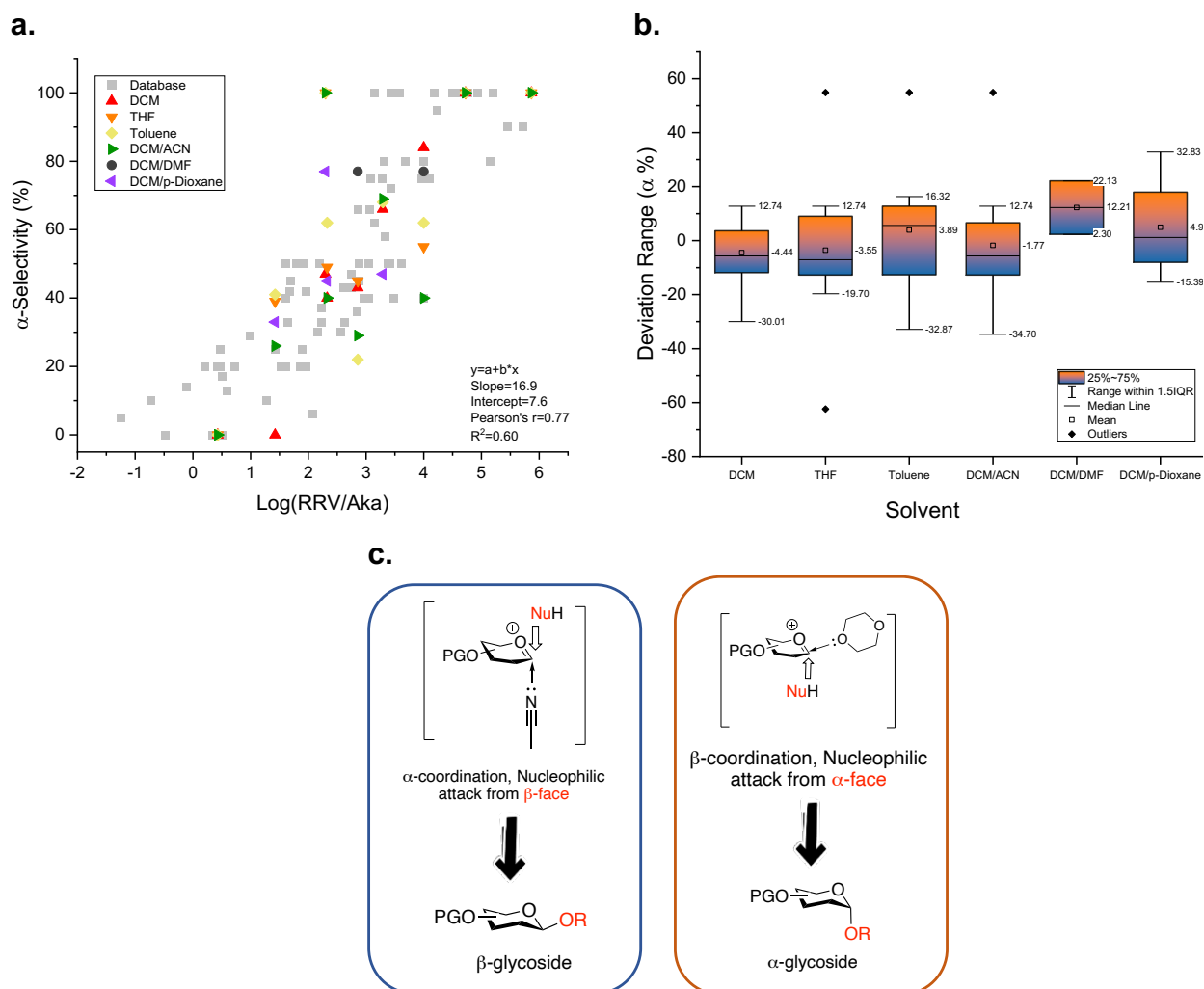
Reactions were performed at -40 °C under NIS/TfOH activation, varying solvents. Solvent polarity and coordination ability significantly influenced both α -ratio and yield. In dichloromethane (DCM), low-reactivity glycosylating agents (e.g., agent **A**, **C**) showed strong β -selectivity, consistent with S_N2-like behavior and minimal dissociation of contact ion pairs (CIPs). For higher-reactivity glycosylating agents (e.g., agent **D**), DCM achieved moderate α -selectivity and high yields. THF improves α -ratios by +23%, reflecting an improved mechanistic balance. For the same glycosylating agents, Dimethylformamide (DMF) increases α -ratios by +47%, consistent with enhanced stabilization of solvent-separated ion pairs (SSIPs) and increased front-side attack. The non-reactivity observed in DCM/*p*-Dioxane underscores the importance of solvent compatibility in stabilizing intermediates and enabling effective activation. Conversely, low EFI values (e.g., 0.00 for DCM with low RRV agents) reflect kinetic control dominated by CIPs and S_N2-like mechanisms, highlighting the critical role of solvent environment in shaping glycosylation outcome.

Supplementary Table 3. The polarity indices for common solvents.

Solvent	Polarity Index (P')
Dichloromethane (DCM)	3.1
Tetrahydrofuran (THF)	4.0
Toluene	2.4
Dimethylformamide (DMF)	6.4
Acetonitrile (ACN)	5.8
<i>p</i> -Dioxane	4.8

These values are sourced from the solvent polarity chart provided by Louisiana State University ([LSU Macro](#)). *P'* were used to obtain EFI values.

2.3.1 System analysis of quantification of solvent parameter



Supplementary Figure 2. Solvent dependence of glycosylation selectivity and mechanism. (a) Correlation between $\log(\text{RRV}/\text{Aka})$ and α -ratio (%) for glycosylation reactions at various solvents (DCM, THF, Toluene, DCM/ACN, DCM/DMF, DCM/*p*-Dioxane). (b) Box plot showing deviation range in selectivity across solvents. (c) Proposed mechanistic pathways for β - and α -glycoside formation. NuH, Nucleophilic alcohol; PGO, protecting group; OR, glycoside product.

2.4 Screening of concentration parameter

Supplementary Table 4. Screening of concentration effect on glycosylation selectivity across matching partners varying RRV and Aka scale.

PGO-(RRV)-STol + R-OH (Aka) $\xrightarrow[\text{DCM, -40 } ^\circ\text{C}]{\text{NIS, TfOH}}$ β -glycoside + α -glycoside

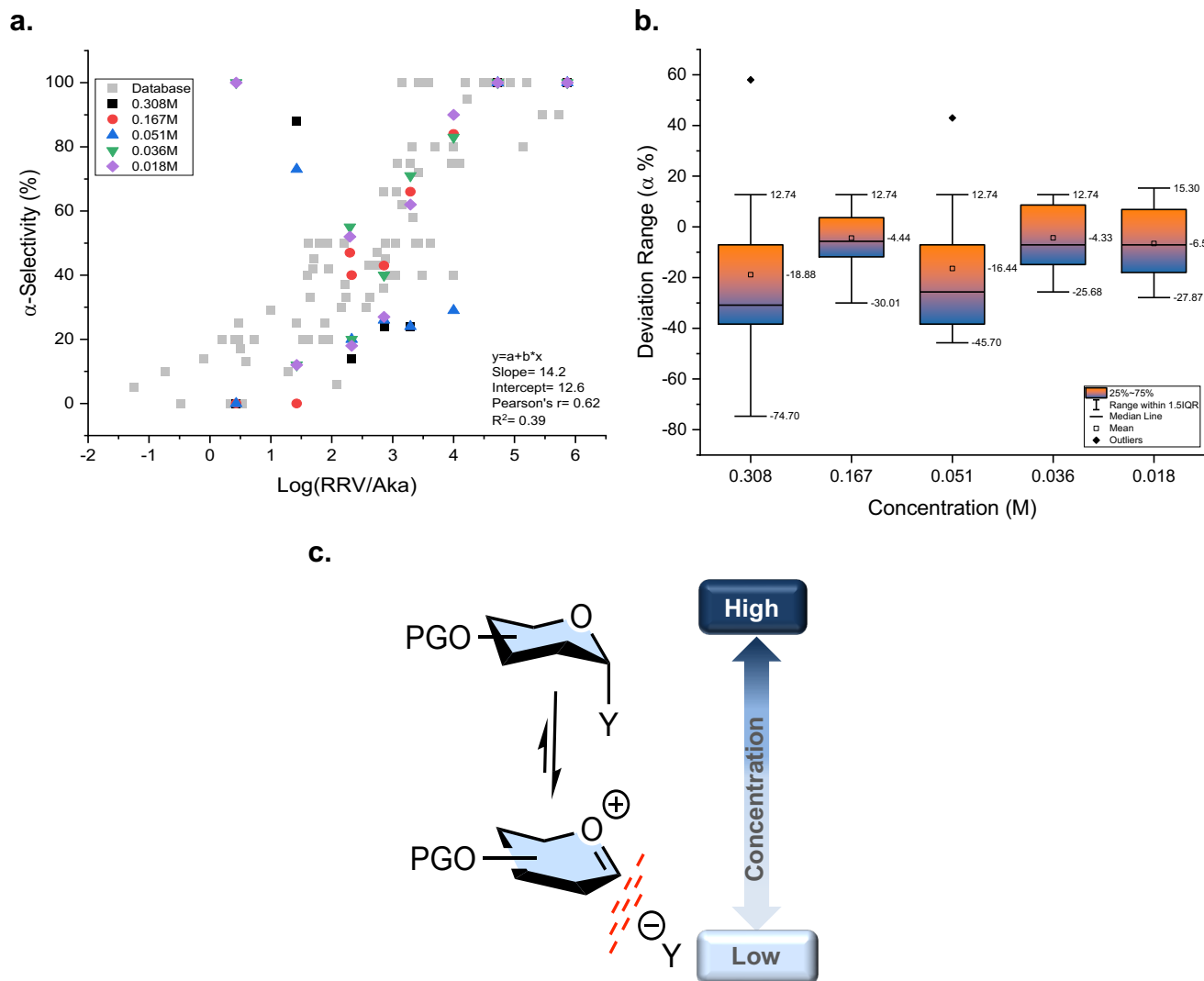
Solvent Conc. (Variable),

Glycosylating agent	Conc. Alcohol	0.308M α -ratio(%) (yield)	0.167M α -ratio(%) (yield)	0.051M α -ratio(%) (yield)	0.036M α -ratio(%) (yield)	0.018M α -ratio(%) (yield)
<p>A RRV = 270</p>	MeOH 51	0% (33%)	0% (62%)	0% (64%)	0% (74%)	0% (87%)
	6-OH-Glc 53	42% (76%)	20% (78%)	38% (72%)	46% (68%)	50% (53%)
	Ph 55	59% (20%)	47% (69%)	55% (60%)	55% (88%)	52% (55%)
	4-OH-Gal 56	31% 82%	28% 62%	24% 72%	26% 70%	30% 68%
<p>B RRV = 2656</p>	MeOH 51	11% (60%)	0% (82%)	27% (88%)	13% (32%)	12% (20%)
	6-OH-Glc 53	38% (62%)	30% ^a (86%)	41% (65%)	32% (61%)	36% (47%)
	Ph 55	71% (73%)	66% (84%)	71% (77%)	71% (90%)	62% (90%)
	4-OH-Gal 56	64% (81%)	72% (52%)	69% (76%)	70% (61%)	68% (65%)
<p>C RRV = 17000</p>	1-adm 52	15% (75%)	40% (94%)	18% (96%)	20% (61%)	19% (70%)
<p>D RRV = 72000</p>	MeOH 51	24% (76%)	59% (90%)	27% (81%)	40% (96%)	27% (72%)
	6-OH-Glc 53	69% (87%)	73% (91%)	70% (78%)	66% (74%)	63% (60%)
	Ph 55	100% (94%)	100% (72%)	100% (78%)	100% (93%)	100% (97%)
	4-OH-Gal 56	62% (89%)	66% (87%)	73% (85%)	72% (85%)	70% (80%)
<p>E RRV = 10⁶</p>	MeOH 51	H.D. ^a	83% (43%)	66% (60%)	83% (56%)	91% (60%)
	6-OH-Glc 53	75% (63%)	78% ^a (74%)	72% (65%)	74% (69%)	70% (45%)
	Ph 55	100% (66%)	100% (64%)	100% (68%)	100% (74%)	100% (60%)
	4-OH-Gal 56	80% (60%)	86% (65%)	78% (58%)	74% (62%)	77% (55%)

α -ratio(%)= 100- β -ratio (%), a= Hydrolyzed glycosylating agent

The concentration parameter in glycosylation reactions profoundly impacts stereoselectivity and yield, governed by ion-pair dynamics, acid availability, and reaction time. At high concentrations (e.g., 0.308 M and 0.167 M), kinetic control dominates due to α -triflate stabilization and the high availability of activating acids such as triflic acid. This abundance of acid accelerates covalent-triflate formation, favoring β -selectivity via S_N2 -like pathway. For low RRV glycosylating agent **A** β -ratios remain dominant across high concentrations via unimolecular pathway, while yields decline by $-7\%/M$. As concentration decreases (e.g., 0.051 M and 0.036 M), partial CIP dissociation into SSIPs occurs, promoting bimolecular pathways. In these intermediate conditions, reduced acid availability and extended reaction rate enable the formation of both kinetically and thermodynamically controlled products. For glycosylating agent **B**, α -ratios improve significantly, increasing by $+20\%/M$, at 0.051 M to 0.036 M, yields remain relatively stable, declining slightly by $-3\%/M$, highlighting a balance between kinetic and thermodynamic control. At low concentrations (e.g., 0.018 M), complete CIP dissociation and longer reaction times favor SSIP formation and thermodynamically stable intermediates, this shift promotes front-side attack via S_N1 -like pathways, yielding higher α -selectivity. For high RRV agents **D** and **E**, α -ratios increase by $+18\%/M$, while yields decrease slightly by $-1\%/M$ due to side reactions or agent decomposition. These trends underscore the enhanced flexibility of intermediates at low concentrations, favoring thermodynamic products over kinetically controlled ones.

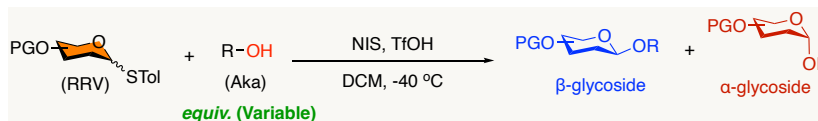
2.4.1 System analysis of quantification of concentration parameter

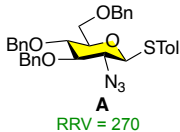
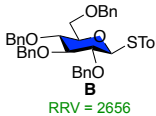
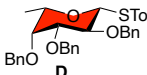
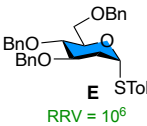


Supplementary Figure 3. Concentration dependence of glycosylation selectivity and mechanism. (a) Correlation between $\log(\text{RRV}/\text{Aka})$ and α -ratio (%) for glycosylation reactions at various concentrations. (b) Box plot showing deviation range in selectivity across various concentrations. (c) Schematic illustration of the mechanistic transition from high to low alcohol concentration, highlighting the shift from contact ion pair to solvent-separated ion pair pathways. Y, any nucleophilic species presents in reaction environment; PGO, protecting group.

2.5 Screening of stoichiometry parameter

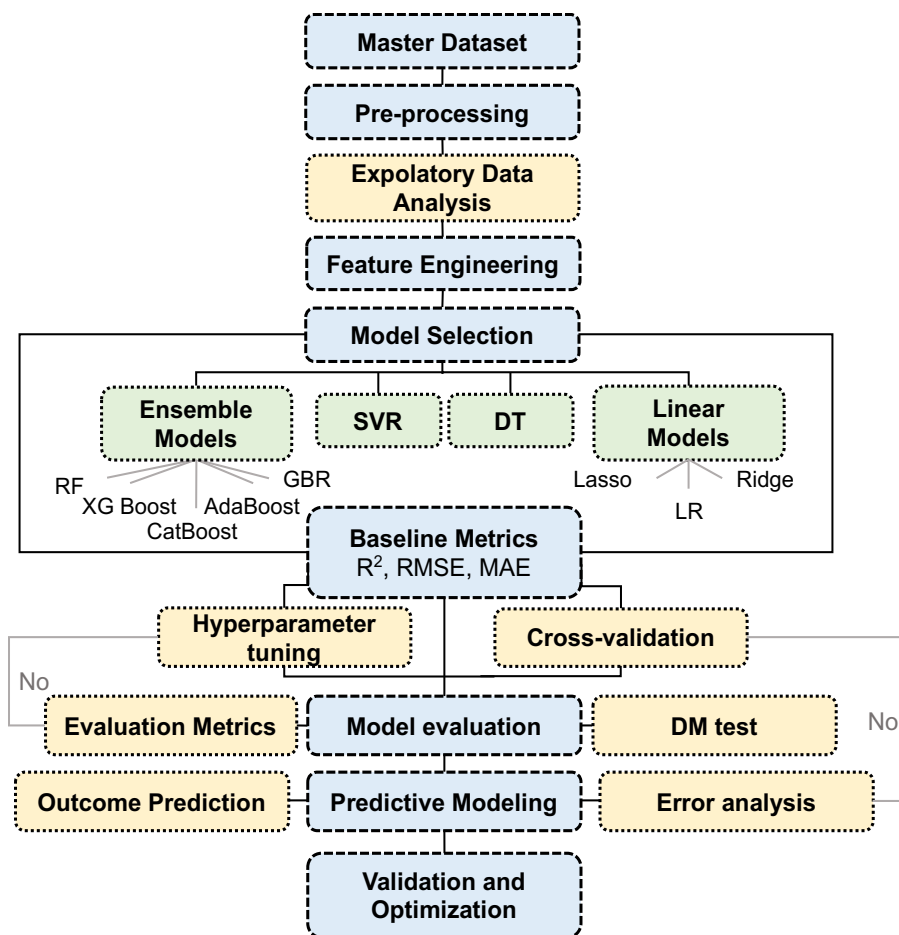
Supplementary Table 5. Screening of stoichiometry effects on glycosylation selectivity across matching partners varying RRV and Aka scale.



		4-OH-Gal 56	Ph 55	4-OH-Glc 54	6-OH-Glc 53	MeOH 51				
Glycosylating agent	<i>equiv.</i>	α -ratio(%) (yield)	α -ratio(%) (yield)	α -ratio(%) (yield)	α -ratio(%) (yield)	α -ratio(%) (yield)				
 A RRV = 270	1:0.66	34% (75%)	100% (35%)	33% (83%)	35% (75%)	0% (30%)				
	1:1.5	28% 62%	87% (69%)	25% (66%)	20% (78%)	0% (62%)				
 B RRV = 2656	1:0.66	75% (50%)	77% (68%)	33% (78%)	33% (75%)	0% (52%)				
	1:1.5	72% (52%)	66% (84%)	45% (77%)	30% (86%)	0% (82%)				
 D RRV = 72000	1:0.66	77% (75%)	100% (53%)	91% (65%)	78% (66%)	21% (50%)				
	1:1.5	66% (87%)	100% (72%)	91% (61%)	73% (91%)	62% (93%)				
 E RRV = 10 ⁶	1:0.66	91% (52%)	100% (37%)	92% (80%)	83% (71%)	30% (66%)				
	1:1.5	86% (65%)	100% (64%)	90% (76%)	78% (74%)	83% (38%)				
α -ratio(%)= 100- β -ratio (%).		100	+80	+60	+50	α (%)	-40	-60	-80	100

Stoichiometry modulates glycosylation outcomes by influencing the availability of reactive intermediates and the competition between glycosylating agents and alcohols. At low agent-to-alcohol ratios (1:0.66), the reduced agent concentration leads to enhanced alcohol competition and limited intermediate stabilization, favoring β -selectivity through kinetic-controlled pathways. Low RRV agents prevails β -selectivity, attributed to a constrained reaction environment and higher likelihood of backside nucleophilic attack. As the ratio increases, intermediate stabilization improves, and the transition to mixed control emerges, facilitating α -selectivity improvements (+45%) and moderate yield increases (+39%) for mid-RRV glycosylating agents. At higher agent ratios, the excess of agent molecules reduces competition, ensuring efficient oxocarbenium ion formation and enhanced α -product. This mechanistic shift results in maximized α -ratios and yields (+51%), reflecting improved intermediate accessibility and prolonged reaction efficacy.

2.6 Comparative performance analysis of ML models in predicting data-driven glycosylation outcomes

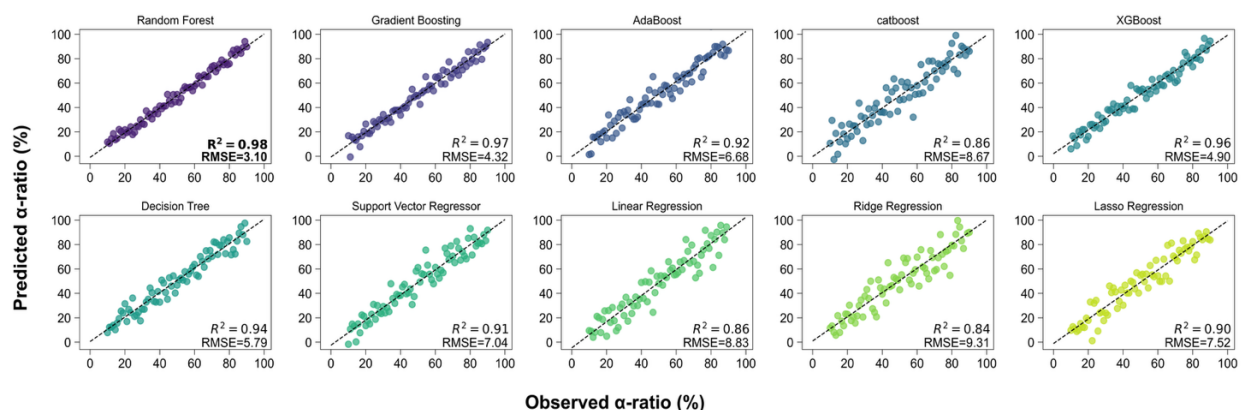


Supplementary Figure 4. Machine learning pipeline for predictive modeling of glycosylation outcomes. The schematic outlines the complete workflow adopted for constructing, evaluating, and optimizing machine learning (ML) models aimed at predicting glycosylation reaction outcomes (e.g., α -ratio). The process begins with a curated master dataset, followed by standard pre-processing steps to ensure data integrity. Exploratory data analysis (EDA) is performed to uncover underlying patterns and guide feature engineering, where domain-specific variables such as RRV, Aka, EFI, temperature, and solvent are computed or selected. Subsequent model selection involves benchmarking multiple algorithm classes, including support vector regression (SVR), decision trees (DT), linear models, and ensemble methods (e.g., random forest, XGBoost). Models are first trained and evaluated using baseline metrics such as R², root mean square error (RMSE), and mean absolute error (MAE). Models failing to meet performance thresholds undergo hyperparameter tuning or k-fold cross-validation to improve generalizability. Statistical robustness is validated via the Diebold-Mariano (DM) test and evaluation metrics. Following this, predictive modeling and error analysis are conducted, leading to final model optimization. The output is a robust, interpretable model for accurate glycosylation outcome prediction, with applications in reaction design and optimization.

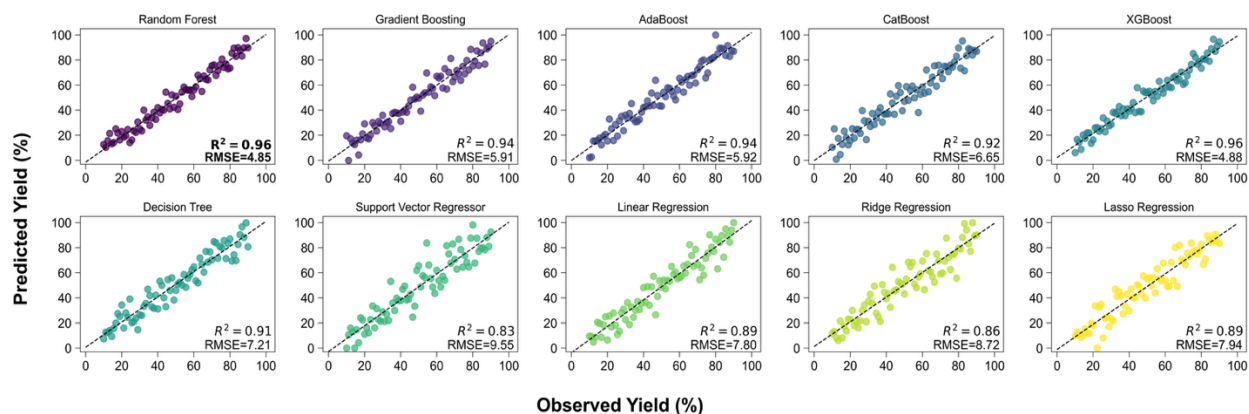
Supplementary Table 6. Molecular and reaction descriptors used to train the models.

Variable	Feature Name
x1	C1-functionality_donor
x2	C1_configuration_donor
x3	C2- functionality_donor
x4	C2_configuration_donor
x5	C3-functionality_donor
x6	C4-functionality_donor
x7	C4_configuration_donor
x8	C6-functionality_donor
x9	RRV
x10	C1-functionality_acceptor
x11	C1_configuration_acceptor
x12	C2- functionality_ acceptor
x13	C3-functionality_ acceptor
x14	C4-functionality_ acceptor
x15	C6-functionality_ acceptor
x16	Alcohol_position
x17	Alcohol_type
x18	Aka
x19	Temperature
x20	Solvent
x21	Concentration
x22	Stoichiometry
x23	Promoter
x24	EFI
y1	α -ratio
y2	Yield

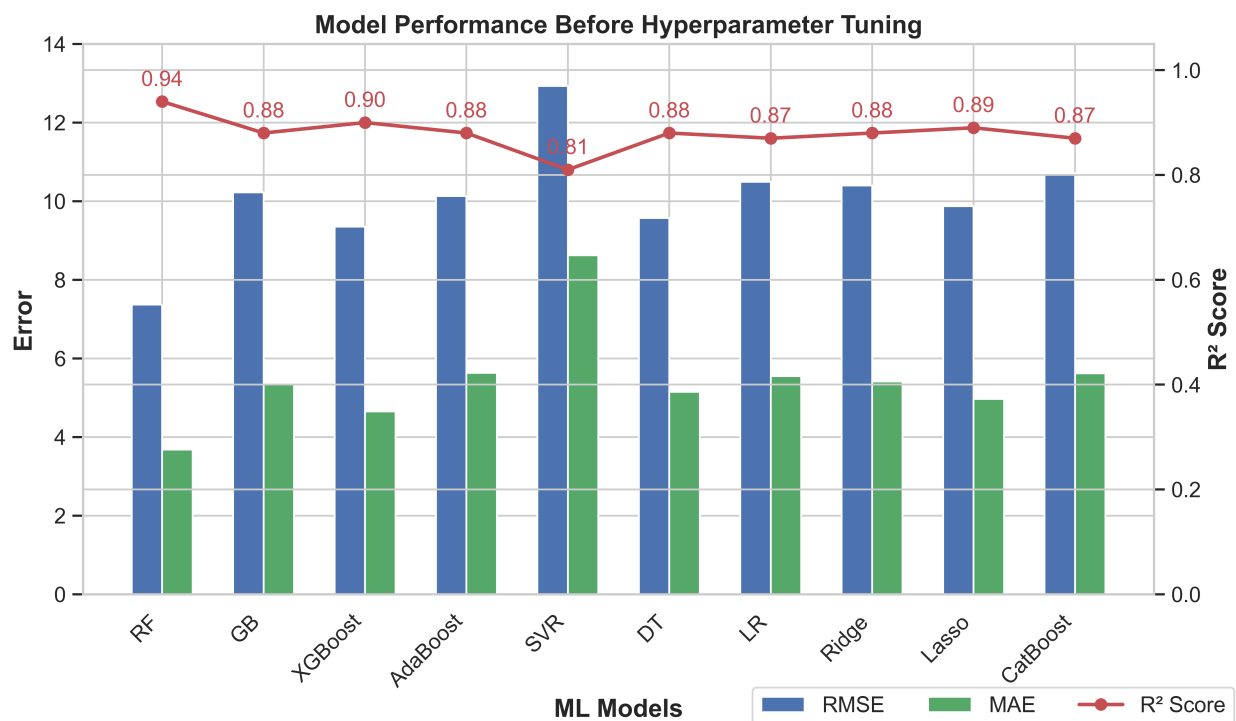
Donor, glycosylating agent; acceptor, nucleophilic alcohol.



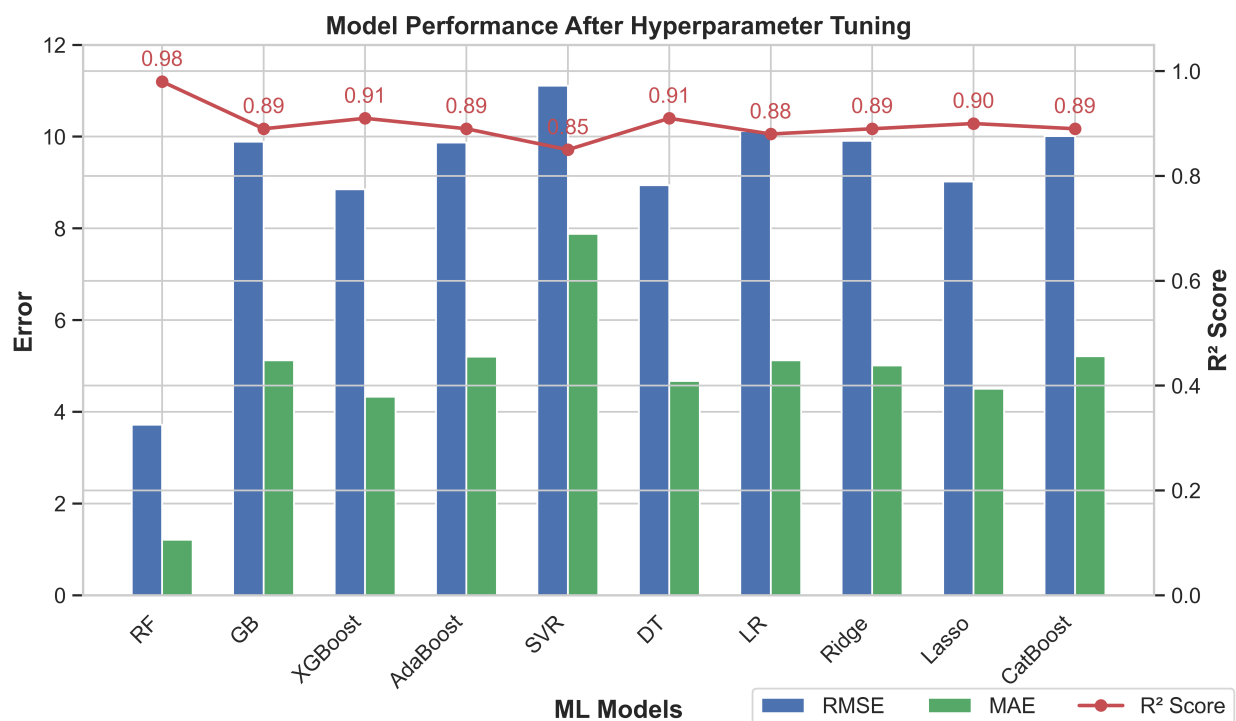
Supplementary Figure 5. Prediction of glycosylation stereoselectivity (α -ratio, %) using 10 individual machine learning models. Each subplot compares predicted versus observed α -ratio values across the test set. Performance is evaluated using coefficient of determination (R^2) and root mean squared error (RMSE). Ensemble tree-based models (e.g., Random Forest, Gradient Boosting) generally outperform linear models followed by XGBoost, reflecting their ability to capture non-linear structure-reactivity relationships.



Supplementary Figure 6. Prediction of glycosylation reaction yield (%) using 10 individual machine learning models. Predicted versus observed yield values are shown across the test set for each model. Performance metrics (R^2 and RMSE) demonstrate that ensemble tree-based models, particularly Random Forest and XGBoost ($R^2 = 0.96$, RMSE ≈ 4.85 –4.88), offer superior predictive accuracy compared to linear or kernel-based methods, highlighting their ability to model nonlinear, context-dependent reaction efficiencies.



Supplementary Figure 7. Comparison of machine learning model performance prior to hyperparameter tuning. Bar plots show the root mean square error (RMSE, blue) and mean absolute error (MAE, green) for each of the 10 machine learning models evaluated on α -ratio prediction. The red line overlay indicates the R^2 score for each model. Random Forest (RF), XGBoost, and Linear Regression (LR) achieved the highest R^2 values (0.90), while Support Vector Regression (SVR) exhibited the lowest performance ($R^2 = 0.81$) with the highest RMSE and MAE. These baseline results illustrate the relative capacity of each model to capture underlying relationships before optimization of models on the glycosylation dataset.



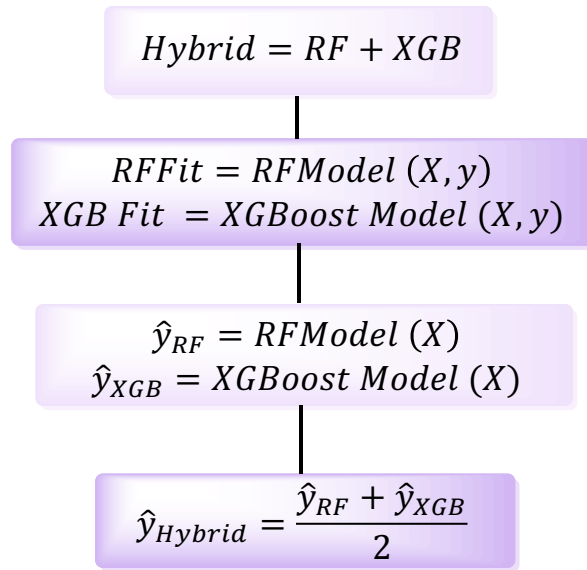
Supplementary Figure 8. Machine learning model performance after hyperparameter tuning for α -ratio prediction. Post-tuning evaluation of 10 models reveals improved accuracy across most metrics. Bar plots represent RMSE (blue) and MAE (green), while the red line indicates R^2 score. Random Forest (RF) shows the best overall performance with the highest R^2 (0.92) and lowest RMSE and MAE. XGBoost and Decision Tree (DT) also improved significantly after tuning ($R^2 = 0.91$). Support Vector Regression (SVR) remains the least performant model ($R^2 = 0.85$), though with reduced error. These results highlight the effectiveness of hyperparameter optimization in enhancing model generalization and predictive power.

Supplementary Table 7. Summary of Hyperparameter Configurations and Tuning Strategies for All Regression Models.

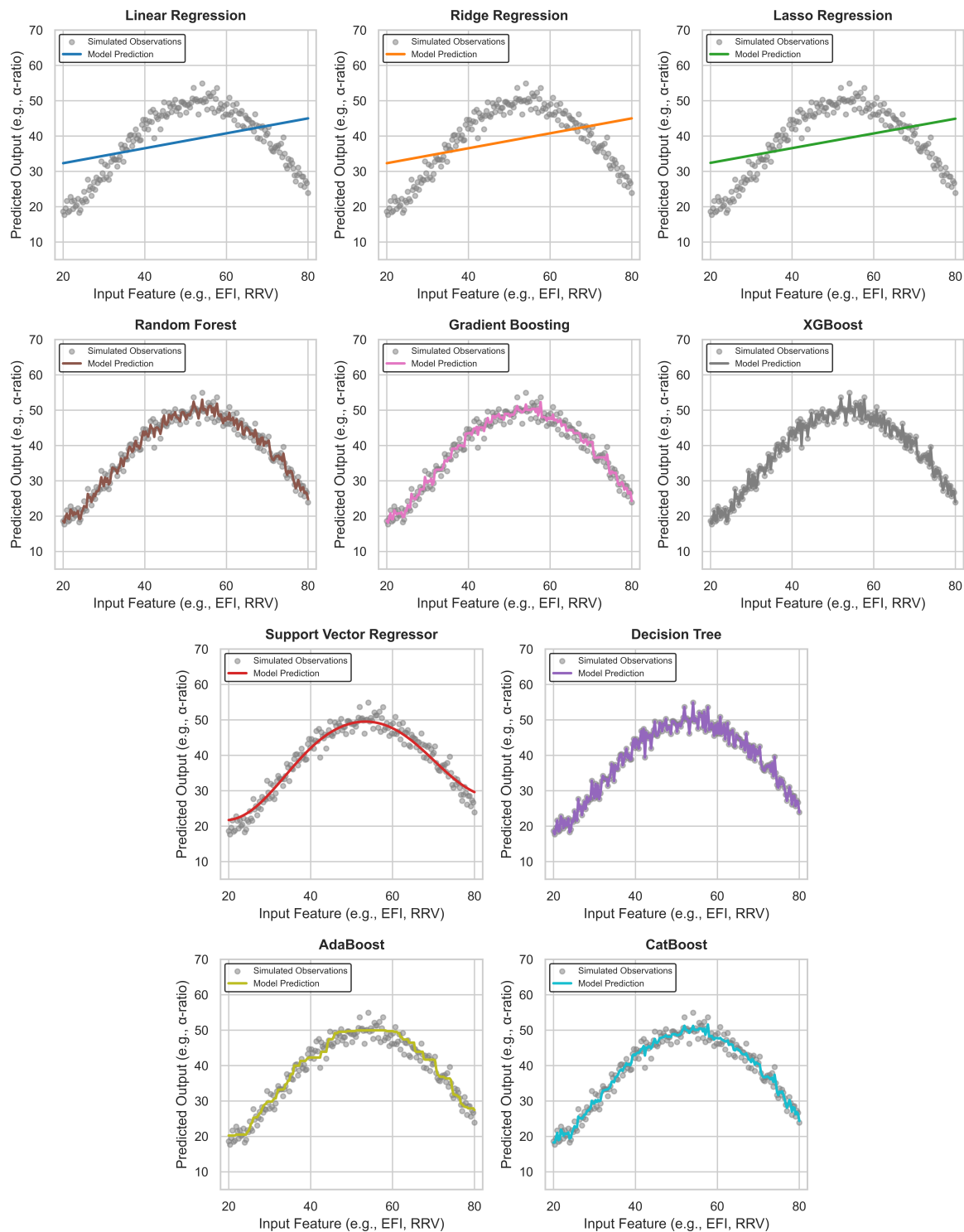
Model	Hyperparameter	Value	Tuning Strategy
Linear Regression	Regularization	None	No tuning required
Ridge Regression	alpha	10.0	Tuned via CV from [0.01, 0.1, 1, 10, 100]
Lasso Regression	alpha	0.1	Tuned via CV from [0.001, 0.01, 0.1, 1]
Support Vector Regressor	kernel	rbf	Best for non-linear data
Support Vector Regressor	C	10	Tuned via grid search
Support Vector Regressor	epsilon	0.1	Tested range: [0.01, 0.05, 0.1]
Decision Tree	max_depth	5	Tuned manually based on validation error
Decision Tree	min_samples_split	20	Tuned to reduce overfitting
Decision Tree	min_samples_leaf	10	Tuned for generalization
Random Forest	n_estimators	1000	Tuned for stable performance
Random Forest	max_depth	None	Allow deep trees, tested shallower variants
Random Forest	min_samples_leaf	1	Default; tested up to 10
Random Forest	max_features	sqrt	Best balance of bias/variance
Random Forest	oob_score	TRUE	Used for internal validation
Gradient Boosting	n_estimators	500	Tuned with early stopping
Gradient Boosting	learning_rate	0.05	Balanced speed and accuracy
Gradient Boosting	max_depth	5	Tuned for bias-variance tradeoff
XGBoost	n_estimators	500	Tuned with early stopping
XGBoost	learning_rate	0.05	Optimal via validation
XGBoost	max_depth	5	Avoided overfitting
XGBoost	subsample	0.9	Improves robustness
XGBoost	colsample_bytree	0.8	Controls tree diversity
XGBoost	reg_alpha	1	Regularization term
XGBoost	reg_lambda	1	Regularization term
AdaBoost	n_estimators	300	Stable after tuning
AdaBoost	learning_rate	0.5	Balanced under/overfitting
CatBoost	iterations	500	Tuned with early stopping
CatBoost	depth	5	Tested [4–8], best performance
CatBoost	learning_rate	0.05	Best trade-off
CatBoost	l2_leaf_reg	3	Controls regularization

This table lists the key hyperparameters applied to each regression model within the study, along with the corresponding values and the tuning strategies or rationale behind their selection.

Conventional models such as Linear, Ridge, and Lasso regression required minimal tuning, while ensemble and kernel-based models (e.g., Random Forest, XGBoost, CatBoost, SVR) underwent extensive grid or cross-validation–based optimization. For Random Forest, out-of-bag (OOB) validation was used to monitor generalization without relying on an external holdout set. Parameters were tuned to balance model complexity, reduce overfitting, and enhance predictive performance on both α -ratio and yield targets. Early stopping and regularization terms were emphasized for boosting-based methods to avoid overfitting on small or noisy datasets.

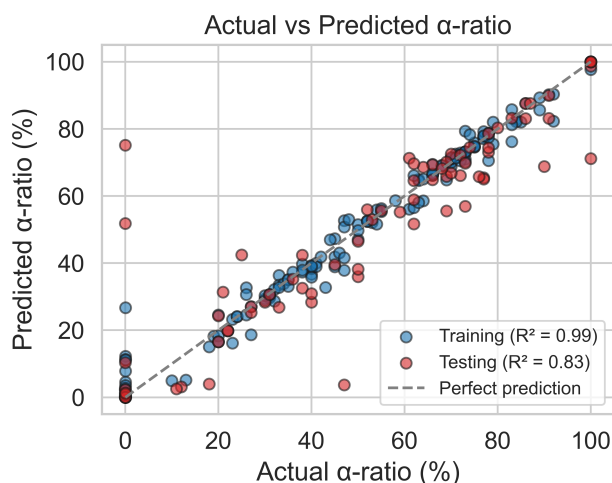


Supplementary Figure 9. Flowchart depicting the development of the hybrid model combining Random Forest (RF) and XGBoost. The process involves initializing the model, training both algorithms, generating individual predictions, and averaging them to form the final unified hybrid prediction.

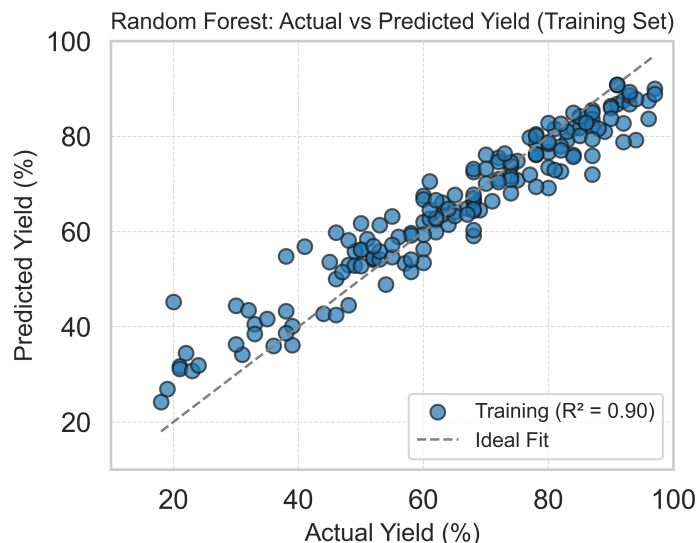


Supplementary Figure 10. Visualization of model behavior on non-linear data. Plots show input–output relationships to understand *non-linearity* in dataset, such as solvent or alcohol type to α -ratio. To evaluate how different ML models respond to non-linear trends often observed in

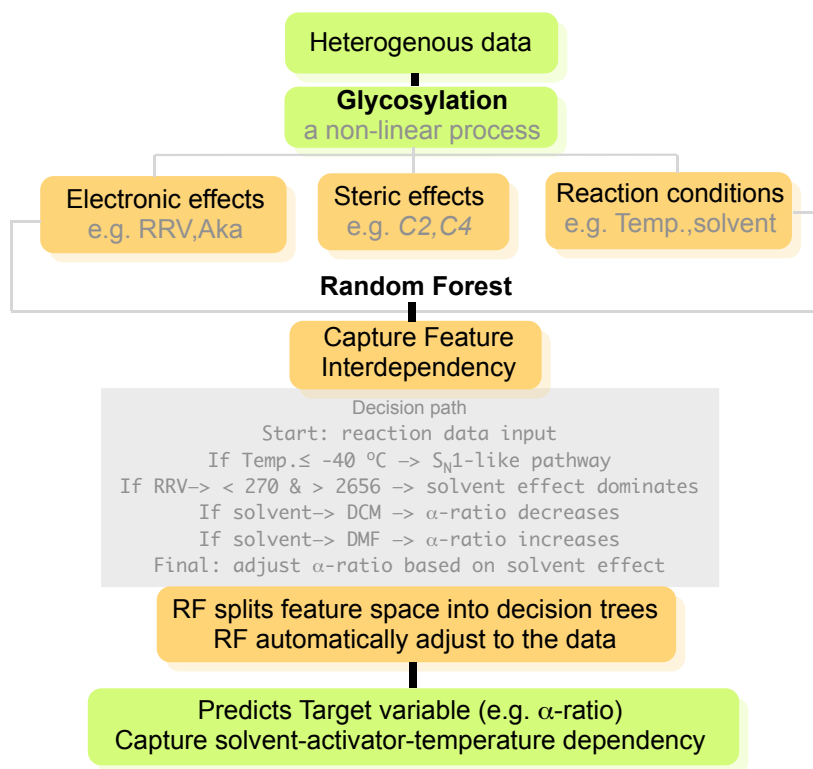
glycosylation data (e.g., solvent or alcohol type influencing α -ratio), we trained ten models on a simulated dataset with a sinusoidal pattern and added noise. The linear models including Linear Regression, Ridge, and Lasso showed strong underfitting, as evident from their inability to capture the curve. These models apply fixed functional forms, making them inadequate for representing complex chemical systems where dependencies between input and output are non-linear. In contrast, non-linear models showed varying degrees of success. Support Vector Regressor (SVR) captured curvature better but lacked the flexibility to model sharper transitions. Decision Tree, while adaptive, exhibited abrupt, step-wise predictions indicating overfitting to local patterns. The ensemble-based models including Random Forest, Gradient Boosting, XGBoost, AdaBoost, and CatBoost offered significant improvements. Among them, Random Forest provided the most consistent and smooth approximation, effectively balancing bias and variance. These results reinforce the suitability of tree-based ensemble learners, particularly Random Forest, in modeling the intricate relationships governing glycosylation.



Supplementary Figure 11. Training and test α -ratio (%) prediction using the Random Forest model for non-linear data. Blue and red points represent the training and testing datasets with 70/30 (%) data splitting, respectively. The dashed gray line indicates perfect prediction ($y = x$). The model achieved excellent predictive performance, with $R^2 = 0.99$ for the training set and $R^2 = 0.83$ for the testing set, indicating strong generalization and minimal overfitting.

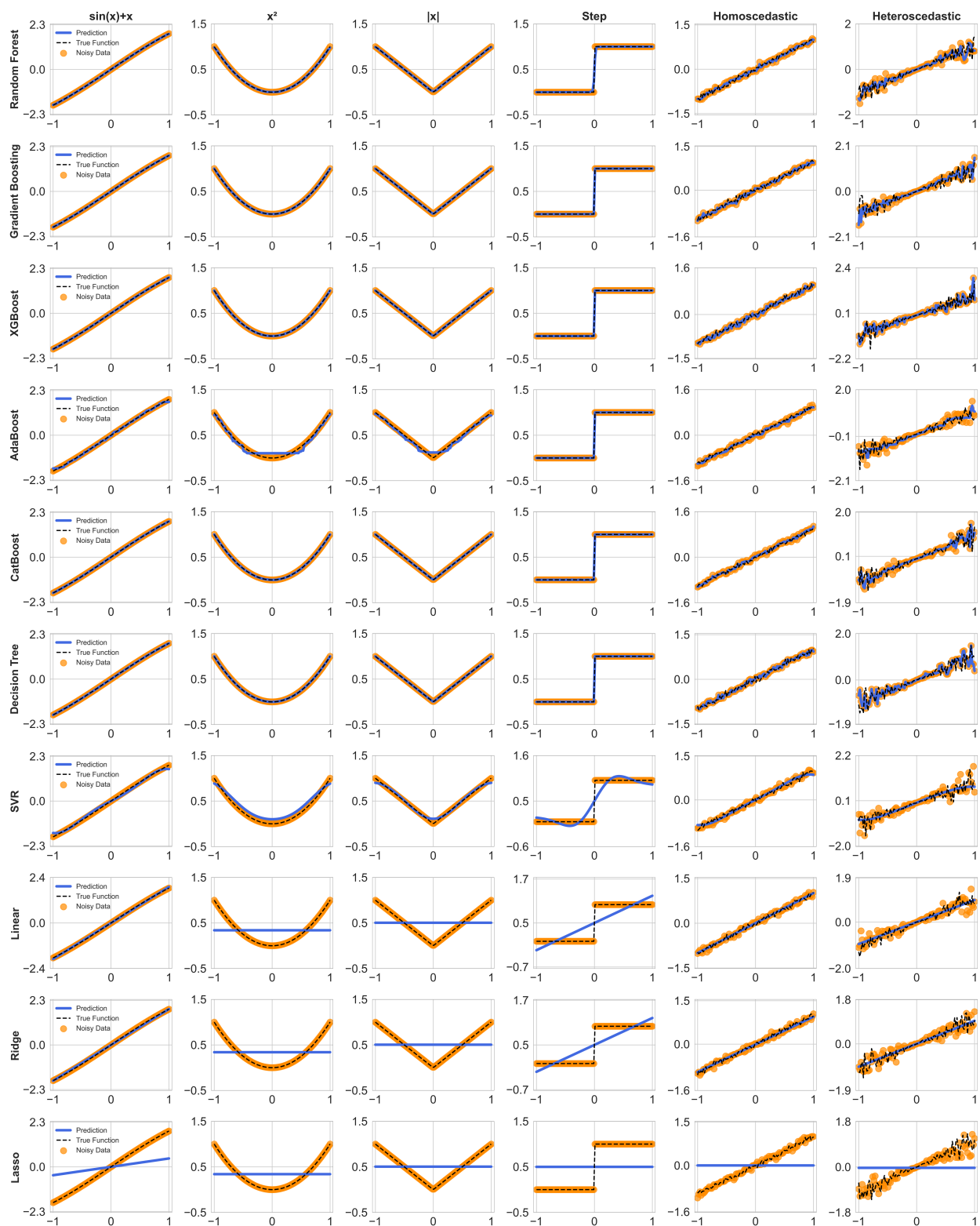


Supplementary Figure 12. Scatter plot comparing actual and predicted reaction yields (%) for the training dataset using a Random Forest model for non-linear data. Each blue point represents a training sample with 70/30 (%) data splitting. The gray dashed line indicates perfect prediction ($y = x$). The model achieved an R^2 of 0.90 on the training set, indicating a strong fit to the training data with minimal residual error.



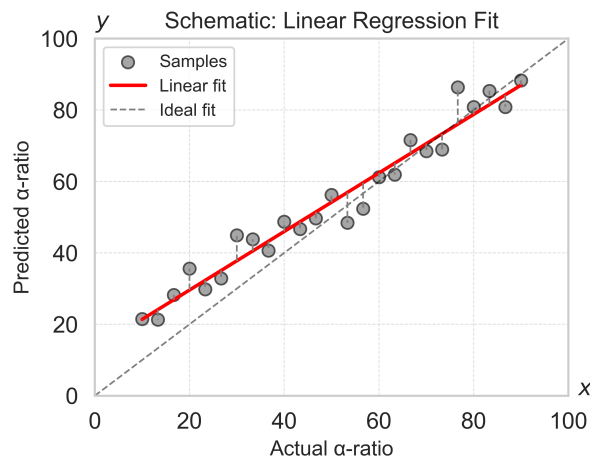
Supplementary Figure 13. Random Forest model architecture for capturing nonlinear dependencies in glycosylation reactions. Heterogeneous input features including electronic

parameters (e.g., relative reactivity value, RRV; nucleophilicity constant, A_{N}), steric descriptors (e.g., C2, C4 substitution), and reaction conditions (e.g., temperature, solvent) are integrated into the RF framework. The model captures feature interdependencies and partitions the feature space into decision trees, adjusting automatically to the data. Example decision paths illustrate how RF encodes mechanistic relationships such as temperature thresholds, solvent polarity, and RRV-based switching to predict glycosylation selectivity (e.g., α -ratio), enabling solvent–promoter–temperature dependent modeling.

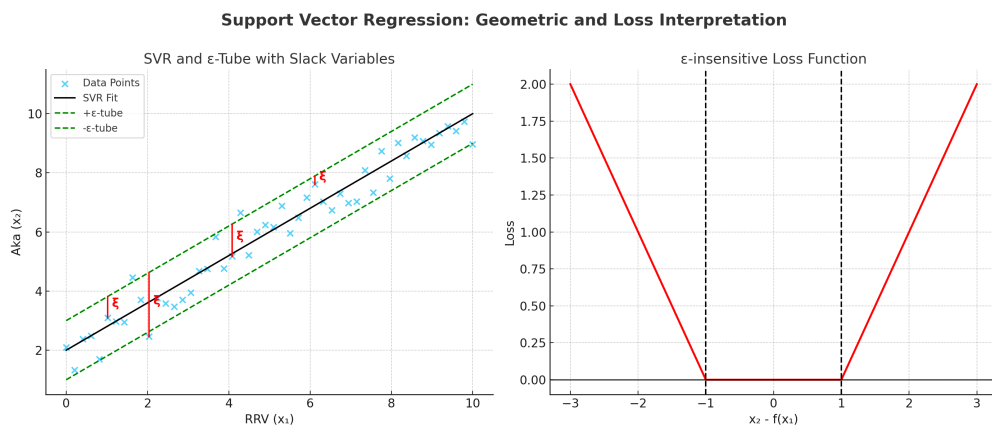


Supplementary Figure 14. Qualitative analysis of all ML models based on 600 batch glycosylation reactions over 5 noise types.

2.7 Core ML model schematics

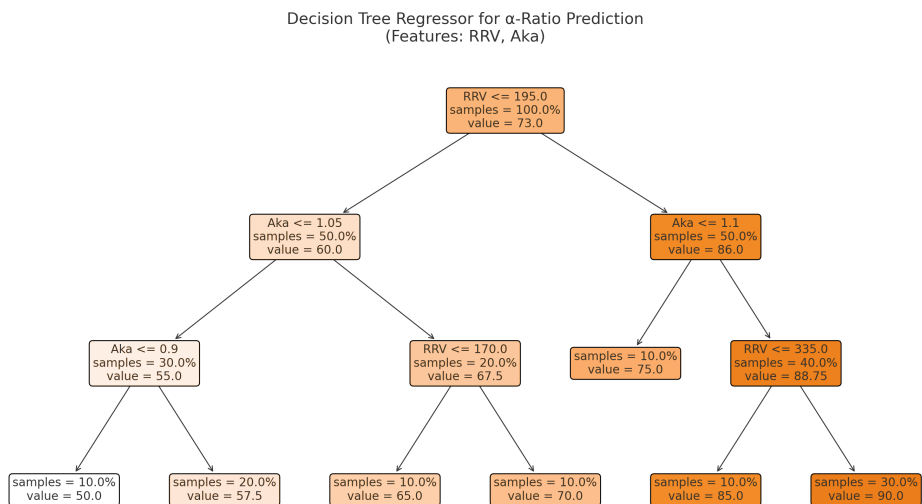


Supplementary Figure 15. Linear regression applied to glycosylation data. This figure illustrates a linear regression model applied to glycosylation data. The x-axis represents the composite input features influencing the stereoselectivity (e.g., *actual or observed* α -ratio), while the y-axis represents the experimental output [*predicted* α -ratio (%)], our target value. Each grey point is an individual glycosylation observation. The red line denotes the fitted linear regression model that minimizes squared error between the predicted and actual α -ratio values. Horizontal black bars reflect the conditional mean of the α -ratio within specified feature intervals.

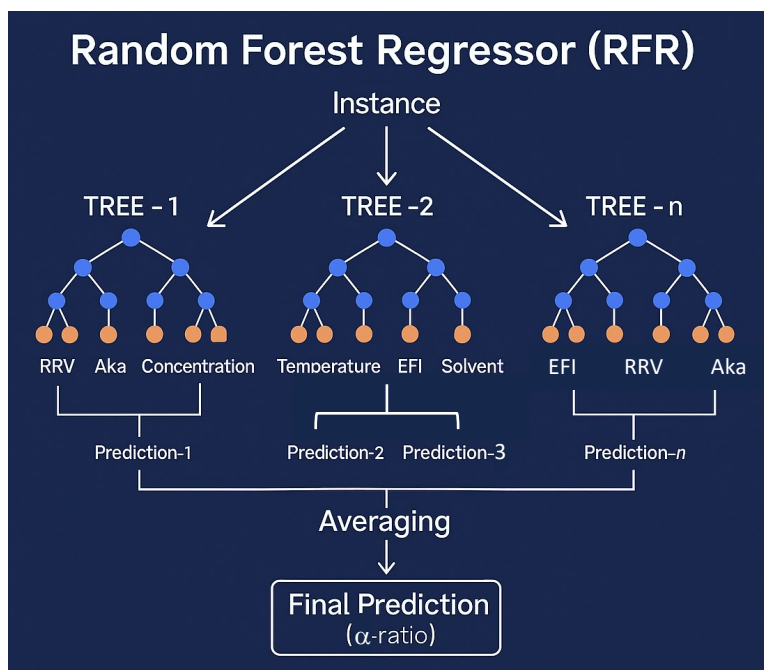


Supplementary Figure 16. Support vector regression (SVR) and ϵ -insensitive loss. Left: The schematic illustrates the SVR concept using a two-dimensional feature space, where the black line represents the regression function. The green boundaries indicate the ϵ -insensitive region (ϵ -tube), within which prediction errors are not penalized. Red stars denote observed data points, and those falling outside the ϵ -tube incur a penalty quantified by slack variables. These slack variables reflect the magnitude by which predictions violate the ϵ -bound and contribute to the total model loss. SVR seeks to minimize the norm of the weight vector while maintaining prediction errors within

the ε -tube whenever possible, thus achieving a balance between model complexity and prediction accuracy. Right: The ε -insensitive loss function. The horizontal axis represents the deviation of predicted values from actual values, while the vertical axis denotes loss. The loss remains zero for deviations within the ε -margin (between $-\varepsilon$ and $+\varepsilon$) and increases linearly beyond that range, as defined by the absolute error beyond ε . This loss structure enables SVR to be robust to small fluctuations and noise, which is particularly relevant in chemical datasets where minor variations in experimental conditions may not significantly impact the mechanistic understanding but could otherwise distort a sensitive model.



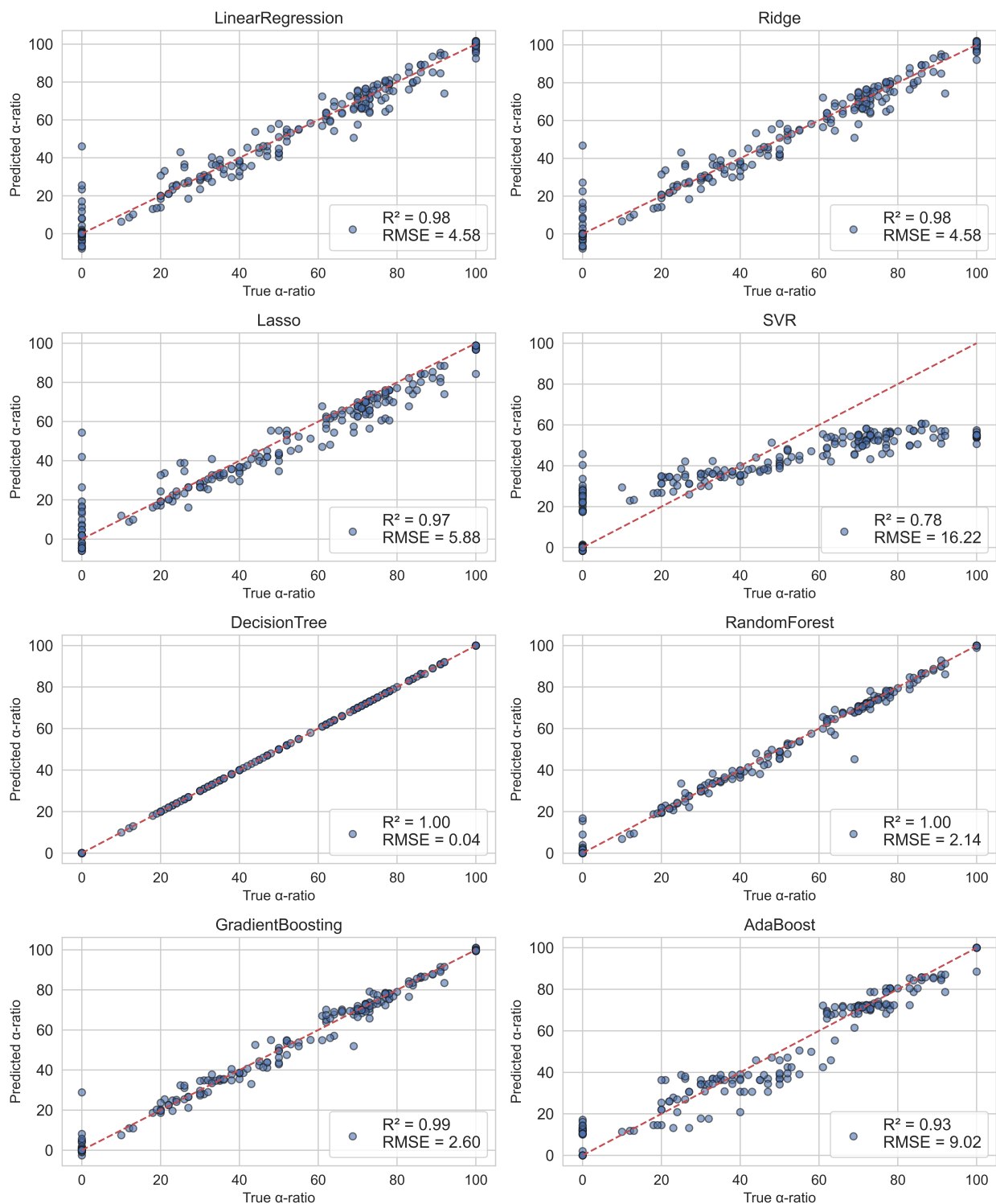
Supplementary Figure 17. A Decision Tree regression model. This was constructed to predict α -ratio outcomes from glycosylation reactions based on key reactivity parameters: the Relative Reactivity Value (RRV) of the glycosylating agent and the nucleophilicity constant (Aka) of the alcohol. The Decision Tree (DT) algorithm partitions the data by applying hierarchical, threshold-based splits (e.g., $RRV < 2656$, $Aka < 1.36$), resulting in a tree structure where each terminal node corresponds to a predicted α -ratio. This model provides a transparent and interpretable mapping between input descriptors and predicted stereoselectivity. The tree captures non-linear dependencies and interaction effects without requiring prior assumptions on variable distributions, reflecting the context-specific reactivity landscape of glycosylation. While useful for mechanistic interpretation and rational design, the DT model's predictive capacity may be limited by overfitting, especially in sparse or noisy datasets; ensemble models such as Random Forests are often employed to mitigate this.

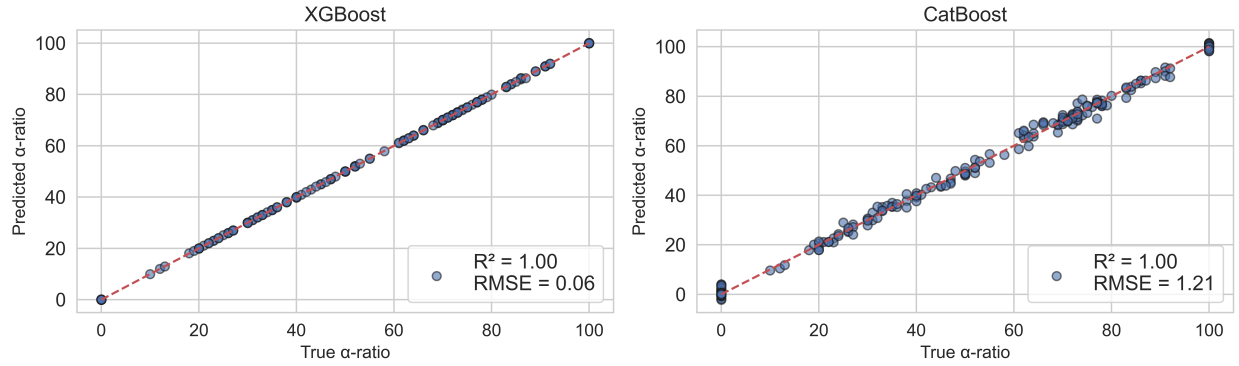


Supplementary Figure 18. Random Forest Regressor (RFR) architecture. An ensemble of decision trees ($\text{Tree}_1, \text{Tree}_2, \dots, \text{Tree}_n$) is shown, where each tree receives the same input instance characterized by features such as RRV (relative reactivity value), Aka (acceptor nucleophilicity constant), concentration, temperature, solvent, and EFI (Environmental Factor Impact index). These features serve as decision nodes throughout the trees. Each tree independently produces a prediction (Prediction-1 to Prediction- n) based on its structure and selected features. The final output is obtained by averaging all individual predictions to generate a robust and accurate α -ratio prediction. This ensemble approach enables the model to capture non-linear and context-dependent interactions among variables while mitigating the risk of overfitting.

2.8 Model performance evaluation on train and validation sets for target prediction

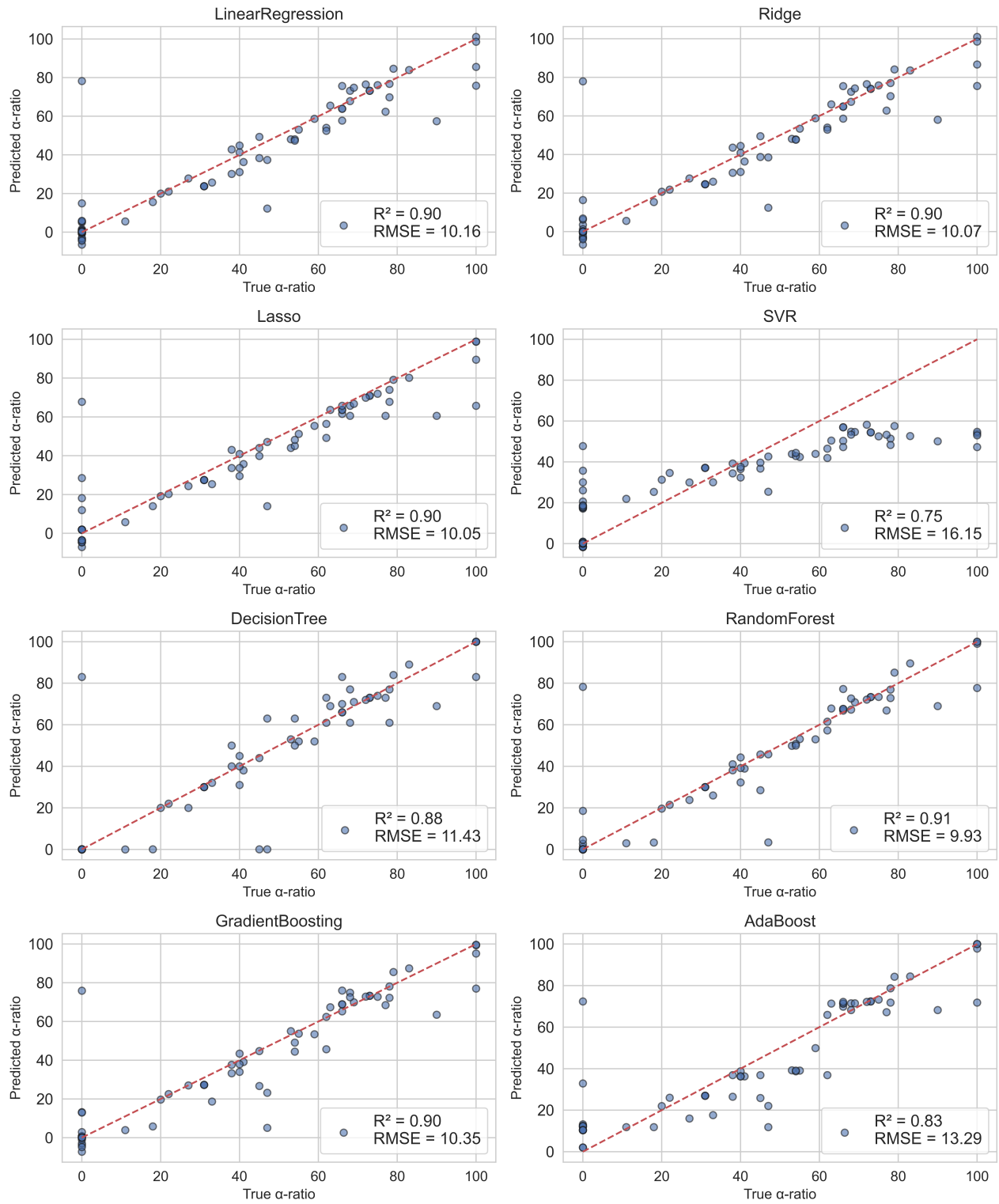
Train: Actual vs Predicted α -ratio for All Models

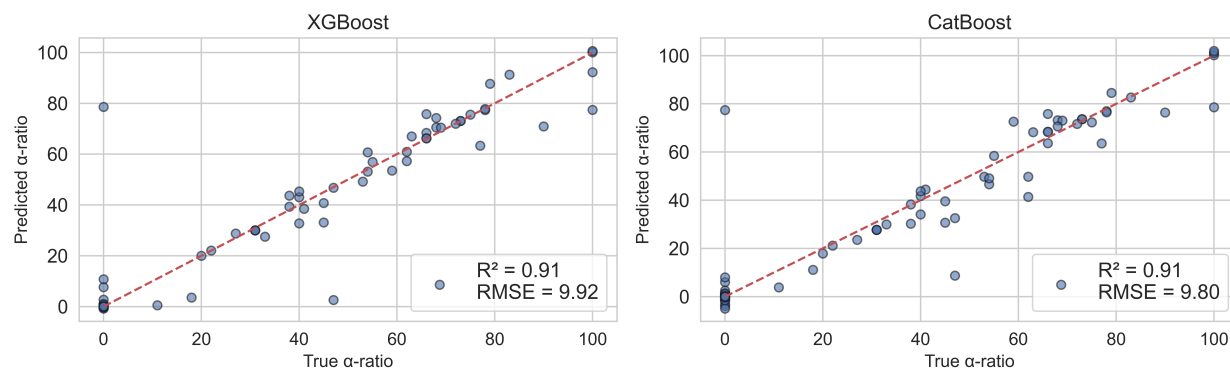




Supplementary Figure 19. Training set evaluation across ten machine learning models for α -ratio (%) prediction. Actual versus predicted α -ratio values for the training dataset using ten different regression models: Linear Regression, Ridge, Lasso, SVR, Decision Tree, Random Forest (RF), Gradient Boosting, AdaBoost, XGBoost, and CatBoost. The diagonal dashed red line indicates the ideal 1:1 relationship. Most models, particularly ensemble-based learners such as RF, XGBoost, and CatBoost, show strong alignment between predicted and observed values, with R^2 values exceeding 0.97 and low RMSEs. Decision Tree achieves a perfect score ($R^2 = 1.00$, $RMSE = 0.04$), suggesting that it has overfit the training data by modeling even minor noise and variance. Linear models (e.g., Ridge and Lasso) achieve reasonable fits, but SVR underperforms ($R^2 = 0.78$), highlighting its limited flexibility in capturing complex nonlinear dependencies. These results demonstrate that models capable of modeling feature interactions and nonlinearity can fit α -ratio effectively on training data, but overfitting must be evaluated on validation performance. So next we performed evaluation of models via validation.

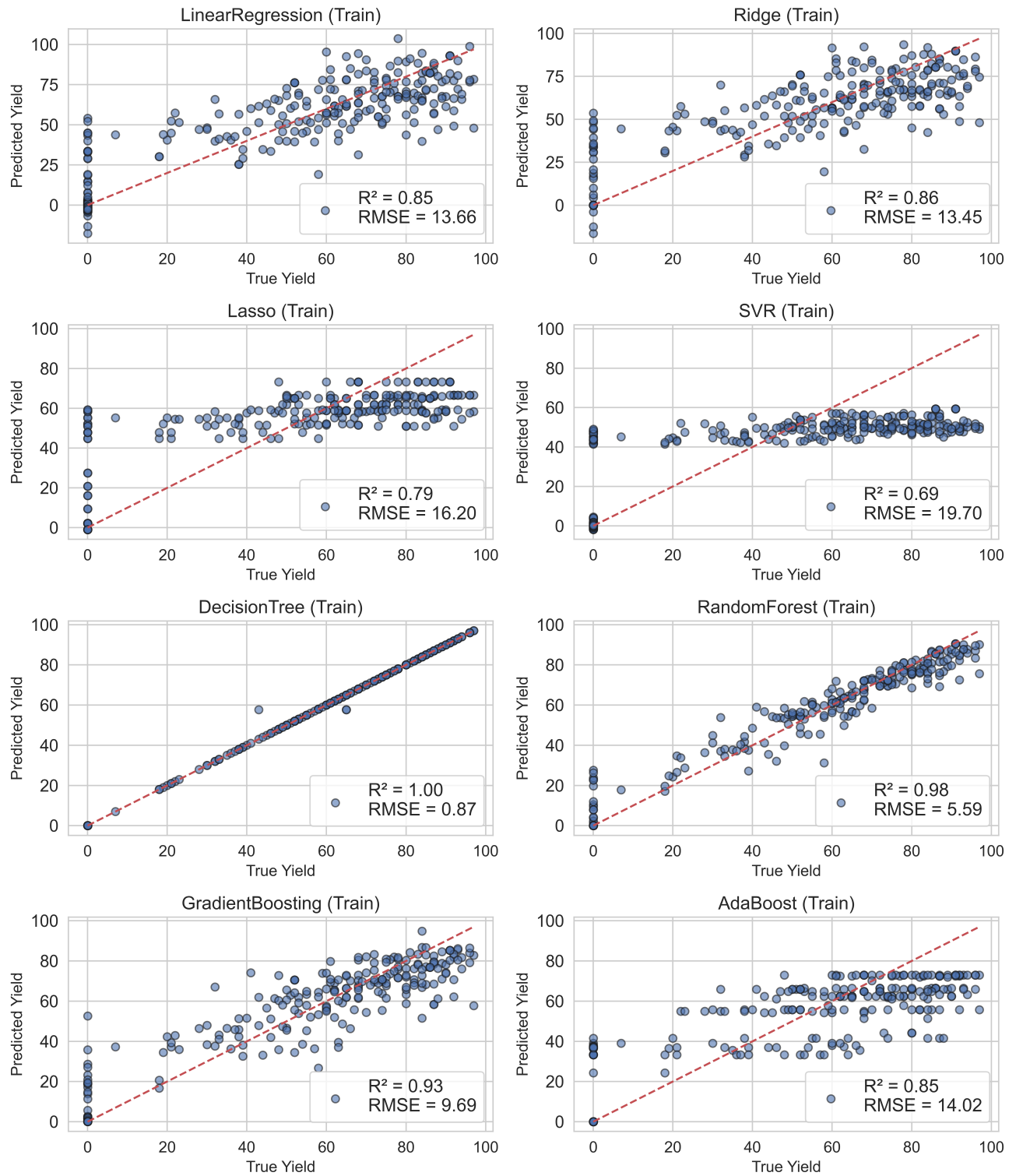
Validation: Actual vs Predicted α -ratio for All Models

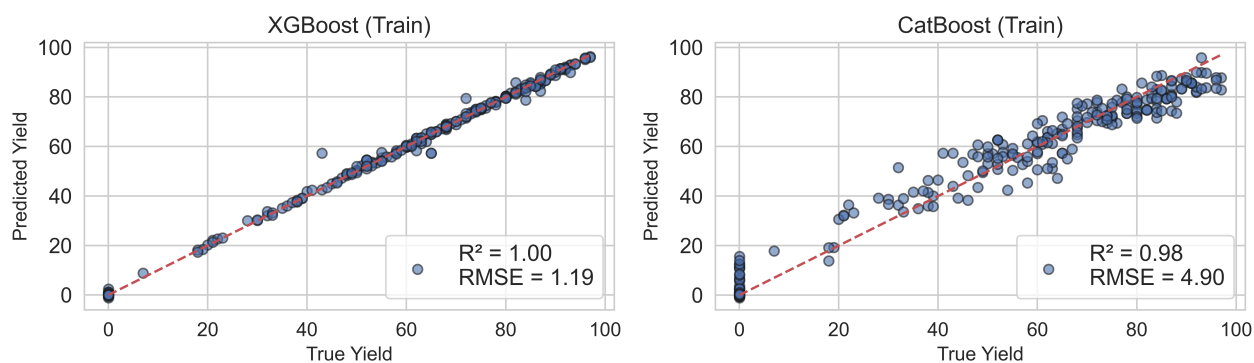




Supplementary Figure 20. Validation set prediction across ten machine learning models for α -ratio (%) prediction. Actual versus predicted α -ratio values for the validation set are plotted for the same ten regression models used in training. RF maintains strong predictive performance ($R^2 = 0.91$, RMSE = 9.93), suggesting effective generalization. In contrast, Decision Tree's performance drops significantly ($R^2 = 0.88$, RMSE = 11.43%), reflecting its poor extrapolation capability due to overfitting. Gradient boosting models (XGBoost, CatBoost) show stable performance with minimal degradation compared to their training results. Linear models (e.g., Ridge, Lasso) and SVR show substantial increases in prediction error and lower R^2 values, indicating reduced robustness when facing unseen data. These findings validate RF's ability to extract stable, generalizable patterns from the descriptor space, while also emphasizing the importance of model complexity control to avoid overfitting in mechanistically intricate prediction tasks like stereoselectivity.

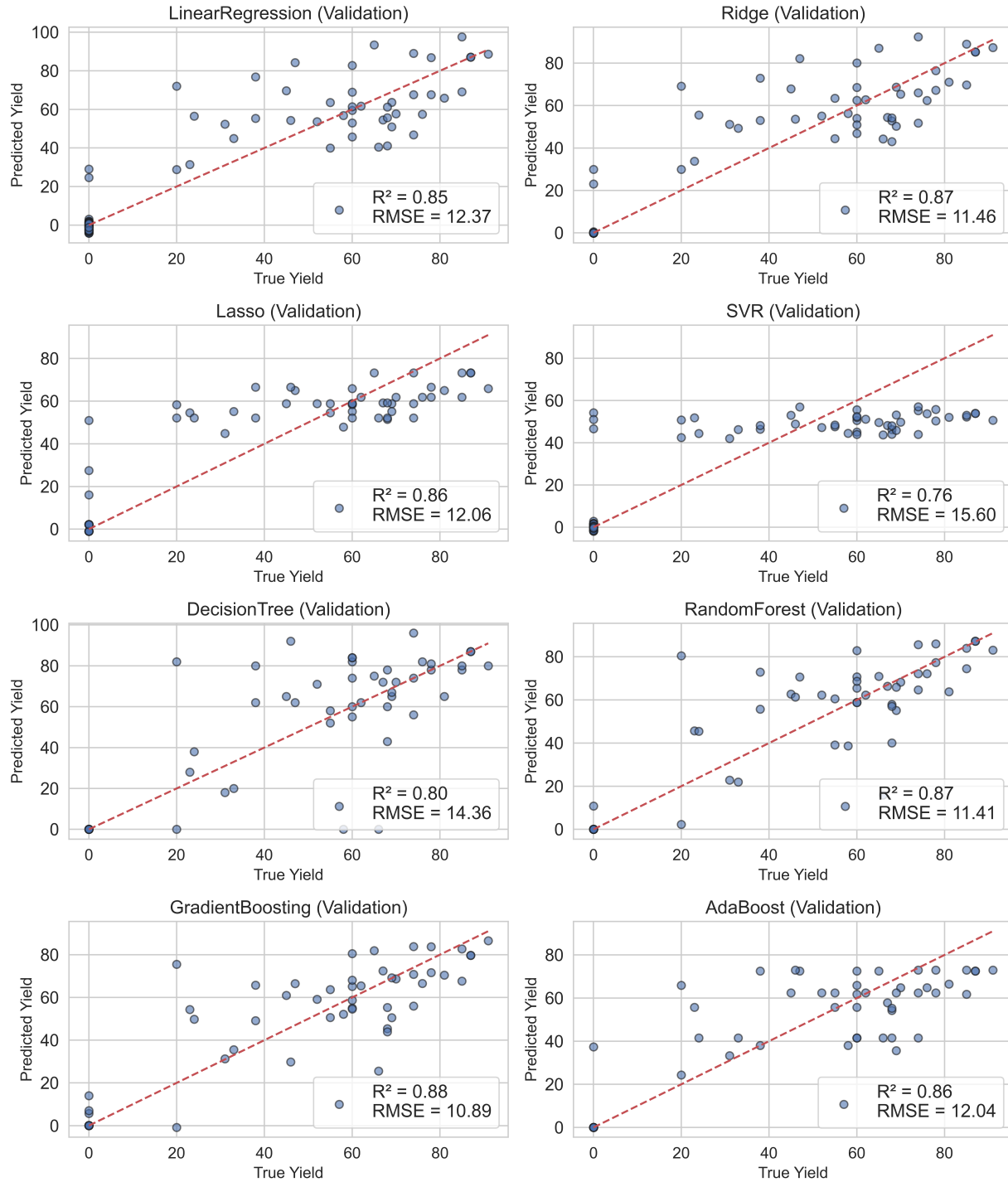
Training: Actual vs Predicted Yield (y2)

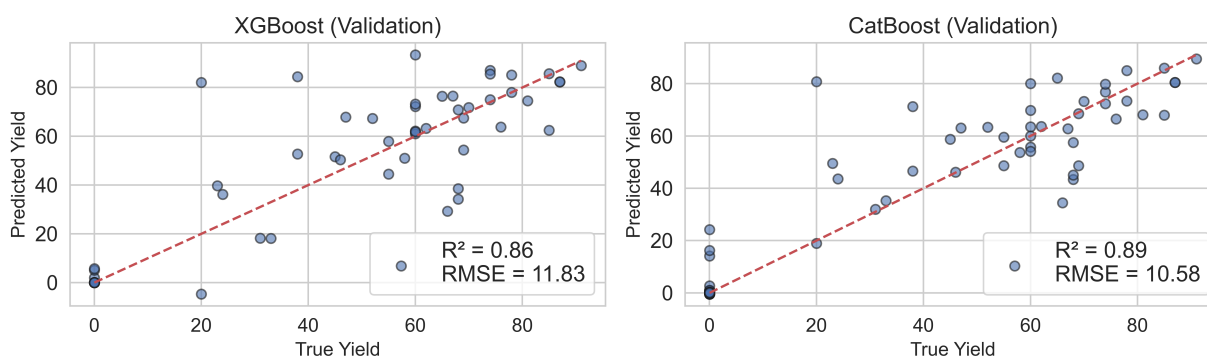




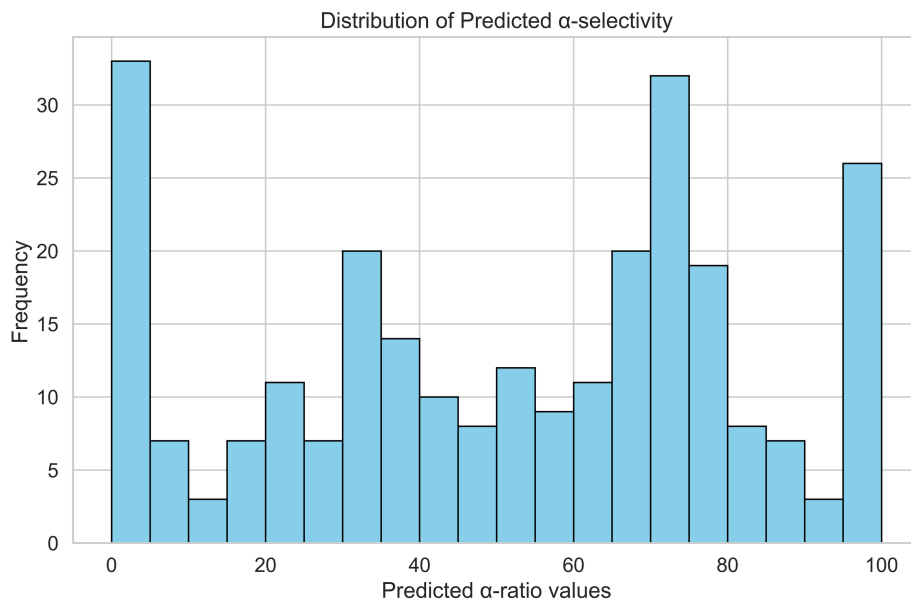
Supplementary Figure 21. Training set evaluation across ten machine learning models for yield (%) prediction. This shows training set performance for yield (y2) prediction using the same ten machine learning models. Yield, compared to α -ratio, introduces greater noise and variance due to experimental uncertainties such as decomposition, solubility issues, and side reactions. Nevertheless, Decision Tree again achieves perfect accuracy ($R^2 = 1.00$, $RMSE = 0.87$), strongly suggesting overfitting. RF achieves high accuracy ($R^2 = 0.98$, $RMSE = 5.59$) while avoiding overfitting, striking a balance between complexity and generalizability. Gradient boosting models perform comparably well. However, models such as SVR, Ridge, and Lasso show increased RMSEs and slightly lower R^2 values, underlining their limited capacity to model non-additive relationships and accommodate variance introduced by reaction conditions. These trends suggest that yield prediction is more challenging than selectivity modeling, requiring methods capable of capturing high-dimensional, nonlinear relationships without overfitting.

Validation: Actual vs Predicted Yield (y2)

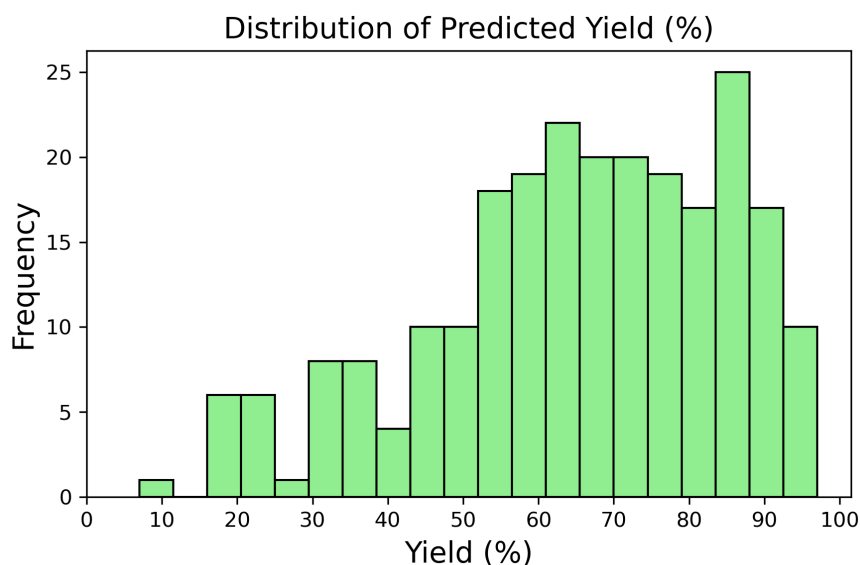




Supplementary Figure 22. Validation set evaluation across ten machine learning models for yield (%) prediction. This figure shows the generalization performance of all ten models on the yield (y2) validation set. RF continues to outperform all others ($R^2 = 0.87$, $RMSE = 11.41$), confirming its robustness in the presence of noisy chemical data. The performance of Decision Tree degrades sharply ($R^2 = 0.80$, $RMSE = 14.36$), reflecting classic overfitting behavior—relatively lower training error but poor generalization. Boosting methods (e.g., CatBoost and XGBoost) retain strong predictive capabilities, albeit with slightly higher variance. SVR, Ridge, and Linear Regression again underperform, particularly in the presence of yield-specific noise. These findings emphasize that while several ML models may fit training data well, only those that balance complexity with structural regularization (e.g., RF and boosting models) deliver reliable predictions under real-world variability. This underscores the importance of assessing model performance on both training and validation sets to ensure robustness, especially for noisy targets like reaction yield.

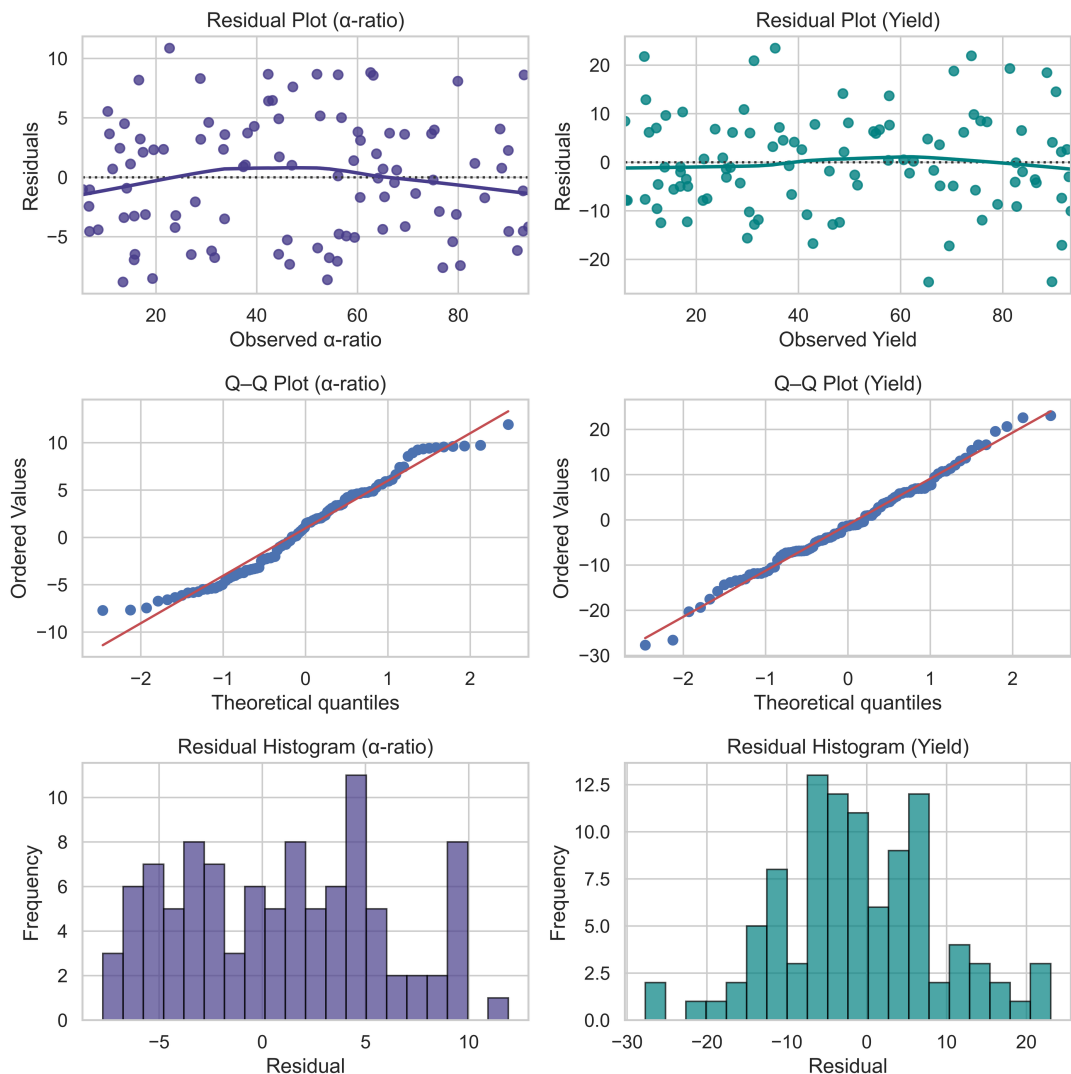


Supplementary Figure 23. Distribution of predicted α -ratio (%) values for new glycosylation reactions. Histogram showing the frequency distribution of machine learning–predicted α -selectivity (α -ratio [%]) values for newly generated glycosylating agent–alcohol pairs, illustrating the diversity and range of model-predicted stereoselectivities across the expanded chemical space. The values shows coverage across the diverse range and exhibits a bimodal pattern consistent with mechanistic expectations, while yield predictions are skewed toward higher conversion regions.



Supplementary Figure 24. Distribution of predicted yield (%) values for new glycosylation reactions. This distribution highlights the model’s predictions over an expanded chemical space, with most reactions yielding between 50–90%. The broad spread reflects the complexity and variability of reaction efficiency due to subtle interactions among structural features and contextual parameters (e.g., solubility, side-product formation). In contrast to α -selectivity, yield predictions

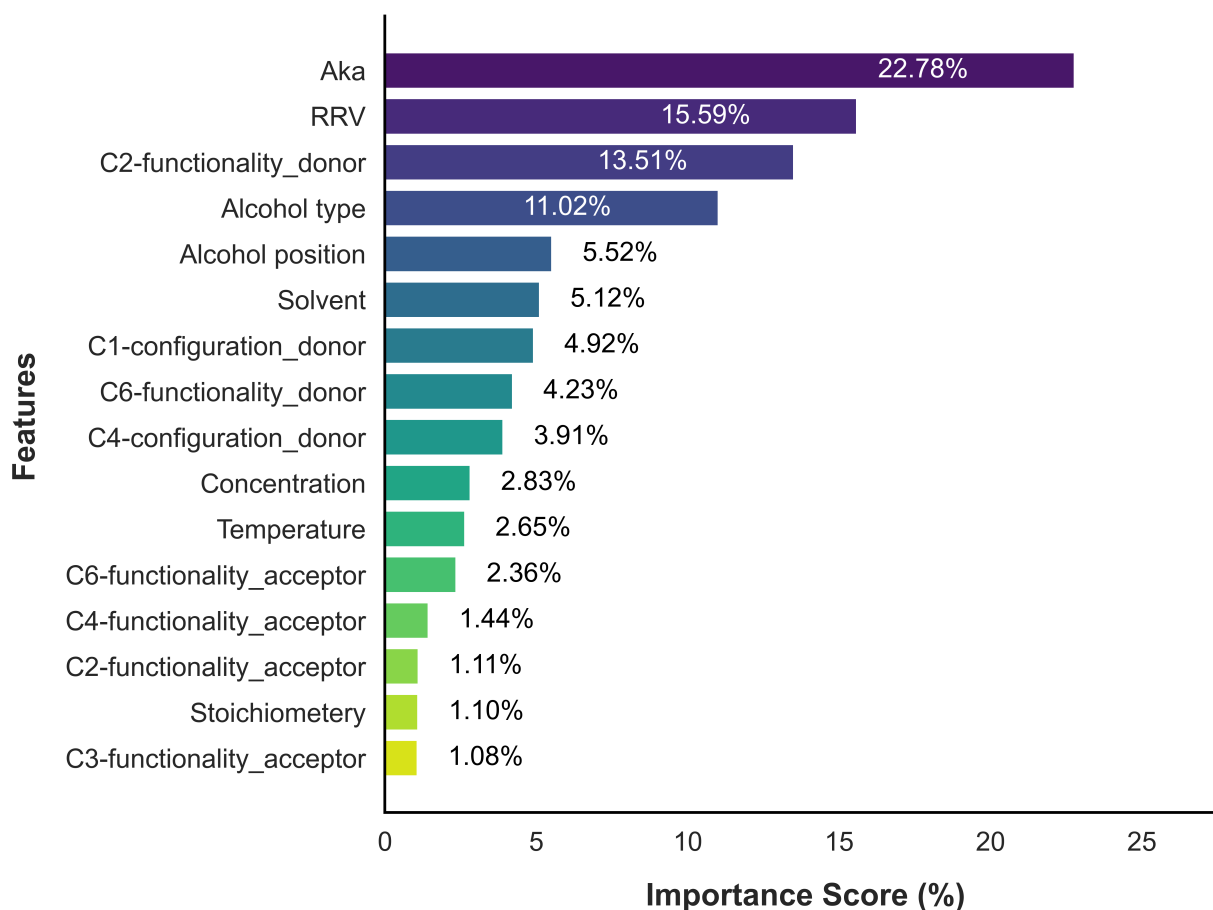
display greater dispersion, underscoring the importance of incorporating reaction conditions for robust modeling.



Supplementary Figure 25. Model residual diagnostics demonstrating generalization capacity.

To evaluate the generalization capacity of our trained models, we analyzed residual diagnostics for both α -ratio and yield on the validation set. The residual plots show no clear heteroscedastic pattern or structural deviation, suggesting that residuals are homoscedastic and randomly distributed — a desirable outcome, particularly for non-linear, heterogeneous datasets such as ours. The Q-Q plots illustrate approximate normality in residual distributions, especially for α -ratio, while histograms of residuals appear symmetric and unimodal. This indicates that the trained models are not substantially biased and maintain consistent error behavior across the prediction range. Although the yield model exhibits slightly lower out-of-sample, the residual analysis suggests that this is not due to systematic model bias or variance heterogeneity, but more likely reflects the intrinsic mechanistic complexity and variability in yield observations. Given that yield is highly influenced by both structural and environmental factors, some predictive variance is

expected. Overall, these diagnostics provide strong support for the validity and robustness of our models in capturing the mechanistic structure–function relationships inherent in the dataset.



Supplementary Figure 26. Bar plot ranking the relative contributions of key features to stereoselectivity. The plot illustrates the relative contributions of molecular and contextual descriptors to the model’s prediction for α -selectivity in glycosylation reactions. Acceptor nucleophilicity constant (Aka), glycosylating agent’s reactivity (RRV), and agents C2-substitution were the most influential features, followed by alcohol type and EFI, underscoring the critical interplay of electronic, structural, and environmental factors in shaping stereoselectivity. Donor, glycosylating agent; acceptor, alcohol.

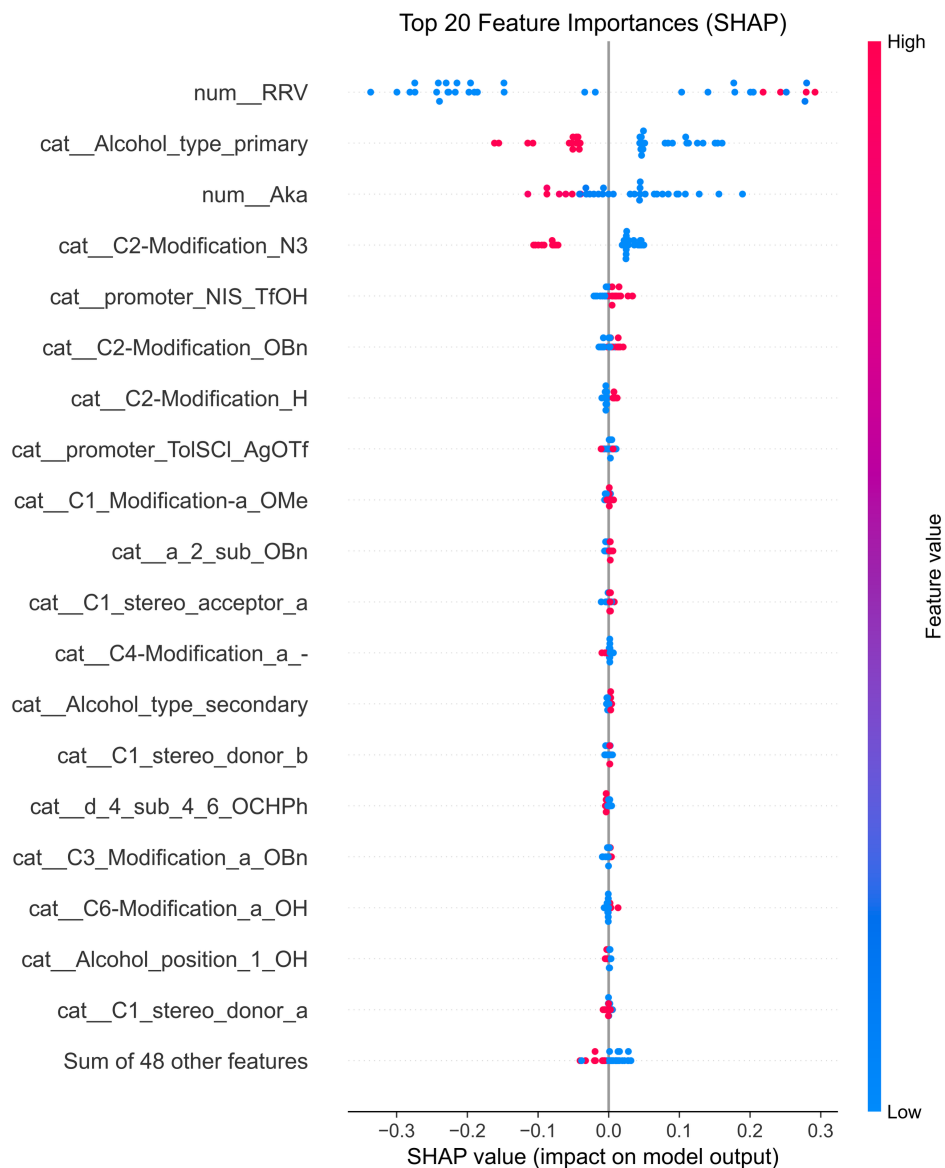


Figure 27. SHAP summary plot derived from the trained hybrid model under *fixed reaction conditions*. Illustrating how individual feature values affect predicted stereoselectivity across the nonlinear dataset. Red denotes high feature values, blue denotes low. RRV shows dominance due to inductive effect.

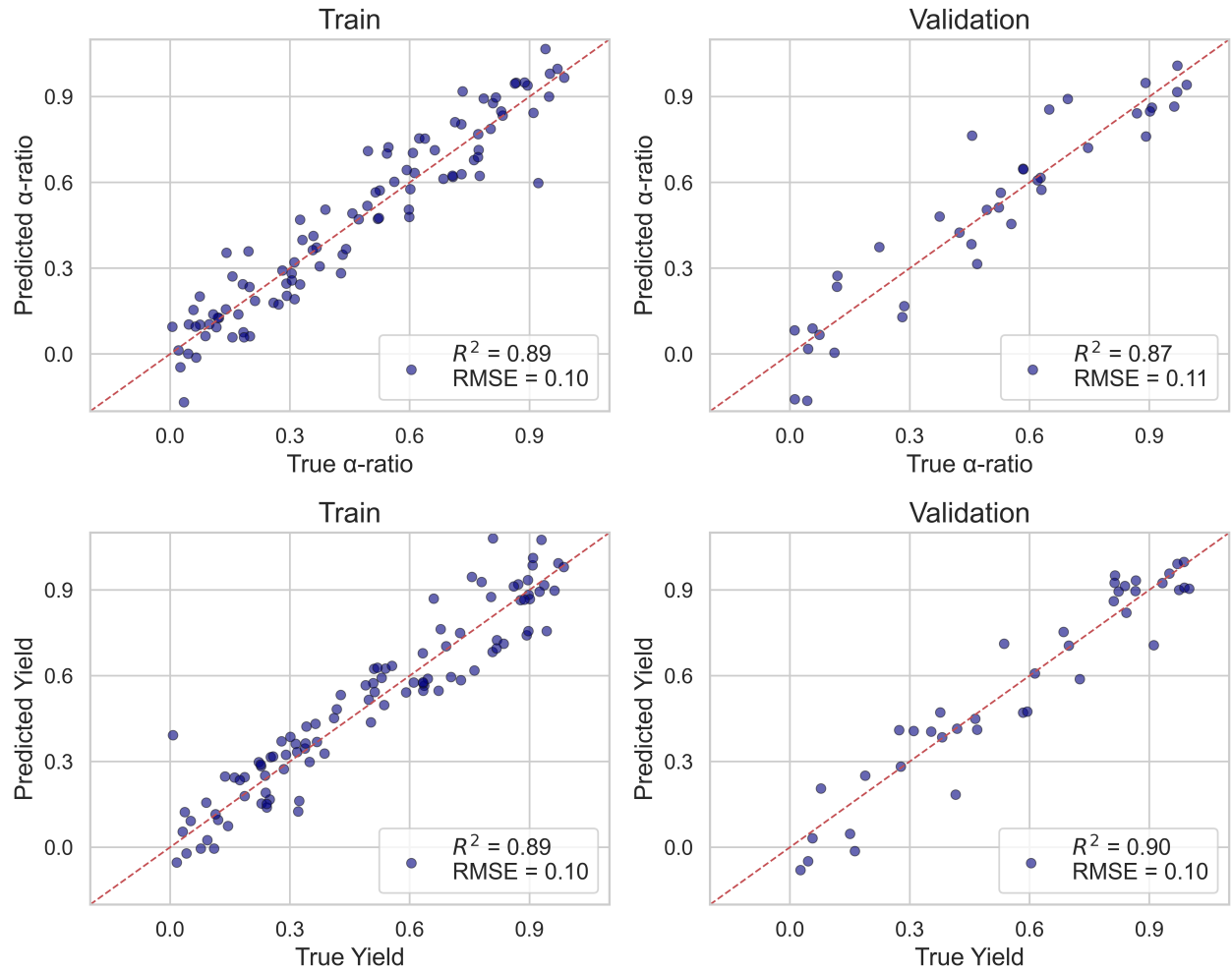
Supplementary Table 8. Diebold-Mariano (DM) test results comparing predictive accuracy of machine learning models to Random Forest for α -ratio (y1).

Model	DM Statistic	p-value	Significance
Gradient Boosting	2.845	4.10×10^{-3}	**
AdaBoost	5.473	4.50×10^{-8}	***
Decision Tree	5.915	2.80×10^{-9}	***
Lasso Regression	6.198	5.70×10^{-10}	***
Ridge Regression	6.252	3.95×10^{-10}	***
Linear Regression	6.318	2.60×10^{-10}	***
CatBoost	6.629	3.40×10^{-11}	***
Support Vector Regressor	7.064	1.65×10^{-12}	***
XGBoost	3.025	2.95×10^{-3}	**

A positive and significant DM statistic indicates the respective model performs worse than Random Forest in predicting α -ratio. All comparisons are statistically significant, reaffirming the robustness of Random Forest as the top-performing model for this task followed by XGB.

Supplementary Table 9. Diebold-Mariano (DM) test results for comparing yield (y2) predictive performance of various machine learning models against the Random Forest baseline.

Model	DM Statistic	p-value	Significance
Gradient Boosting	2.765	5.25×10^{-3}	**
AdaBoost	5.162	8.10×10^{-8}	***
Decision Tree	5.804	3.15×10^{-9}	***
Lasso Regression	6.104	6.05×10^{-10}	***
Ridge Regression	6.189	4.15×10^{-10}	***
Linear Regression	6.278	2.95×10^{-10}	***
CatBoost	6.574	3.70×10^{-11}	***
Support Vector Regressor	7.012	1.75×10^{-12}	***
XGBoost	2.941	3.20×10^{-3}	**



Supplementary Figure 28. Scatter plots of predicted vs. true values for both α -ratio (y1) and yield (y2) across training and validation sets using the *trained* generalized Random Forest model. Each subplot includes a diagonal reference line (ideal prediction) and performance metrics (R^2 and RMSE) shown in the lower-right corner.

2.9 Empirical analysis of ML models

Regression Models

The first two regression methods we consider are ridge regression and lasso regression, both of which aim to "shrink" or minimize the magnitude of the model's predictor coefficients, while retaining all features. These techniques help prevent overfitting by reducing the influence of less important predictor variables. Ridge regression shrinks coefficients towards zero, whereas lasso regression can set some coefficients exactly to zero, effectively eliminating certain variables from the model. By reducing model variance, these methods improve both accuracy and interpretability. To explain ridge and lasso regression, we start with the baseline model of linear regression, where the conditional expectation of the response variable is approximated as a linear function of the predictors. Ridge and lasso extend this by adding regularization (penalty) terms to control the size of the coefficients, thereby enhancing model stability and preventing overfitting. The baseline linear model is given as:

$$g(y_{t-1}; \Omega) = y_t - \mathbf{1}'\Omega \quad (S3)$$

The traditional method for estimating parameters in linear regression is Ordinary Least Squares (OLS). The objective of OLS is to minimize the sum of squared residuals, which represent the differences between the observed and predicted values. This is achieved by minimizing the following objective function:

$$L(\Omega) = \frac{1}{T} \sum_{t=1}^T (\omega_t - g(y_{t-1}; \Omega))^2 \quad (S4)$$

Minimizing $L(\Omega)$ produces the Ordinary Least Squares (OLS) estimator. However, while OLS can fit data well, it may lead to overfitting when dealing with high-dimensional data or multicollinearity. This modification leads to the ridge and lasso regression objective functions. For Ridge function the penalty term, that is the proportional to the sum of square coefficient. This is where ridge and lasso regression come in, adding penalty terms to the OLS objective function to control the size of the coefficients and improve the generalizability of the model.

$$L((\Omega) = \sum_{i=1}^t (\omega_i - g_i\beta)^2 + \lambda \sum_{j=1}^n |\beta_j|^2, \quad (S5)$$

For Lasso function the penalty term which will be the proportional to the sum of absolute value of the coefficient which represents below.

$$L((\Omega) = \sum_{i=1}^t (\omega_i - g_i\beta)^2 + \lambda \sum_{j=1}^n |\beta_j|, \quad (S6)$$

where, λ is the tuning parameters which control the strength of penalty term. And allow to the balance between fitting the data and keep the model coefficient to small and reduce to zero.

The modified objective function is expressed as:

$$L(\Omega; \lambda) = L(\Omega) + \phi(\Omega; \lambda) \quad (S7)$$

where the penalty term defines as below.

$$\phi(\Omega; \lambda) = \lambda \|\Omega\|_p \quad (S8)$$

where, $\lambda \|\Omega\|_p$ denotes the ℓ_p norm of vector Ω defined as:

$$\|\Omega\|_p = \sum_{t=1}^T |\Omega_t|^p \quad (S9)$$

For lasso, $p=1$ which results in L1 norm penalty, and for ridge regression, $p=2$ represents to the L2 norm penalty. While λ represents a positive tuning parameter that determine the influence of the penalty term. In the case if $\lambda=0$ the penalty has no impact, as $\lambda \rightarrow \infty$ then the estimated coefficient shrinkage to zero.

Ensemble Models

Ensemble methods, including Decision Trees (DT), Random Forests (RF), Gradient Boosting, and XGBoost Regressor, combine multiple learners to improve regression performance. Random Forests enhance bagging by selecting a random subset of size ($m = \sqrt{p}$), where (p) is the total feature count) at each split, reducing tree correlation and overfitting. Gradient Boosting sequentially builds models, each correcting prior errors, enhancing accuracy and minimizing bias. Predictions are aggregated across (B) trees, typically via averaging for regression, with each tree's contribution weighted to optimize the final model.

$$\hat{g}(y_{t-1}; d, B) = \frac{1}{B} \sum_{b=1}^B \hat{g}_b(y_{t-1}; \hat{\Omega}_b, d) \quad (S10)$$

Where, ' d ' is the total number of splits in each tree which is controlling the complexity of the model. The final model aggregates all the trees to make the prediction, with each tree contributing to the overall prediction as follows:

$$\hat{g}_b(y_{t-1}; B, \mathcal{Q}, d) = \sum_{b=1}^B \mathcal{Q} \hat{f}_b(y_{t-1}) \quad (S11)$$

Where ($b-1$) represents the (b th) tree, and (\mathcal{Q}) controls the contribution of each tree to the final model. By focusing on the errors of previous models, gradient boosting progressively enhances prediction accuracy and reduces bias.

Additive combination of weak learners h_t , fit sequentially with reweighted data:

$$F_T(x) = \sum_{t=1}^T \alpha_t h_t(x),$$

where α_t is chosen to minimize the weighted squared error at step t . $F_T(x)$ represents ensemble prediction after t boosting iteration. $h_t(x)$ is weak learner fitted at iteration.

Random Forest Regressor (RFR)

Random Forest (RF) used for predictions of multiple trees trained on the bootstrapped subsets, which reduce the variance and fixed the overfitting, as a result it provides a robustness against the noise in the data. RF combines predictions from multiple decision trees to improve prediction accuracy and control overfitting it shown as by following equation.

$$\bar{y} = \frac{1}{N} \sum_{i=1}^N p_i(x), \quad (S12)$$

where,

\bar{y} is the forecast value denotes the total number of trees while $p_i(x)$ represents the prediction from the i^{th} decision tree. The study used 100 estimators that is 100 decision trees in the forest and 42 random state which are fixed for reproducibility.

Gradient Boosting Regressor

Gradient Boosting sequentially fits weak learners to minimize prediction error by focusing on correcting previous errors, resulting in improved the accuracy and reduced bias. It iteratively builds an additive model by sequent fitting trees to residuals are:

$$\bar{y} = F_0(x), \quad (S13)$$

$$r_i^{(t)} = y_i - F_{t-1}(x_i), \quad (S14)$$

$$h_t \approx \arg \min_h \sum_i \left(r_i^{(t)} - h(x_i) \right)^2, \quad (S15)$$

$$F_t(x) = F_{t-1}(x) + \nu h_t(x), \quad (S16)$$

where,

The model starts with a constant prediction which is equal to the mean of all the target values \bar{y} .

$r_i^{(t)}$ is the difference between the actual value y_i and the prediction from the previous iteration which is $F_{t-1}(x_i)$. The each iteration t , a new base learner $h_t(x)$ is trained to predict the residuals $r_i^{(t)}$ which is a shallow decision tree. $F_t(x)$ adds the new weak learner $h_t(x)$ to ensemble with a scaling factor ν (learning rate). $\nu \in (0,1)$ controls how much influence the new learner has.

XGBoost Regressor

The objective function of XGBoost consists of two segments. The training loss and a regularization term. The objective function as following:

$$Obj(\alpha) = \sum_{i=1}^n l(y_i, \hat{y}_i) + \sum_{k=1}^T \left(\gamma T_k + \frac{1}{2} \lambda \sum_{j=1}^{T_k} \omega_{kj}^2 \right), \quad (S17)$$

where,

$\hat{y}_i = \sum_k f_k(x_i)$ is the predicted value for i , which is obtained by summing the outputs of all k trees. $l(y_i, \hat{y}_i)$ is the loss function that measuring the difference between the actual and predicted values. T_k is the number of leaves in the K^{th} tree. ω_{kj} denotes the weight for j^{th} leaf in the K^{th} tree. γ is the regularization parameter penalizing the complexity of each tree λ is the L2 regularization term on the leaf weights. While α represents the total objective function, combining both the training loss and regularization penalties.

The first segment objective function is training loss and the second function is regularization term. The first Segment, $\sum l(y_i, \hat{y}_i)$, measures the discrepancy between the actual and predicted values, ensuring that the model fits the data accurately. The second module, $\sum_{k=1}^T \left(\gamma T_k + \frac{1}{2} \lambda \sum_{j=1}^{T_k} \omega_{kj}^2 \right)$, penalizes the complexity of the model by adding a cost for each additional leaf in the trees and for large leaf weights. This regularization helps to prevent overfitting by favoring simpler, more generalizable models. By iteratively minimizing this combined objective, XGBoost constructs an ensemble of decision trees that progressively refine the predictive performance while maintaining control over model complexity.

CatBoost Regressor

CatBoost efficiently handles categorical features and leverages ordered target-based encoding, significantly reducing prediction bias and improving generalization.

$$L(F) = \sum_{i=1}^n (y_i - F(X_i))^2 + \lambda \sum_{j=1}^J \|w_j\|^2, \quad (S18)$$

where,

$L(F)$ is the loss function including a regularization component. λ controls regularization function. while w_j denotes the tree parameters.

Support Vector Regressor (SVR)

SVR aims to fit the best hyperplane within an acceptable margin of error with support vectors controlling the model's complexity and generalization. Assuming normalized input features represented by the vector x_i , and corresponding photovoltaic power outputs denoted by y_i for each data point i in the dataset, the entire dataset can be expressed as a collection of pairs $\{(x_i, y_i)\}_{i=1}^N$ where N is the total number of data point. Support Vector Regression (SVR) aims to approximate the underlying function using the expression: It solves the following optimization problem:

$$\frac{1}{2} \|w_j\|^2 + C \sum_{i=1}^n (\eta_i - \eta_i^*), \quad (S19)$$

$$\text{Subject to: } y_i - (W \cdot \varphi(x_i)) + b \leq \epsilon + \eta_i, (W \cdot \varphi(x_i)) + b - y_i \leq \epsilon + \eta_i^*, \quad (S20)$$

where,

ϵ denotes tolerance margin C is the penalty for error while $\varphi(x_i)$ is the kernel transformation.

Decision Tree Regressor

A decision tree regressor models the output \hat{y} by splitting the input space into disjoint regions and assigning a constant value in each region. The prediction function is defined as:

$$\hat{y}(x) = \sum_{k=1}^K ck \cdot \mathbb{I}(x \in N_k), \quad (S21)$$

where,

K represents the number of leaf nodes, N_k denotes the region k , which is the subset of input space. ck denotes the constant prediction values in region N_k . $\mathbb{I}(x \in N_k)$ indicate the indicator function which is equal to 1 if $x \in N_k$, otherwise 0.

At each node, the model select the best feature K and threshold s that minimizes the sum of squared errors:

$$\min_{k,s} \left[\min_{CL} \sum_{x_i \in RL(K,S)} (y_i - CL)^2 + \min_{CR} \sum_{x_i \in RR(K,S)} (y_i - CR + \min_{CR})^2 \right], \quad (S22)$$

where,

$R_L(K, S) = \{x_i | x_{ik} \leq s\}$ and $R_R(K, S) = \{x_i | x_{ik} > s\}$ while C_L and C_R represents the predictions in the left and right regions.

For optimal value in each region the best constant prediction value for region N_k is the mean of the target values in that region:

$$C_j = \frac{1}{|N_k|} \sum_{x_i \in R_j} y_i, \quad (S23)$$

where,

$|N_k|$ belongs to number of data point in region N_k .

After constructiong the tree and determining optimal region N_k and $\hat{y}(x) = C_j$ where $x \in N_k$

Or the full indicator function represent as:

$$\hat{y}(x) = \sum_{k=1}^K \left(\frac{1}{|N_k|} \sum_{x_i \in R_j} y_i \right) \cdot \mathbb{I}(x \in N_k), \quad (S24)$$

2.10 Performance Metrics

Mean Absolute Error (MAE)

The MAE is the loss function for regression model, which is the sum of the absolute values of the difference between the target and predicted values. The MAE only measures the average modulus length of the error for the predicted value. The MAE function can be shown as:

$$MAE = \frac{1}{p} \sum_{i=1}^p |f_i - y_i| \quad (S25)$$

where p stands for the numbers of data, f_i refers to the predictive value, and y_i can be described as actual value.

Root Means Square Error (RMSE)

The RMSE is a statistical test used in regression tasks to determine the accuracy of a prediction model. In order to give greater error more weight. The lower RMSE values, the better the model performance. The test can be performed as follow:

$$RMSE = \sqrt{\frac{1}{n} \sum_{i=1}^n (y_i - \hat{y}_i)^2} \quad (S26)$$

where $\frac{1}{n}$ is the number of data point in the dataset, y_i stand for the value of the dependent variable, while \hat{y}_i refer to the predicted value of the dependent variable.

The Diebold-Mariano (DM)

The Diebold-Mariano (DM) test Diebold and Mariano, (1995) evaluates the predictive accuracy of ML models. This test identifies significant differences in model accuracy through quantitative analysis. Suppose that two predictions f_1, \dots, f_n and g_1, \dots, g_n for a time series are linked with y_1, \dots, y_n . Let e_i and r_i be the residuals for the two forecasts, i.e.

The forecast residuals are defined as follows:

$$e_i = y_i - f_i, \quad r_i = y_i - g_i, \quad (S27)$$

Forecast residuals are defined as follows:

$$d_i = e_i^2 - r_i^2 \quad \text{or} \quad d_i = |e_i| - |r_i|, \quad (S28)$$

and let d_i be defined as one of the following.

The time series is called the loss-differential. The key assumption for using the Diebold-Mariano test is that the loss differential time series d_i is stationary. The first of these formulas is related to the MSE error statistic, and the second is related to the MAE error statistic. Now define Loss-differential mean as:

$$\bar{d} = \frac{1}{n} \sum_{i=1}^n d_i \quad \mu = E[d_i], \quad (S29)$$

For $n > k \geq 1$, define:

$$r_k = \frac{1}{n} \sum_{i=k+1}^n (d_i - \bar{d})(d_{i-k} - \bar{d}), \quad (S30)$$

where autocovariance is at lag k .

As described in Autocorrelation Function r_k is the autocovariance at lag k .

$$DM = \frac{\bar{d}}{\sqrt{[r_0 + 2 \sum_{k=1}^{h-1} r_k]/n}}, \quad (S31)$$

For $h \geq I$, we define the Diebold-Mariano (DM) statistic, where the value $h = n^{1/3} + I$.

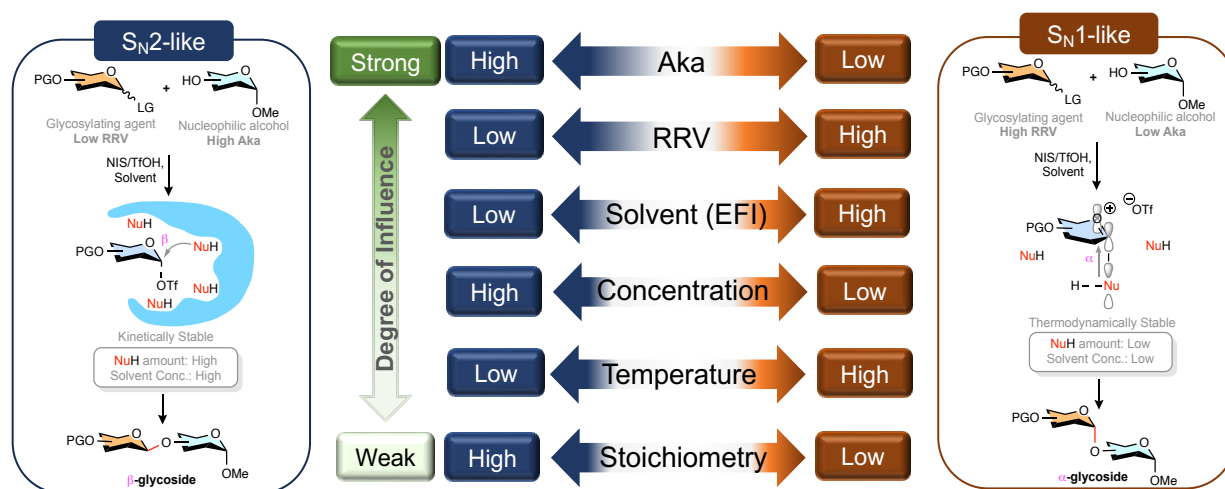
The DM test is based on a standard normal distribution. The null hypothesis indicates that an equal predictive capacity exists between the models. The alternative hypothesis regarding the higher predictability of the model has the lowest value of the loss function.

Table 10. Performance metrics and model comparison for different regression models used for predicting α -ratio and yield.

Model	Mean Normalized RMSE (↓)	Mean Normalized Spearman (↑)	Mean Normalized R² (↑)	Mean Normalized MAE (↓)	Mean RMSE (↓)	Mean Spearman (↑)	Mean R² (↑)	Mean MAE (↓)	Wins RMSE (↓)	Wins Spearman (↑)	Wins R² (↑)	Wins MAE (↓)
Hybrid Model	0.024	0.986	0.973	0.019	2.408	0.986	0.973	1.923	1	1	1	1
Random Forest	0.03	0.978	0.959	0.024	3.002	0.978	0.959	2.378	0	0	0	0
XGBoost	0.035	0.969	0.943	0.028	3.527	0.969	0.943	2.812	0	0	0	0
CatBoost	0.045	0.952	0.91	0.035	4.45	0.952	0.91	3.538	0	0	0	0
Gradient Boosting	0.054	0.933	0.868	0.043	5.372	0.933	0.868	4.252	0	0	0	0
AdaBoost	0.059	0.919	0.841	0.047	5.894	0.919	0.841	4.74	0	0	0	0
Ridge Regression	0.059	0.918	0.839	0.048	5.939	0.918	0.839	4.751	0	0	0	0
Support Vector Regressor	0.061	0.918	0.832	0.048	6.068	0.918	0.832	4.784	0	0	0	0
Decision Tree	0.066	0.901	0.798	0.054	6.639	0.901	0.798	5.388	0	0	0	0
Lasso Regression	0.069	0.892	0.779	0.055	6.942	0.892	0.779	5.532	0	0	0	0

The table presents Mean Normalized and Mean values for key performance indicators: RMSE (↓), Spearman (↑), R² (↑), and MAE (↓), along with the Wins column for each metric.

2.11 Mechanistic mapping of reaction space



Supplementary Figure 29. Contextual mapping of stereoselectivity pathways governed by glycosylating agent, alcohol, and environmental parameters. This schematic summarizes the mechanistic drivers of α/β -selectivity across the S_N2-like (blue) and S_N1-like (orange) pathways in glycosylation. On the left, S_N2-like reactivity is favored by low RRV donors and highly nucleophilic acceptors (high Aka), especially under high solvent concentration and nucleophile excess, stabilizing kinetically driven transition states. In contrast, S_N1-like reactivity on the right is facilitated by high RRV donors and poor nucleophiles (low Aka), with low solvent concentration and reduced nucleophile loading, enabling thermodynamically stable ion pair intermediates. The center gradient ranks the degree of influence of each variable on model predictions, highlighting Aka and RRV as primary drivers, while environmental factors such as EFI (solvent), concentration, and temperature provide secondary modulation. Stoichiometry exerts the weakest relative impact. These trends, identified by the model, were found to be consistent with experimental observations. Green scale shows from strongest (green) to weakest (light green) influence on glycosylation

2.12 Programming details

Software and environment

- Anaconda Navigator v2.6.3 (includes Conda v24.9.2, Python 3.12.7)
- **Jupyter Notebook** v7.2.2 (launched via Navigator)

▪ Required Python packages:

- pandas
- numpy
- scikit-learn
- pandas_datareader
- openpyxl
- matplotlib
- seaborn

▪ Creating and activating your Conda environment

1. Open Anaconda Navigator

- Click the “**Environments**” tab on the left.
- Click “**Create**”, name it “glycoenv”, select **Python 3.8+**.

2. **Activate** it by selecting “glycoenv” from the list.

▪ Installing Packages

Open a terminal or Anaconda prompt

Install core data libraries;

```
e.g., Conda install pandas numpy scipy scikit-learn matplotlib  
seaborn openpyxl
```

install needed models;

```
pip install optional package (e.g., catboost, xgboost, joblib)
```

- **Data Preparation**

Place the primary data file, "data_ML_FIZZA.csv", in the same folder as the notebooks. Missing data cleaned, special y_1 , and y_2 values mapped to 0.01 and failed reactions mapped to 0.00- One-hot encoding for x_1 - x_{24} - y_1/y_2 column converted to float.

- **Running the Analysis**

In Anaconda Navigator (with glycoenv active), select **Jupyter Notebook**, then click **Launch**.

- **Open and execute**

01_feature_importance.ipynb

Reads the data CSV, computes feature-importance scores, and saves
—feature_importance_plot.png

02_modeling_y1/y2.ipynb

Cleans the y_1/y_2 target column, trains ten ML pipelines (Random Forest, Gradient Boosting, XGBoost, CatBoost, Support Vector Regressor, AdaBoost, Linear Regression, Ridge regression, Lasso Regression, Decision tree) on a 70/30 or 90/10 train/test split on case/ n , and evaluates MAE, RMSE, Pearson's r , and R^2 With `sklearn.metrics`. Hyperparameter tuning with `GridSearchCV`.

—Saves

—model_performance_results.csv/PNG

Observed vs. predicted scatter plots and bar charts (displayed inline and exportable as PNGs).

- **Model Optimization**

Used `scipy.optimize.minimize` (L-BFGS-B)

Decoded categorical features with `LabelEncoder`

Displayed optimal settings with `Pandas`

Generated predictions and histograms

Used `matplotlib` for plots

Created download links via `IPython.display.HTML`

Note:

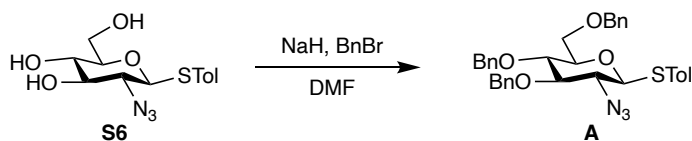
- If you move data “data_ML_FIZZA.csv”, update the “file_path” variable in the first cell of each notebook.
- Any package-import errors can be resolved by re-running the `Conda install` or `pip install` commands above.

All datasets and code generated during this study are available from the corresponding author upon reasonable request.

3 Experimental Section for Synthesis

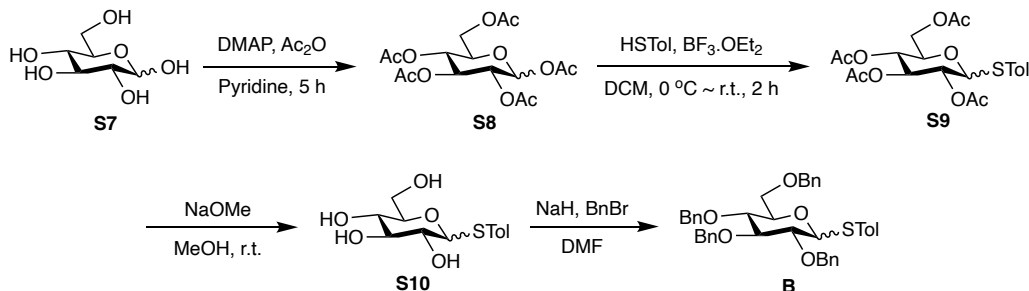
3.1 Synthesis of glycosylating agents

p-Tolyl 2-azido-3,4,6-tri-*O*-benzyl-2-deoxy- β -D-thioglucopyranoside (**A**)



To a solution of compound **S6** (0.8 g, 2.60 mmol) in DMF was added NaH (0.4 g, 60% NaH dispersion in mineral oil, 10.42 mmol) and BnBr (1.6 mL, 13.02 mmol) at 0°C. The reaction mixture was stirred at room temperature for 4 h. The mixture was extracted with EtOAc twice. The organic layer was dried over anhydrous MgSO₄, filtered, and concentrated under reduced pressure. The concentrate was purified by silica gel chromatography with hexane/EtOAc (9:1) as eluent. The titled compound **A** was obtained as a colorless oil (57.2 mg, 81%, α : β = 29:71). The RRV of β -anomer referring to previous report is 270 (13). $[\alpha]^{24}_D +54.0$ (*c* 0.6, CHCl₃); IR (CHCl₃) ν 2105, 1493, 1453, 1272, 1074, 809, 771, 733, 695 cm⁻¹; ¹H NMR (400 MHz, CDCl₃) δ 7.51-7.05 (m, 38H, Ar-H), 5.54 (d, *J* = 5.3 Hz, 1H, H-1 α), 4.93-4.42 (m, 12H, CH₂Ph), 4.39 (ddd, *J* = 10.0, 4.3, 2.1 Hz, 1H, H-5 α), 4.35 (d, *J* = 10.1 Hz, 1H, H-1 β), 3.93 (dd, *J* = 10.0, 5.3 Hz, 1H, H-2 α), 3.82-3.72 (m, 4H, H-4 α , H-6 α α , H-6 α β , H-6 α β), 3.64 (dd, 1H, *J* = 10.5, 1.2 Hz, H-6 α β), 3.58 (t, *J* = 10.1 Hz, 1H, H-4 β), 3.50 (t, *J* = 10.1 Hz, 1H, H-3 β), 3.46 (ddd, *J* = 9.7, 3.5, 2.1 Hz, 1H, H-5 β), 3.30 (t, *J* = 10.1 Hz, 1H, H-2 β), 2.31 (s, 6H, ArCH₃); ¹³C NMR (100 MHz, CDCl₃) δ 138.7 (C), 138.3 (C), 137.9 (C), 137.73 (C), 137.65 (C), 134.3 (CH), 132.7 (CH), 130.0 (CH), 129.8 (CH), 129.7 (CH), 128.48 (CH), 128.45 (CH), 128.4 (CH), 128.2 (CH), 128.1 (CH), 128.0 (CH), 127.9 (CH), 127.8 (CH), 127.7 (CH), 127.7 (CH), 127.6 (CH), 87.6 (CH), 85.9 (CH), 85.1 (CH), 81.8 (CH), 79.4 (CH), 78.4 (CH), 77.6 (CH), 75.9 (CH₂), 75.7 (CH₂), 75.1 (CH₂), 73.5 (CH₂), 71.7 (CH), 68.8 (CH₂), 68.4 (CH₂), 64.9 (CH), 64.2 (CH₂), 21.1 (CH₃); HRMS (ESI) calcd. for C₃₄H₃₅N₃O₄NaS [M + Na]⁺ 604.2246, found 604.2360.

p-Tolyl 2,3,4,6-tetra-*O*-benzyl-1-thio- β -D-glucopyranoside (**B**)



To a solution of compound **S7** (56 mmol, 10 g) in pyridine (60 mL), DMAP (5.4 mmol, 0.67 g) was added. The mixture was cooled to 0 °C, and acetic anhydride (Ac₂O) (358 mmol, 36 mL) was added dropwise while maintaining the temperature. The mixture was stirred at room

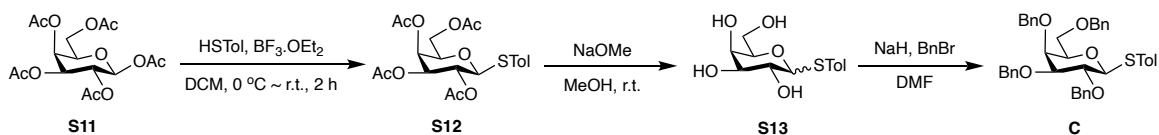
temperature under N₂ for 5 h and then quenched with ethanol (20 mL) at 0 °C. The mixture was concentrated, and the resulting residue was diluted with ethyl acetate (300 mL), and washed with water, saturated NaHCO₃, 10% aqueous hydrochloric acid, and brine. The organic phase was dried over MgSO₄ and then filtered and concentrated. Silica gel column chromatography (2:1 hexanes-/EtOAc) afforded 20.3 g (93%) of 1,2,3,4,6-penta-*O*-acetyl- D-glucopyranoside **S8** as white solid. $[\alpha]_D^{27} +9.54$ (CHCl₃, *c* 0.21); ¹H NMR (400 MHz, CDCl₃) δ 5.7 (d, *J* = 8.4 Hz, 1H), 5.24 (dd, *J* = 9.6 and 9.2 Hz, 1H), 5.12 (dd, *J* = 9.2 and 8.4 Hz, 1H), 5.11 (dd, *J* = 10.0 and 9.6 Hz, 1H), 4.27 (dd, *J* = 12.4 and 4.8 Hz, 1H), 4.10 (dd, *J* = 12.4 and 2.4 Hz, 1H), 3.83 (ddd, *J* = 10.0, 4.8 and 2.4 Hz, 1H), 2.10 (s, 3H), 2.07 (s, 3H), 2.02 (s, 6H), 1.99 (s, 3H); ¹³C NMR (100 MHz, CDCl₃) δ 170.5, 170.0, 169.3, 169.2, 168.9, 91.7, 72.7 (2C), 70.2, 67.7, 61.4, 20.7, 20.6, 20.5 (3C).

To a solution of compound **S8** (12.8 mmol, 5 g) in DCM (50 mL), HSTol (15.36 mmol, 1.90 g) was added. The mixture was cooled to 0 °C, and EF₃.OEt₂ (6.4 mmol, 0.9 g) was added. The mixture was stirred at room temperature under N₂. The mixture was concentrated, and the resulting residue was diluted with ethyl acetate (300 mL), and washed with water, saturated NaHCO₃. Organic layer was dried over MgSO₄. White solid *p*-Tolyl 2,3,4,6-tetra-*O*-acetyl-1-thio-β-D-glucopyranoside **S9** was obtained after recrystallization from a mixture of dichloromethane and hexanes, followed by drying under reduced pressure. β-anomer (5.22 g, 90%). ¹H NMR (500 MHz, CDCl₃) δ 7.39 (d, *J* = 7.2 Hz, 2H, Ar-H), 7.12 (d, *J* = 8.1 Hz, 2H, Ar-H), 5.20 (t, *J* = 9.5 Hz, 1H, H-3), 5.02 (t, *J* = 9.5 Hz, 1H, H-4), 4.93 (dd, *J* = 10.2, 9.5 Hz, 1H, H-2), 4.63 (d, *J* = 10.2 Hz, 1H, H-1), 4.20 (td, *J* = 12.3, 4.9 Hz, 1H, H-6a), 4.18 (td, *J* = 12.3, 2.6 Hz, 1H, H-6b), 3.70 (ddd, *J* = 9.5, 4.9, 2.6 Hz, 1H, H-5), 2.35 (s, 3H, CH₃), 2.09 (s, 3H, OAc), 2.08 (s, 3H, OAc), 2.01 (s, 3H, OAc), 1.98 (s, 3H, OAc); ¹³C NMR (125 MHz, CDCl₃) δ 170.6 (C), 170.2 (C), 169.4 (C), 169.2 (C), 138.8 (C), 133.8 (CH), 129.7 (CH), 127.5 (C), 85.8 (CH), 75.7 (CH), 74.0 (CH), 69.9 (CH), 68.2 (CH), 65.1 (CH₂), 21.2 (CH₃), 20.8 (CH₃), 20.7 (CH₃), 20.6 (CH₃).

Compound **S9** (5.0 g, 11.00 mmol) was dissolved in MeOH (50 mL) and NaOMe (59.4 mg, 1.10 mmol) was added into the mixture. The reaction was processed at room temperature for 12 h. Amberlite 120 (H⁺) was used to neutralize the reaction. After filtration, MeOH was evaporated, and the desired white-solid **S10** was dried under high vacuum system. The **S10** in DMF (32 ml) was mixed with BnBr (6.4 ml, 52.80 mmol) and stirred for 1 h at 0 °C. NaH (3.5 g, 88.00 mmol) was added into the mixture slowly at 0 °C. The reaction underwent at room temperature for overnight. Water was added into reaction to quench NaH in an ice-bath. The mixture was washed with H₂O (10 mL). The aqueous layer was extracted with EtOAc (3 × 5 mL), dried with anhydrous MgSO₄, filtered, and concentrated *in vacuo*. The mixture was purified by flash column chromatography (*n*-Hexane/EtOAc 6:1) on silica gel to give white-solid product **B** (5.7 g, 80%). The RRV referring to previous report is 2656 (*13*). $[\alpha]_D^{27} -3.3$ (*c* 0.8, CH₂Cl₂); IR (CH₂Cl₂) ν 2864, 1067, 735, 697 cm⁻¹; ¹H NMR (500 MHz, CD₂Cl₂) δ 7.47 (d, *J* = 8.2 Hz, 2H, Ar-H), 7.41-7.24 (m, 18H, Ph-H), 7.21 (dd, *J* = 7.8, 2.0 Hz, 2H, Ar-H), 7.08 (d, *J* = 7.8 Hz, 2H, Ar-H), 4.89, 4.84 (ABq, *J* = 11.0 Hz, 2H, CH₂Ph), 4.89, 4.64 (ABq, *J* = 10.5 Hz, 2H, CH₂Ph), 4.82, 4.59 (ABq, *J* = 10.2

Hz, 2H, CH₂Ph), 4.63 (d, J = 9.8 Hz, 1H, H-1), 4.59, 4.53 (ABq, J = 11.9 Hz, 2H, CH₂Ph), 3.77 (dd, J = 10.8, 1.9 Hz, 1H, H-6a), 4.72 (dd, J = 10.8, 5.7 Hz, 1H, H-6b), 3.68 (t, J = 9.8 Hz, 1H, H-3), 3.61 (t, J = 9.8 Hz, 1H, H-4), 3.48 (ddd, J = 9.8, 5.7, 1.9 Hz, 1H, H-5), 3.46 (dd, J = 9.8, 5.7 Hz, 1H, H-2), 2.32 (s, 3H, CH₃); ¹³C NMR (125 MHz, CD₂Cl₂) δ 139.1 (C), 138.83 (C), 138.79 (C), 138.76 (C), 138.1 (C), 132.5 (CH), 130.5 (C), 130.0 (CH), 128.7 (CH), 128.6 (CH), 128.5 (CH), 128.3 (CH), 128.12 (CH), 128.10 (CH), 128.0 (CH), 127.91 (CH), 127.89 (CH), 88.1 (CH), 87.0 (CH), 81.3 (CH), 79.3 (CH), 78.2 (CH), 75.9 (CH₂), 75.5 (CH₂), 75.2 (CH₂), 73.7 (CH₂), 69.5 (CH₂), 21.2 (CH₃); HRMS (ESI) calcd. for C₄₁H₄₂O₅NaS [M + Na]⁺ 669.2651, found 669.2648.

p-Tolyl 2,3,4,6-tetra-*O*-benzyl-1-thio- β -D-galactopyranoside (**C**)

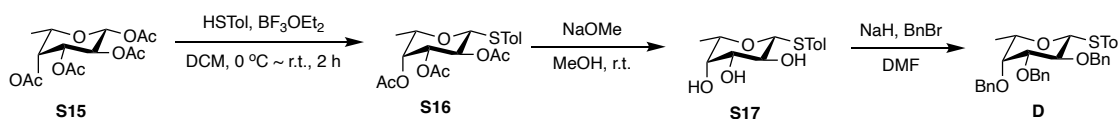


To a solution of compound **S11** (51.2 mmol, 20 g) in DCM (200 mL), HSTol (61.4 mmol, 7.63 g) was added. The mixture was cooled to 0 °C, and EF₃.OEt₂ (74.6 mmol, 9.32 ml) was added. The mixture was stirred at room temperature under N₂. The mixture was concentrated, and the resulting residue was diluted with ethyl acetate (300 mL), and washed with water, saturated NaHCO₃, organic layer was dried over MgSO₄. *p*-Tolyl 2,3,4,6-tetra-*O*-acetyl-1-thio- β -D-galactopyranoside **S12** (white solid) was obtained after recrystallization from a mixture of dichloromethane and hexanes, followed by drying under reduced pressure (13). β -anomer (22.26 g, 96%). ¹H NMR (400 MHz, CDCl₃): δ 7.09 (dd, J = 8.7, 0.6 Hz, 2H), 6.90 (d, J = 8.6 Hz, 2H), 5.47 (dd, J = 9.8, 7.3 Hz, 1H), 5.45 (dd, J = 3.3, 1.1 Hz, 1H), 5.10 (dd, J = 10.5, 3.4 Hz, 1H), 4.99 (d, J = 8.0 Hz, 1H), 4.20 (ddd, J = 27.9, 11.3, 6.7 Hz, 2H), 4.04 (td, J = 6.9, 1.1 Hz, 1H), 2.30 (s, 3H), 2.18 (s, 3H), 2.07 (s, 3H), 2.06 (s, 3H), 2.01 (s, 3H). ¹³C NMR (400 MHz, CDCl₃): δ 170.48, 170.39, 170.26, 169.52, 155.07, 132.97, 130.12 (2C), 117.09 (2C), 100.24, 71.07, 71.01, 68.85, 67.04, 61.48, 20.87, 20.80, 20.79, 20.73.

Compound **C** was derived from compound **S13** (5.0 g, 11.00 mmol) with the same general procedure as compound **B**. The white-solid product **C** was obtained with the yield of 5.7 g, 80%. The RRV referring to previous report is 17000 (13). [α]_D²⁷ -1.5 (*c* 0.5, CH₂Cl₂); IR (CH₂Cl₂) ν 2862, 1089, 1028, 733, 696 cm⁻¹; ¹H NMR (500 MHz, CD₂Cl₂) δ 7.44 (d, J = 8.1 Hz, 2H, Ar-H), 7.38-7.27 (m, 20H, Ph-H), 7.03 (d, J = 7.9 Hz, 2H, Ar-H), 4.94, 4.57 (ABq, J = 11.2 Hz, 2H, CH₂Ph), 4.77, 4.74 (ABq, J = 10.3 Hz, 2H, CH₂Ph), 4.76, 4.71 (ABq, J = 11.5 Hz, 2H, CH₂Ph), 4.59 (d, J = 9.6 Hz, 1H, H-1), 4.49, 4.44 (ABq, J = 11.7 Hz, 2H, CH₂Ph), 3.98 (d, J = 2.6 Hz, 1H, H-4), 3.81 (t, J = 7.7 Hz, 1H, H-2), 3.65-3.59 (m, 4H, H-6a, H-6b, H-5, H-3), 2.32 (s, 3H, CH₃); ¹³C NMR (125 MHz, CD₂Cl₂) δ 139.3 (C), 139.1 (C), 138.9 (C), 138.6 (C), 137.7 (C), 132.3 (CH), 130.8 (C), 129.9 (CH), 128.7 (CH), 128.6 (CH), 128.5 (CH), 128.2 (CH), 128.02 (CH), 127.96 (CH), 127.92 (CH), 127.86 (CH), 88.3 (CH), 84.5 (CH), 77.9 (CH), 77.6 (CH), 75.8 (CH₃), 75.0

(CH₃), 74.4 (CH), 73.8 (CH₃), 73.0 (CH₃), 69.4 (CH₃), 21.2 (CH₃); HRMS (ESI) calcd. for C₄₁H₄₂O₅NaS [M + Na]⁺ 669.2651, found 669.2656.

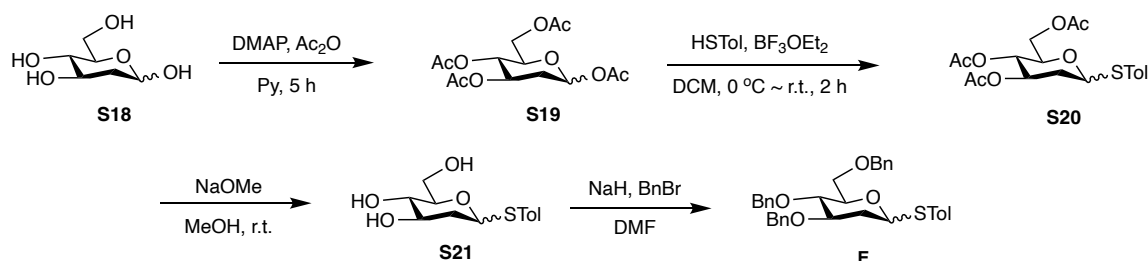
***p*-Tolyl 2,3,4-tri-*O*-benzyl-6-methoxy-1-thio-*L*-fucopyranoside (**D**)**



To a solution of compound **S15** (56.2 mmol, 20 g) in DCM (200 mL), HSTol (67.3 mmol, 8.37 g) was added. The mixture was cooled to 0 °C, and EF₃.OEt₂ (82.4 mmol, 10.3 ml) was added. The mixture was stirred at room temperature under N₂. The mixture was concentrated, and the resulting residue was diluted with ethyl acetate (300 mL), and washed with water, saturated NaHCO₃. Organic layer was dried over MgSO₄. The obtained crude was recrystallized by EtOAc/hexanes to give *p*-Tolyl 2,3,4-tri-*O*-acetyl-1-thio-β-*L*-fucopyranoside **S16** as white solid (12.57 g, 54%). ¹H NMR (600 MHz, CDCl₃): δ 1.15 (d, 3H, *J*_{5,6} = 6.6 Hz, H-6), 1.90, 2.01, 2.07 (3s, 9H, 3 x COCH₃), 2.26 (s, 3H, SPhCH₃), 3.74 (m, 1H, H-5), 4.58 (d, 1H, *J*_{1,2} = 10.2 Hz, H-1), 4.98 (dd, 1H, *J*_{2,3} = 9.6 Hz, *J*_{3,4} = 3.0 Hz, H-3), 5.13 (t, 1H, *J* = 9.6 Hz, H-2), 5.18 (d, 1H, *J*_{3,4} = 3.0 Hz, H-4), 7.00–7.09 (m, 2H), 7.30–7.39 (m, 2H); ¹³C NMR (150 MHz, CDCl₃): 16.7, 20.8, 20.9, 21.1, 21.3, 67.5, 70.5, 72.6, 73.2, 86.9, 129.3, 129.8, 133.0, 138.3, 169.6, 170.3, 170.8. ESI-MS calcd. for [M + Na]⁺ C₁₉H₂₄NaO₇S 419.1, found 419.2

Compound **D** was derived from compound **S17** (5.0 g, 11.00 mmol) with the same general procedure as compound **B**. The white-solid product **D** was obtained with the yield of 9.4 g, 75% for two steps. The RRV referring to previous report is 72000 (13). ¹H NMR (500 MHz, CDCl₃) δ 7.50–7.48 (m, 2H), 7.40–7.27 (m, 15H), 7.01 (d, *J* = 8.1 Hz, 2H), 5.00 (d, *J* = 11.8 Hz, 1H), 4.80 (d, *J* = 10.3 Hz, 1H), 4.73–4.71 (m, 3H), 4.66 (d, *J* = 11.8 Hz, 1H), 4.54 (d, *J* = 9.6 Hz, 1H), 3.89 (t, *J* = 9.6 Hz, 1H), 3.62–3.61 (m, 1H), 3.58 (dd, *J* = 9.6, 3.0 Hz, 1H), 3.52–3.48 (m, 1H), 2.29 (s, 3H), 1.25 (d, *J* = 6.2 Hz, 3H); HRMS (*m/z*) calcd. for C₃₄H₃₆O₄SNa [M + Na]⁺ 563.2226, found 563.2220.

***p*-Methylphenyl 3,4,6-tri-*O*-benzyl-2-deoxy-1-thio-*D*-glucopyranoside (**E**)**



To a solution of compound **S18** (30.4 mmol, 5 g) in pyridine (50 mL), DMAP (2.97 mmol, 0.36 g) was added. The mixture was cooled to 0 °C, and acetic anhydride (Ac₂O) (194.5 mmol, 18.7 mL) was added dropwise while maintaining the temperature. The mixture was stirred at room temperature under N₂ for 5 h and then quenched with ethanol (20 mL) at 0 °C. The mixture was concentrated, and the resulting residue was diluted with ethyl acetate (250 mL), and washed with water, saturated NaHCO₃, 10% aqueous hydrochloric acid, and brine. The organic phase was dried over MgSO₄ and then filtered and concentrated. Silica gel column chromatography (2:1 hexanes-/EtOAc) afforded 8.31 g (82%) of 1,3,4,6-tetra-*O*-acetyl-2-deoxy-D-glucopyranoside **S19** as colorless oil. ¹H-NMR (400 MHz, CDCl₃): δ 5.77 (dd, *J* = 10.0, 2.20 Hz, 1H), 5.08–4.97 (m, 2H), 4.31–4.26 (m, 1H), 4.01–4.03 (m, 1H), 3.74–3.70 (m, 1H), 2.35–2.29 (m, 1H), 2.09–1.90 (m, 12H). ¹³C-NMR (100 MHz, CDCl₃): δ 170.71, 170.10, 169.76, 168.79, 91.08, 72.87, 70.15, 68.26, 61.95, 34.73, 20.96, 20.86, 20.77, 20.71. HRMS (*m/z*): calcd. for C₁₄H₂₀O₉ [M + Na]⁺ 355.0999, found 355.1006.

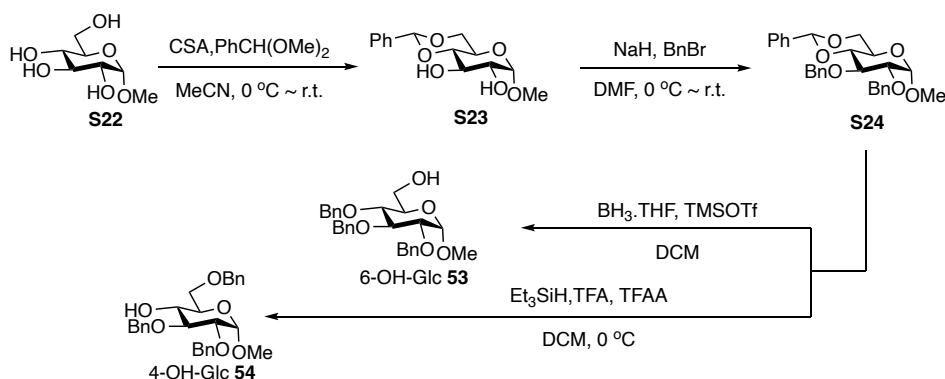
To a solution of compound **S19** (25 mmol, 8.3 g) in DCM (80 mL), HSTol (50 mmol, 6.2 g) was added. The mixture was cooled to 0 °C, and EF₃.OEt₂ (62.5 mmol, 7.8 ml) was added. The mixture was stirred at room temperature under N₂. The mixture was concentrated, and the resulting residue was diluted with ethyl acetate (300 mL), and washed with water, saturated NaHCO₃. Organic layer was dried over MgSO₄. The organic phase was dried over MgSO₄ and then filtered and concentrated. Silica gel column chromatography (2:1 hexanes-/EtOAc) afforded 6.9 g (83%) of *p*-Tolyl 3,4,6-tri-*O*-acetyl-2-deoxy-1-thio-D-glucopyranoside **S20** as colorless oil.

Compound **E** was derived from compound **S21** (4.0 g, 14.7 mmol), and compound **S21** was derived from compound **S20** (6.97 g, 17.5 mmol) with the same general procedure as compound **B**. The colorless syrup product **E** was obtained with the yield of 7 g, 88% for two steps (13). α-anomer: Colorless syrup; [α]²⁶_D = +186.5° (*c* 1.0, CHCl₃); ¹H NMR (400 MHz, CDCl₃) δ 7.36–7.24 (m, 15H, Ph), 7.19 (dd, 2H, *J* = 7.7 and 1.9 Hz, Ph), 7.02 (d, 2H, *J* = 8.0 Hz, Ph), 5.59 (d, 1H, *J* = 5.3 Hz), 4.88 (d, 1H, CH₂Ph, *J* = 10.8 Hz), 4.65 (ABq, 2H, CH₂Ph, *J* = 11.5 Hz), 4.58 (d, 1H, CH₂Ph, *J* = 12.0 Hz), 4.52 (d, 1H, CH₂Ph, *J* = 10.8 Hz), 4.43 (d, 1H, CH₂Ph, *J* = 12.0 Hz), 4.30 (ddd, 1H, *J* = 9.8, 4.0 and 1.8 Hz), 3.95 (ddd, 1H, *J* = 11.7, 8.8 and 4.8 Hz), 3.80 (dd, 1H, *J* = 10.6 and 4.9 Hz), 3.64 (dd, 1H, *J* = 11.0 and 1.9 Hz), 3.61 (t, 1H, *J* = 9.2 Hz), 2.43 (dd, 1H, *J* = 12.9 and 4.9 Hz), 2.28 (s, 3H), 2.08 (ddd, 1H, *J* = 13.2, 11.7 and 5.6 Hz); ¹³C NMR (100 MHz, CDCl₃) δ 138.7 (C), 138.6 (C), 138.4 (C), 137.4 (C), 132.0 (CH), 131.3 (C), 129.8 (CH), 128.6 (CH), 128.5 (CH), 128.4 (CH), 128.06 (CH), 128.0 (CH), 127.9 (CH), 127.8 (CH), 127.78 (CH), 127.7 (CH), 84.5 (CH), 78.7 (CH), 78.1 (CH), 75.1 (CH₂), 73.5 (CH₂), 72.06 (CH₂), 71.9 (CH), 69.2 (CH₂), 36.3 (CH₂), 21.2 (CH₃); IR (thin film): ν = 3035, 2929, 1496, 1456, 1089, 750, 698, 649 cm⁻¹; HRMS (ESI) calcd. for C₃₄H₃₆NaSO₄ [M+Na⁺] 563.2232, found 563.2227. β-anomer: Colorless syrup; [α]²⁹_D = -38.0° (*c* 5.0, CH₂Cl₂); ¹H NMR (400 MHz, CDCl₃) δ 7.40 (d, 2H, *J* = 8.1 Hz, Ph), 7.32–7.19 (m, 15H, Ph), 7.01 (d, 2H, *J* = 8.1 Hz, Ph), 4.86 (d, 1H, CH₂Ph, *J* = 10.9 Hz), 4.65 (dd, 1H, *J* = 11.7 and 2.0 Hz), 4.658 (d, 1H, CH₂Ph, *J* = 11.7 Hz), 4.57 (d, 2H, CH₂Ph, *J* = 11.6 Hz),

4.56 (d, 1H, CH₂Ph, *J* = 10.9 Hz), 4.51 (d, 1H, CH₂Ph, *J* = 11.8 Hz), 3.77 (dd, 1H, *J* = 10.9 and 1.8 Hz), 3.70 (dd, 1H, *J* = 10.9 and 4.6 Hz), 3.65 (ddd, 1H, *J* = 11.2, 8.1 and 5.3 Hz), 3.47 (t, 1H, *J* = 9.7 Hz), 3.43 (ddd, 1H, *J* = 9.6, 4.8 and 1.6 Hz), 2.41 (ddd, 1H, *J* = 12.8, 5.2 and 1.8 Hz), 2.28 (s, 3H), 1.75 (q, 1H, *J* = 11.7 Hz); ¹³C NMR (100 MHz, CDCl₃) δ 138.7 (C), 138.6 (C), 138.4 (C), 137.7 (C), 132.5 (CH), 130.1 (C), 129.8 (CH), 128.6 (CH), 128.5 (CH), 128.4 (CH), 128.1 (CH), 127.8 (CH), 127.6 (CH), 82.5 (CH), 80.9 (CH), 79.6 (CH), 78.1 (CH), 75.2 (CH₂), 73.6 (CH₂), 71.8 (CH₂), 69.7 (CH₂), 37.1 (CH₂), 21.3 (CH₃); IR (thin film): ν = 3064, 2887, 1496, 1456, 1276, 1080, 750, 698 cm⁻¹; HRMS (ESI) calcd. for C₃₄H₃₆NaSO₄ [M+Na⁺] 563.2232, found 563.2239.

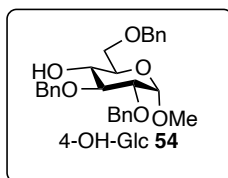
3.2 Synthesis of alcohols

Methyl 2,3,4-tri-*O*-benzyl-α-D-glucopyranoside (53)



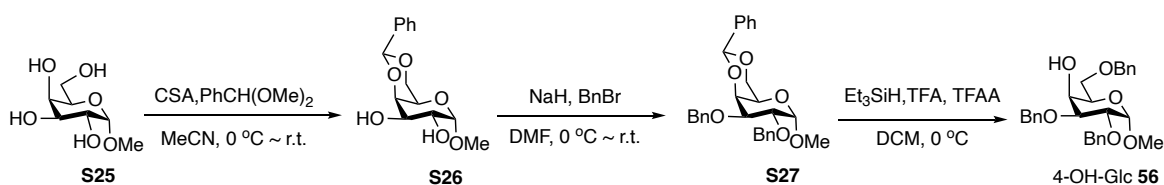
To a solution of compound methyl 2,3-di-*O*-benzyl-4,6-*O*-benzylidene-α-D-glucopyranoside **S24** (0.3 g, 0.65 mmol) in BH₃·THF (0.47 mL, 4.86 mmol). The reaction was stirred for 10 min, and then TMSOTf (0.024 mL, 0.13 mmol) was added. The reaction was stirred at 0 °C gradually to room temperature for 2 h, and quenched by MeOH (5 mL) and evaporated under reduced pressure. The crude product was purified by flash column chromatography on silica gel using EtOAc/ hexane (1:2) as the eluent to obtain product as a colorless oil (0.316 g, 99%). [α]_D²⁸ -204.2 (*c* 1.3, CHCl₃); IR: ν 2959, 1069, 1051, 737, 697 cm⁻¹; ¹H NMR (500 MHz, CDCl₃) δ 7.33-7.26 (m, 15H, Ph-H), 4.98 (d, *J* = 10.9 Hz, 1H, CH₂Ph), 4.85 (d, *J* = 10.9 Hz, 1H, CH₂Ph), 4.82 (d, *J* = 12.2 Hz, 1H, CH₂Ph), 4.68 (d, *J* = 10.9 Hz, 1H, CH₂Ph), 4.66 (d, *J* = 11.0 Hz, 1H, CH₂Ph), 4.59 (d, *J* = 3.6 Hz, 1H, H-1), 4.03 (dd, *J* = 9.7, 9.3 Hz, 1H, H-3), 3.79 (dd, *J* = 11.7, 6.5 Hz, 1H, H-6a), 3.71 (dd, *J* = 11.7, 3.8 Hz, 1H, H-6b), 3.69 (t, *J* = 4.2 Hz, 1H, H-5), 3.54 (dd, *J* = 9.3, 5.2 Hz, 1H, H-4), 3.52 (dd, *J* = 9.7, 3.6 Hz, 1H, H-2), 3.35 (s, 3H, CH₃); ¹³C NMR (100 MHz, CDCl₃) δ 138.8 (C), 138.2 (C), 138.0 (C), 128.6 (CH), 128.5 (CH), 128.3 (CH), 128.1 (CH), 128.0 (CH), 127.9 (CH), 127.7 (CH), 127.4 (CH), 126.0 (CH), 98.2 (CH), 82.0 (CH), 80.0 (CH), 77.5 (CH), 75.7 (CH₂), 75.0 (CH₂), 73.4 (CH₂), 70.7 (CH), 61.9 (CH), 55.2 (CH₃); HRMS (ESI) calcd. for C₂₈H₃₂O₆Na [M + Na]⁺ 487.2097, found 487.2053.

Methyl 2,3,6-tri-*O*-benzyl- α -D-glucopyranoside (**54**)



Methyl 2,3-di-*O*-benzyl-4,6-*O*-benzylidene- α -D-glucopyranoside **S24** (0.4 g, 0.865 mmol) was dissolved in DCM and then added Et₃SiH (1.24 mL, 7.78 mmol), TFA (0.5 mL, 6.48 mmol) and TFPA (0.025 mL, 0.173 mmol) in the same batch. The reaction was stirred at -40 °C for 6 h and quenched by Et₃N (5 mL). The mixture was extracted with EtOAc (20 mL) and NaHCO₃ (20 mL \times 2). The organic layers were combined, dried over anhydrous MgSO₄, filtered, and evaporated under reduced pressure. The crude product was purified by flash column chromatography on silica gel using EtOAc/ hexane (1/3) as the eluent to obtain product as a colorless oil (0.365 g, 91 %) (*13*). $[\alpha]^{28}_D$ -290.6 (*c* 0.5, CHCl₃); IR: ν 2922, 1055, 1028, 736, 697 cm⁻¹; ¹H NMR (500 MHz, CDCl₃) δ 7.35-7.28 (m, 15H, Ar-H), 4.98 (d, *J* = 11.4 Hz, 1H, CH₂Ph), 4.78 (d, *J* = 12.1 Hz, 1H, CH₂Ph), 4.75 (d, *J* = 11.4 Hz, 1H, CH₂Ph), 4.67 (d, *J* = 12.1 Hz, 1H, CH₂Ph), 4.64 (d, *J* = 3.6 Hz, 1H, H-1), 4.60 (d, *J* = 12.2 Hz, 1H, CH₂Ph), 4.55 (d, *J* = 12.2 Hz, 1H, CH₂Ph), 3.79 (t, *J* = 9.1 Hz, 1H, H-3), 3.74-3.67 (m, 3H, H-5, H-6a, H-6b), 3.61 (t, *J* = 9.1 Hz, 1H, H-4), 3.54 (dd, *J* = 9.1, 3.6 Hz, 1H, H-2), 3.39 (s, 3H, CH₃), 2.30 (d, *J* = 2.1 Hz, 1H, OH); ¹³C NMR (125 MHz, CDCl₃) δ 138.8 (C), 138.2 (C), 138.0 (C), 128.6 (CH), 128.5 (CH), 128.3 (CH), 128.1 (CH), 128.0 (CH), 127.9 (CH), 127.7 (CH), 127.4 (CH), 126.0 (CH), 98.2 (CH), 81.4 (CH), 79.6 (CH), 75.4 (CH₂), 73.6 (CH₂), 73.2 (CH₂), 70.7 (CH), 69.9 (CH), 69.5 (CH), 55.2 (CH₃); HRMS (ESI) calcd. for C₂₈H₃₂O₆Na [M + Na]⁺ 487.2097, found 487.2146.

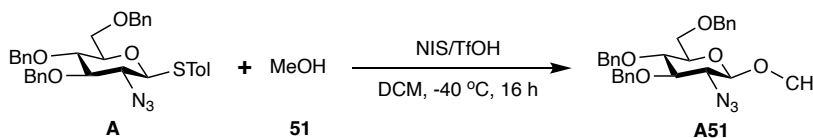
Methyl 2,3,6-tri-*O*-benzyl- α -D-galactopyranoside (**56**)



To a solution of methyl 2,3-di-*O*-benzyl-4,6-*O*-benzylidene- α -D-galactopyranoside **S27** (1.65 g, 3.57 mmol) in DCM, Et₃SiH (3.5 mL, 21.42 mmol), TFA (1.4 mL, 17.85 mmol) and TFPA (101 μ L, 0.714 mmol) was added. The reaction was stirred at 0 °C for overnight and quenched by Et₃N (1.5 mL). The mixture was extracted with EtOAc (20 mL \times 3) and water (20 mL). The organic layers were combined, dried over anhydrous MgSO₄, filtered, and evaporated under reduced pressure. The crude product was purified by flash column chromatography EtOAc/Hexane (1/3) on silica gel to give colorless oil product (1.16 g, 70%) (*13*). $[\alpha]^{26}_D$ +62.7 (*c* 1.0, CH₂Cl₂); IR (CH₂Cl₂) ν 3476, 3062, 3030, 2910, 1604, 1496, 1454, 1096, 1049, 738, 698 cm⁻¹; ¹H NMR (600 MHz, CDCl₃) δ 7.38-7.28 (m, 15H, Ph-H), 4.82 (ABq, *J* = 12.5 Hz, 1H, CH₂Ph), 4.80 (ABq, *J* =

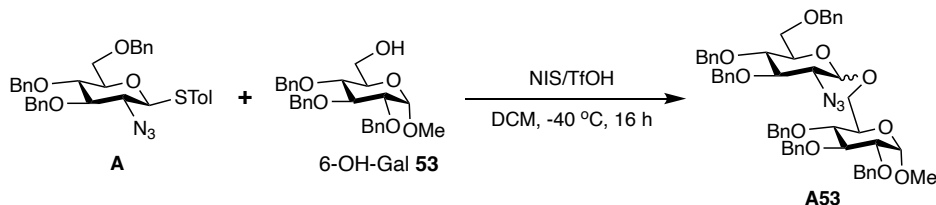
12.3 Hz, 1H, CH₂Ph), 4.71 (ABq, $J = 12.3$ Hz, 1H, CH₂Ph), 4.69 (d, $J = 2.8$ Hz, 1H, H-1), 4.67 (ABq, $J = 12.5$ Hz, 1H, CH₂Ph), 4.60 (ABq, $J = 11.9$ Hz, 1H, CH₂Ph), 4.56 (ABq, $J = 11.9$ Hz, 1H, CH₂Ph), 4.06 (d, $J = 1.0$ Hz, 1H, H-4), 3.90 (td, $J = 5.6, 1.0$ Hz, 1H, H-5), 3.88-3.87 (m, 2H, H-2, H-3), 3.74 (dd, $J = 10.1, 5.6$ Hz, 1H, H-6a), 3.68 (dd, $J = 10.1, 6.2$ Hz, 1H, H-6b), 3.39 (s, 3H, OCH₃); ¹³C NMR (150 MHz, CDCl₃) δ 138.3 (C), 138.1 (C), 138.0 (C), 128.5 (CH), 128.4 (CH), 128.0 (CH), 127.82 (CH), 127.79 (CH), 127.77 (CH), 127.6 (CH), 98.6 (CH), 77.6 (CH), 75.7 (CH), 73.6 (CH₂), 73.5 (CH₂), 72.7 (CH₂), 69.6 (CH₂), 68.3 (CH), 68.1 (CH), 55.3 (CH₃); HRMS (ESI) calcd. for C₂₈H₃₂O₆Na [M + Na]⁺ 487.2097, found 487.2106.

Methyl 2-azido-3,4,6-tri-*O*-benzyl-2-deoxy- β -D-glucopyranoside (A51)



$[\alpha]^{25}_{\text{D}} -0.2$ (c 1.2, CHCl₃); IR (CHCl₃) ν 2920, 2108, 1453, 1272, 1218, 1057, 772, 697 cm⁻¹; ¹H NMR (400 MHz, CDCl₃) δ 7.37-7.16 (m, 15H, Ph-H), 4.90-4.79 (m, 3H, CH₂Ph), 4.64-4.53 (m, 3H, CH₂Ph), 4.17 (d, 1H, $J = 7.4$ Hz, H-1), 3.75-3.68 (m, 2H, H-6_{ax}, H-6_{eq}), 3.63 (t, $J = 8.8$ Hz, 1H, H-4), 3.58 (s, 3H, OCH₃), 3.47-3.35 (m, 3H, H-2, H-6a, H-6b); ¹³C NMR (125 MHz, CDCl₃) δ 138.0 (C), 137.9 (C), 128.5 (CH), 128.43 (CH), 128.37 (CH), 128.0 (CH), 127.9 (CH), 127.8 (CH), 127.7 (CH), 102.9 (CH), 83.2 (CH), 77.8 (CH), 75.5 (CH), 75.1 (CH₂), 75.0 (CH), 73.5 (CH₂), 68.6 (CH₂), 66.3 (CH), 57.1 (CH₃); HRMS (ESI) calcd. for C₂₈H₃₁N₃O₅Na [M+Na]⁺ 512.2161, found 512.2203.

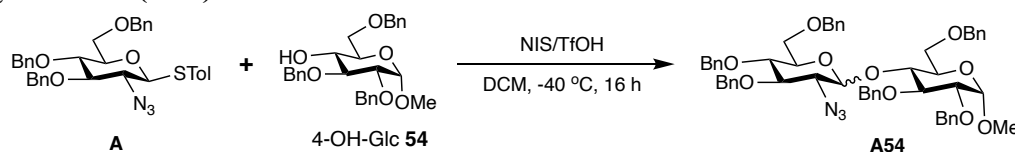
Methyl 6-*O*-(2-azido-3,4,6-tri-*O*-benzyl-2-deoxy- β -D-glucopyranosyl)-2,3,4-tri-*O*-benzyl- α -D-glucopyranoside (A53)



$[\alpha]^{19}_{\text{D}} = 5.27$ (c 1.2, CHCl₃); IR (CHCl₃) ν 2922, 2108, 1453, 1359, 1060, 735, 696 cm⁻¹; ¹H NMR (400 MHz, CDCl₃) δ 7.38-7.16 (m, 30H, Ph-H), 5.06-4.64 (m, 10H, CH₂Ph), 4.63 (s, 1H, H-1), 4.60-4.45 (m, 2H, CH₂Ph), 4.21 (d, $J = 7.7$ Hz, 1H, H-1'), 4.17 (dd, $J = 11.1, 2.0$ Hz, 1H, H-6a), 4.05 (t, $J = 9.3$ Hz, 1H, H-3), 3.85 (ddd, $J = 10.5, 4.2, 1.8$ Hz, 1H, H-5), 3.76-3.68 (m, 3H, H-6b, H-6'a, H-6'b), 3.65-3.58 (m, 3H, H-2, H-4, H-4'), 3.53-3.40 (m, 6H, H-2', H-3', H-5', OCH₃); ¹³C NMR (100 MHz, CDCl₃) δ 138.8 (C), 138.4 (C), 138.1 (CH), 138.0 (C), 137.8 (C), 128.4 (CH), 128.3 (CH), 128.1 (CH), 128.0 (CH), 127.9 (CH), 127.82 (CH), 127.80 (CH), 127.7 (CH), 127.60 (CH), 127.55 (CH), 127.50 (CH), 102.1 (CH), 98.1 (CH), 83.2 (CH), 82.0 (CH), 79.8 (CH), 77.72 (CH), 77.70 (CH), 75.6 (CH₂), 75.5 (CH₂), 75.2 (CH), 74.94 (CH₂), 74.88 (CH₂), 74.8 (CH₂),

74.4 (CH₂), 69.7 (CH), 68.6 (CH₂), 68.4 (CH₂), 66.3 (CH), 55.1 (CH₃); HRMS (ESI) calcd. for C₅₅H₅₉N₃O₁₀Na [M + Na]⁺ 944.4098, found 944.4083 (13).

Methyl 4-*O*-(2-azido-3,4,6-tri-*O*-benzyl-2-deoxy-β-*D*-glucopyranosyl)-2,3,6-tri-*O*-benzyl-α-*D*-glucopyranoside (A54)



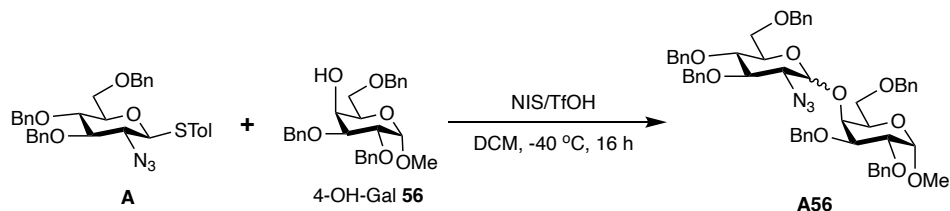
Data for β-anomer (**A54β**): $[\alpha]_{\text{D}}^{15} = -11.4^\circ$ (c 1.09, CHCl₃); IR (CHCl₃) ν 3009, 2910, 2870, 2112, 1496, 1454, 1361, 1277, 1087, 750 cm⁻¹; ¹H NMR (500 MHz, CDCl₃) δ 3.18 (ddd, *J*=1.7, 4.3, 9.6 Hz, 1H, H-5'), 3.24 (dd, *J*=8.9, 9.8 Hz, 1H, H-3'), 3.31 (dd, *J*=8.0, 9.8 Hz, 1H, H-2'), 3.38 (s, 3H, OCH₃), 3.47–3.50 (m, 2H, H-2, H-6'a), 3.59 (dd, *J*=8.9, 9.6 Hz, 1H, H-4'), 3.62 (dd, *J*=1.7, 11.1 Hz, 1H, H-6'b), 3.70 (dd, *J*=1.6, 10.9 Hz, 1H, H-6a), 3.78 (ddd, *J*=1.6, 3.2, 9.8 Hz, 1H, H-5), 3.89 (dd, *J*=8.9, 9.5 Hz, 1H, H-3), 3.92 (dd, *J*=3.2, 10.9 Hz, 1H, H-6b), 3.96 (dd, *J*=8.9, 9.8 Hz, 1H, H-4), 4.26 (d, *J*=8.0 Hz, 1H, H-1'), 4.35 (d, *J*=12.1 Hz, 1H, OCHPh), 4.40 (d, *J*=12.1 Hz, 1H, OCHPh), 4.47 (d, *J*=12.1 Hz, 1H, OCHPh), 4.54 (d, *J*=11.0 Hz, 1H, OCHPh), 4.58 (d, *J*=12.1 Hz, 1H, OCHPh), 4.59 (d, *J*=3.6 Hz, 1H, H-1), 4.67 (d, *J*=12.1 Hz, 1H, OCHPh), 4.74 (d, *J*=12.1 Hz, 1H, OCHPh), 4.76 (d, *J*=11.0 Hz, 1H, OCHPh), 4.781 (d, *J*=11.4 Hz, 1H, OCHPh), 4.782 (d, *J*=10.7 Hz, 1H, OCHPh), 4.82 (d, *J*=10.7 Hz, 1H, OCHPh), 5.02 (d, *J*=11.4 Hz, 1H, OCHPh), 7.17–7.36 (m, 30H, Ar-H); ¹³C NMR (126 MHz, CDCl₃) δ 55.3, 66.9, 68.2, 68.6, 69.7, 73.3, 73.47, 73.51, 74.7, 75.19, 75.24, 75.4, 77.9, 79.1, 80.3, 83.3, 98.3 (C-1), 100.9 (C-1'), 127.0, 127.4, 127.5, 127.65, 127.67, 127.70, 127.72, 127.8, 127.95, 127.98, 128.1, 128.2, 128.3, 128.36, 128.42, 128.5, 137.8, 137.9, 138.0, 138.3, 138.4, 139.5; HRMS (ESI) calcd. for C₅₅H₅₉N₃O₁₀Na [M+Na]⁺ 944.4089, found 944.4092. Data for α-anomer (**A54α**): $[\alpha]_{\text{D}}^{15} = +39.1^\circ$ (c 0.78, CHCl₃); IR (CHCl₃) ν 3013, 2910, 2870, 2112, 1602, 1454, 1361, 1221, 1049, 713 cm⁻¹; ¹H NMR (500 MHz, CDCl₃) δ 3.27 (dd, *J*=3.9, 10.4 Hz, 1H, H-2'), 3.34 (brd, *J*=11.0 Hz, 1H, H-6'a), 3.38 (s, 3H, OCH₃), 3.52 (dd, *J*=1.4, 11.0 Hz, 1H, H-6'b), 3.57 (dd, *J*=3.6, 9.6 Hz, 1H, H-2), 3.65 (dd, *J*=1.9, 11.0 Hz, 1H, H-6a), 3.66–3.70 (m, 2H, H-4', H-5'), 3.72 (dd, *J*=4.3, 11.0 Hz, 1H, H-6b), 3.79 (ddd, *J*=1.9, 4.3, 10.0 Hz, 1H, H-5), 3.86 (m, 1H, H-3'), 3.91 (dd, *J*=8.6, 10.0 Hz, 1H, H-4), 4.08 (dd, *J*=8.6, 9.6 Hz, 1H, H-3), 4.25 (d, *J*=12.1 Hz, 1H, OCHPh), 4.45 (d, *J*=10.9 Hz, 1H, OCHPh), 4.49 (d, *J*=12.1 Hz, 1H, OCHPh), 4.50 (s, 2H, OCH₂Ph), 4.61 (d, *J*=3.6 Hz, 1H, H-1), 4.62 (d, *J*=12.2 Hz, 1H, OCHPh), 4.74 (d, *J*=10.9 Hz, 1H, OCHPh), 4.75 (d, *J*=12.2 Hz, 1H, OCHPh), 4.83 (d, *J*=10.9 Hz, 1H, OCHPh), 4.85 (d, *J*=10.9 Hz, 1H, OCHPh), 4.86 (d, *J*=10.7 Hz, 1H, OCHPh), 5.10 (d, *J*=10.7 Hz, 1H, OCHPh), 5.73 (d, *J*=3.9 Hz, 1H, H-1'), 7.12 (m, 2H, Ar-H), 7.20–7.35 (m, 28H, Ar-H); ¹³C NMR (126 MHz, CDCl₃) δ 55.3, 63.3, 67.9, 69.3, 69.5, 71.4, 73.27, 73.31, 73.5, 74.9, 75.0, 75.3, 78.1, 80.1, 80.5, 82.0, 97.69 (C-1'), 97.73 (C-1), 127.2, 127.4, 127.45, 127.53, 127.66, 127.71, 127.8, 127.9, 128.1, 128.26, 128.32, 128.4, 128.5, 137.8, 137.9, 138.0, 138.1, 138.2, 138.7; HRMS (ESI) calcd. for C₅₅H₅₉N₃O₁₀Na [M+Na]⁺ 944.4089, found 944.4093.

Phenyl 2-azido-3,4,6-tri-*O*-benzyl-2-deoxy-D-glucopyranoside (**A55**)



Data for **A55**: IR (CHCl₃) ν 2919, 2851, 2108, 1455, 1222, 1056, 755, 696 cm⁻¹; ¹H NMR (500 MHz, CDCl₃) δ 7.49-7.32 (m, 26.1H, Ar-H), 7.28-7.24 (m, 3.7H, Ar-H), 7.21-7.17 (m, 3.3H, Ar-H), 7.15-7.10 (m, 1.9H, Ar-H), 5.67 (d, J = 3.4 Hz, 1H, H-1 α), 5.05-4.99 (m, 2.7H, CH₂Ph), 4.93-4.84 (m, 3.24H, H-1 β , CH₂Ph), 4.70-4.58 (m, 4.3H, CH₂Ph), 4.52 (d, J = 11.95 Hz, 1H, CH₂Ph), 4.31 (dd, J = 9.5 Hz, 9.5 Hz, 1H, H-3 α), 4.04 (m, 1H, H-5 α), 3.94 (dd, J = 9.1 Hz, 9.1 Hz, 1H, H-4 α), 3.87-3.76 (m, 3.7H, H-6 $\alpha\alpha$, H-2 β , H-4 β , H-6 $\alpha\beta$, H-6 $\beta\beta$), 3.71-3.68 (dd, J = 10.9 Hz, 1.6 Hz, 1H, H-6 $\beta\alpha$), 3.67-3.64 (m, 1H, H-5 β), 3.60-3.56 (m, 1.8H, H-2 α , H-3 β); ¹³C NMR (125 MHz, CDCl₃) δ 157.01 (C), 156.26 (C), 137.89 (C), 137.83 (C), 137.81 (C), 137.79 (C), 137.72 (C), 137.64 (C), 134.26 (CH), 129.68 (CH), 129.54 (CH), 129.48 (CH), 128.42 (CH), 128.40 (CH), 128.38 (CH), 128.36 (CH), 128.31 (CH), 128.28 (CH), 127.98 (CH), 127.84 (CH), 127.81 (CH), 127.74 (CH), 127.69 (CH), 127.64 (CH), 127.57 (CH), 122.99 (CH), 122.75 (CH), 116.94 (CH), 116.69 (CH), 100.49 (CH), 96.76 (CH), 82.92 (CH), 80.03 (CH), 77.93 (CH), 77.49 (CH), 75.53 (CH₂), 75.39 (CH₂), 75.23 (CH), 74.99 (CH₂), 73.42 (CH₂), 73.39 (CH₂), 71.29 (CH), 68.48 (CH₂), 68.01 (CH₂), 66.05 (CH), 63.12 (CH); HRMS (ESI) calcd. for C₃₃H₃₃N₃O₅Na [M+Na]⁺ 574.2312, found 574.2313.

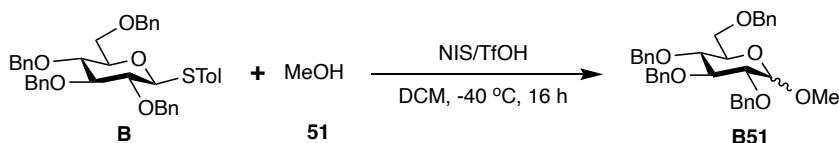
Methyl 4-*O*-(2-azido-3,4,6-tri-*O*-benzyl-2-deoxy- β -D-glucopyranosyl)-2,3,6-tri-*O*-benzyl- α -D-galactopyranoside (**A56**)



The α - and β -glycosides were separated by flash column chromatography with 15:1 toluene/AcOEt. Data for β -anomer (**A56** β): $[\alpha]_D^{19} = +3.32^\circ$ (c 0.74, CHCl₃); IR (CHCl₃) 3020, 2930, 2868, 2114, 1454, 1358, 1277, 1089 cm⁻¹; ¹H NMR (500 MHz, CDCl₃) δ 3.27 (ddd, J = 1.9, 3.9, 9.9 Hz, 1H, H-5'), 3.34 (dd, J = 8.8, 9.8 Hz, 1H, H-3'), 3.37 (s, 3H, OCH₃), 3.40 (dd, J = 7.6, 9.8 Hz, 1H, H-2'), 3.58-3.65 (m, 4H, H-6a, H-4', H-6'a, H-6'b), 3.73 (dd, J = 4.7, 10.5 Hz, 1H, H-6b), 3.90-3.94 (m, 2H, H-3, H-5), 4.13 (dd, J = 3.7, 10.1 Hz, 1H, H-2), 4.16 (brd, J = 3.0 Hz, 1H, H-4), 4.37 (d, J = 12.0 Hz, 1H, OCHPh), 4.44 (d, J = 12.0 Hz, 1H, OCHPh), 4.48 (d, J = 12.1 Hz, 1H, OCHPh), 4.52 (d, J = 12.1 Hz, 1H, OCHPh), 4.54 (d, J = 12.1 Hz, 1H, OCHPh), 4.64 (d, J = 3.7 Hz, 1H, H-1), 4.67 (d, J = 12.1 Hz, 1H, OCHPh), 4.69 (d, J = 12.1 Hz, 1H, OCHPh), 4.73 (d, J = 7.6 Hz, 1H, H-1'), 4.77-4.80 (m, 2H, OCHPh \times 2), 4.84 (d, J = 12.1 Hz, 1H, OCHPh), 4.91 (d, J = 10.8 Hz, 1H, OCHPh), 4.92 (d, J = 12.1 Hz, 1H, OCHPh), 7.15 (m, 2H, Ar-H), 7.24-7.37 (m, 28H, Ar-

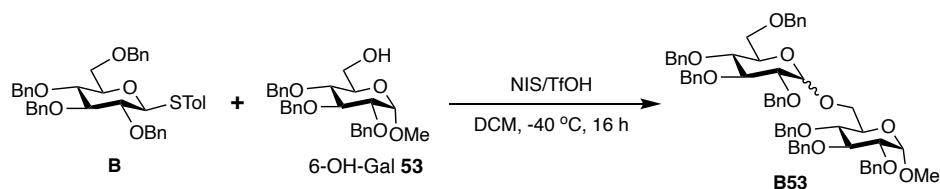
H); ^{13}C NMR (126 MHz, CDCl_3) δ 55.3, 66.6, 68.9, 69.4, 70.2, 73.2, 73.4, 73.5, 73.8, 74.3, 74.8, 75.0, 75.5, 76.6, 77.7, 78.4, 83.1, 98.8 (C-1), 101.6 (C-1'), 127.2, 127.3, 127.4, 127.5, 127.6, 127.7, 127.80, 127.82, 127.9, 128.0, 128.2, 128.27, 128.32, 128.36, 128.42, 128.44, 137.9, 138.05, 138.14, 138.58, 138.61, 138.9; HRMS (ESI) calcd. for $\text{C}_{55}\text{H}_{59}\text{N}_3\text{O}_{10}\text{Na}$ $[\text{M}+\text{Na}]^+$ 944.4084, found 944.4093. Data for α -anomer (**A56a**): $[\alpha]_{\text{D}}^{18} = +44.5^\circ$ (c 0.21, CHCl_3); IR (CHCl_3) 3018, 2930, 2870, 2114, 1454, 1358, 1277, 1089 cm^{-1} ; ^1H NMR (500 MHz, CDCl_3) δ 3.03 (dd, $J=1.7$, 11.1 Hz, 1H, H-6'a), 3.28 (dd, $J=2.0$, 11.1 Hz, 1H, H-6'b), 3.35 (dd, $J=3.6$, 9.2 Hz, 1H, H-2'), 3.36 (s, 3H, OCH_3), 3.54 (dd, $J=10.4$, 12.9 Hz, 1H, H-5), 3.75 (dd, $J=9.4$, 10.1 Hz, 1H, H-4'), 3.83–3.92 (m, 5H, H-2, H-3, H-6a, H-6b, H-3'), 4.18 (d, $J=12.2$ Hz, 1H, OCHPh), 4.20 (d, $J=2.9$ Hz, 1H, H-4), 4.23 (ddd, $J=1.7$, 2.0, 10.1 Hz, 1H, H-5'), 4.43 (d, $J=12.2$ Hz, 1H, OCHPh), 4.46 (d, $J=12.2$ Hz, 1H, OCHPh), 4.52 (d, $J=11.8$ Hz, 1H, OCHPh), 4.55 (d, $J=11.8$ Hz, 1H, OCHPh), 4.69–4.74 (m, 4H, H-1, $\text{OCHPh}\times 3$), 4.77 (d, $J=11.9$ Hz, 1H, OCHPh), 4.80–4.82 (m, 2H, $\text{OCHPh}\times 2$), 4.86 (d, $J=10.6$ Hz, 1H, OCHPh), 4.94 (d, $J=3.6$ Hz, 1H, H-1'), 7.13 (m, 2H, Ar-H), 7.17–7.37 (m, 28H, Ar-H); ^{13}C NMR (126 MHz, CDCl_3) δ 55.4, 64.1, 67.3, 67.5, 68.9, 70.7, 73.16, 73.19, 73.3, 73.6, 74.8, 74.9, 75.27, 75.33, 78.2, 80.4, 98.5, 98.6, 127.4, 127.5, 127.6, 127.66, 127.73, 127.8, 127.95, 127.99, 128.03, 128.26, 128.31, 128.33, 128.4, 128.5, 137.6, 137.9, 138.1, 138.2, 138.4, 138.7; HRMS (ESI) calcd. for $\text{C}_{55}\text{H}_{59}\text{N}_3\text{O}_{10}\text{Na}$ $[\text{M}+\text{Na}]^+$ 944.4084, found 944.4093.

Methyl 2,3,4,6-tetra-*O*-benzyl-D-glucopyranoside (**B51**)



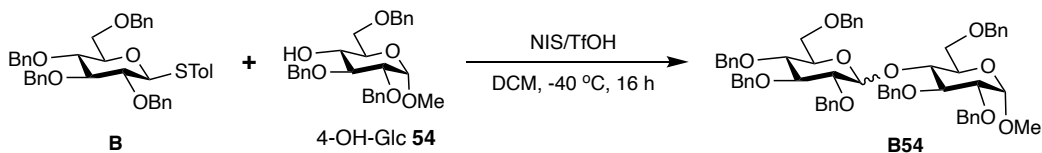
Data for **B51**: $[\alpha]_{\text{D}}^{26} +31.0$ (c 2.9, CH_2Cl_2); IR (CH_2Cl_2) ν 1067, 1046, 1026, 732, 694 cm^{-1} ; ^1H NMR (400 MHz, CDCl_3) δ 7.41–7.18 (m, 40H, ArH), 5.05–4.05 (m, 16H, ArCH), 4.65 (d, $J=3.6$ Hz, 1H, H-1 α), 4.37 (d, $J=8.0$ Hz, 1H, H-1 β), 4.04 (t, $J=9.2$ Hz, 1H, H-3 α), 3.82–3.60 (m, 8H, H-3 β , H-4 α , H-5 α , H-6 α , H-6 β , H-4 β), 3.75 (dd, $J=9.2$, 3.6 Hz, 1H, H-2 α), 3.63 (s, 3H, CH_3), 3.52 (ddd, $J=9.2$, 4.8, 1.6 Hz, 1H, H-5 β), 3.50 (dd, $J=8.4$, 8.0 Hz, 1H, H-2 β), 3.42 (s, 3H, CH_3) ppm; ^{13}C NMR (100 MHz, CDCl_3) δ 138.8 (C), 138.6 (C), 138.5 (C), 138.2 (C), 138.1 (C), 137.9 (C), 128.3 (CH), 128.2 (CH), 128.0 (CH), 127.9 (CH), 127.8 (CH), 127.7 (CH), 127.6 (CH), 127.5 (CH), 104.6 (C- β), 98.1 (C- α), 84.6 (CH), 82.2 (CH), 82.0 (CH), 79.8 (CH), 77.8 (CH), 77.6 (CH), 75.6 (CH $_2$), 75.5 (CH $_2$), 74.9 (CH $_2$), 74.8 (CH $_2$), 74.6 (CH), 73.4 (CH $_2$), 70.0 (CH), 68.9 (CH $_2$), 68.5 (CH $_2$), 57.0 (CH $_3$), 55.1 (CH $_3$) ppm; HRMS (ESI-TOF, m/z) calcd. for $\text{C}_{35}\text{H}_{38}\text{O}_6\text{Na}$ $[\text{M}+\text{Na}]^+$ 577.2566, found 577.2565 (13).

Methyl 2,3,4-tri-*O*-benzyl-6-*O*-(2,3,4,6-tetra-*O*-benzyl-D-glucopyranosyl)- α -D-glucopyranoside (**B53**)



Data for **B53**: $[\alpha]_D^{26} +66.9$ (*c* 1.2, CH₂Cl₂); IR (CH₂Cl₂) ν 1067, 1026, 732, 694 cm⁻¹; ¹H NMR (400 MHz, CDCl₃) δ 7.38–7.14 (m, 105H, ArH), 5.03–4.93 (m, 10H), 4.86 (m, 2H), 4.83 (m, 3H), 4.81 (m, 4H), 4.76 (m, 2H), 4.73 (m, 2H), 4.70 (m, 5H), 4.67 (m, 2H), 4.65 (m, 2H), 4.61 (m, 3H), 4.59 (m, 6H), 4.55 (m, 2H), 4.51 (m, 2H), 4.46 (m, 2H), 4.51–4.44 (m, 2H), 4.39 (d, 1H), 4.22 (dd, *J* = 10.8, 2.0 Hz, 0.5 H), 4.02 (m, 5H), 3.84 (m, 5H), 3.75 (m, 4H), 3.69 (m, 5H), 3.66 (m, 3H), 3.63 (m, 2H), 3.59 (m, 6H), 3.55 (m, 2H), 3.48 (m, 3H), 3.39 (s, 6H), 3.36 (s, 3H) ppm; ¹³C NMR (100 MHz, CDCl₃) δ 138.8 (C), 138.5 (C), 138.4 (C), 138.2 (C), 137.9 (C), 128.4 (CH), 128.3 (CH), 128.2 (CH), 128.1 (CH), 128.0 (CH), 127.9 (CH), 127.8 (CH), 127.7 (CH), 127.6 (CH), 127.5 (CH), 127.4 (CH), 103.8 (CH), 98.0 (CH), 97.9 (CH), 97.2 (CH), 84.8 (CH), 82.1 (CH), 81.9 (CH), 81.6 (CH), 80.1 (CH), 80.0 (CH), 79.8 (CH), 77.9 (CH), 77.8 (CH), 77.6 (CH), 77.3 (CH), 75.6 (CH₂), 75.4 (CH₂), 75.0 (CH), 74.9 (CH₂), 74.8 (CH₂), 73.4 (CH₂), 73.3 (CH₂), 72.3 (CH₂), 70.3 (CH), 70.2 (CH), 69.0 (CH₂), 68.5 (CH₂), 66.0 (CH₂), 55.2 (CH₃), 55.1 (CH₃) ppm; HRMS (ESI-TOF, *m/z*) calcd. for C₆₂H₆₆O₁₁Na [M + Na]⁺ 1009.4503, found 1009.4511 (13).

Methyl 2,3,6-tri-*O*-benzyl-4-*O*-(2,3,4,6-tetra-*O*-benzyl-D-glucopyranosyl)- α -D-glucopyranoside (B54)



Data for **B54- α** : ¹H NMR (500 MHz, CDCl₃) δ 7.31 – 7.20 (m, 33H), 7.12 (dd, *J* = 7.1, 2.4 Hz, 2H), 5.71 (d, *J* = 3.6 Hz, 1H), 5.05 (d, *J* = 11.6 Hz, 1H), 4.90 (d, *J* = 10.9 Hz, 1H), 4.84 – 4.78 (m, 3H), 4.71 (d, *J* = 12.1 Hz, 1H), 4.63 – 4.57 (m, 3H), 4.57 – 4.50 (m, 4H), 4.44 (d, *J* = 10.9 Hz, 1H), 4.30 (d, *J* = 12.2 Hz, 1H), 4.13 – 4.03 (m, 2H), 3.95 – 3.90 (m, 1H), 3.89 – 3.82 (m, 2H), 3.74 (d, *J* = 10.0 Hz, 1H), 3.69 – 3.64 (m, 2H), 3.61 (dd, *J* = 9.2, 3.6 Hz, 1H), 3.51 (dd, *J* = 10.0, 3.5 Hz, 2H), 3.43 – 3.38 (m, 4H). ¹³C NMR (126 MHz, CDCl₃) δ 139.10, 138.90, 138.63, 138.31, 138.12, 138.07, 128.56, 128.45, 128.42, 128.42, 128.38, 128.35, 128.34, 128.15, 128.05, 127.96, 127.94, 127.83, 127.76, 127.69, 127.62, 127.49, 127.38, 127.21, 126.89, 97.90, 96.77, 82.17, 82.15, 80.34, 79.60, 77.78, 75.67, 75.06, 74.55, 73.58, 73.50, 73.36, 73.27, 72.46, 71.10, 69.66, 69.16, 68.30, 55.28. Data for **B54- β** : ¹H NMR (600 MHz, CDCl₃) δ 7.44 – 7.39 (m, 2H), 7.33 – 7.16 (m, 33H), 5.09 (d, *J* = 11.3 Hz, 1H), 4.87 (d, *J* = 10.9 Hz, 1H), 4.83 – 4.72 (m, 6H), 4.62 – 4.53 (m, 4H), 4.44 (d, *J* = 12.1 Hz, 1H), 4.41 – 4.35 (m, 3H), 3.97 (dd, *J* = 10.0, 8.9 Hz, 1H), 3.88 – 3.81 (m, 2H), 3.72 (dd, *J* = 11.0, 1.9 Hz, 1H), 3.62 – 3.57 (m, 2H), 3.55 (dd, *J* = 11.0, 4.7 Hz, 1H), 3.51 –

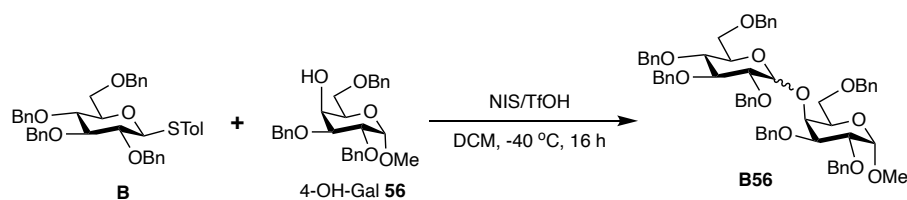
3.44 (m, 3H),), 3.38 – 3.35 (m, 1H), 3.37 (s, 3H), 3.29 (ddd, $J = 9.8, 4.7, 1.9$ Hz, 1H). ^{13}C NMR (126 MHz, CDCl_3) δ 139.73, 138.75, 138.73, 138.55, 138.47, 137.99, 128.59, 128.51, 128.49, 128.48, 128.38, 128.25, 128.15, 128.12, 127.94, 127.92, 127.90, 127.88, 127.78, 127.73, 127.67, 127.65, 127.45, 127.22, 102.63, 98.57, 85.02, 82.96, 80.57, 78.97, 78.19, 76.75, 75.73, 75.52, 74.93, 73.78, 73.50, 73.48, 70.11, 69.15, 68.00, 55.44. HRMS (ESI) calcd. for $\text{C}_{62}\text{H}_{66}\text{O}_{11}\text{Na}$ $[\text{M}+\text{Na}]^+$ 1009.4197, found 1009.4497.

Phenyl 2,3,4,6-tetra-*O*-benzyl-D-glucopyranoside (**B55**)



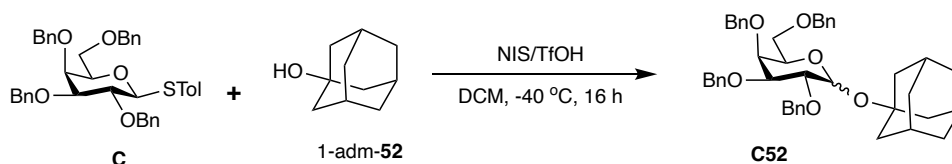
Data for **B55- α** : ^1H -NMR (500 MHz, CD_2Cl_2) 3.61 (dd, $J = 10.9$ Hz, 1H, C-6), 3.72-3.75 (m, 2H, C-4 and C-6), 3.74 (dd, $J = 9.6, 3.7$ Hz, 1H, C-2), 3.90 (ddd, $J = 10.1, 3.8, 1.9$ Hz, 1H, C-5), 4.18 (t, $J = 9.3$ Hz, 1H, C-3), 4.43 (d, $J = 11.8$ Hz, 1H, CH_2Ph), 4.51 (d, $J = 11.8$ Hz, 1H, CH_2Ph), 4.59 (d, $J = 11.8$ Hz, 1H, CH_2Ph), 4.70 (d, $J = 11.7$ Hz, 1H, CH_2Ph), 4.77 (d, $J = 11.7$ Hz, 1H, CH_2Ph), 4.84 (d, $J = 11.9$ Hz, 1H, CH_2Ph), 4.89 (d, $J = 10.9$ Hz, 1H, CH_2Ph), 5.03 (d, $J = 10.9$ Hz, 1H, CH_2Ph), 5.56 (d, $J = 3.5$ Hz, 1H, C-1), 7.03-7.06 (m, 1H, C-10), 7.11-7.13 (m, 2H, C-8), 7.22-7.40 (m, 22H, C-9 and Ph). **B55- β** : ^1H -NMR (500 MHz, CD_2Cl_2) 3.62-3.65 (m, 1H, C-5), 3.66-3.70 (m, 1H, C-4), 3.70-3.74 (m, 3H, C-2, C-3 and C-6), 3.81 (dd, $J = 10.7, 1.9$ Hz, 1H, C-6), 4.52 (d, $J = 10.9$ Hz, 1H, CH_2Ph), 4.60 (d, $J = 10.9$ Hz, 1H, CH_2Ph), 4.83-4.87 (m, 2H, CH_2Ph), 4.84 (d, $J = 11.0$ Hz, 1H, CH_2Ph), 4.88 (d, $J = 10.8$ Hz, 1H, CH_2Ph), 4.95 (d, $J = 11.0$ Hz, 1H, CH_2Ph), 5.03 (d, $J = 11.0$ Hz, 1H, CH_2Ph), 5.04 (d, $J = 6.4$ Hz, 1H, C-1), 7.06-7.07 (m, 1H, C-10), 7.08-7.11 (m, 2H, C-8), 7.22-7.40 (m, 22H, C-9 and Ph). ^{13}C -NMR (101 MHz, CD_2Cl_2) = 69.1 (C-6 α), 69.4 (C-6 β), 71.5 (C-5 α), 73.5 ($\text{CH}_2\text{Ph}\alpha$), 73.6 ($\text{CH}_2\text{Ph}\alpha$), 73.7 ($\text{CH}_2\text{Ph}\alpha$), 75.2 ($\text{CH}_2\text{Ph}\beta$), 75.31 ($\text{CH}_2\text{Ph}\beta$), 75.34 ($\text{CH}_2\text{Ph}\alpha$), 75.4 (C-5 β), 75.90 ($\text{CH}_2\text{Ph}\beta$), 75.91 ($\text{CH}_2\text{Ph}\beta$), 78.0 (C-4 α), 78.1 (C-4 β), 80.4 (C-2 α), 82.2 (C-3 α), 82.3 (C-2 β), 85.0 (C-3 β), 95.9 (C-1 α), 101.8 (C-1 β), 117.1 (C-8 β), 117.3 (C-8 α), 122.8 (C-10 α), 123.0 (C-10 β), 127.87 (Ph), 127.91 (Ph), 127.94 (Ph), 127.96 (Ph), 128.02 (Ph), 128.07 (Ph), 128.12 (Ph), 128.16 (Ph), 128.21 (Ph), 128.24 (Ph), 128.28 (Ph), 128.33 (Ph), 128.34 (Ph), 128.6 (Ph), 128.65 (Ph), 128.66 (Ph), 128.67 (Ph), 128.68 (Ph), 128.69 (Ph), 128.8 (Ph), 129.88 (C-9 α), 129.93 (C-9 β), 138.67 (Ph), 138.68 (Ph), 138.75 (Ph), 138.78 (Ph), 138.95 (Ph), 138.98 (Ph), 139.2 (Ph), 139.5 (Ph), 157.3 (C-7 α), 157.8 (C-7 β). IR: 3063, 3031, 2917, 2864, 1589, 1598, 1494, 1453, 1360, 1226, 1068, 1027, 733 cm^{-1} . HRMS: calcd. for $\text{C}_{40}\text{H}_{40}\text{NaO}_6$ $[\text{M}+\text{Na}]^+$ 639.2717, found 639.2699.

Methyl 2,3,4-tri-*O*-benzyl-4-*O*-(2,3,4,6-tetra-*O*-benzyl-D-glucopyranosyl)- α -D-galactopyranoside (**B56**)



Data for **B56**: IR (CHCl₃) ν 2919, 1454, 1095, 1071, 1047, 737, 699 cm⁻¹; ¹H NMR (500 MHz, CDCl₃) δ 7.45-7.15 (m, 62.60H, Ar-H), 5.14 (d, J = 11.35 Hz, 0.53H, CH₂Ph), 5.07 (d, J = 3.4 Hz, 1H, H-1' α), 5.00-4.94 (m, 2.47H, H-1' β , CH₂Ph), 4.90-4.71 (m, 13.84H, H-1 α , H-1 β , CH₂Ph), 4.65-4.40 (m, 7.44H, CH₂Ph), 4.34-4.16 (m, 6.19H, H-5' α , H-4 α , CH₂Ph), 4.04-3.91 (m, 7.61H, H-3' α , H-2 α , H-3 α , H-5 α , H-6 $\alpha\alpha$, H-2 β , H-3 β , H-4 β , H-5 β), 3.83-3.56 (m, 8.36H, H-2' α , H-4' α , H-3' β , H-4' β , H-6' $\alpha\beta$, H-6' $\beta\beta$, H-6 $\beta\alpha$, H-6 $\beta\beta$, H-6 $\beta\alpha$, H-6 $\beta\beta$), 3.49-3.38 (m, 7.73H, H-2' β , H-5' β , H-6 α' , OCH₃ α , OCH₃ β), 3.13 (dd, J = 10.65 Hz, J = 1.75 Hz 1.03H, H-6 $\beta'\alpha$); ¹³C NMR (125 MHz, CDCl₃) δ 138.83 (C), 138.76 (C), 138.72 (C), 138.59 (C), 138.56 (C), 138.49 (C), 138.40 (C), 138.26 (C), 138.16 (C), 138.09 (C), 137.89 (C), 129.99 (CH), 129.65 (CH), 128.90 (CH), 128.31 (CH), 128.28 (CH), 128.27 (CH), 128.20 (CH), 128.16 (CH), 128.14 (CH), 128.11 (CH), 127.99 (CH), 127.91 (CH), 127.83 (CH), 127.77 (CH), 127.73 (CH), 127.67 (CH), 127.62 (CH), 127.51 (CH), 127.46 (CH), 127.42 (CH), 127.38 (CH), 127.33 (CH), 127.31 (CH), 127.26 (CH), 102.64 (CH), 99.58 (CH), 98.69 (CH), 98.55 (CH), 84.49 (CH), 82.37 (CH), 82.08 (CH), 80.22 (CH), 78.44 (CH), 77.81 (CH), 77.73 (CH), 77.69 (CH), 76.97 (CH), 76.45 (CH), 75.49 (CH₂), 75.33 (CH₂), 74.94 (CH), 74.87 (CH₂), 74.79 (CH₂), 74.51 (CH), 74.12 (CH₂), 73.83 (CH₂), 73.58 (CH₂), 73.29 (CH₂), 73.26 (CH₂), 73.22 (CH₂), 72.92 (CH₂), 72.81 (CH₂), 70.64 (CH), 70.58 (CH₂), 69.56 (CH), 69.30 (CH), 69.12 (CH₂), 67.99 (CH₂), 67.54 (CH₂), 55.24 (CH₃), 55.18 (CH₃); HRMS (ESI) calcd. for C₆₂H₆₆O₁₁Na [M+Na]⁺ 1009.4197, found 1009.4497.

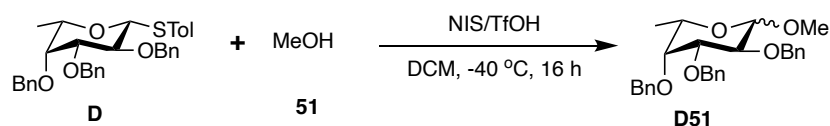
1- Admantyl 2,3,4,6-tetra-*O*-benzyl-D-galactopyranoside (C52)



Data for **C52**: IR (CHCl₃) ν 3826, 2918, 2850, 1453, 1071, 735, 696 cm⁻¹; ¹H NMR (500 MHz, CDCl₃) δ 7.43-7.26 (m, 26.49H, Ar-H), 5.35 (d, J = 3.45 Hz, 0.22H, H-1 α), 5.03-4.95 (m, 2.38H, CH₂Ph), 4.87 (d, J = 11.6 Hz, 0.26H, CH₂Ph), 4.80-4.59 (m, 6.74H, H-1 β , CH₂Ph), 4.53-4.43 (m, 2.70H, CH₂Ph), 4.22 (dd, J = 6.6 Hz, J = 6.6 Hz, 0.26H, H-5 α), 4.07-4.00 (m, 0.79H, H-2 α , H-3 α , H-4 α), 3.90 (d, J = 2.65 Hz, 1H, H-4 β), 3.83 (dd, J = 7.85 Hz, J = 9.6 Hz, 1.08H, H-2 β), 3.63-3.54 (m, 5.10H, H-6 $\alpha\alpha$, H-6 $\beta\alpha$, H-3 β , H-5 β , H-6 $\beta\beta$, H-6 $\beta\beta$), 2.16 (m, 4.16H, CH, CH₂), 1.97-1.84 (m, 8.29H, CH₂), 1.74 (d, J = 2.45 Hz, 0.29H, CH₂), 1.68-1.62 (m, 8.43H, CH₂); ¹³C NMR (125 MHz, CDCl₃) δ 138.98 (C), 138.84 (C), 138.80 (C), 138.69 (C), 138.66 (C), 138.60 (C), 138.09 (C), 137.99 (C), 128.32 (CH), 128.29 (CH), 128.23 (CH), 128.16 (CH), 128.14 (CH), 128.06 (CH), 128.02 (CH), 127.88 (CH), 127.70 (CH), 127.61 (CH), 127.53 (CH), 127.45 (CH), 127.39 (CH), 127.36 (CH), 127.31 (CH), 96.46 (CH), 90.43 (CH), 82.62 (CH), 79.52 (CH), 79.10 (CH), 76.50 (CH), 75.20 (CH), 75.16 (CH₂), 74.89 (CH), 74.63 (CH₂), 74.33 (CH₂), 74.17 (CH), 73.63 (CH),

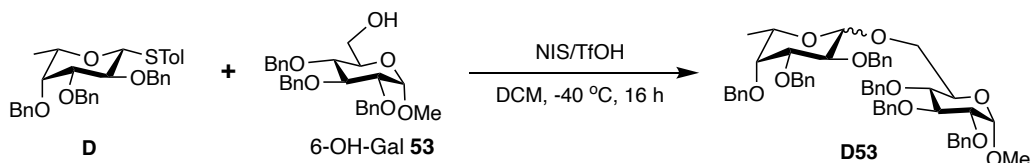
73.44 (CH₂), 73.35 (CH₂), 73.14 (CH), 73.07 (CH₂), 72.89 (CH₂), 72.83 (CH₂), 69.28 (CH₂), 69.04 (CH₂), 68.63 (CH), 60.32 (CH₂), 45.18 (CH₂), 42.62 (CH₂), 42.36 (CH₂), 36.25 (CH₂), 30.60 (CH); HRMS (ESI) calcd. for C₄₄H₅₀O₆Na [M+Na]⁺ 697.3491, found 697.3499.

Methyl 2,3,4-tri-*O*-benzyl-6-deoxy-L-fucopyranoside (**D51**)



Data for **D51**: IR (CHCl₃) ν 2910, 2850, 1455, 1103, 735, 698 cm⁻¹; ¹H NMR (500 MHz, CDCl₃) δ 7.42-7.26 (m, 24H, Ar-H), 5.00-4.69 (m, 9H, CH₂Ph), 4.67 (d, J = 3.7 Hz, 0.6H, H-1 α), 4.25 (d, J = 7.7 Hz, 1H, H-1 β), 4.05 (dd, J = 3.7 Hz, 3.7 Hz, 0.6H, H-2 α), 3.94 (dd, J = 2.9 Hz, 2.9 Hz, 0.6H, H-3 α), 3.85 (q, J = 6.5 Hz, 0.6H, H-5 α), 3.81 (dd, J = 9.7 Hz, 9.7 Hz, 1H, H-2 β), 3.65 (d, J = 2.0 Hz, 0.6H, H-4 α), 3.57 (d, J = 2.6 Hz, 1H, H-4 β), 3.55 (s, 3H, OCH₃ β), 3.52 (dd, J = 2.9 Hz, 3.0 Hz, 1H, H-3 β), 3.47 (q, J = 6.4 Hz, 1H, H-5 β), 3.37 (s, 1.8H, OCH₃ α), 1.21 (d, J = 6.4 Hz, 3H, CH₃ β), 1.13 (d, J = 6.6 Hz, 1.8H, CH₃ α); ¹³C NMR (125 MHz, CDCl₃) δ 138.93 (C), 138.90 (C), 138.60 (C), 138.58 (C), 138.54 (C), 128.39 (CH), 128.33 (CH), 128.28 (CH), 128.21 (CH), 128.14 (CH), 128.06 (CH), 127.62 (CH), 127.51 (CH), 127.46 (CH), 127.43 (CH), 104.85 (CH), 98.78 (CH), 82.46 (CH), 79.48 (CH), 79.38 (CH), 76.74 (CH), 76.31 (CH₂), 76.27 (CH₂), 75.02 (CH₂), 74.79 (CH₂), 74.50 (CH₂), 73.44 (CH), 73.33 (CH), 73.10 (CH), 70.25 (CH), 66.04 (CH), 56.84 (CH), 55.25 (CH), 16.81 (CH₃), 16.56 (CH₃); HRMS (ESI) calcd. for C₂₈H₃₂O₅Na [M+Na]⁺ 471.2133, found 471.2142.

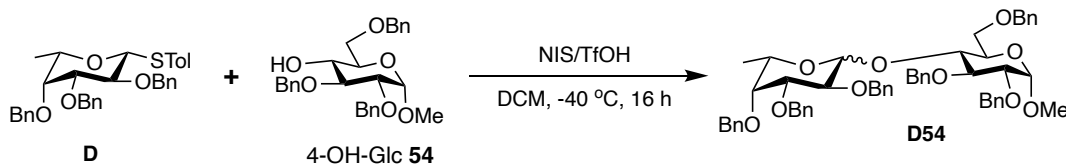
Methyl 2,3,4-tri-*O*-benzyl-6-*O*-(2,3,4-tri-*O*-benzyl-6-deoxy-L-fucopyranosyl)- α -D-glucopyranoside (**D53**)



Data for **D53**: IR (CHCl₃) ν 2921, 2850, 1455, 1095, 1070, 741, 697 cm⁻¹; ¹H NMR (500 MHz, CDCl₃) δ 7.45-7.24 (m, 37.88H, Ar-H), 5.07-5.03 (m, 3.53H, CH₂Ph), 4.97-4.69 (m, 11.31H, H-1' α , CH₂Ph), 4.67-4.64 (m, 2.23H, H-1 α , H-1 β , CH₂Ph), 4.49 (d, J = 7.6 Hz, 1H, H-1' β), 4.27-4.24 (m, 1H, H-6a β), 4.12 (dd, J = 9.95 Hz, J = 3.15 Hz, 0.34H, H-2' α), 4.08-4.04 (m, 1.52H, H-3' α , H-3 β), 3.99-3.97 (m, 0.38H, H-5' α), 3.91-3.88 (m, 1.38H, H-2' β , H-6a α), 3.85-3.82 (m, 2.25H, H-3 α , H-5 β , H-6b β), 3.76-3.73 (m, 1.61H, H-5 α , H-4 β , H-6b α), 3.67 (dd, J = 9.75 Hz, J = 9 Hz, 0.45H, H-4' α), 3.62-3.58 (m, 2.37H, H-3' β , H-4' β , H-2 α , H-4 α), 3.53-3.51 (m, 2.11H, H-5' β , H-2 β), 3.40 (s, 3.8H, OCH₃ α , OCH₃ β), 1.24 (d, J = 6.2 Hz, 2.96H, CH₃ β), 1.18 (d, J = 6.35 Hz, 0.76H, CH₃ α); ¹³C NMR (125 MHz, CDCl₃) δ 138.85 (C), 138.81 (C), 138.72 (C), 138.70 (C), 138.57 (C), 138.33 (C), 138.20 (C), 138.15 (C), 128.28 (CH), 128.25 (CH), 128.24 (CH), 128.21 (CH), 128.11 (CH), 128.07 (CH), 128.02 (CH), 127.89 (CH), 127.76 (CH), 127.69 (CH), 127.61 (CH), 127.53 (CH), 127.51 (CH), 127.43 (CH), 127.38 (CH), 127.36 (CH), 127.33 (CH), 127.24 (CH), 103.65 (CH), 97.93 (CH), 97.87 (CH), 82.33 (CH), 81.99 (CH), 81.86 (CH), 80.16 (CH),

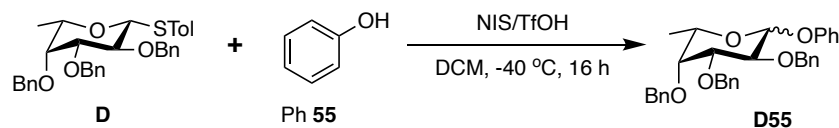
79.98 (CH), 79.36 (CH), 79.04 (CH), 77.67 (CH), 77.54 (CH), 76.50 (CH), 76.18 (CH), 75.67 (CH₂), 75.54 (CH₂), 74.95 (CH₂), 74.82 (CH₂), 74.72 (CH₂), 74.49 (CH₂), 73.30 (CH₂), 73.20 (CH₂), 73.07 (CH₂), 73.02 (CH₂), 72.76 (CH₂), 70.22 (CH), 69.97 (CH), 67.38 (CH₂), 66.33 (CH₂), 66.21 (CH), 54.98 (CH₃), 16.77 (CH₃), 16.52 (CH₃); HRMS (ESI) calcd. for C₅₅H₆₀O₁₀Na [M+Na]⁺ 903.4076, found 903.4078.

Methyl 2,3,6-tri-*O*-benzyl-4-*O*-(2,3,4-tri-*O*-benzyl-6-deoxy-L-fucopyranosyl)- α -D-glucopyranoside (D54)



Data for **D54**: IR (CHCl₃) ν 2920, 1454, 1099, 1044, 740, 697 cm⁻¹; ¹H NMR (500 MHz, CDCl₃) δ 7.48-7.26 (m, 36.3H, Ar-H), 5.13 (d, J = 10.9 Hz, 1H, CH₂Ph), 5.09 (d, J = 3.5 Hz, 1H, H-1' α), 5.07-5.03 (m, 0.47H, CH₂Ph), 4.96 (d, J = 11.6 Hz, 1H, CH₂Ph), 4.92-4.88 (m, 0.53H, H-1' β , CH₂Ph), 4.86-4.57 (m, 11.26H, H-1 α , H-1 β , CH₂Ph), 4.43 (q, J = 10.85 Hz, 2H, CH₂Ph), 4.10-4.03 (m, 2.17H, H-5' α , H-2 α , H-4 β), 4.00-3.83 (m, 4.54H, H-3' α , H-3 α , H-4 α , H-5 α , H-5 β , H-6 $\alpha\beta$, H-6 $\beta\beta$), 3.80-3.69 (m, 2.41H, H-2' β , H-6 $\alpha\alpha$, H-6 $\beta\alpha$), 3.65 (dd, J = 9.5 Hz, J = 3.55 Hz, 1H, H-2 α), 3.60-3.55 (m, 0.60H, H-4' β , H-2 β , H-3 β), 3.49 (s, 0.55H, OCH₃ β), 3.47-3.46 (m, 0.12H, H-3' β), 3.42 (s, 3.9H, H-4' α , OCH₃ α), 3.36 (q, J = 6.5 Hz, 0.25H, H-5' β), 1.13 (d, J = 6.35 Hz, 0.7H, CH₃ β), 0.77 (d, J = 6.4 Hz, 2.89H, CH₃ α); ¹³C NMR (125 MHz, CDCl₃) δ 138.79 (C), 138.74 (C), 138.67 (C), 138.57 (C), 138.32 (C), 137.91 (C), 128.39 (CH), 128.32 (CH), 128.28 (CH), 128.20 (CH), 128.16 (CH), 128.08 (CH), 128.05 (CH), 128.01 (CH), 127.91 (CH), 127.81 (CH), 127.69 (CH), 127.55 (CH), 127.49 (CH), 127.45 (CH), 127.41 (CH), 127.38 (CH), 127.32 (CH), 127.23 (CH), 103.60 (CH), 102.81 (CH), 99.76 (CH), 97.75 (CH), 97.68 (CH), 97.50 (CH), 82.60 (CH), 82.20 (CH), 82.11 (CH), 80.48 (CH), 80.13 (CH), 79.87 (CH), 79.61 (CH), 79.32 (CH), 77.51 (CH), 76.24 (CH), 75.45 (CH₂), 75.26 (CH₂), 75.20 (CH₂), 74.63 (CH₂), 74.45 (CH₂), 74.20 (CH₂), 73.75 (CH), 73.66 (CH), 73.28 (CH₂), 73.21 (CH₂), 73.16 (CH₂), 73.10 (CH₂), 73.04 (CH₂), 72.97 (CH₂), 72.62 (CH₂), 70.25 (CH), 70.16 (CH), 69.69 (CH), 69.00 (CH₂), 68.50 (CH₂), 66.56 (CH), 55.15 (CH₃), 54.90 (CH₃), 16.56 (CH₃), 16.14 (CH₃); HRMS (ESI) calcd. for C₅₅H₆₀O₁₀Na [M+Na]⁺ 903.4070, found 903.4079.

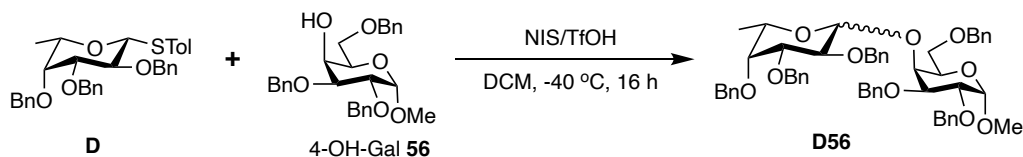
Phenyl 2,3,4-tri-*O*-benzyl-6-deoxy-L-fucopyranoside (D55)



Data for **D55**: IR (CHCl₃) ν 2955, 2924, 2870, 1492, 1453, 1130, 1100, 1028, 755, 734, 695 cm⁻¹; ¹H NMR (500 MHz, CDCl₃) δ 7.49 (d, J = 11.35 Hz 7.35H, Ar-H), 7.44-7.28 (m, 17.94H, Ar-H), 7.15-7.10 (m, 2.89H, Ar-H), 7.05 (dd, J = 7.35 Hz, J = 7.35 Hz, 1.14H, Ar-H), 5.55 (d, J = 3.45 Hz, 1H, H-1 α), 5.07 (d, J = 11.45 Hz, 1.30H, CH₂Ph), 5.02-4.98 (m, 1.16H, H-1 β , CH₂Ph), 4.92-

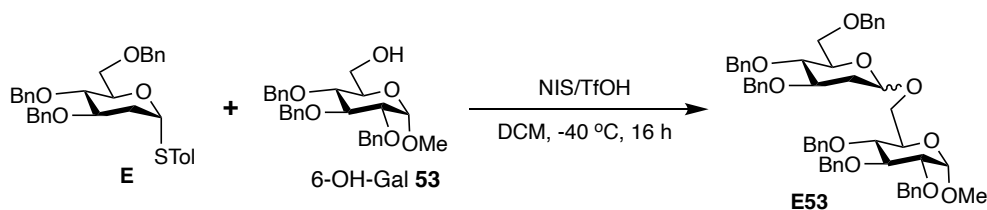
4.71 (m, 4.74H, CH₂Ph), 4.27-4.19 (m, 1.99H, H-2 α , H-3 α , H-3 β), 4.16 (dd, J = 8.3 Hz, J = 8.3 Hz, 0.18H, H-2 β), 4.06 (q, J = 6.45 Hz, 1.01H, H-5 α), 3.77 (d, J = 2.15 Hz, 1H, H-4 α), 3.67-3.62 (m, 0.48H, H-4 β , H-5 β), 1.28 (d, J = 6.3 Hz, 0.52H, CH₃ β), 1.15 (d, J = 6.5 Hz, 3H, CH₃ α); ¹³C NMR (125 MHz, CDCl₃) δ 157.56 (C), 157.24 (C), 139.23 (C), 138.85 (C), 138.53 (C), 138.48 (C), 138.36 (C), 137.37 (C), 133.84 (C), 129.73 (CH), 129.34 (CH), 129.30 (CH), 128.49 (CH), 128.27 (CH), 128.22 (CH), 128.17 (CH), 128.12 (CH), 127.87 (CH), 127.59 (CH), 127.58 (CH), 127.54 (CH), 127.52 (CH), 127.47 (CH), 127.43 (CH), 122.29 (CH), 122.02 (CH), 116.90 (CH), 116.85 (CH), 101.85 (CH), 96.29 (CH), 82.35 (CH), 79.22 (CH), 79.03 (CH), 77.62 (CH), 76.10 (CH), 75.27 (CH₂), 74.91 (CH₂), 74.60 (CH₂), 73.29 (CH₂), 73.22 (CH₂), 73.14 (CH₂), 70.62 (CH), 67.14 (CH), 16.89 (CH₃), 16.55 (CH₃); HRMS (ESI) calcd. for C₃₃H₃₄O₅Na [M+Na]⁺ 533.2292, found 533.2299.

Methyl 2,3,6-tri-*O*-benzyl-4-*O*-(2,3,4-tri-*O*-benzyl-6-deoxy-L-fucopyranosyl)- α -D-galactopyranoside (D56)



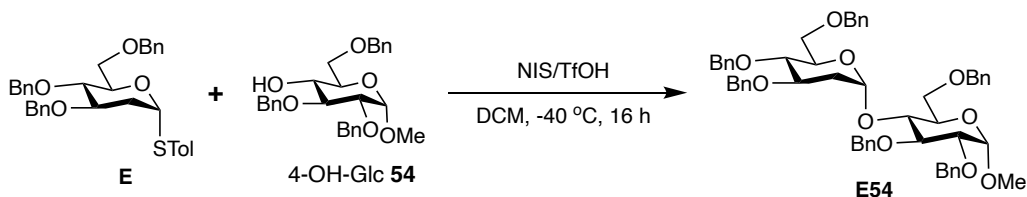
Data for **D56**: IR (CHCl₃) ν 2916, 2849, 1454, 1099, 1040, 735, 698 cm⁻¹; ¹H NMR (500 MHz, CDCl₃) δ 7.51-7.17 (m, 45.9H, Ar-H), 5.84 (d, J = 3.8 Hz, 1H, H-1' α), 5.04-4.68 (m, 13.3H, H-1 α , H-1 β , CH₂Ph), 4.62-4.42 (m, 6.60H, H-1' β , H-5 β , CH₂Ph), 4.37 (d, J = 11.95 Hz, 1H, CH₂Ph), 4.33 (d, J = 1.25 Hz, 1H, H-4 α), 4.14 (dd, J = 10.1 Hz, 3.65 Hz, 1H, H-2 α), 4.05-3.90 (m, 6.49H, H-2' α , H-3' α , H-3 α , H-5 α , H-2' β , H-2 β , H-3 β , H-4 β , H-6 $\alpha\beta$), 3.86 (q, J = 6.5 Hz, 1H, H-5' α), 3.65 (d, J = 1.55 Hz, 1H, H-4' α), 3.63-3.61 (m, 2.5H, H-6 $\alpha\alpha$, H-6 $\beta\alpha$, H-6 $\beta\beta$), 3.56 (d, J = 2.45 Hz, 0.56H, H-4' β), 3.46-3.42 (m, 4.9H, H-3' β , OCH₃ α , OCH₃ β), 3.33 (q, J = 6.15 Hz, 0.5H, H-5' β), 1.19 (d, J = 6.4 Hz, 1.5H, CH₃ β), 1.05 (d, J = 6.45 Hz, 3H, CH₃ α); ¹³C NMR (125 MHz, CDCl₃) δ 139.12 (C), 139.01 (C), 138.87 (C), 138.74 (C), 138.68 (C), 138.52 (C), 138.30 (C), 138.00 (C), 137.88 (C), 128.57 (CH), 128.46 (CH), 128.37 (CH), 128.32 (CH), 128.26 (CH), 128.16 (CH), 128.13 (CH), 128.08 (CH), 127.98 (CH), 127.95 (CH), 127.73 (CH), 127.70 (CH), 127.65 (CH), 127.59 (CH), 127.55 (CH), 127.48 (CH), 127.45 (CH), 127.43 (CH), 127.36 (CH), 127.31 (CH), 127.12 (CH), 127.05 (CH), 126.97 (CH), 103.52 (CH), 98.96 (CH), 98.75 (CH), 96.55 (CH), 82.67 (CH), 79.52 (CH), 79.42 (CH), 78.66 (CH), 77.52 (CH), 76.95 (CH), 76.88 (CH), 76.77 (CH), 76.07 (CH), 75.79 (CH), 74.88 (CH₂), 74.71 (CH₂), 74.63 (CH₂), 73.83 (CH₂), 73.49 (CH₂), 73.42 (CH₂), 73.30 (CH₂), 73.12 (CH₂), 73.09 (CH₂), 72.16 (CH), 71.76 (CH₂), 71.12 (CH), 70.46 (CH), 69.99 (CH₂), 69.78 (CH), 68.74 (CH), 68.05 (CH₂), 66.55 (CH), 55.28 (CH₃), 16.92 (CH₃), 16.68 (CH₃); HRMS (ESI) calcd. for C₅₅H₆₀O₁₀Na [M+Na]⁺ 903.4075, found 903.4079.

Methyl 2,3,4-tri-*O*-benzyl-6-*O*-(3,4,6-tri-*O*-benzyl-2-deoxy-D-glucopyranosyl)- α -D-glucopyranoside (E53)



Data for **E53- α** : ^1H NMR (500 MHz, CDCl_3): δ 7.37-7.23 (m, 30H), 7.14-7.12 (m, 2H), 4.98 (d, J = 10.6 Hz, 2H), 4.89 (dd, J = 23.8, 11.1 Hz, 2H), 4.81- 4.77 (m, 2H), 4.66 (dd, J = 13.9, 12.1 Hz, 1H), 4.61-4.59 (m, 2H), 4.55 (t, J = 12 Hz, 2H), 4.98 (d, J = 10.9 Hz, 1H), 4.91 (d, J = 12.1 Hz, 1H), 3.98-3.95 (m, 1H), 3.92 (ddd, J = 11.2, 5.0, 3.7 Hz, 1H), 3.81 (dd, J = 11.3, 4.3 Hz, 1H), 3.74-3.71 (m, 1H), 3.66 (d, J = 9.8 Hz, 1H), 3.61-3.55 (m, 3H), 3.53-3.47 (m, 3H), 3.34 (s, 3H), 2.29 (dd, J = 12.9, 5.0 Hz, 1H), 1.70-1.65 (m, 1H); ^{13}C NMR (125 MHz, CDCl_3) δ 138.7, 138.6, 138.3, 138.2, 128.4, 128.4, 128.3, 128.3, 128.2, 128.2, 128.0, 128.0, 127.8, 127.7, 127.7, 127.5, 127.4, 114.7, 97.9, 97.8, 82.2, 8.0, 78.1, 77.8, 75.7, 74.8, 74.8, 73.4, 73.2, 71.7, 70.9, 69.7, 68.7, 65.7, 55.1, 35.2, 29.7; LRMS (ESI) clacd. for $\text{C}_{55}\text{H}_{60}\text{O}_{10}\text{Na}$ $[\text{M}+\text{Na}]^+$ 904.0517, found 903.4032. Data for **E53- β** : ^1H NMR (500 MHz, CDCl_3): δ 7.34-7.26 (m, 30H), 7.20-7.19 (m, 2H), 4.99 (d, J = 10.8 Hz, 1H), 4.88 (d, J = 1.5 Hz, 1H), 4.86 (d, J = 2.3 Hz, 1H), 4.87-4.77 (m, 2H), 4.65 (d, J = 11.8 Hz, 2H), 4.60-4.51 (m, 6H), 4.16 (dd, J = 9.6, 1.5 Hz, 1H), 4.07 (dd, J = 10.6, 1.7 Hz, 1H), 3.99 (t, J = 9.2 Hz, 1H), 3.75-3.71 (m, 2H), 3.44-3.41 (m, 1H), 3.35 (m, 4H), 2.17-2.14 (m, 1H), 1.42 (dd, J = 22.1, 9.7 Hz, 1H); ^{13}C NMR (125 MHz, CDCl_3) δ 138.8, 138.4, 138.4, 138.4, 138.3, 138.1, 128.4, 128.4, 128.3, 128.3, 128.1, 128.0, 127.9, 127.8, 127.7, 127.6, 127.6, 127.4, 100.0, 98.0, 82.2, 79.8, 79.3, 78.2, 77.4, 75.7, 74.9, 74.7, 73.4, 73.3, 71.4, 69.6, 69.5, 67.6, 55.1, 36.5; LRMS (ESI) clacd. for $\text{C}_{55}\text{H}_{60}\text{O}_{10}\text{Na}$ $[\text{M}+\text{Na}]^+$ 903.4084, found 903.4086.

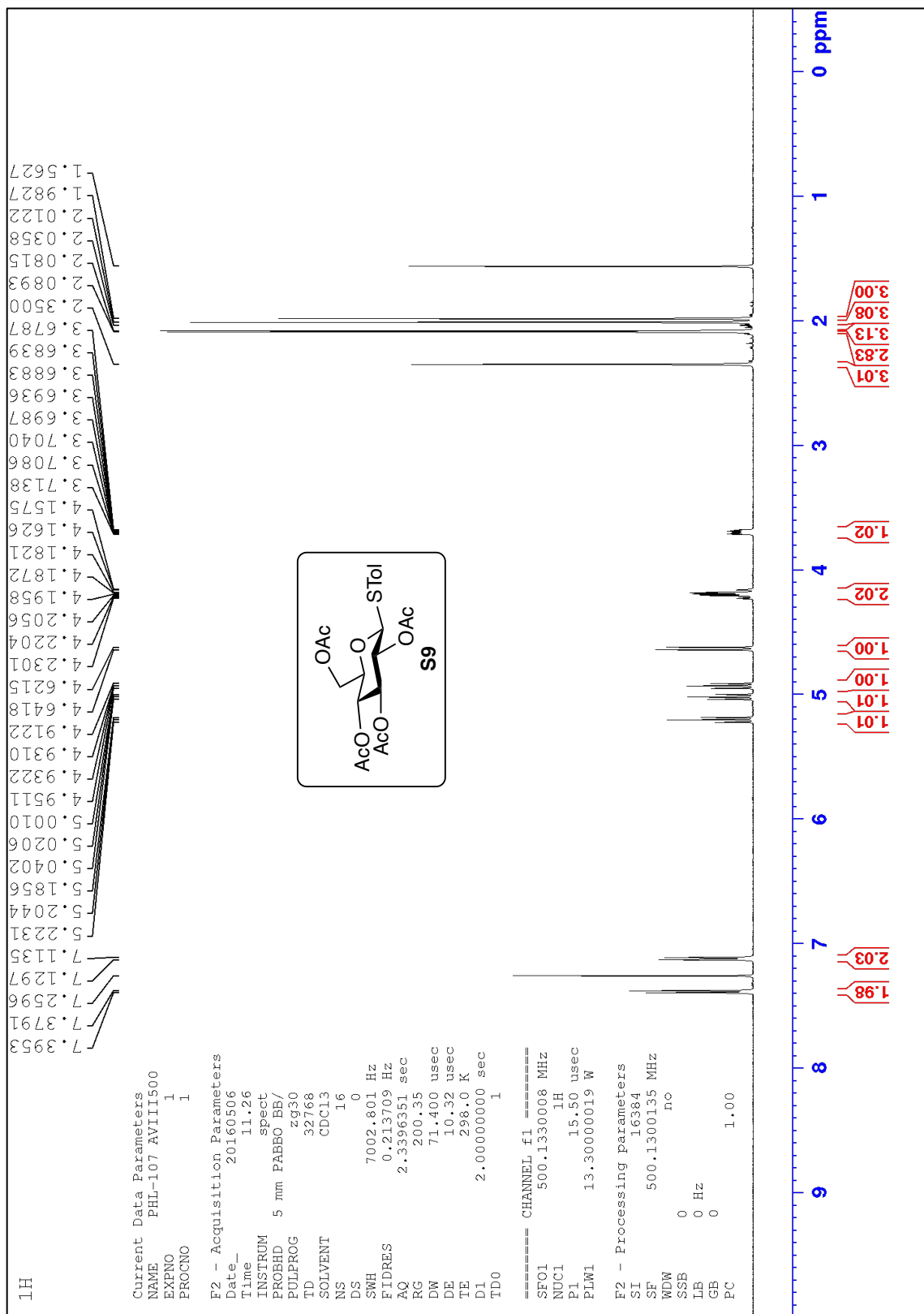
Methyl 2,3,6-tri-*O*-benzyl-4-*O*-(3,4,6-tri-*O*-benzyl-2-deoxy- α -D-glucopyranosyl)- α -D-glucopyranoside (E54)



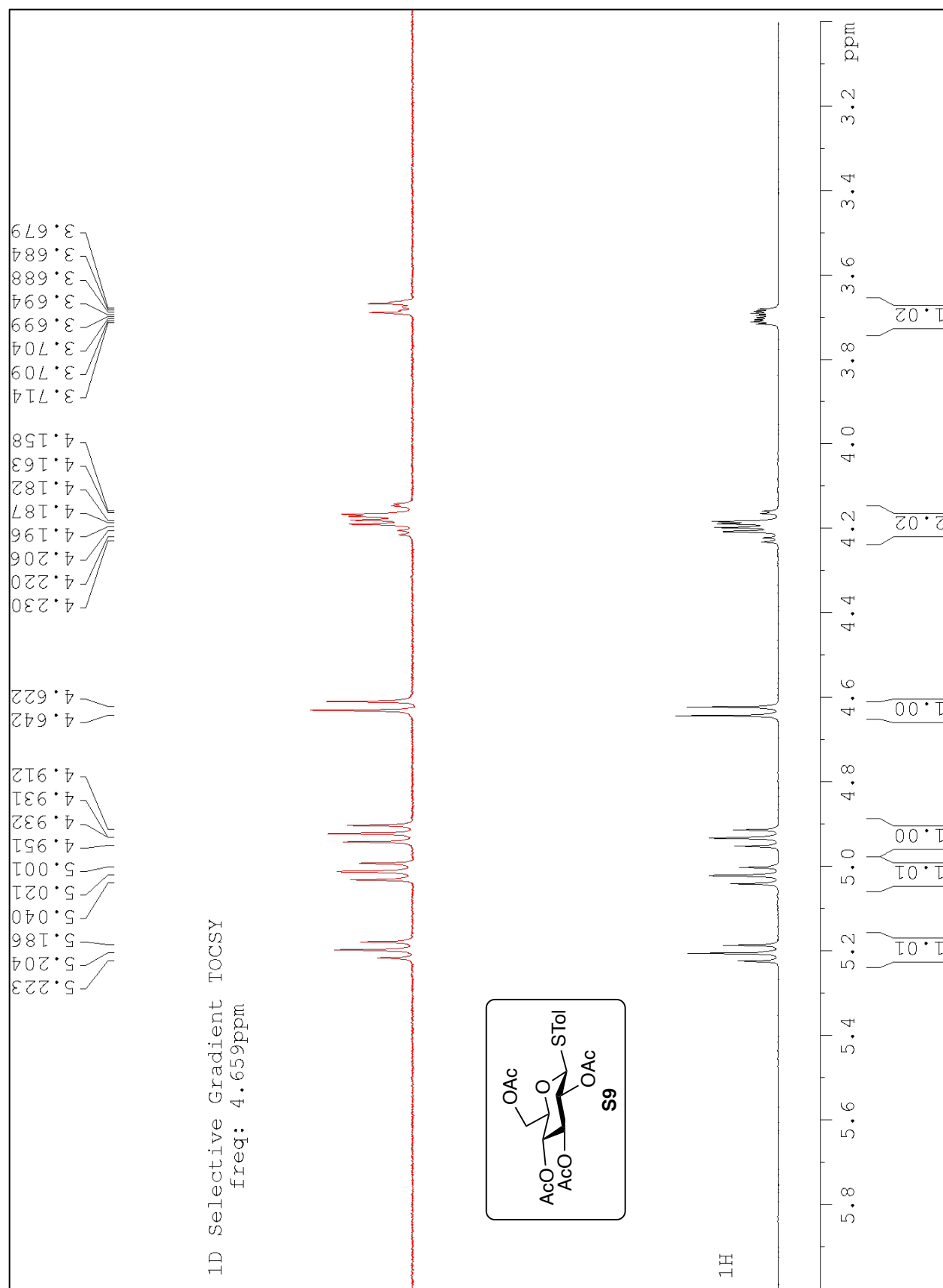
Data for **E54**: $[\alpha]^{26}_{\text{D}} = +41.9^\circ$ (c 1.0, CHCl_3); ^1H NMR (400 MHz, CDCl_3) δ 7.36-7.18 (m, 30H, PH), 5.44 (d, 1H, J = 2.7 Hz, H-1'), 5.05 (d, 1H, CH_2Ph , J = 11.2 Hz), 4.87 (d, 1H, CH_2Ph , J = 10.9 Hz), 4.74 (d, 1H, CH_2Ph , J = 12.0 Hz), 4.66-4.61 (m, 3H, CH_2Ph), 4.57-4.54 (m, 4H, CH_2Ph), 4.50 (d, 1H, CH_2Ph , J = 11.0 Hz), 4.46 (d, 1H, CH_2Ph , J = 12.0 Hz), 4.38 (d, 1H, CH_2Ph , J = 12.1 Hz), 3.92-3.84 (m, 2H), 3.76-3.67 (m, 5H), 3.65-3.53 (m, 3H), 3.44 (dd, 1H, J = 10.3 and 1.7 Hz), 3.41 (s, 3H), 2.09 (ddd, 1H, J = 12.9, 5.0, and 1.1 Hz, H-2eq'), 1.58 (td, 1H, J = 12.9 and 3.8 Hz, H-2ax'); ^{13}C NMR (100 MHz, CDCl_3) δ 138.89 (C), 138.84 (C), 138.8 (C), 138.5 (C), 138.3 (C),

138.2 (C), 128.6 (CH), 128.57 (CH), 128.5 (CH), 128.4 (CH), 128.2 (CH), 128.0 (CH), 127.69 (CH), 127.6 (CH), 127.5 (CH), 99.5 (CH), 97.9 (CH), 82.3 (CH), 80.3 (CH), 78.3 (CH), 77.4 (CH), 76.4 (CH), 75.5 (CH₂), 74.9 (CH₂), 73.6 (CH₂), 73.4 (CH₂), 73.3 (CH₂), 72.0 (CH), 71.8 (CH₂), 70.0 (CH), 69.7 (CH₂), 68.9 (CH₂), 55.3 (CH₃), 35.9 (CH₂); IR ν 3039, 2935, 1456, 1367, 1278, 1099, 1047, 750, 738 cm⁻¹; HRMS (ESI) calcd for C₅₅H₆₀NaO₁₀ [M+Na]⁺ 903.4084, found 903.4070 (13).

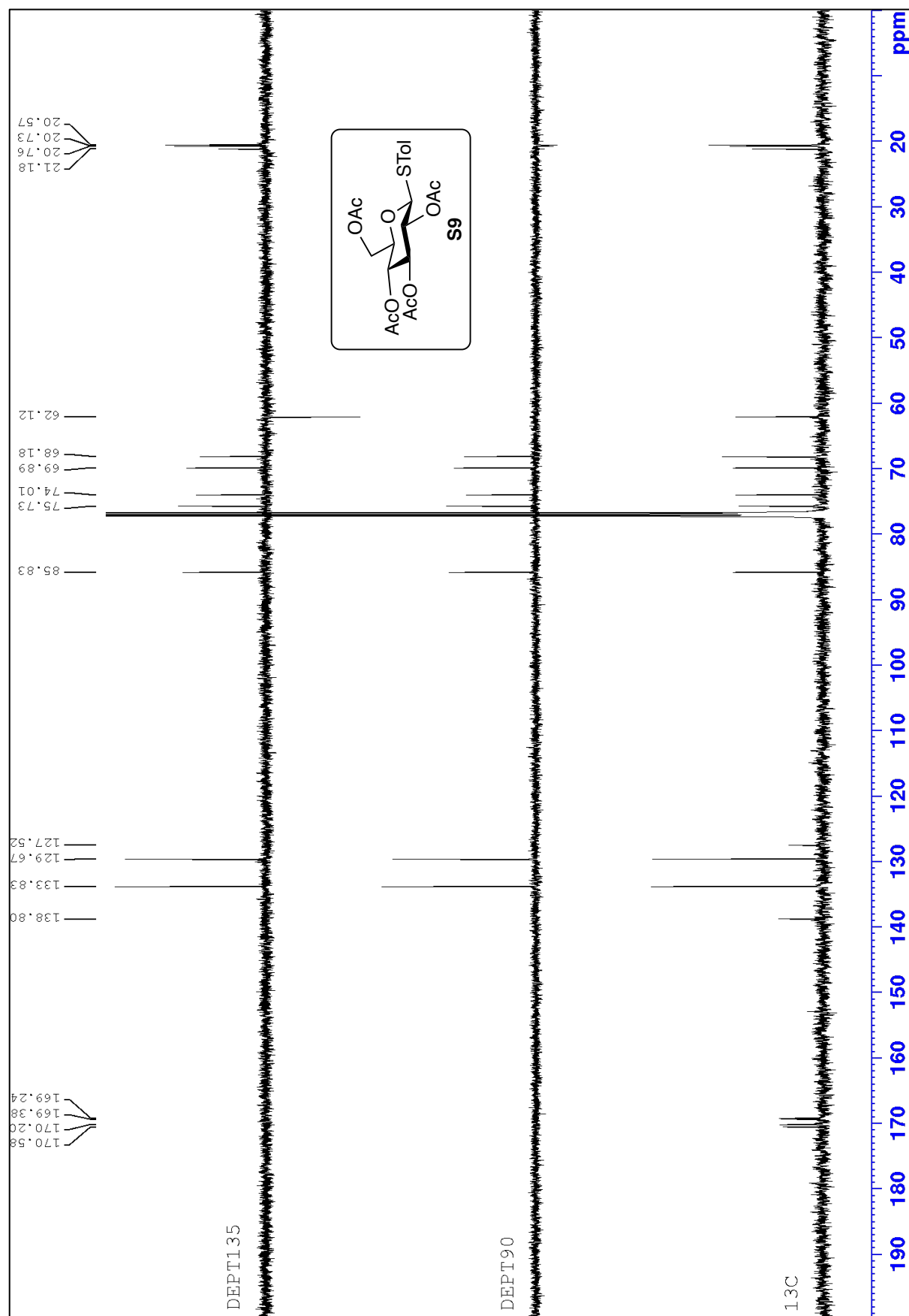
4 NMR Spectra



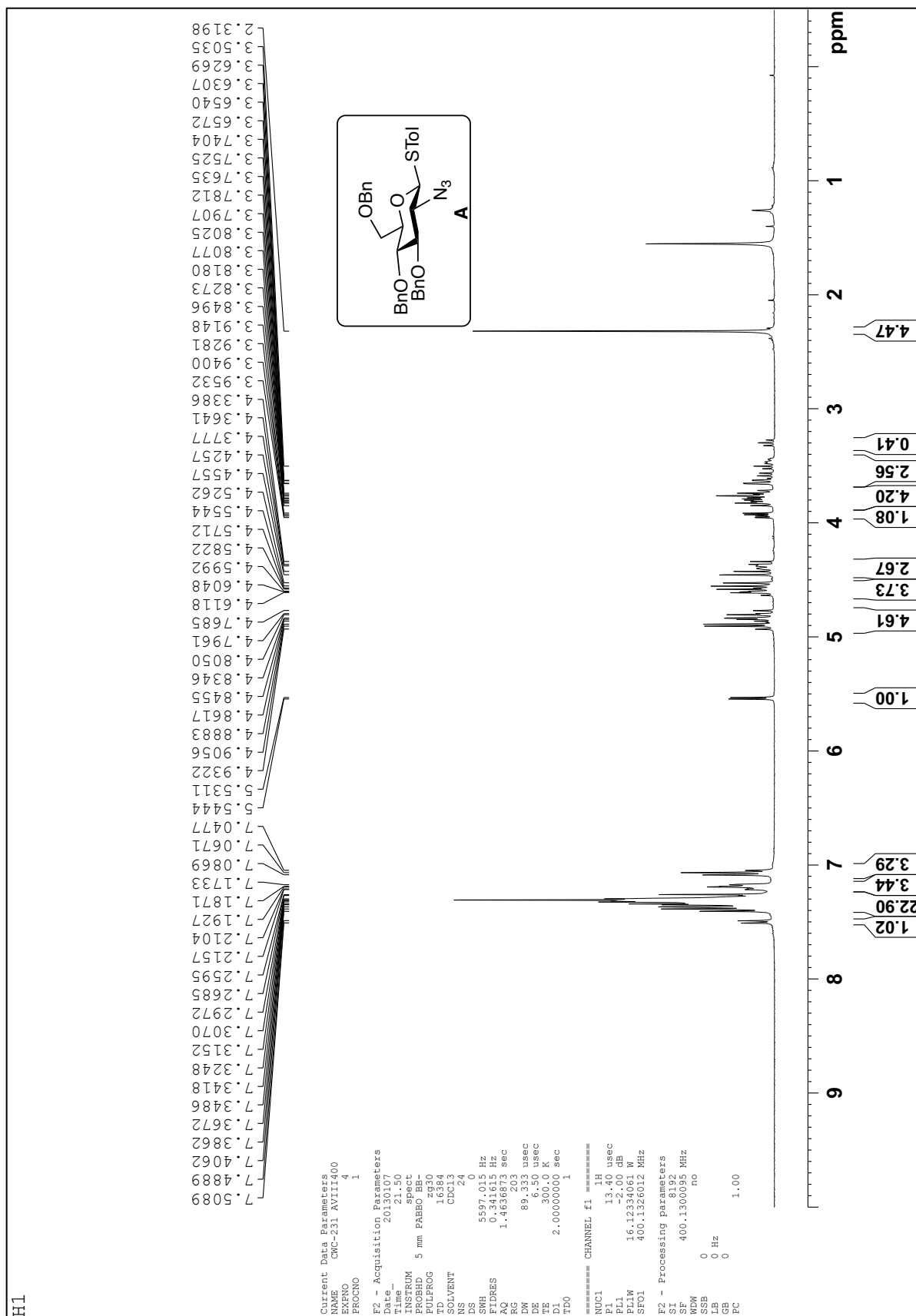
The ¹H Spectrum in CDCl₃ of Compound S9.

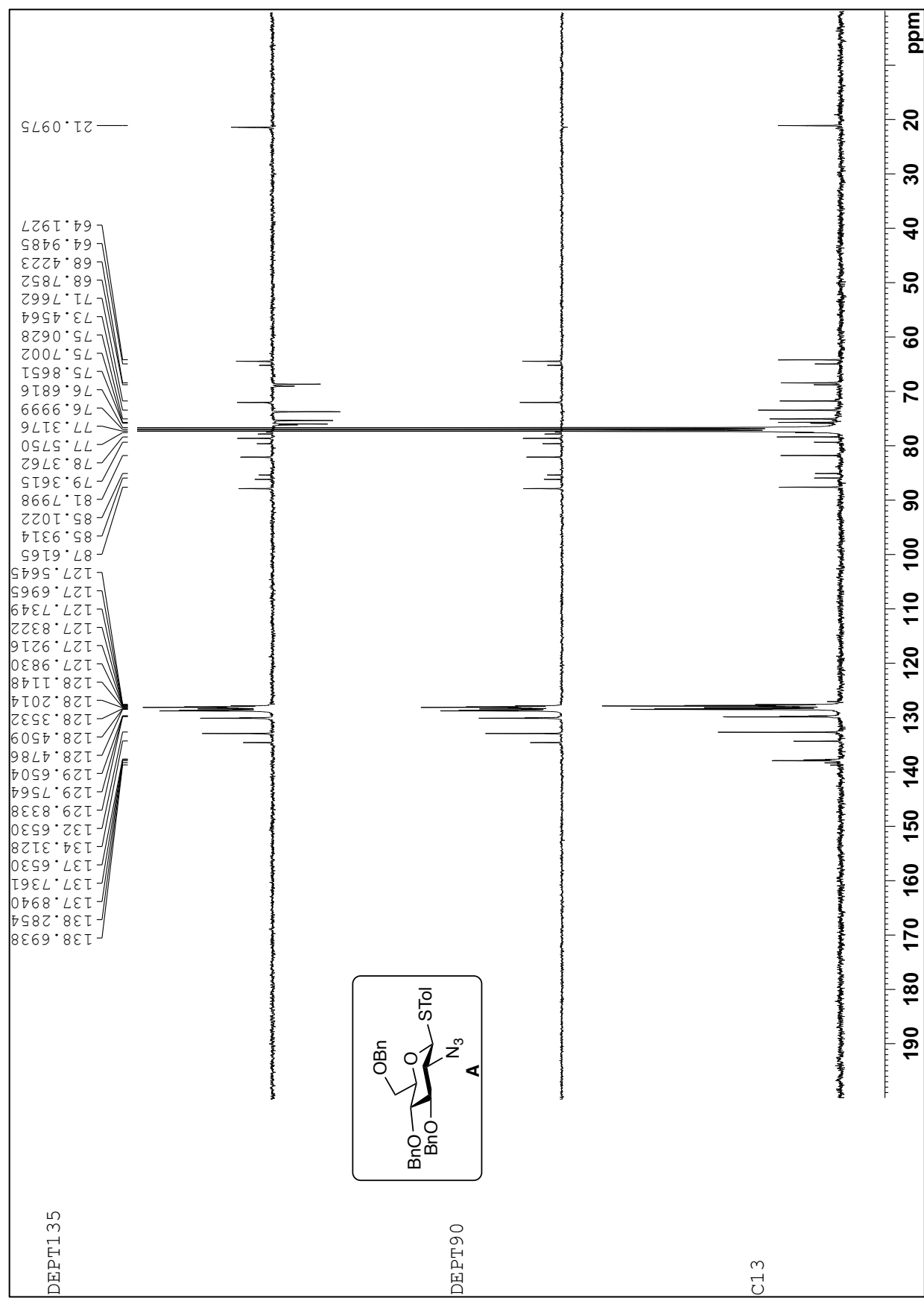


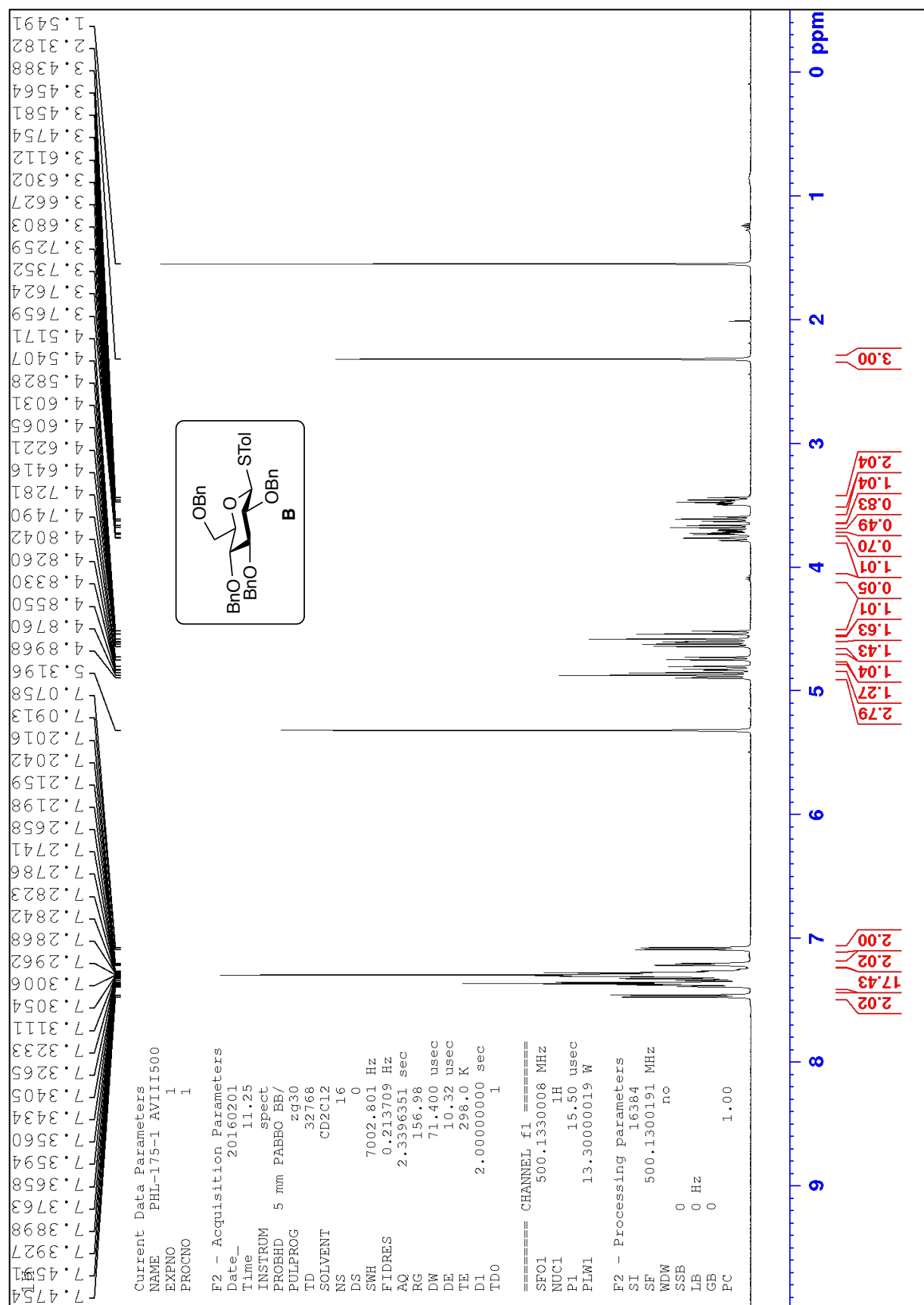
The 1D-TOCSY Spectrum in CD_2Cl_2 of Compound S9.

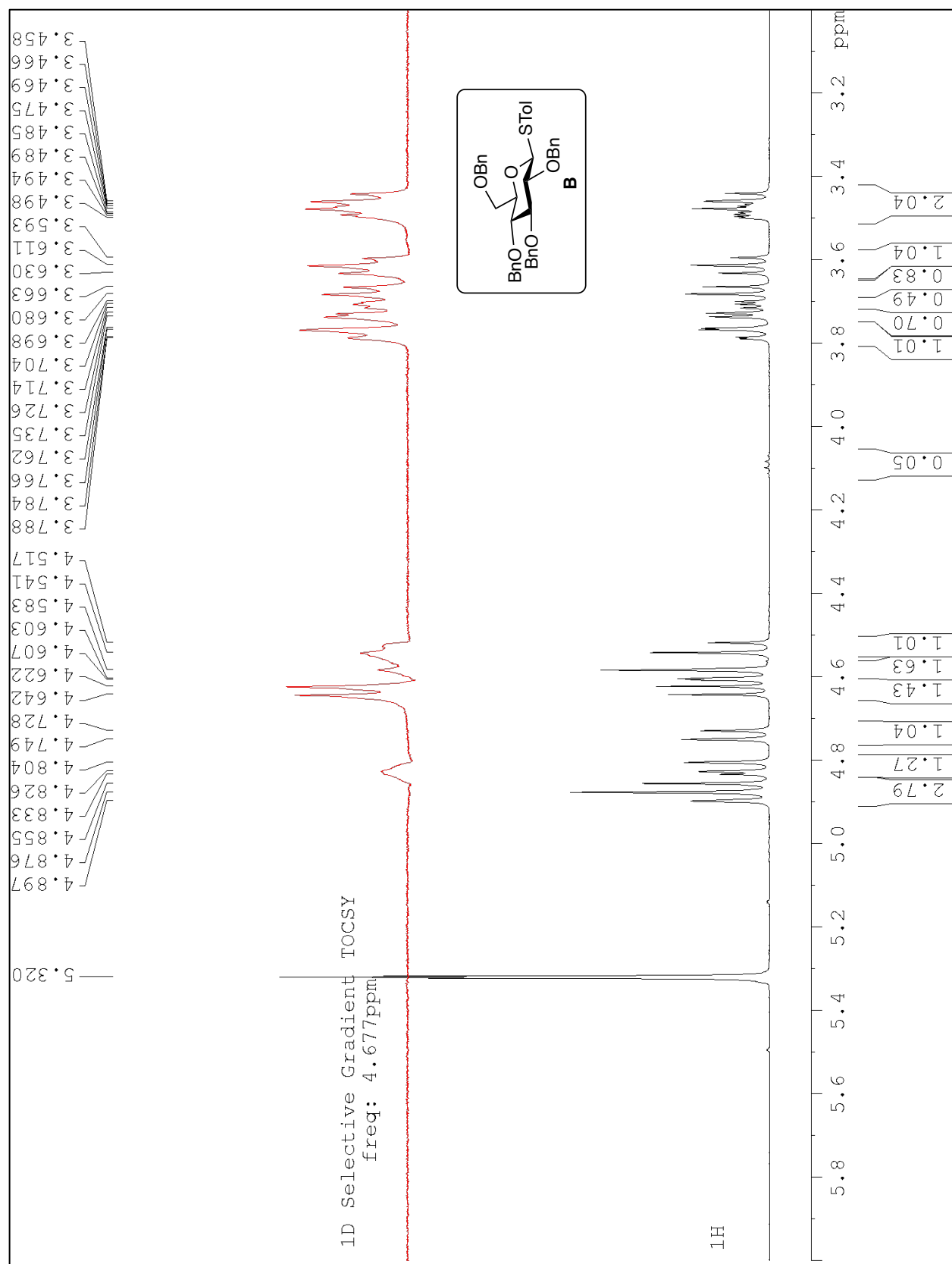


The 1D-TOCSY Spectrum in CD_2Cl_2 of Compound S9.

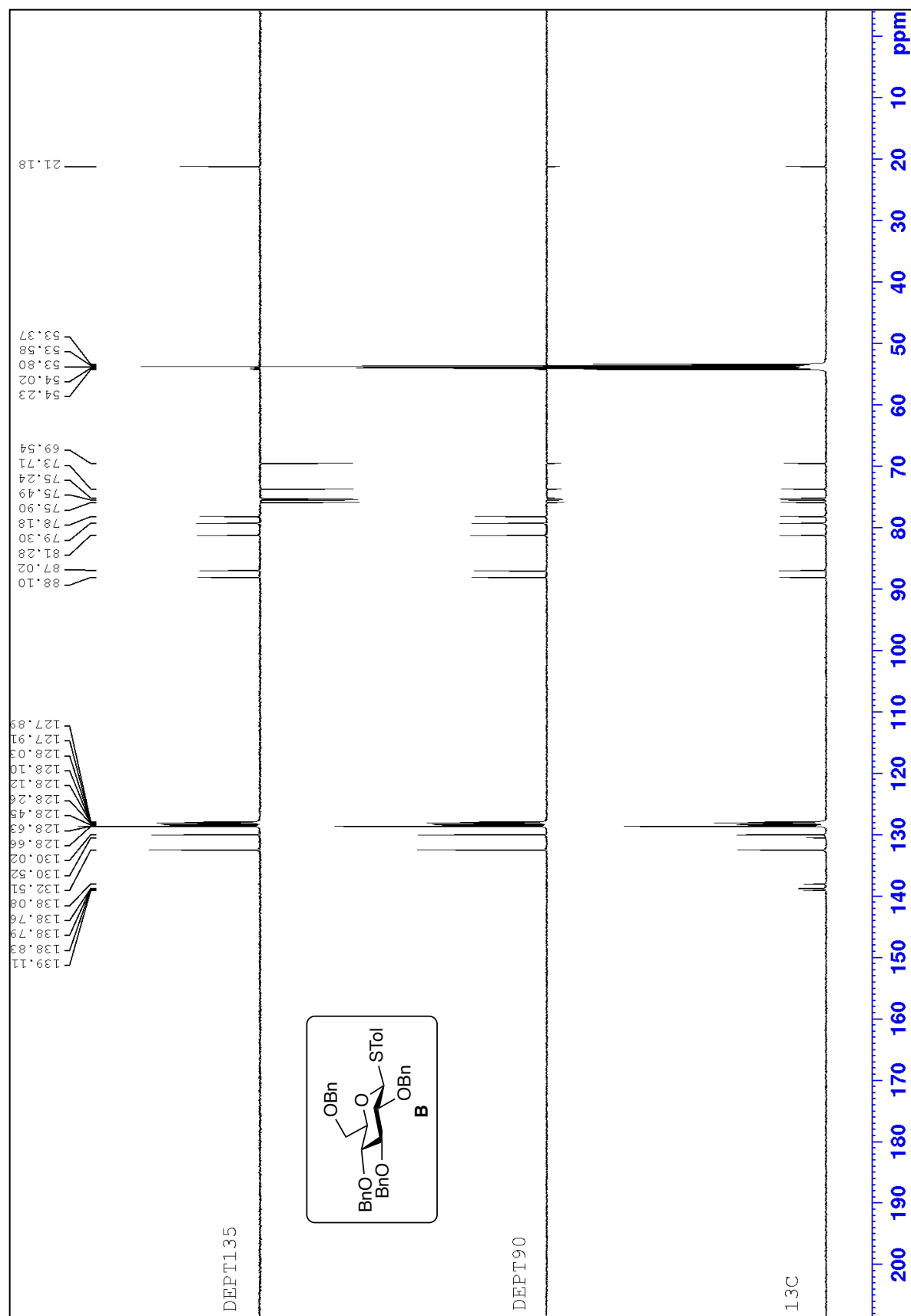




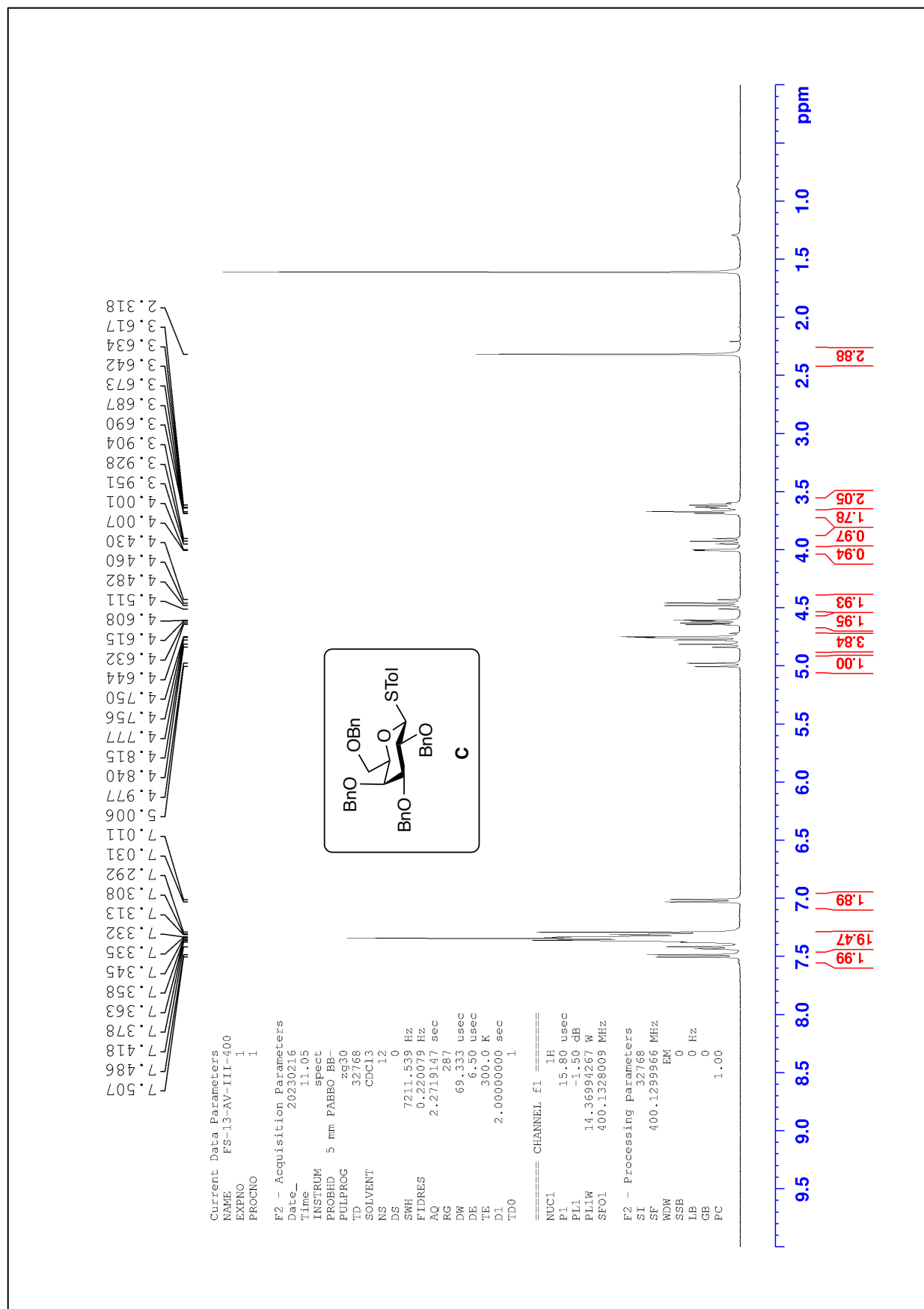




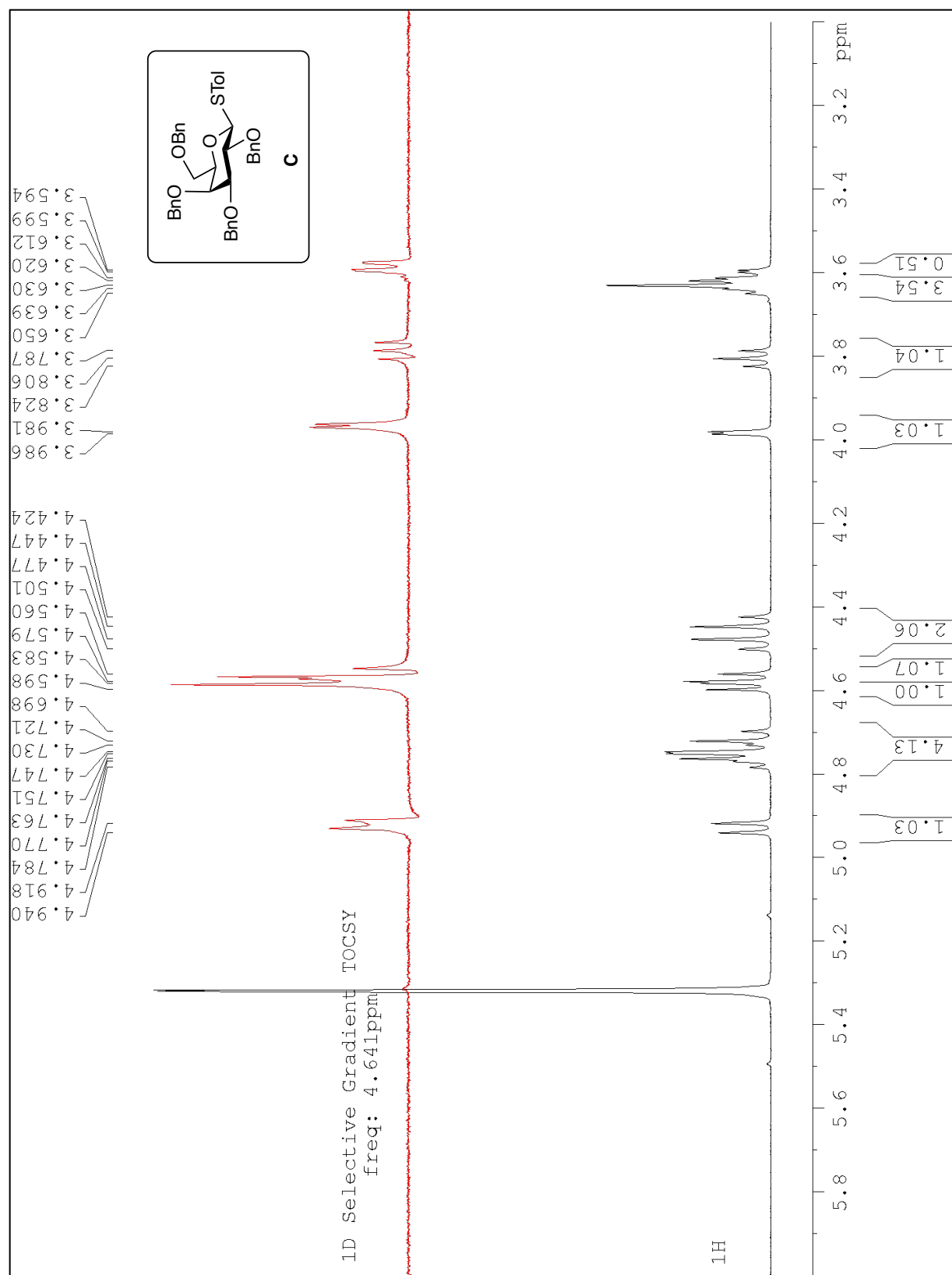
The 1D-TOCSY Spectrum in CD_2Cl_2 of Compound B.



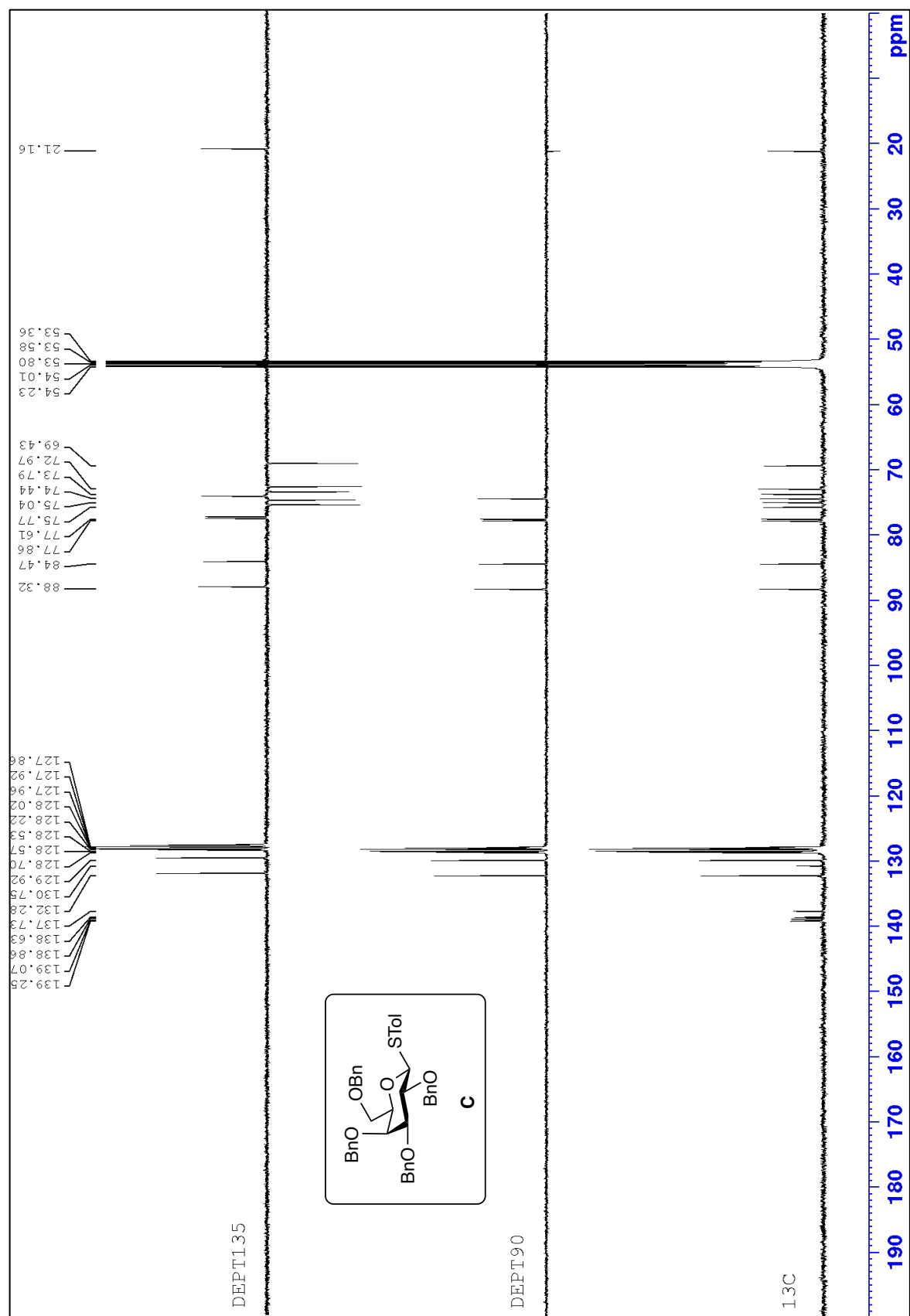
The ¹³C Spectrum in CD₂Cl₂ of Compound B.



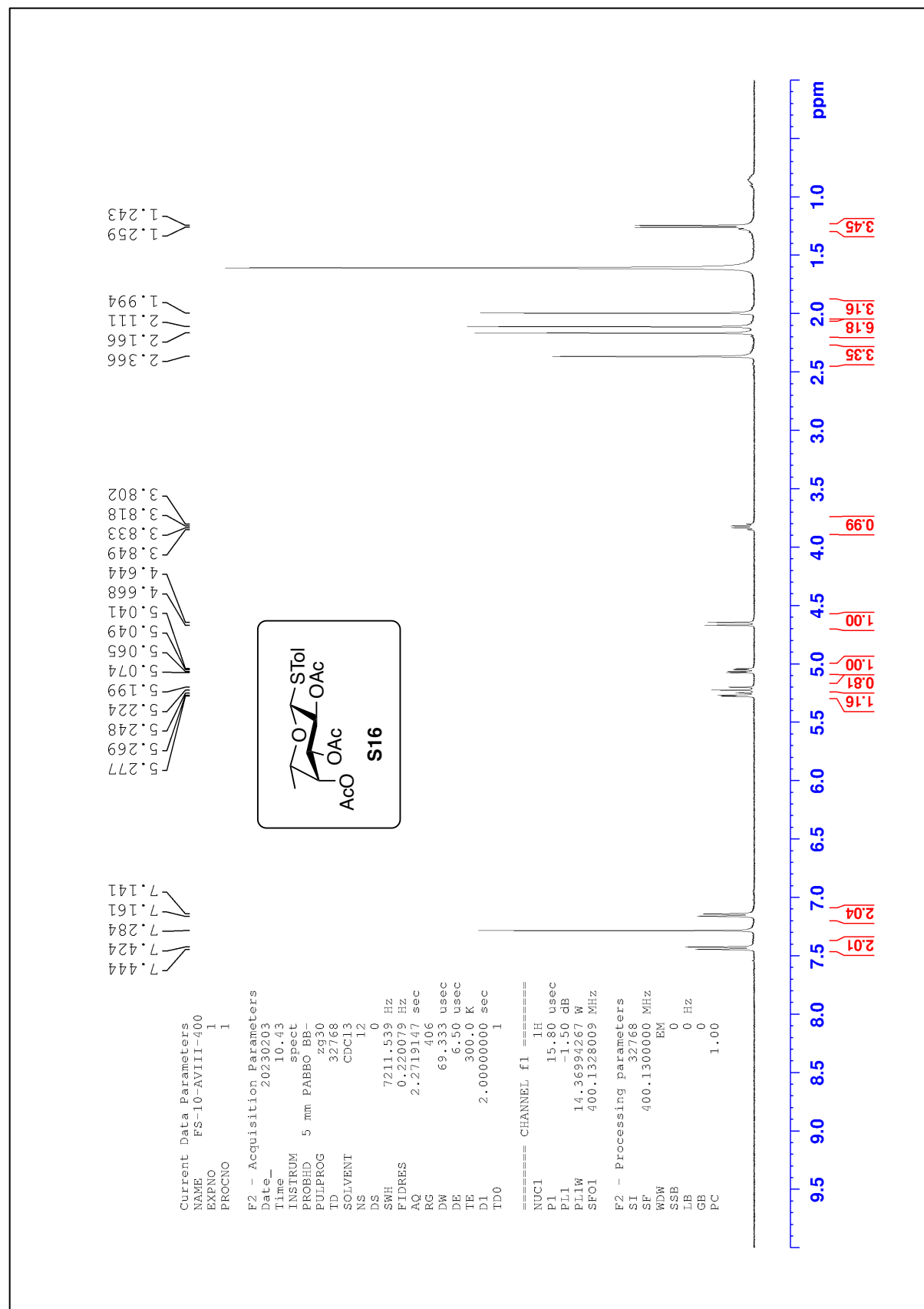
The ^1H Spectrum in CD_2Cl_2 of Compound C.



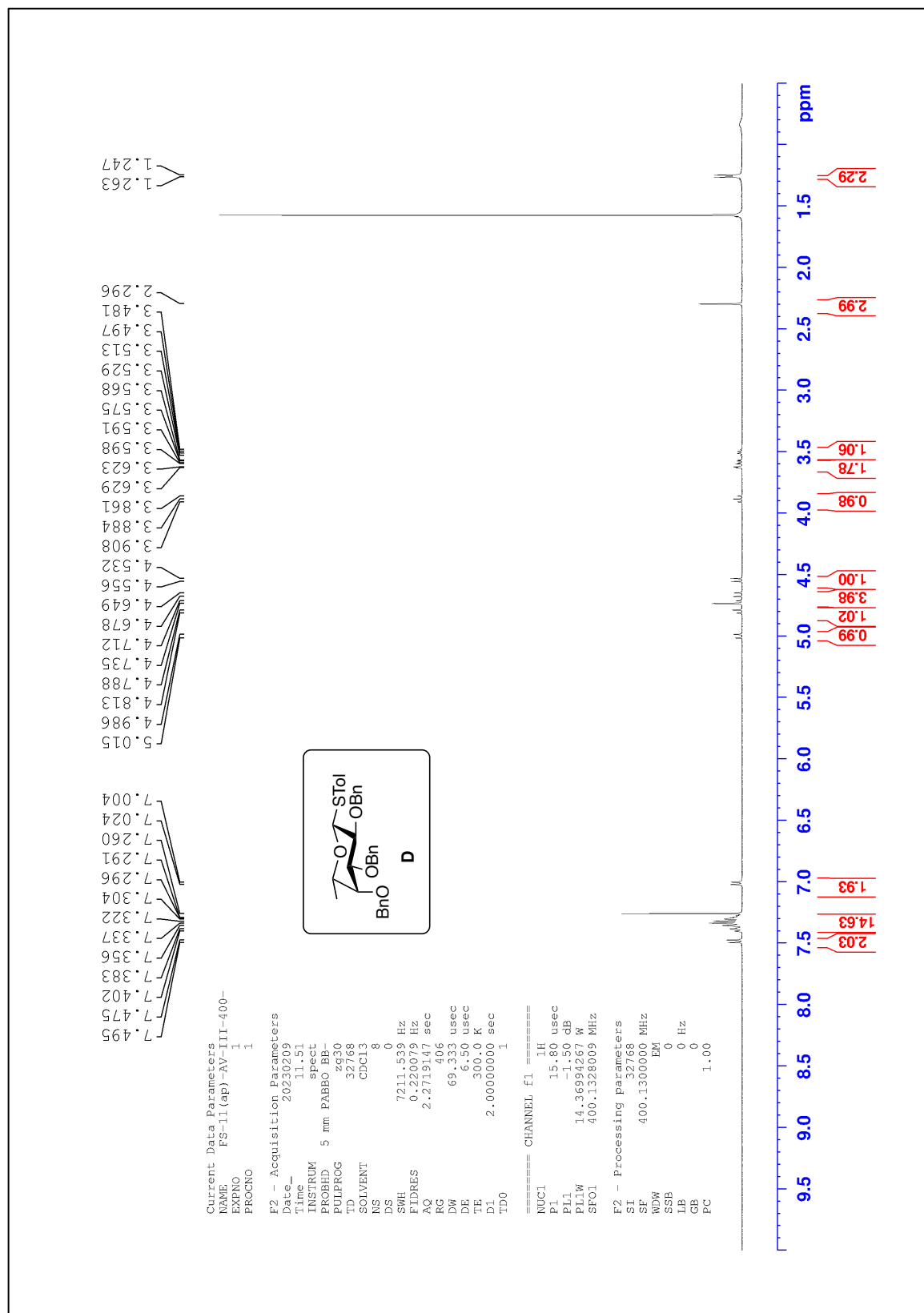
The 1D-TOCSY Spectrum in CD₂Cl₂ of Compound C.



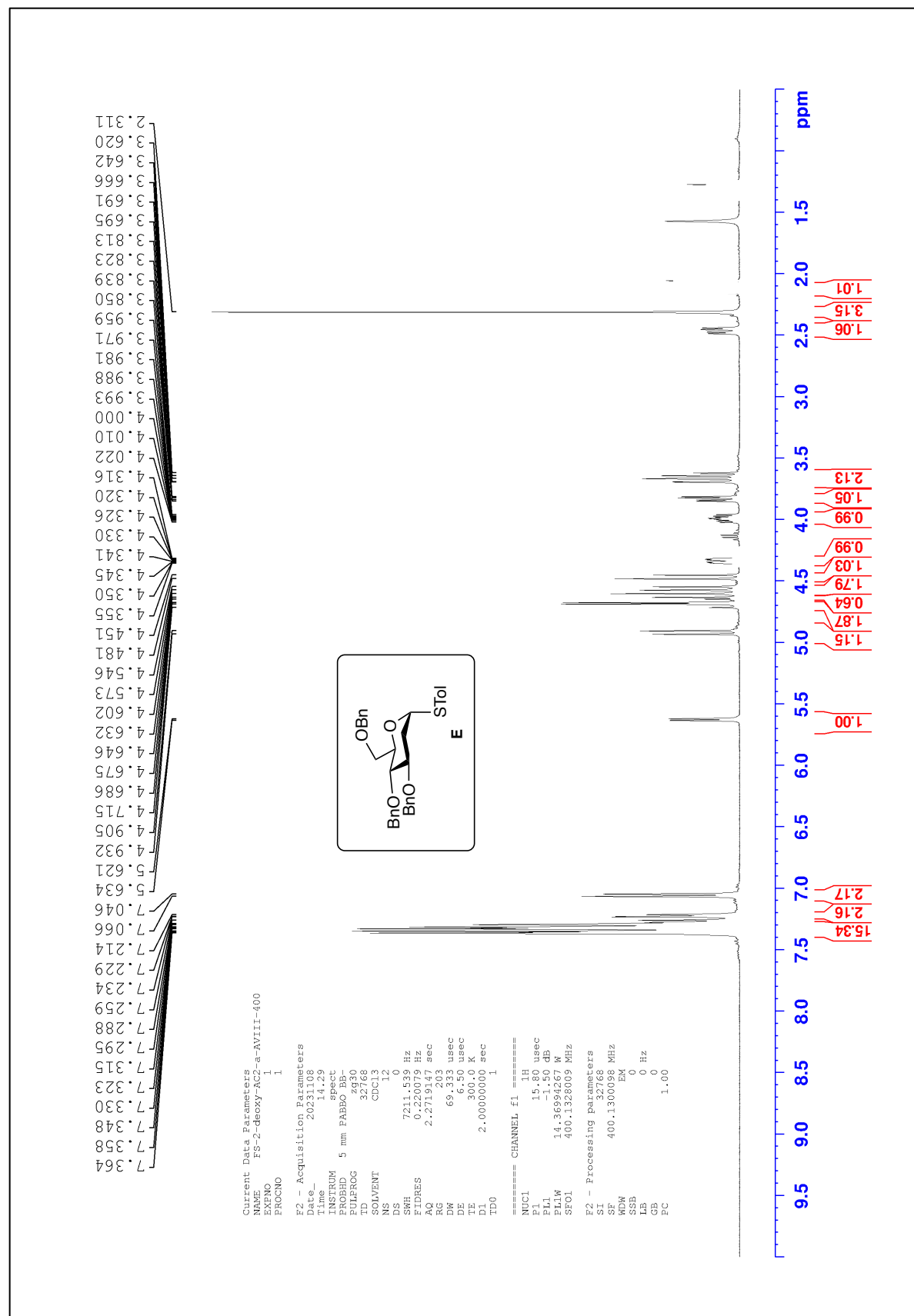
The ^{13}C Spectrum in CD_2Cl_2 of Compound C.



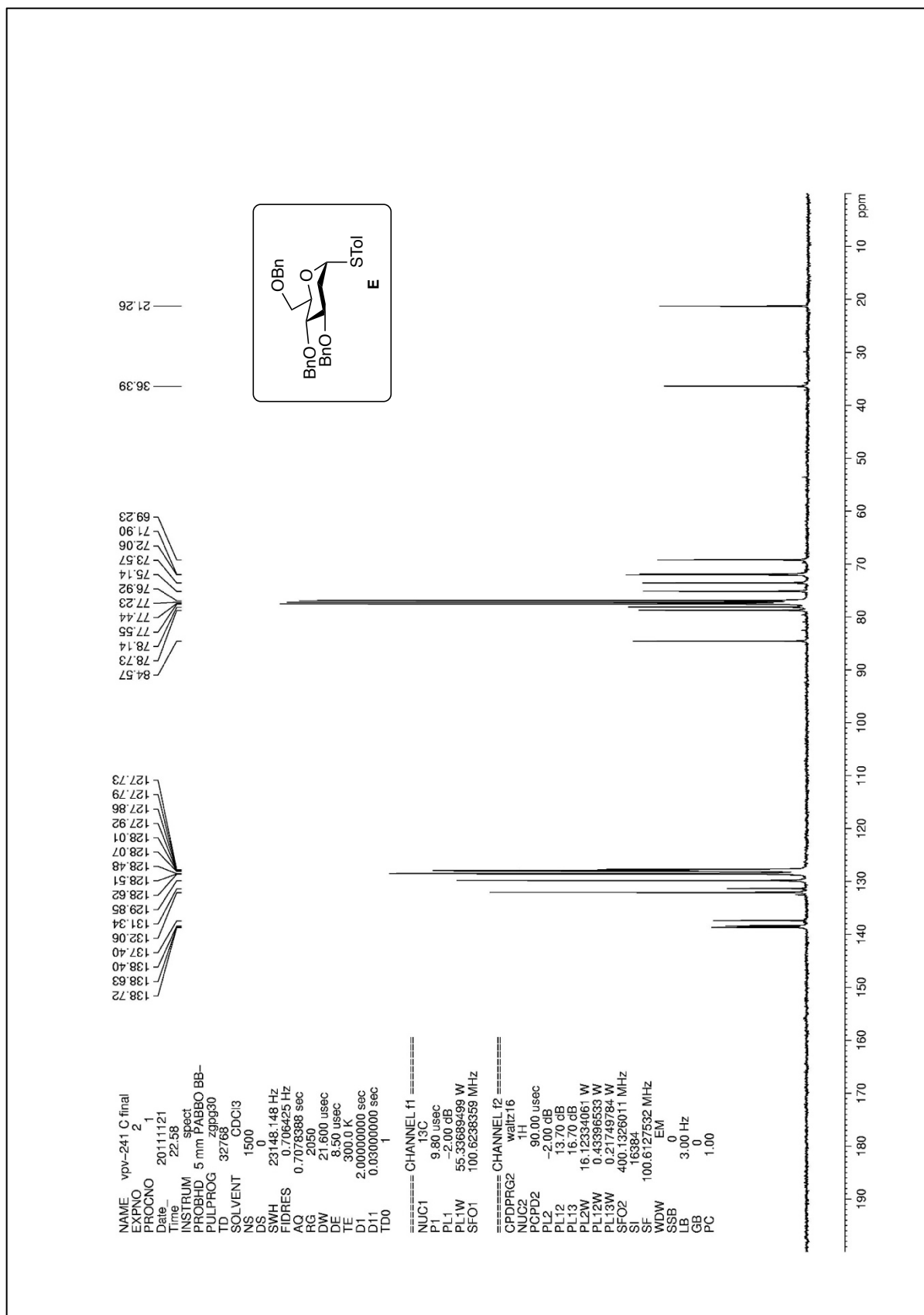
The ¹H Spectrum in CD₂Cl₂ of Compound S16.



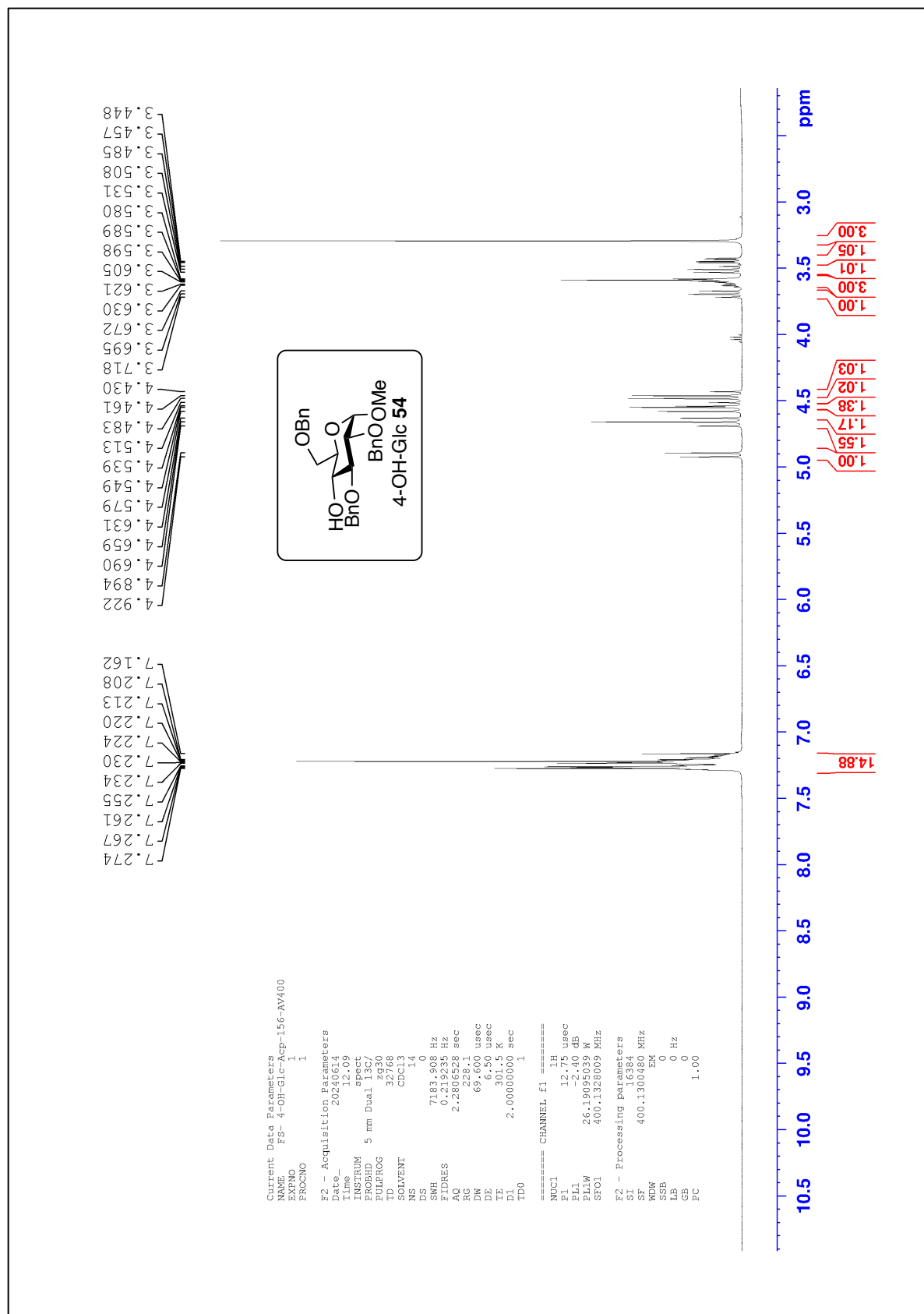
The ¹H Spectrum in CD₂Cl₂ of Compound D.



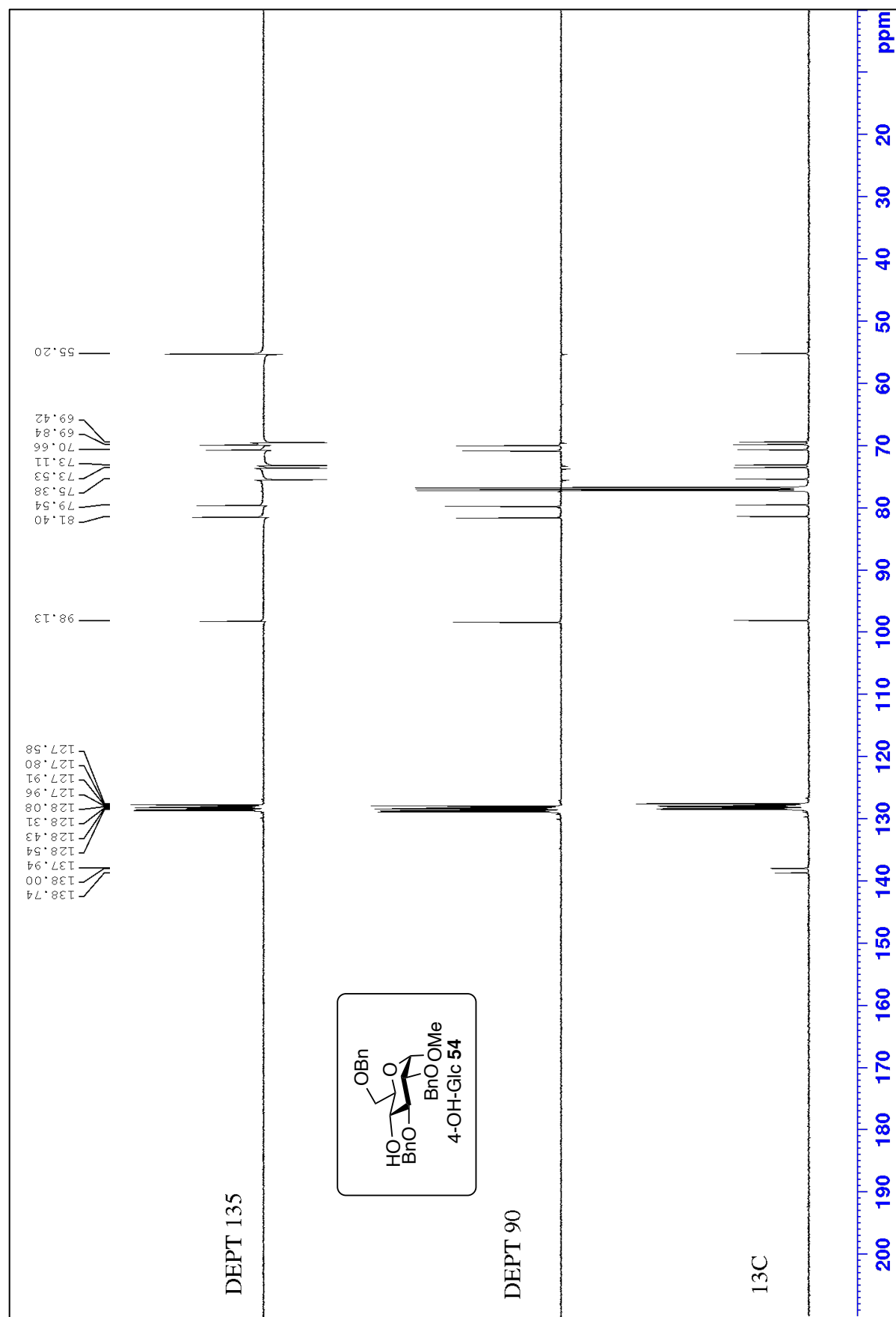
¹³C Spectrum in CDCl₃ of Compound E.



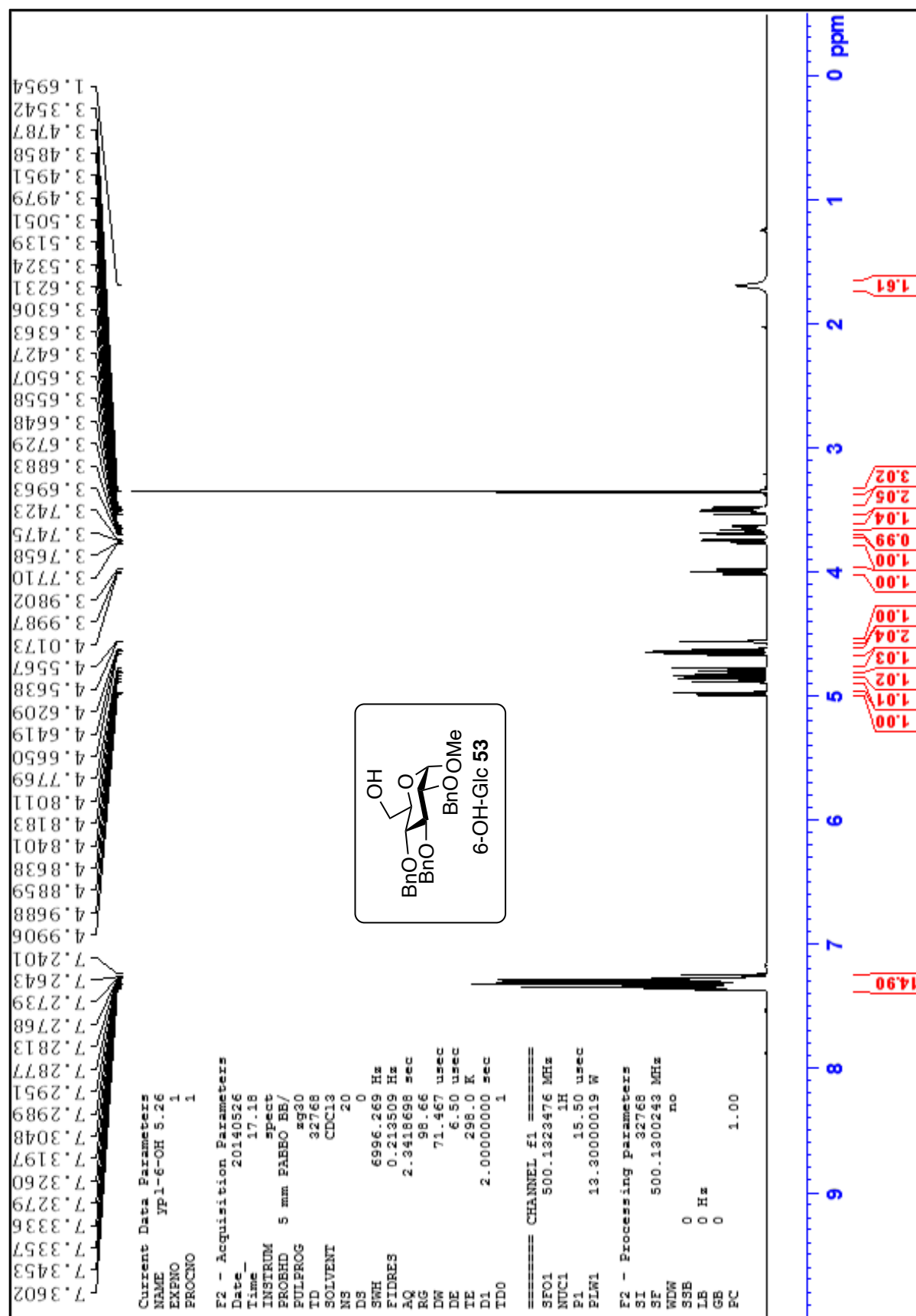
The ^{13}C Spectrum in CDCl_3 of Compound E.



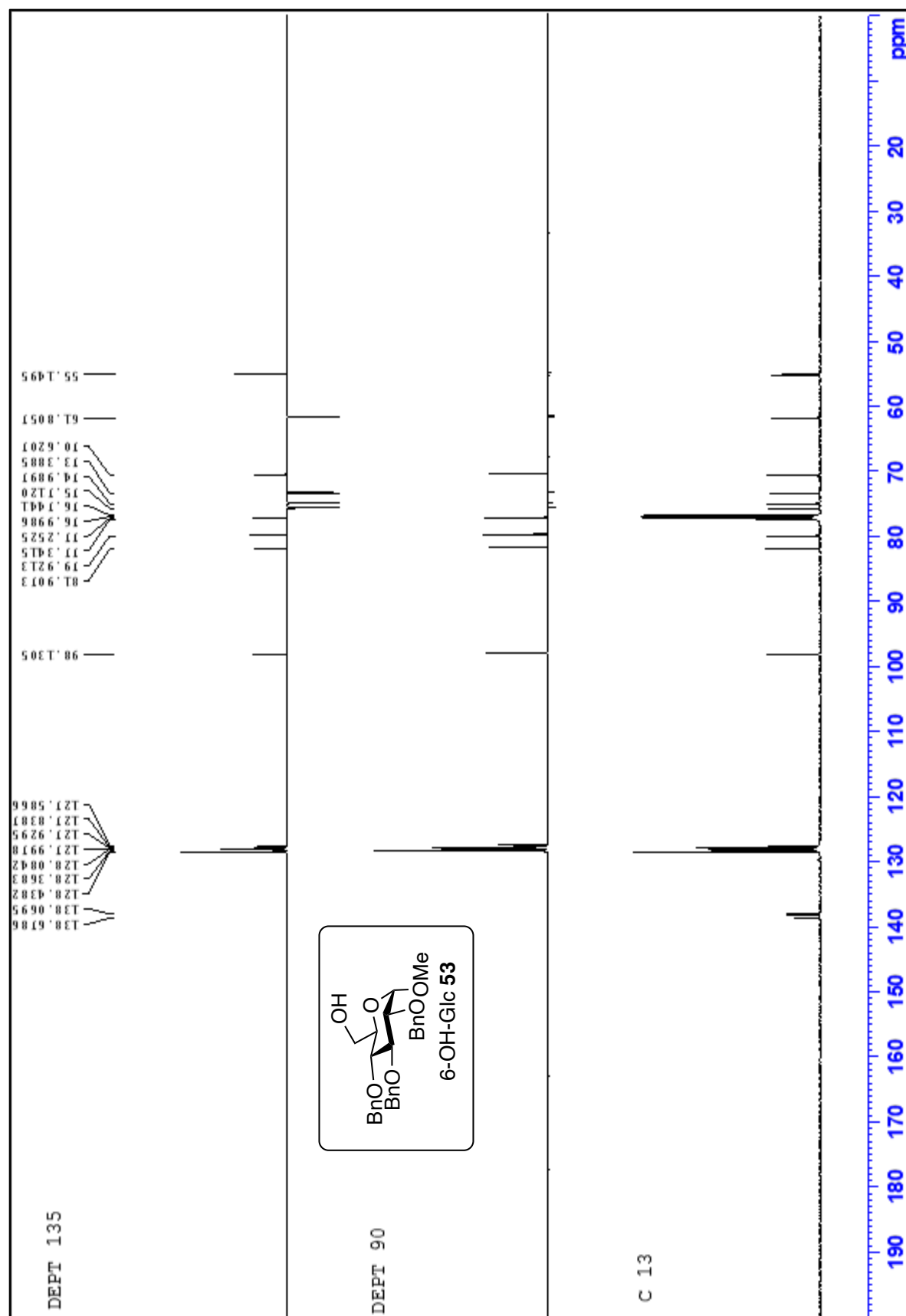
The ^1H Spectrum in CDCl_3 of Compound 54.



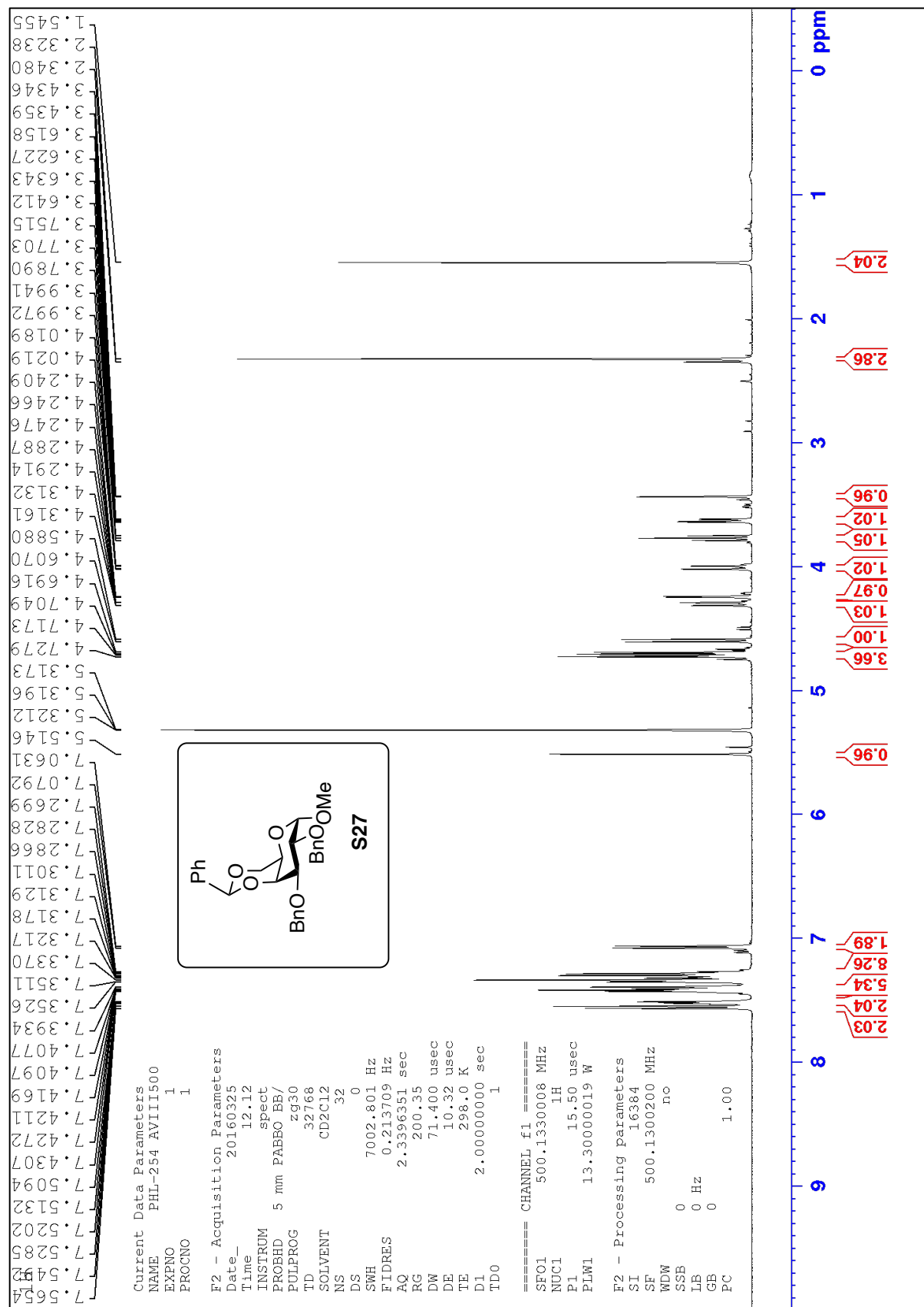
The ¹³C Spectrum in CDCl₃ of Compound 54.

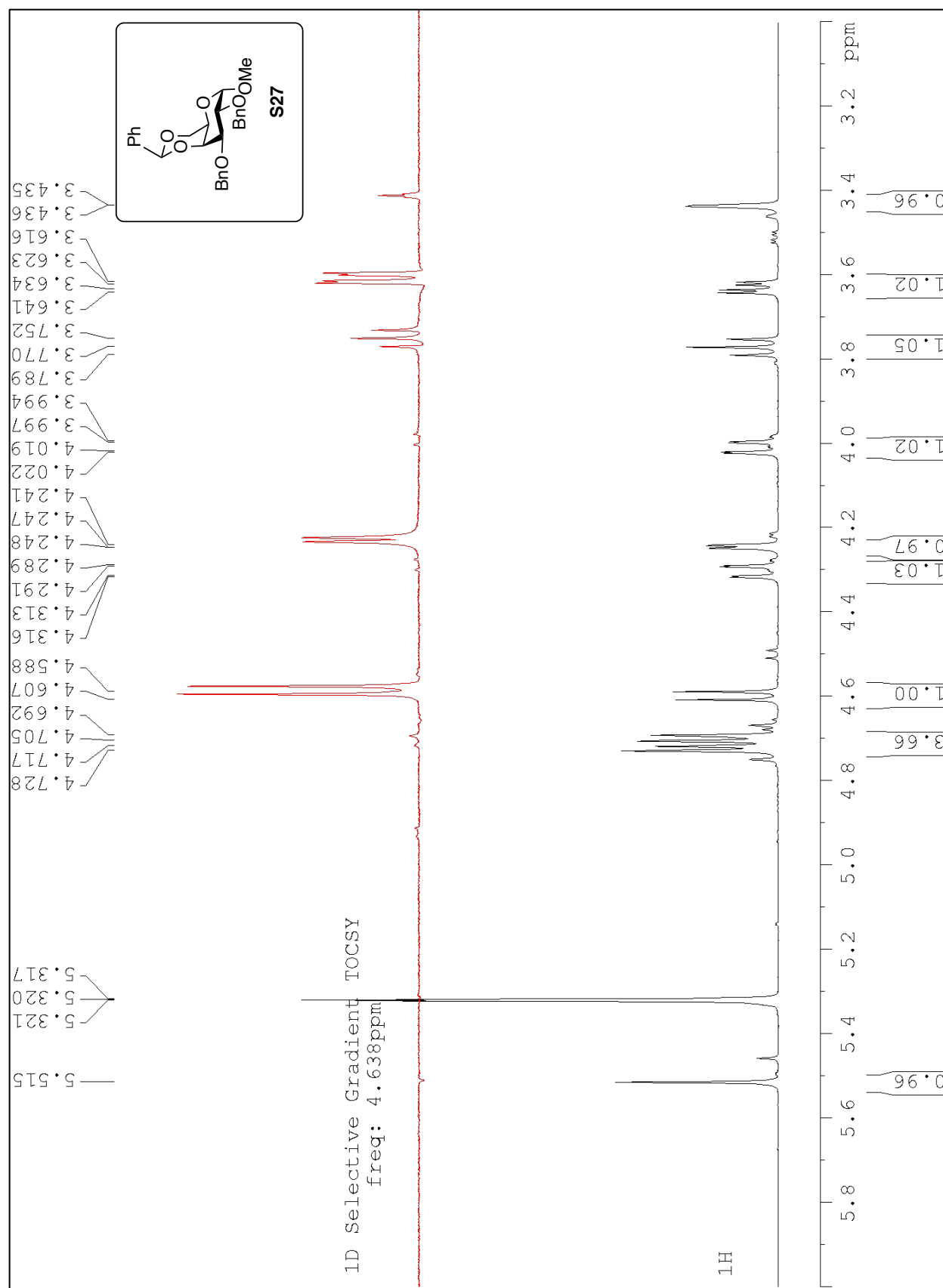


The ^1H Spectrum in CDCl_3 of Compound 53.

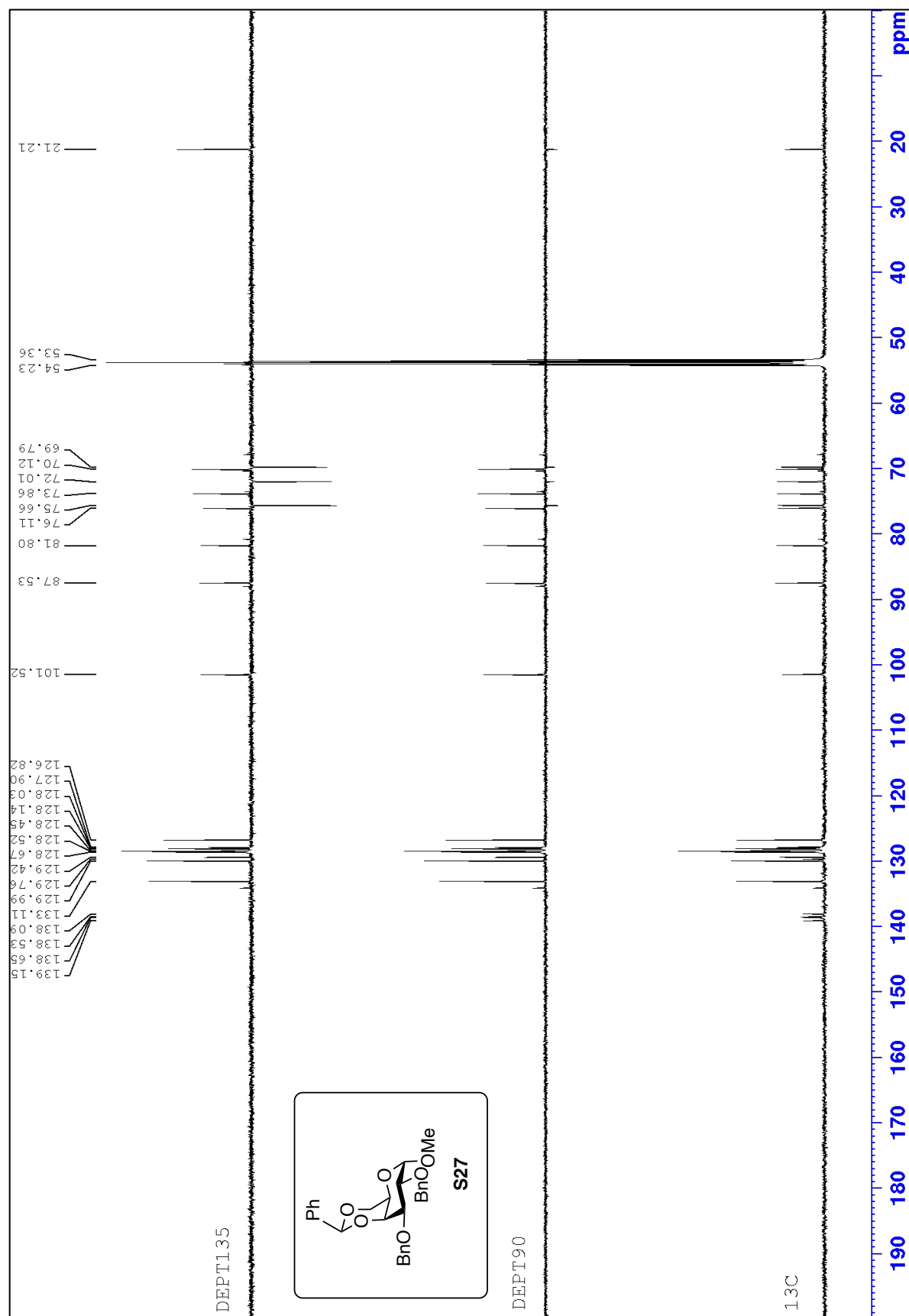


The ^{13}C Spectrum in CDCl_3 of Compound 53.





The 1D-TOCSY Spectrum in CD_2Cl_2 of Compound S27.



The ^{13}C Spectrum in CD_2Cl_2 of Compound S27.

¹H



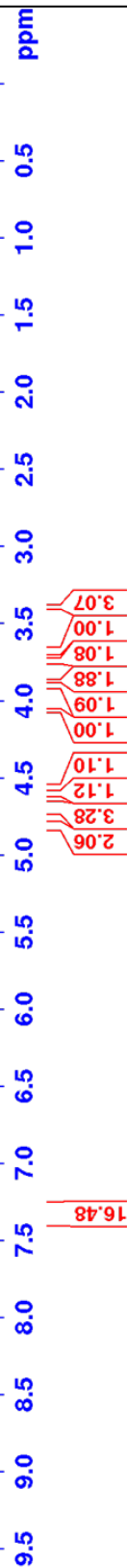
Current Data Parameters
NAME MHL-098 N600
EXPNO 2
PROCNO 1

F2 - Acquisition Parameters
Date_ 20180412
Time 18.33 h
INSTRUM spect
PROBHD zg30
PULPROG zg30
TD 32768
SOLVENT CDCl3
NS 24
DS 2

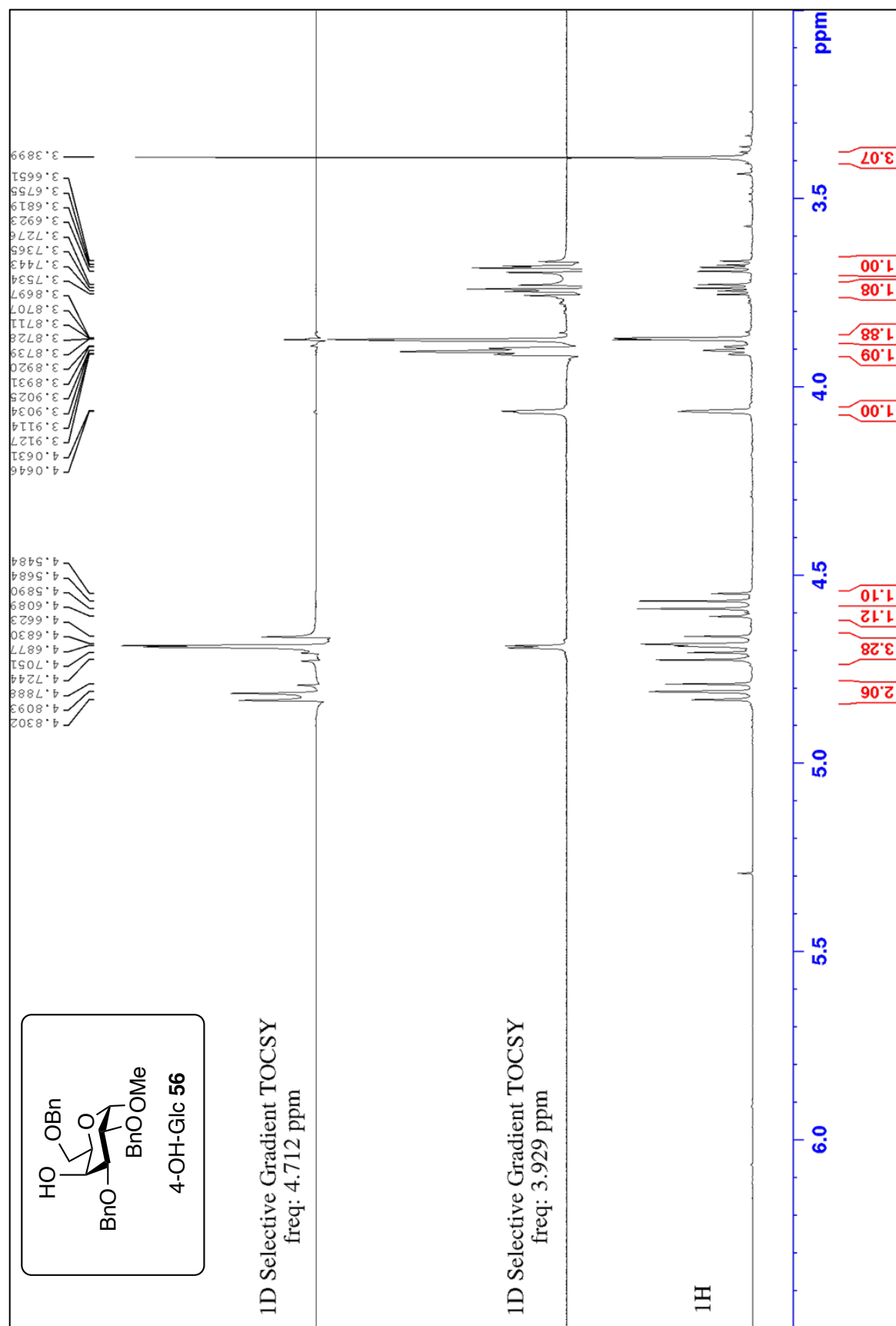
SWH 7796.258 Hz
FIDRES 0.237923 Hz
AQ 2.1015210 sec
RG 59.11
DW 64.133 usec
DE 10.47 usec
TE 300.0 K
D1 2.0000000 sec

TD0 1
SFO1 600.1836011 MHz
NUC1 1H
P1 10.00 usec
PLW1 24.79599953 W

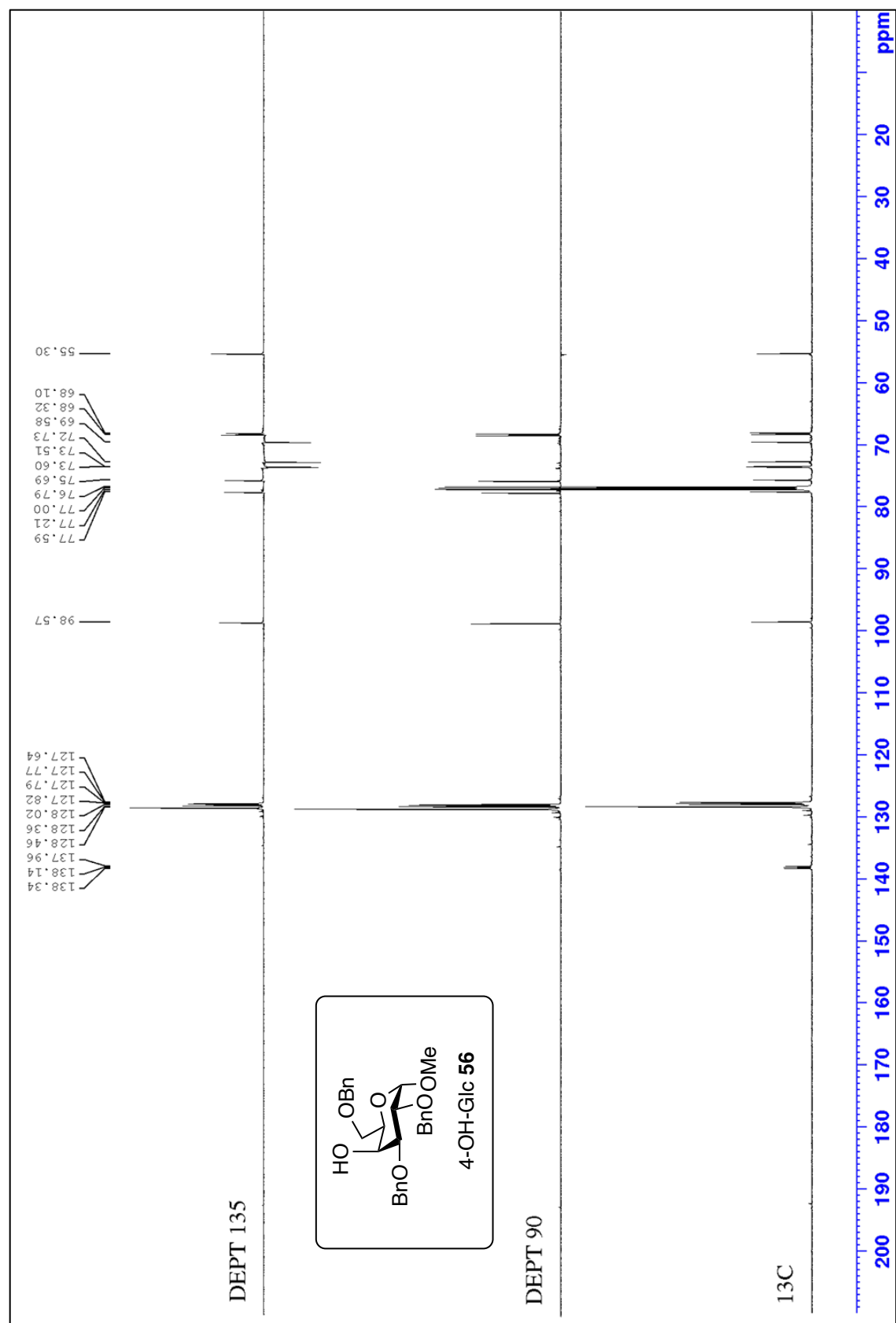
F2 - Processing parameters
SI 16384
SF 600.1800151 MHz
WDW no
SSB 0
LB 0 Hz
GB 0
PC 1.00



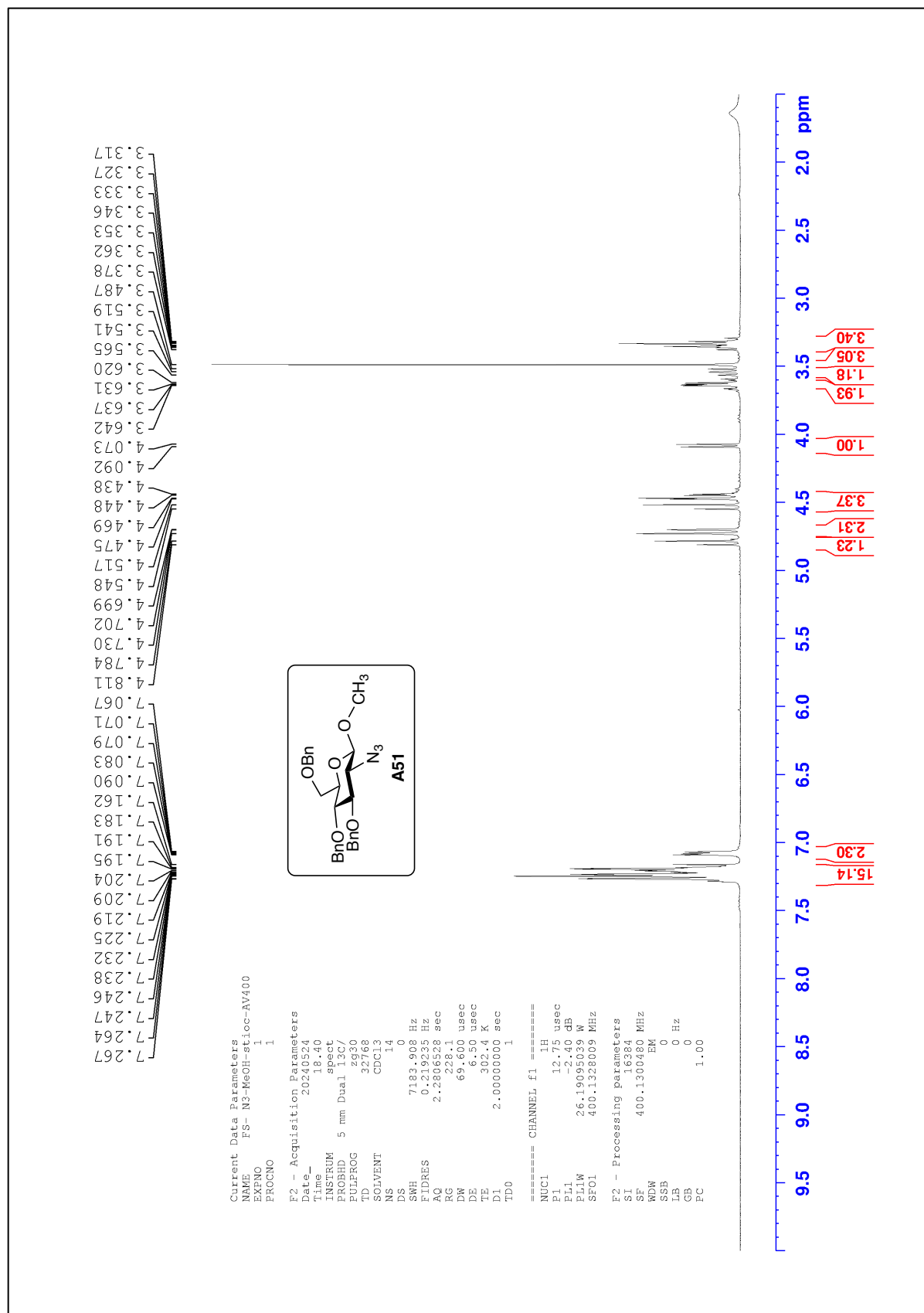
The ¹H Spectrum in CDCl₃ of Compound 56.



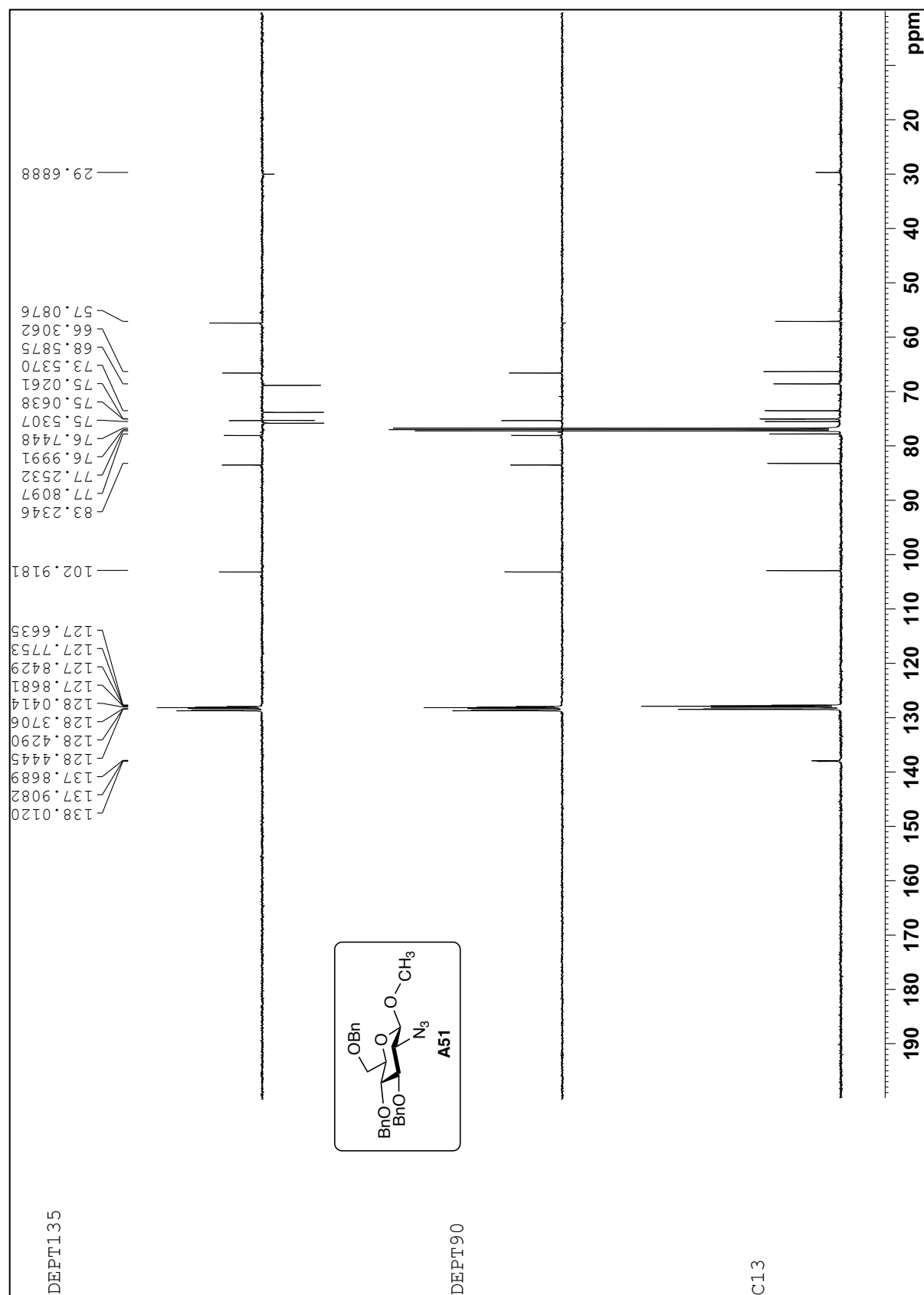
The 1D-TOCSY Spectrum in CDCl₃ of Compound **56**.



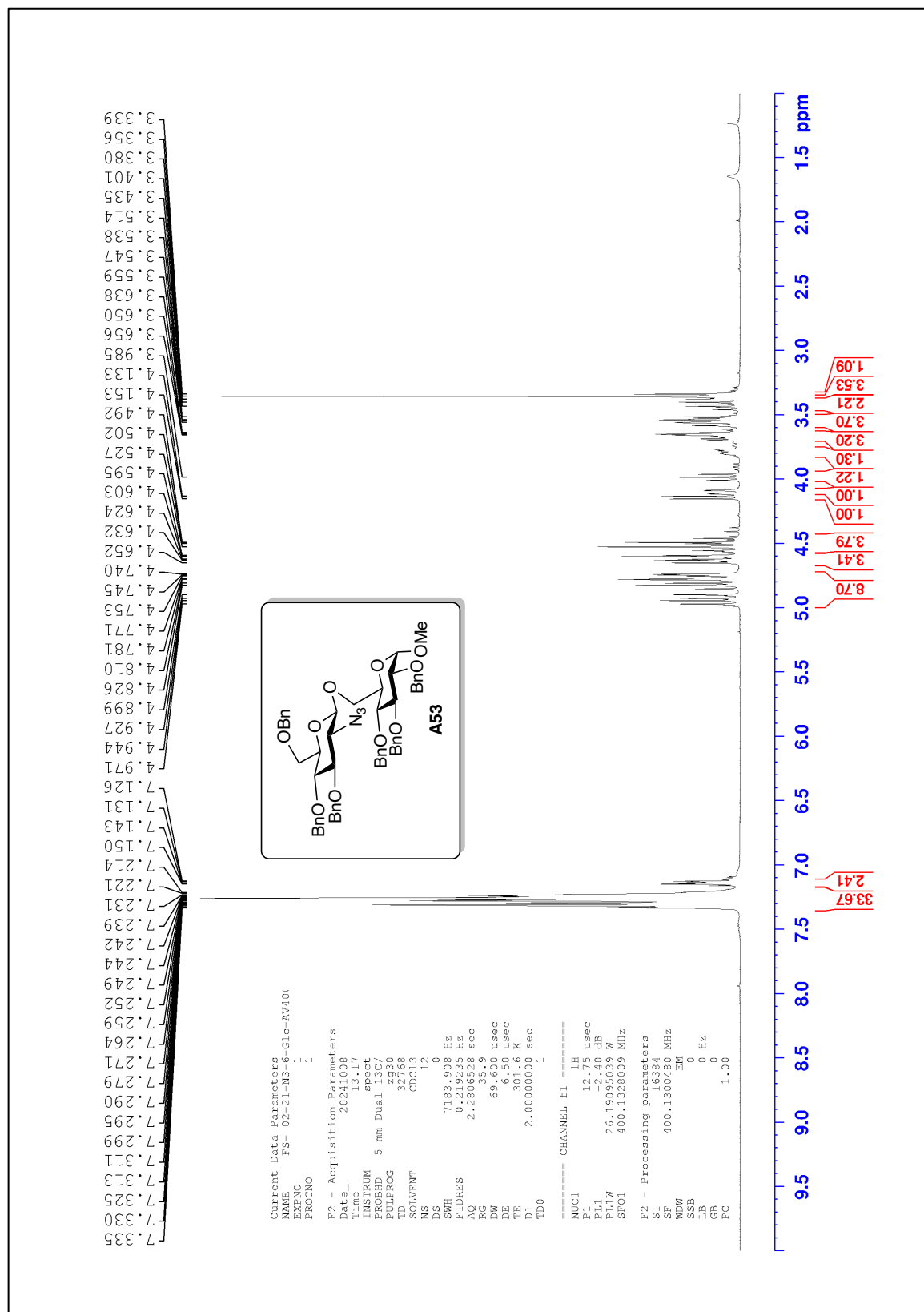
The ¹³C Spectrum in CDCl₃ of Compound 56.



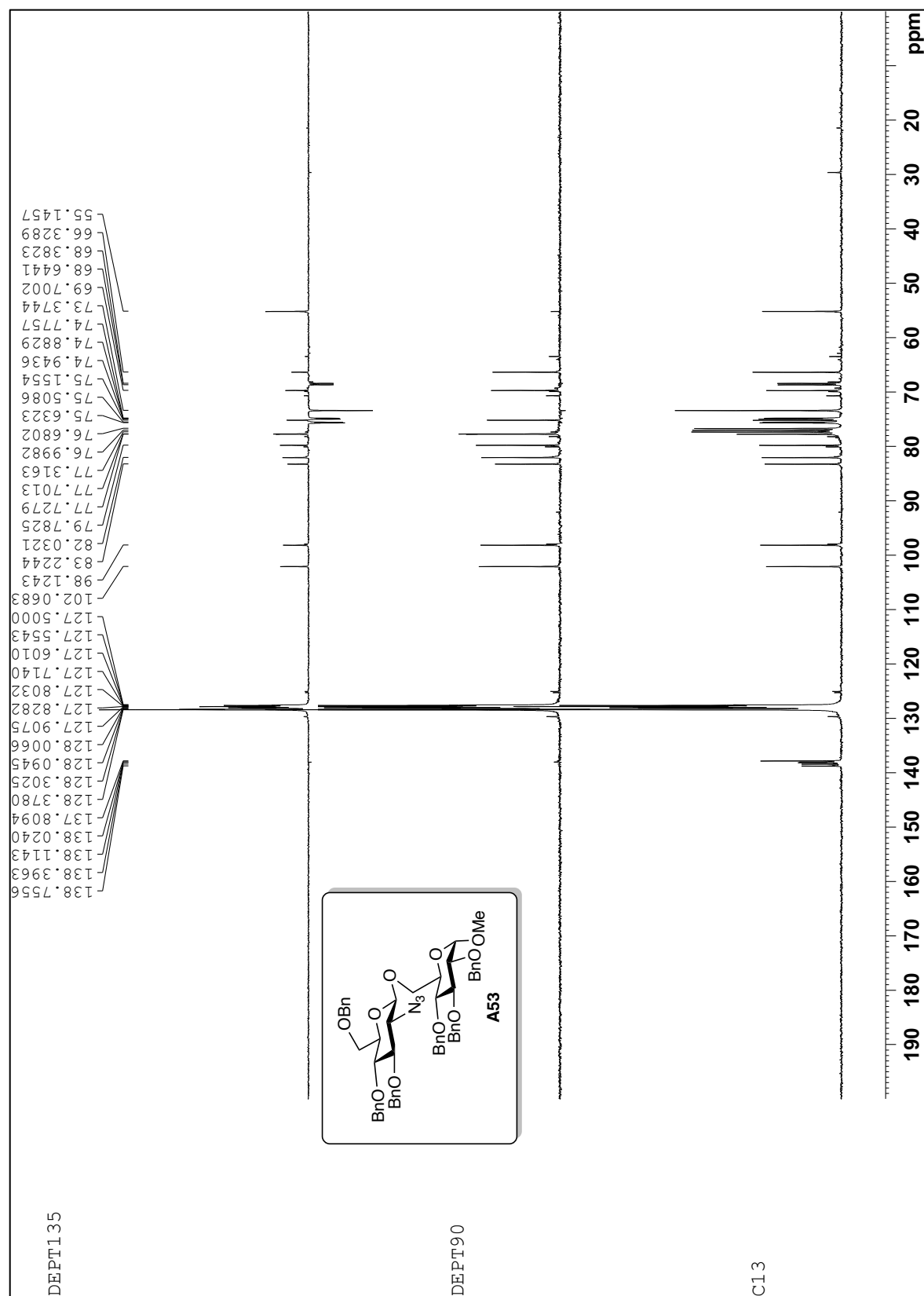
The ^1H Spectrum in CDCl_3 of Compound A51- β .



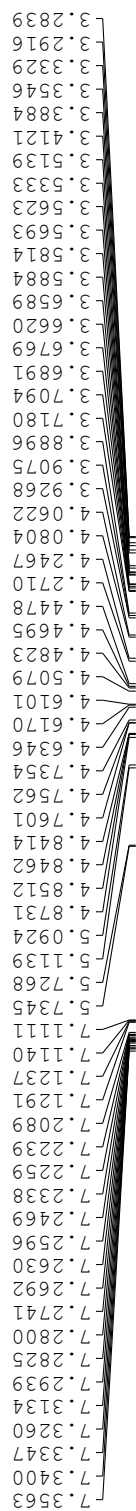
The ¹³C Spectrum in CDCl₃ of Compound A51-β.



The ^1H Spectrum in CDCl_3 of Compound A53- β .



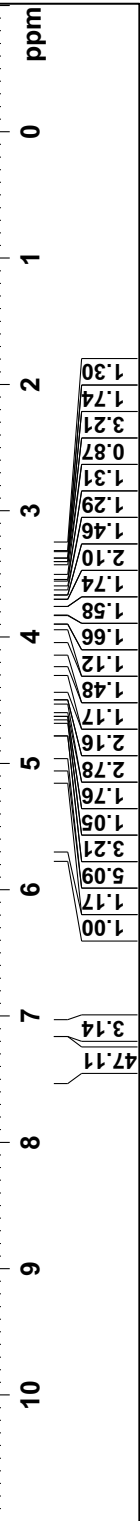
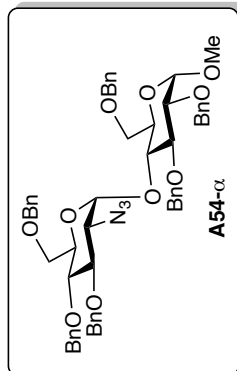
¹H



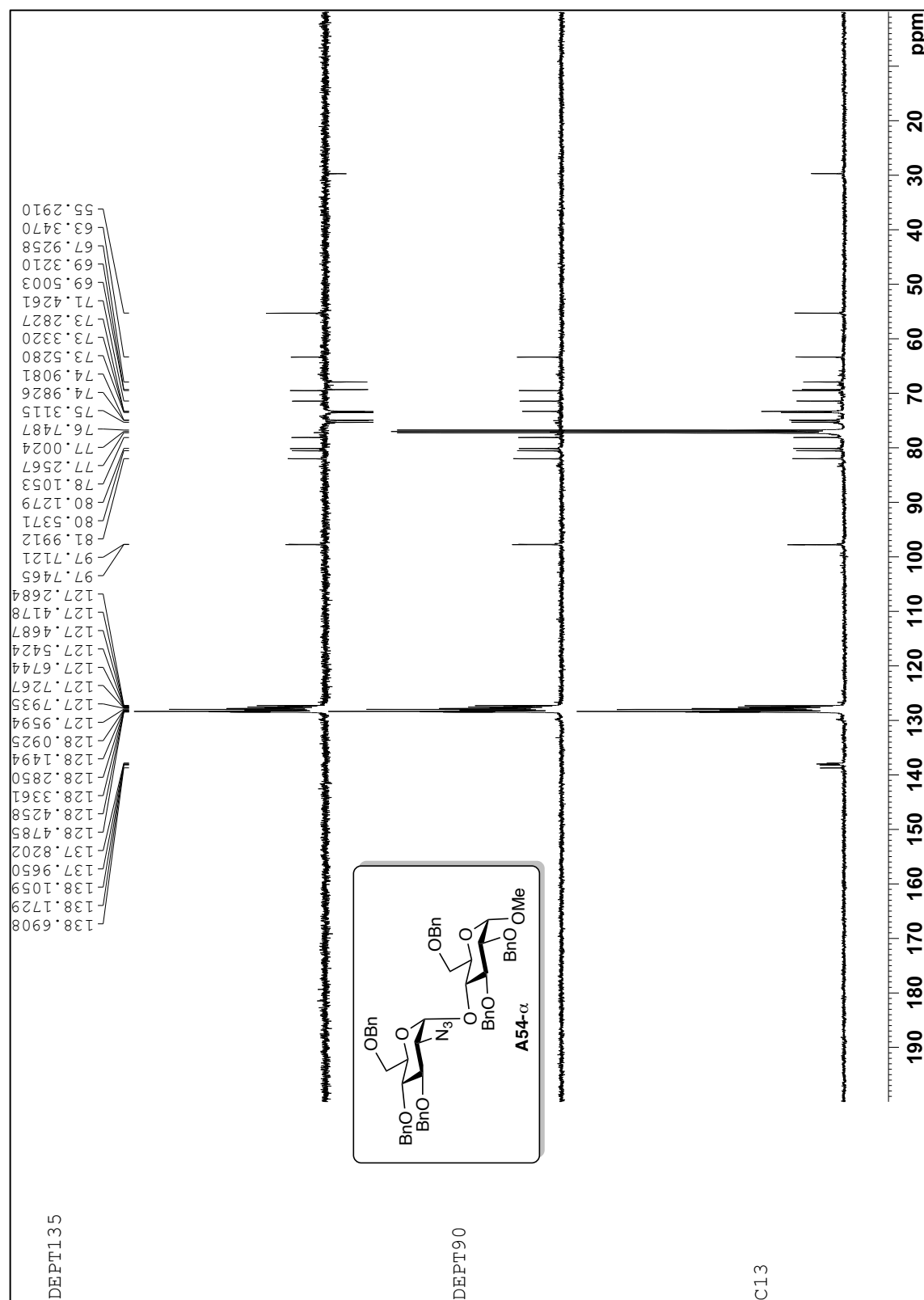
Current Data Parameters
NAME CWC-269 BRX500
EXPNO 1
PROCNO 1

F2 - Acquisition Parameters
Date_ 20100810
Time 10:08
INSTRUM spect
PROBHD 5 mm PABBO BB/
PULPROG zg30
TD 32768
SOLVENT CDCl3
NS 24
DS 0
SWH 8992.806 Hz
FIDRES 0.274439 Hz
AQ 1.8219508 sec
RG 327.68
DM 55.600 usec
DE 6.50 usec
TE 298.0 K
D1 1.00000000 sec
TDO 1

===== CHANNEL f1 =====
NUC1 1H
P1 13.00 usec
PL1 -5.00 dB
SFO1 500.1330008 MHz
F2 - Processing Parameters
SI 16394
SF 500.1300140 MHz
WDW no
SSB 0
LB 0 Hz
GB 0
PC 1.00



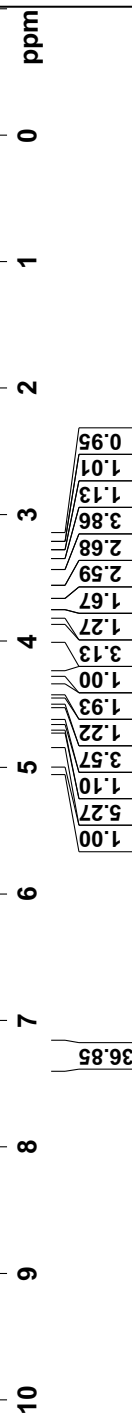
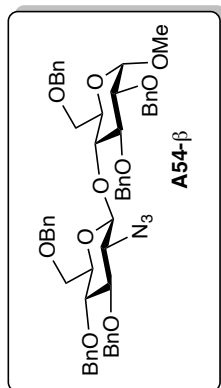
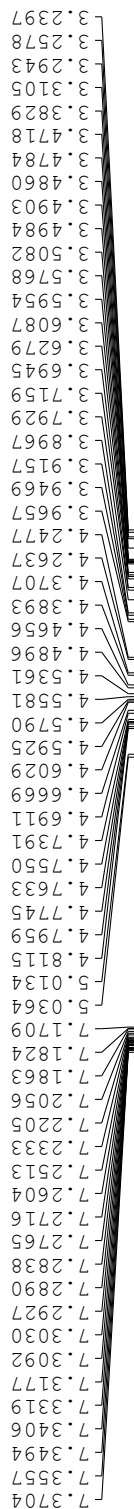
The ¹H Spectrum in CDCl₃ of Compound A54-α.



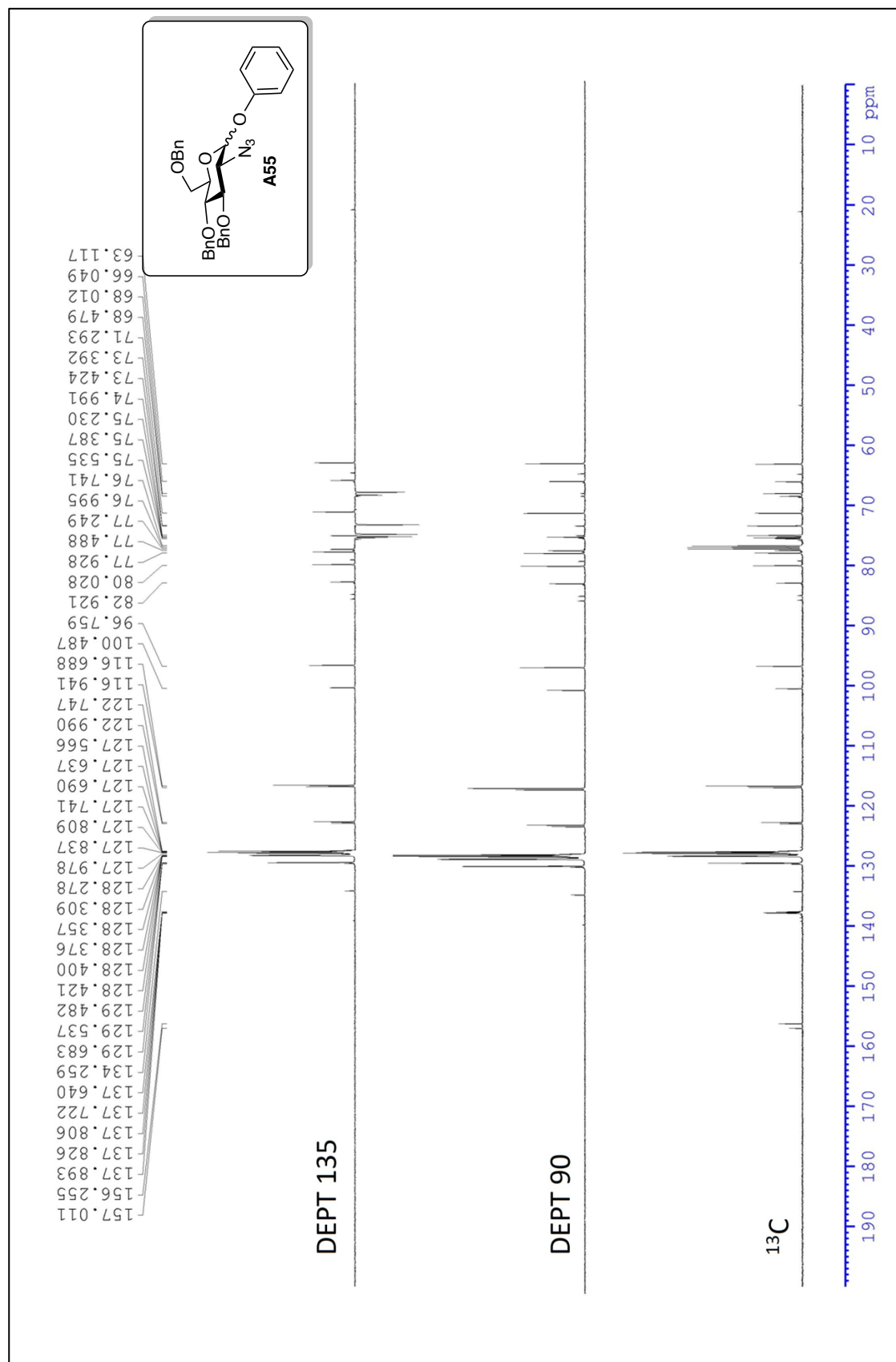
The ^{13}C Spectrum in CDCl_3 of Compound A54- α .

¹H

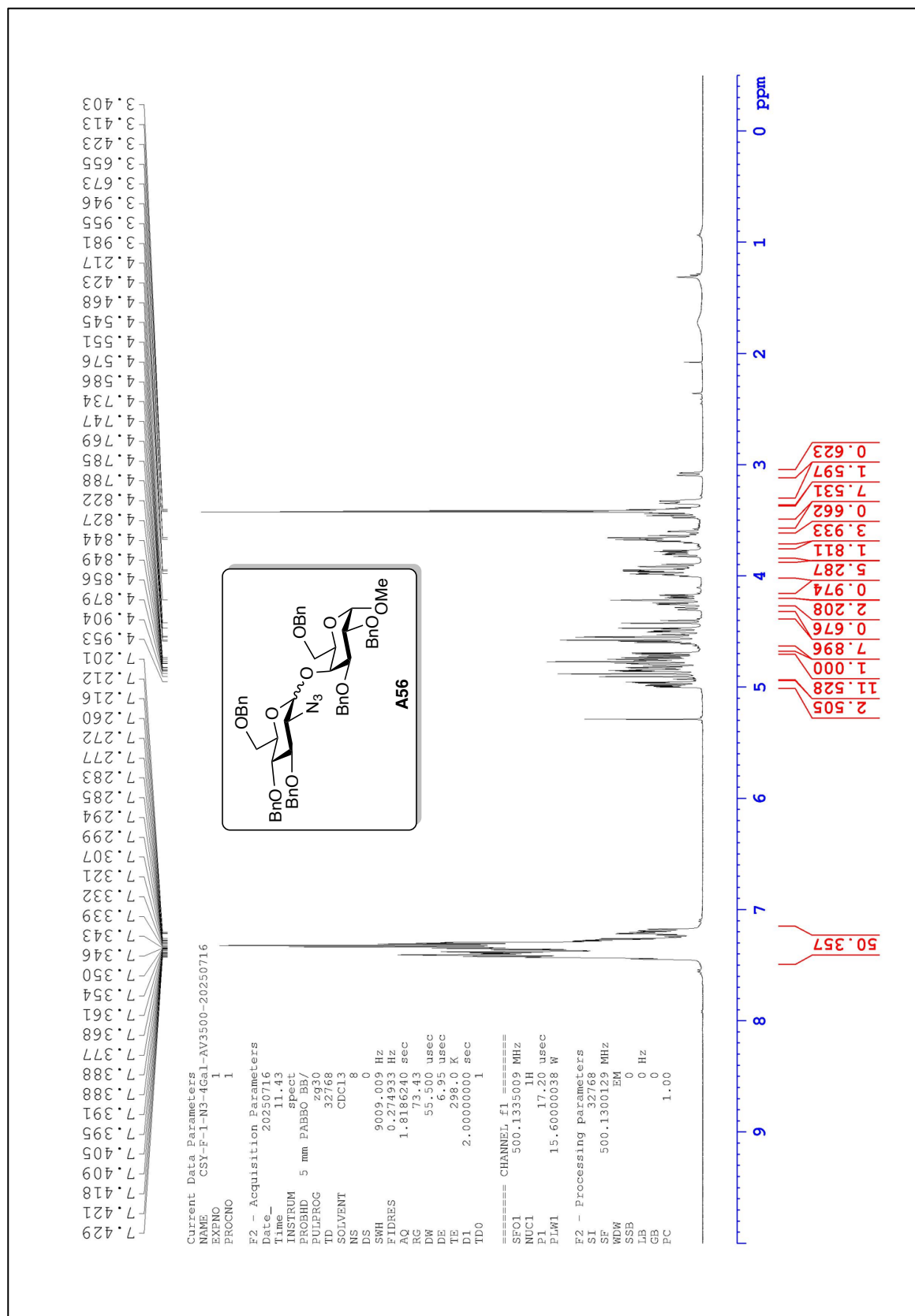
Current Data Parameters
NAME CWC-253 DRX500
EXPNO 4
PROCNO 1
F2 - Acquisition Parameters
Date_ 20130109
Time 16.03
INSTRUM spect
PROBHD 5 mm PABBO BBI/1H
PULPROG zgpg30
TD 32768
SOLVENT CDCl3
NS 1
DS 0
SWH 892.806 Hz
FIDRES 0.2211508 Hz
AQ 1.6211508 sec
RG 322.5
DW 55.600 usec
DE 6.50 usec
TE 298.4 K
D1 1.00000000 sec
TDO 1
===== CHANNEL f1 =====
NUC1 1H
P1 11.40 usec
PL1 0.00 dB
SFO1 500.133008 MHz
F2 - Processing parameters
SI 16384
SF 500.1300134 MHz
WDW no
SSB 0
LB 0 Hz
GB 0
PC 1.00



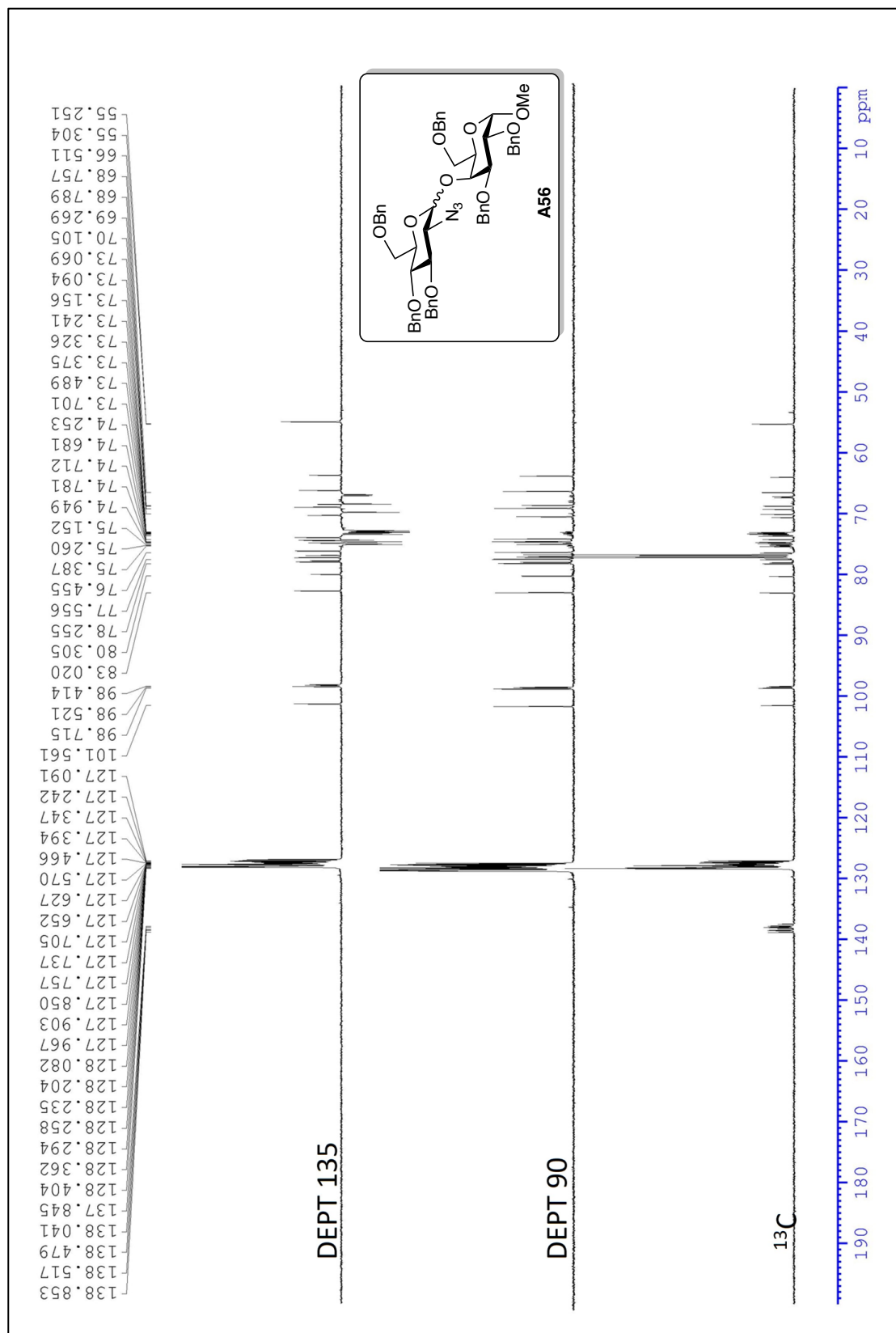
The ¹H Spectrum in CDCl₃ of Compound A54-β.



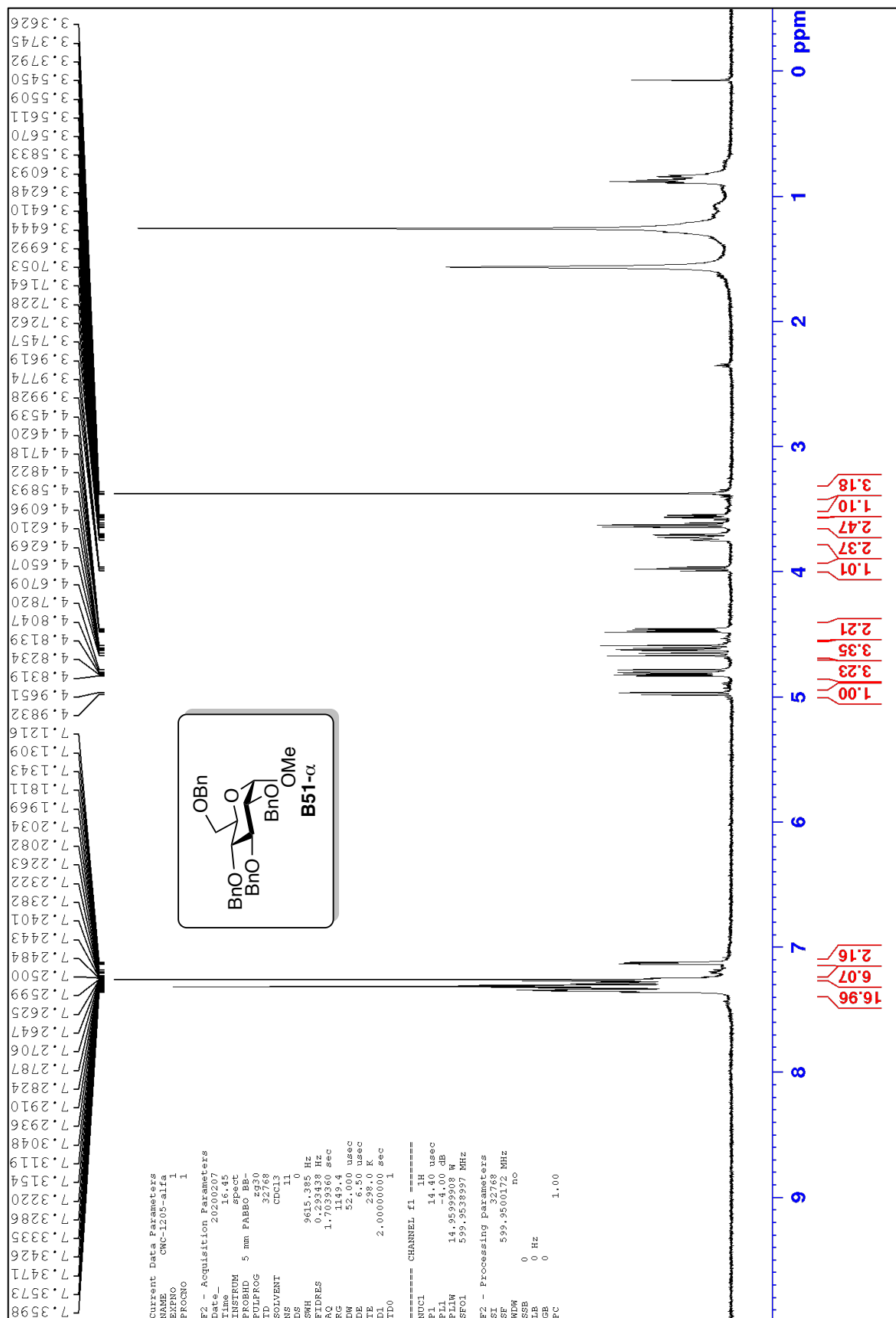
The ¹³C Spectrum in CDCl₃ of Compound A55



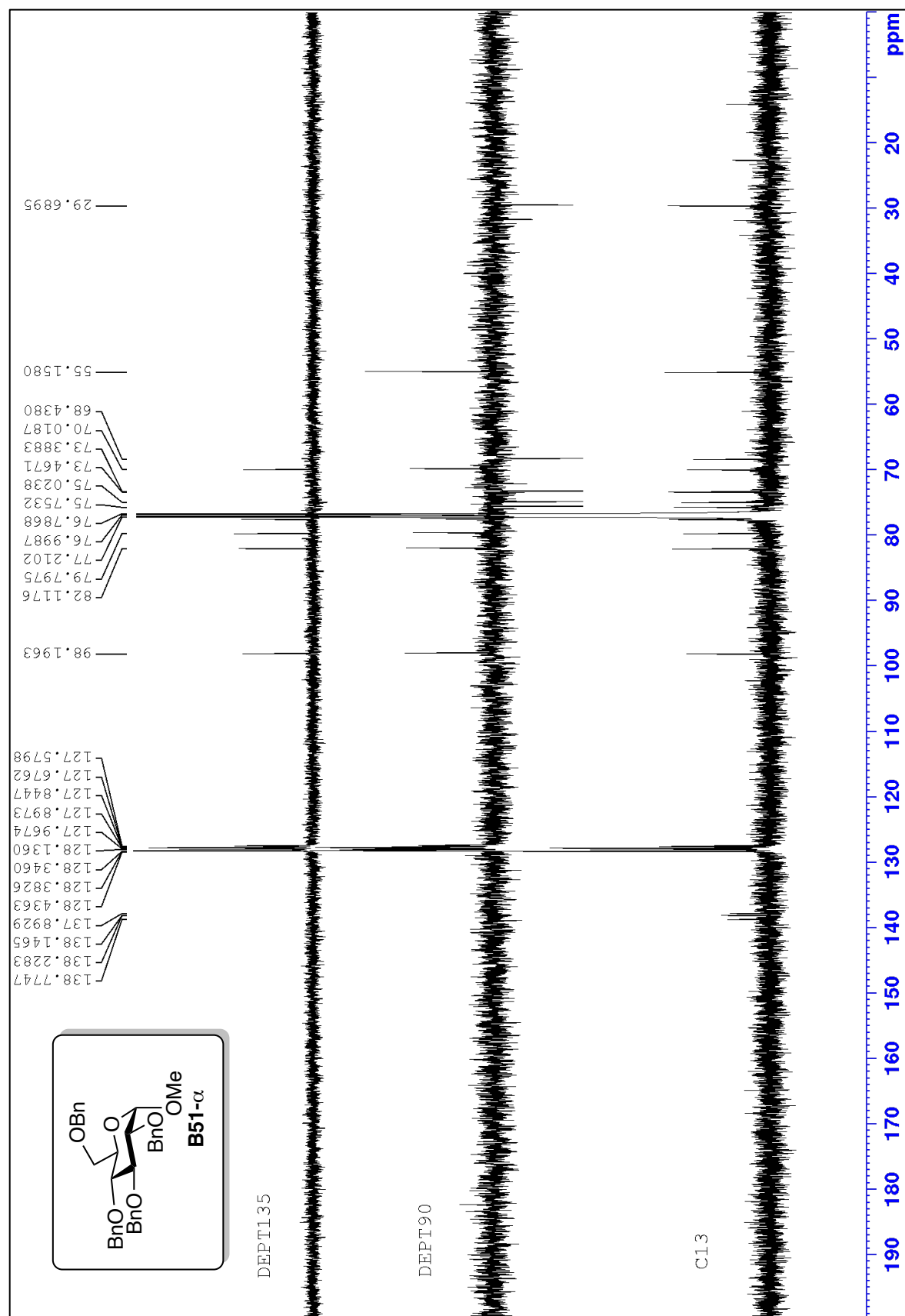
The ^1H Spectrum in CDCl_3 of Compound A56



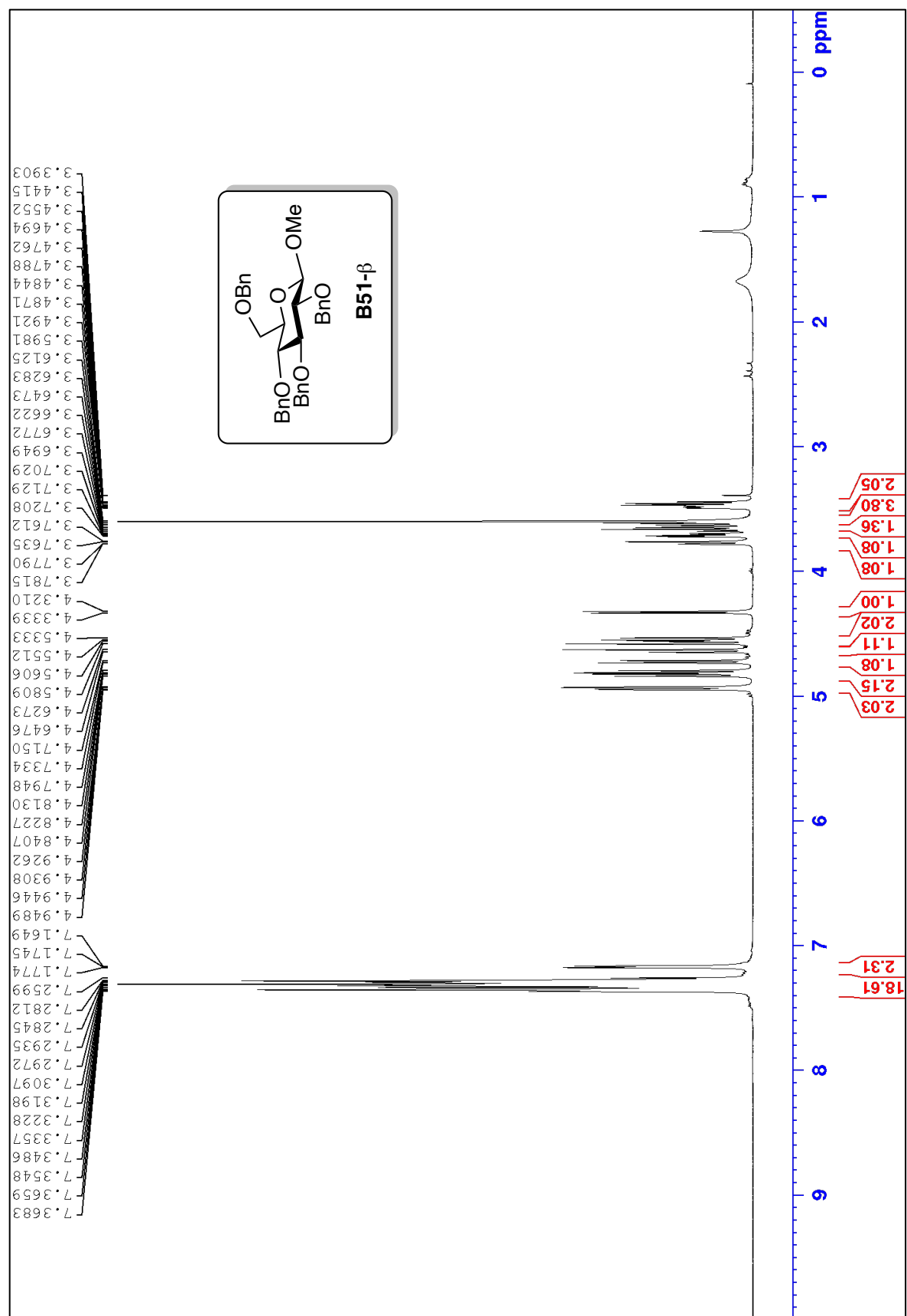
The ^{13}C Spectrum in CDCl_3 of Compound A56



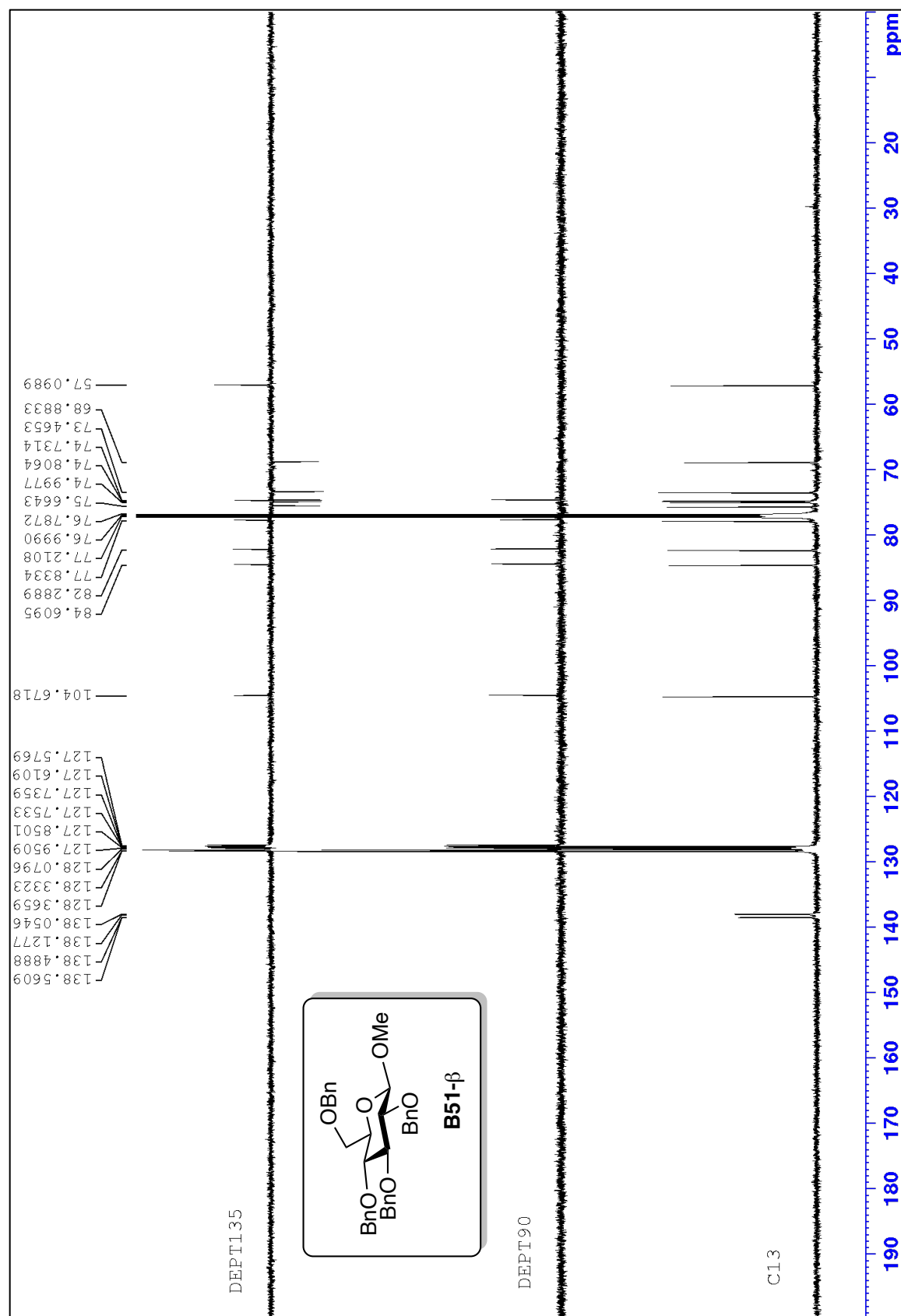
The ^1H Spectrum in CDCl_3 of Compound B51- α .



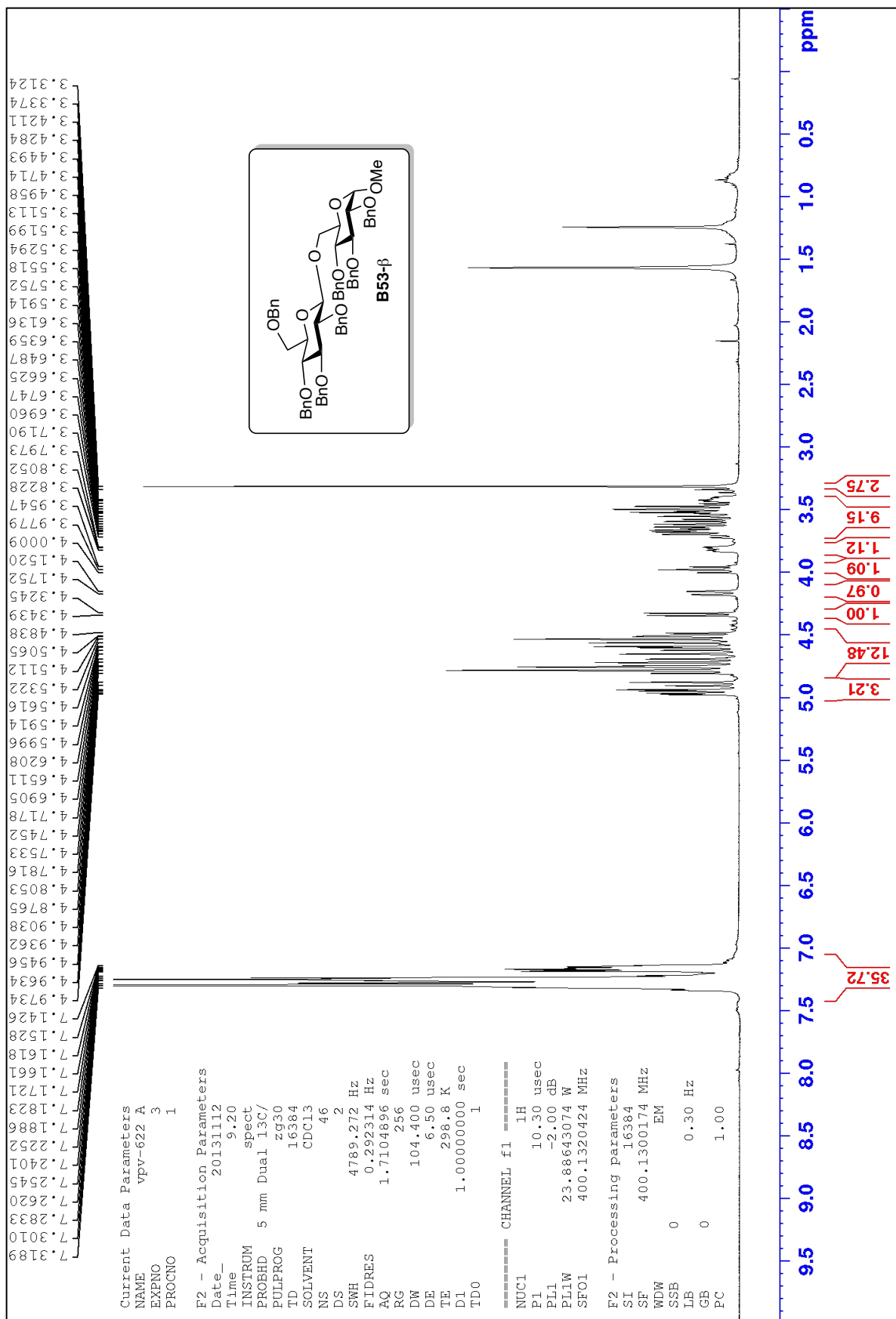
The ^{13}C Spectrum in CDCl_3 of Compound B51- α .



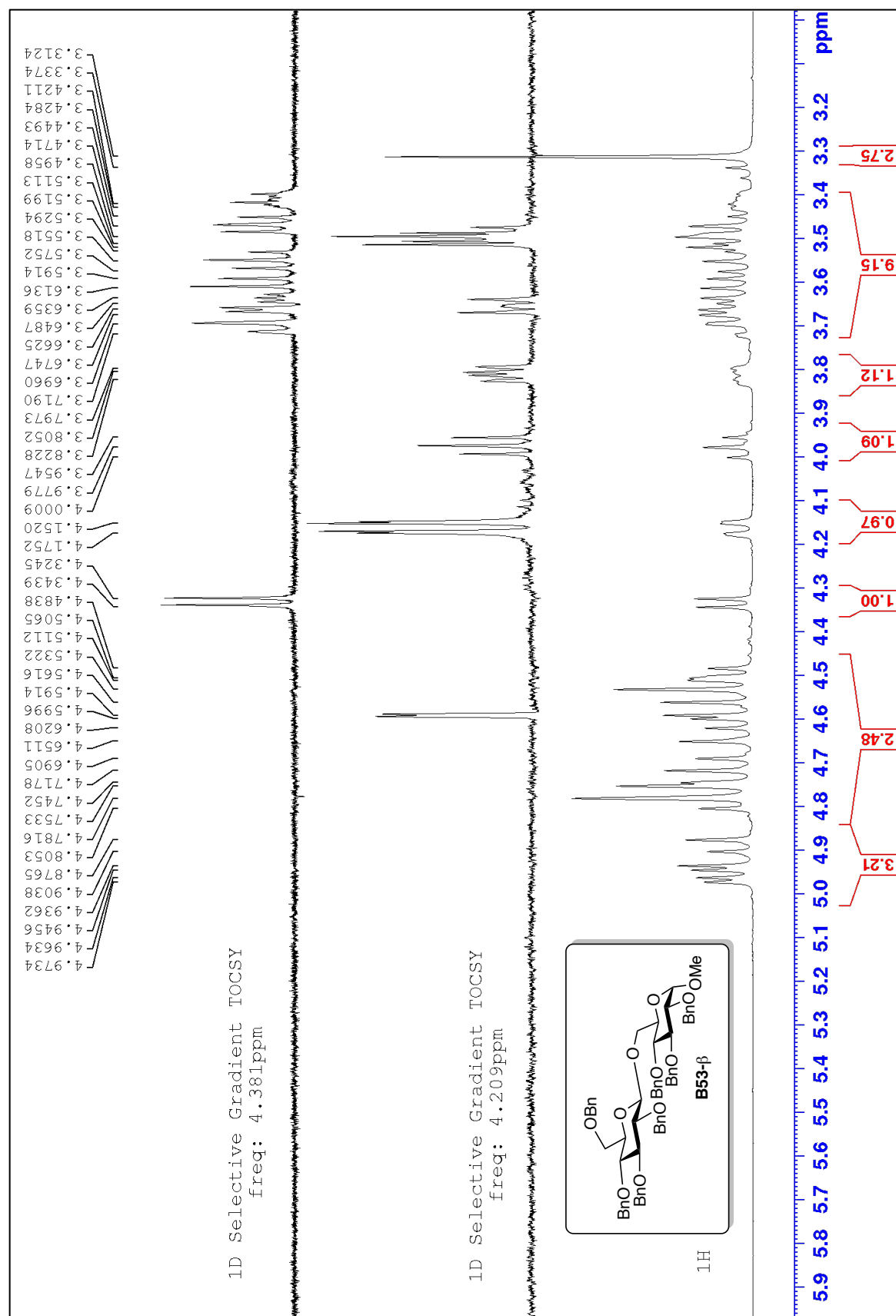
The ¹H Spectrum in CDCl₃ of Compound B51-β.



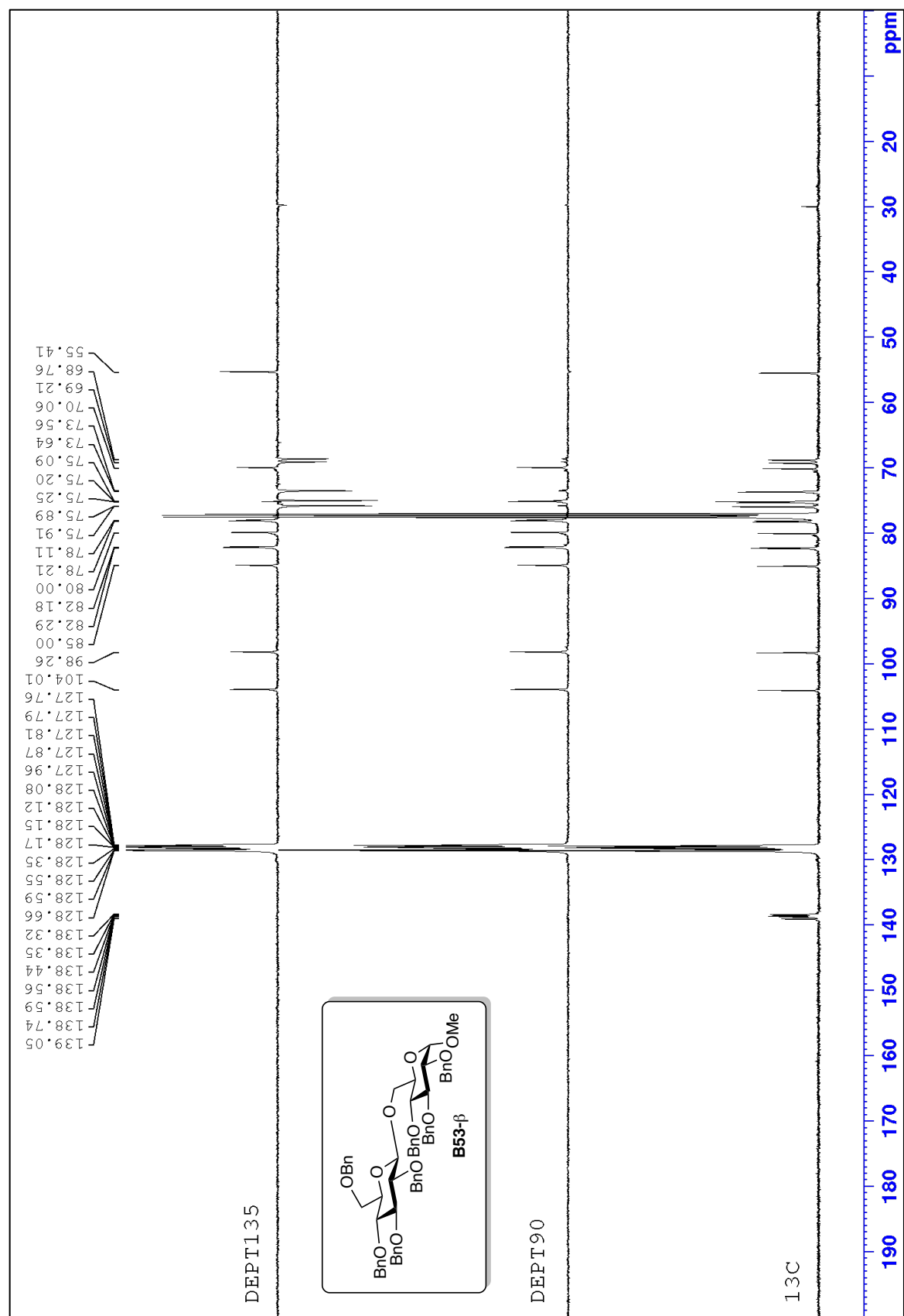
The ^{13}C Spectrum in CDCl_3 of Compound B51-β.



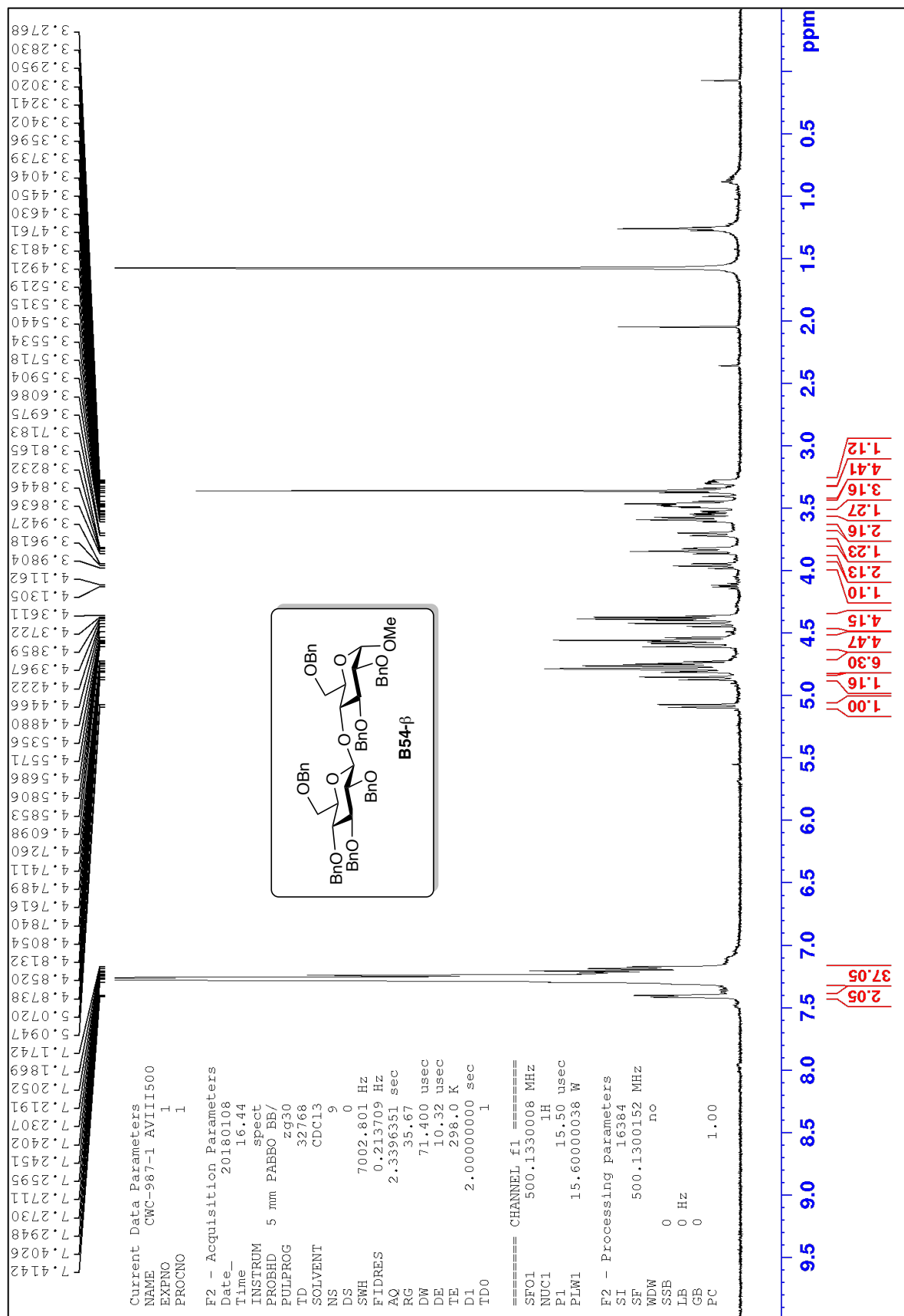
The ^1H Spectrum in CDCl_3 of Compound B53- β .



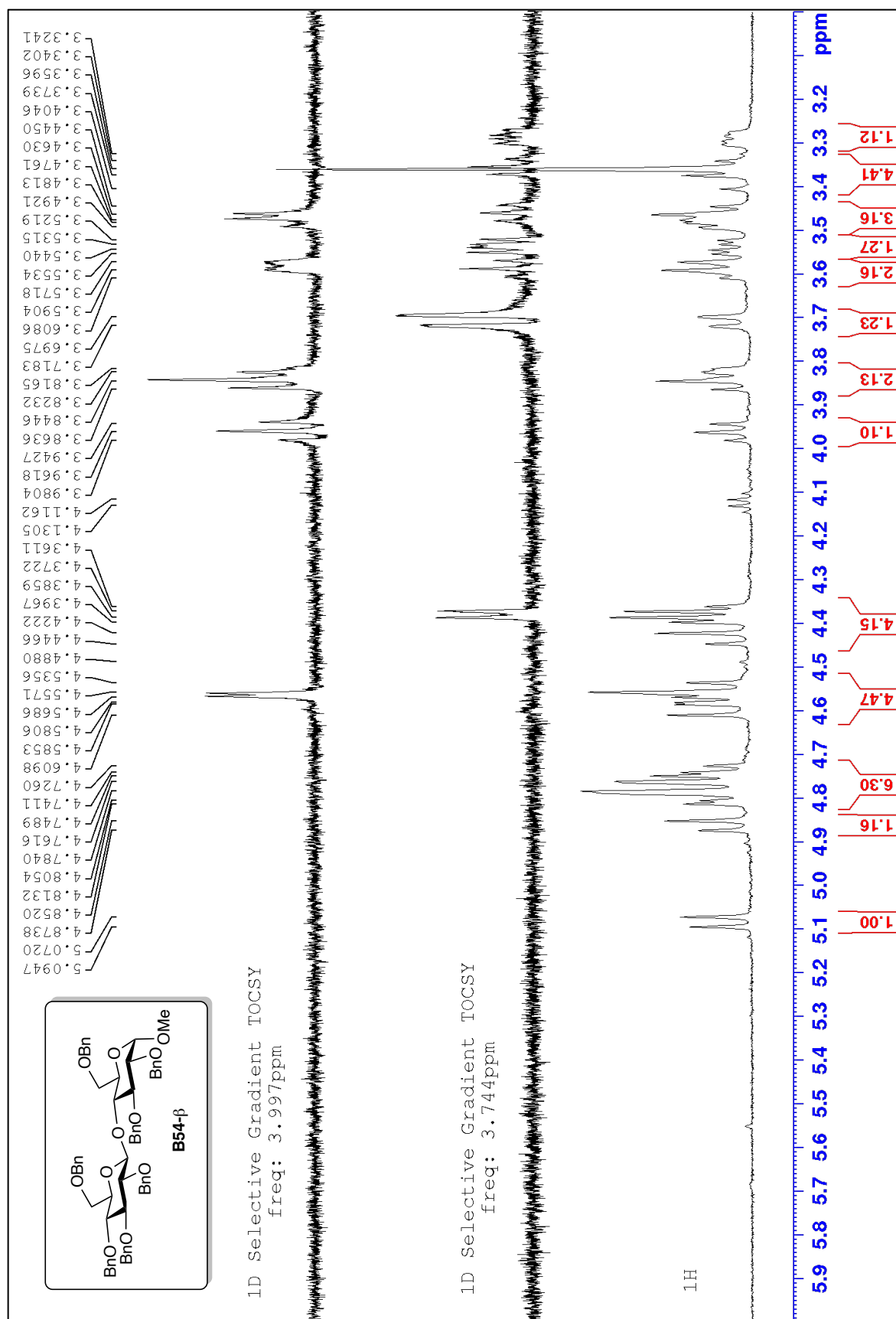
The 1D-TOCSY Spectrum in CDCl_3 of Compound B53-β.



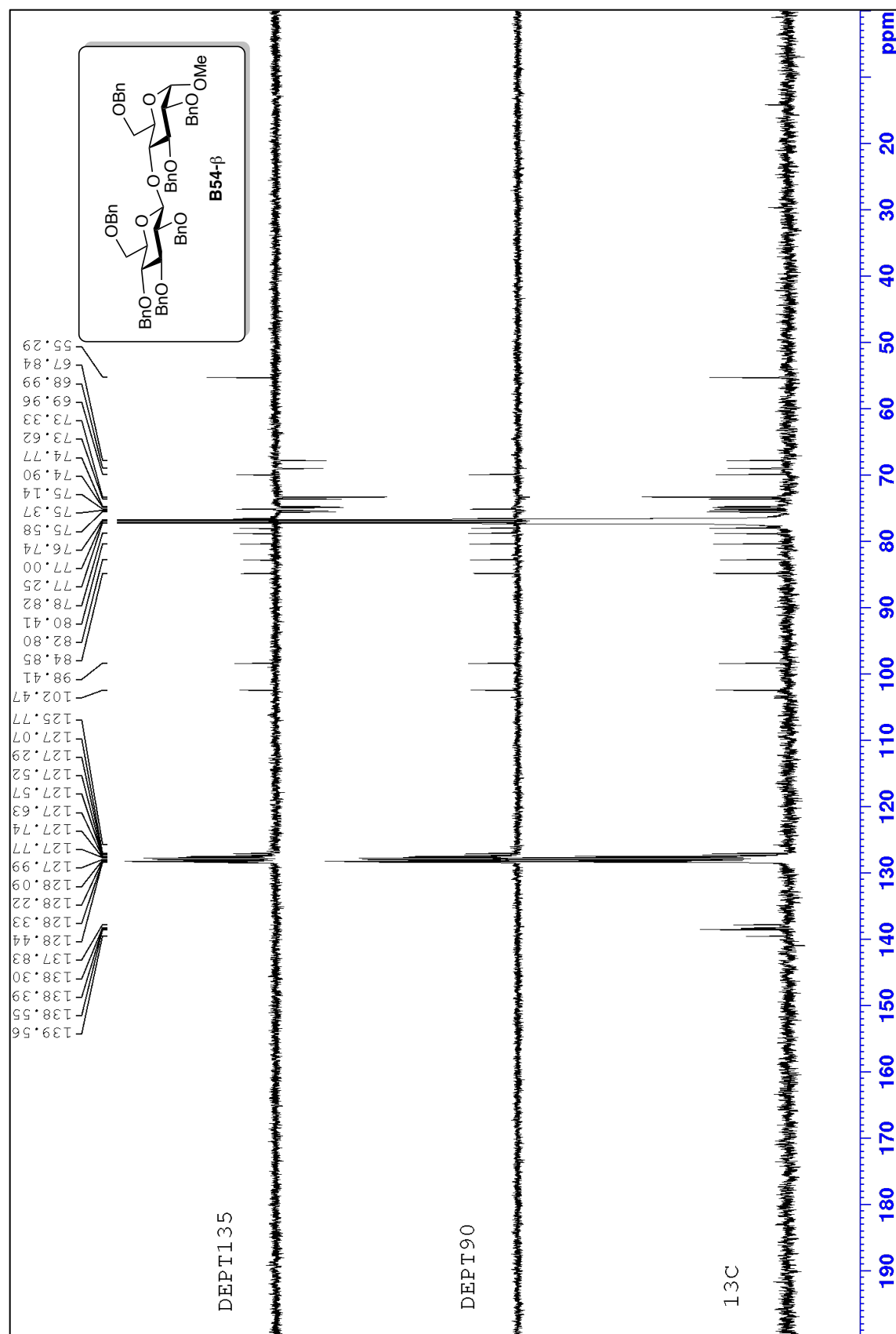
The ^{13}C Spectrum in CDCl_3 of Compound B53-β.



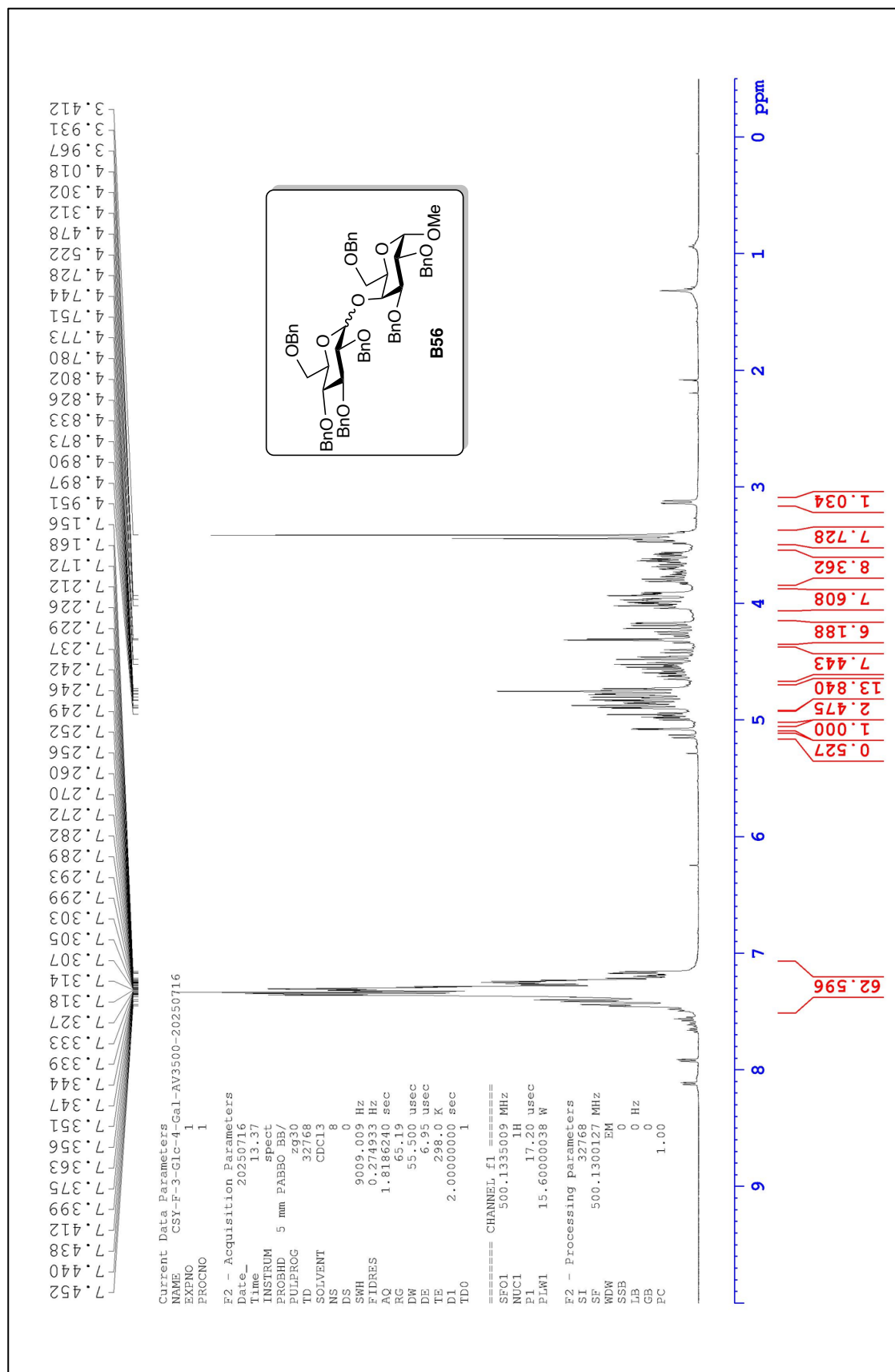
The ^1H Spectrum in CDCl_3 of Compound B54- β .



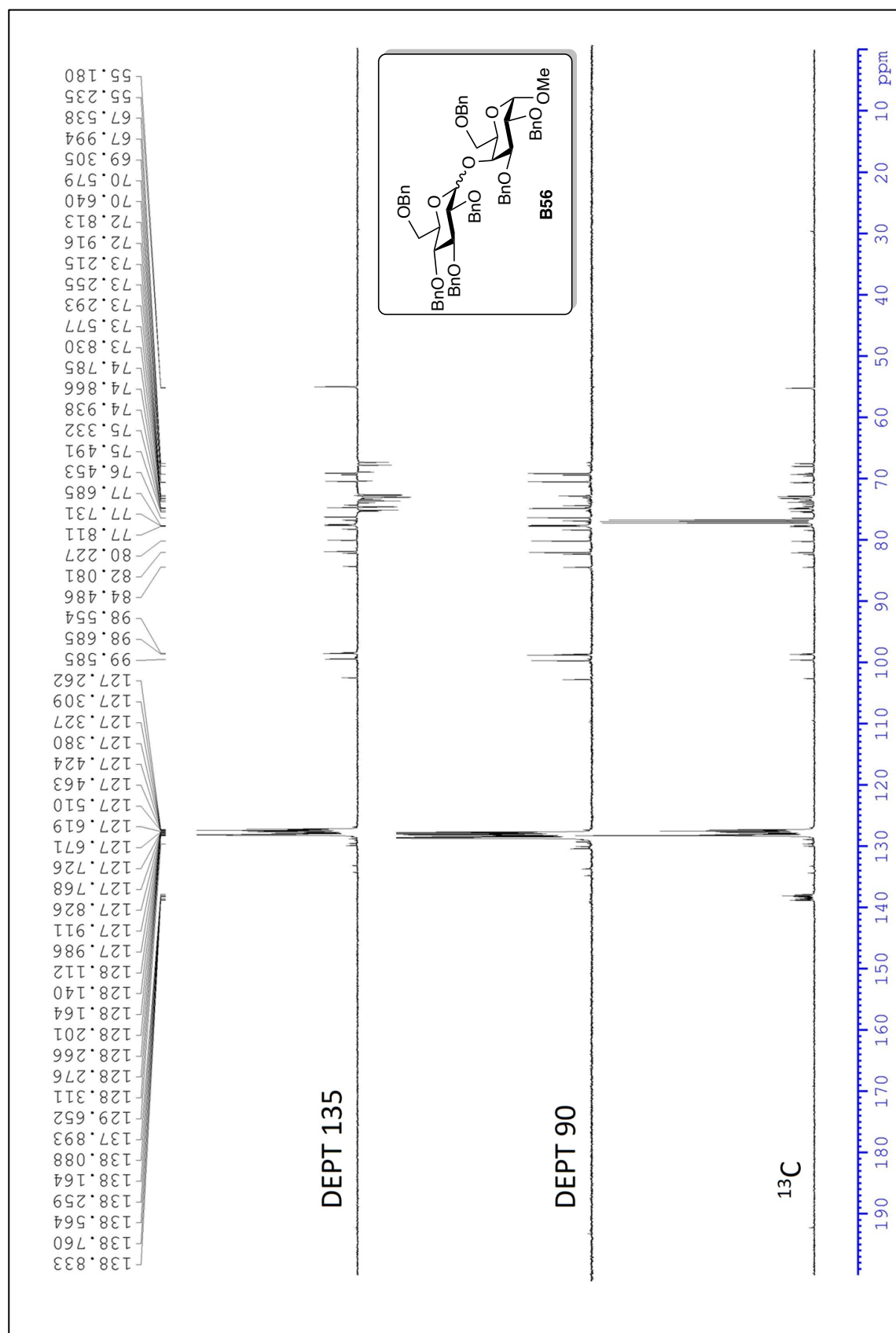
The 1D-TOCSY Spectrum in CDCl₃ of Compound B54-β.



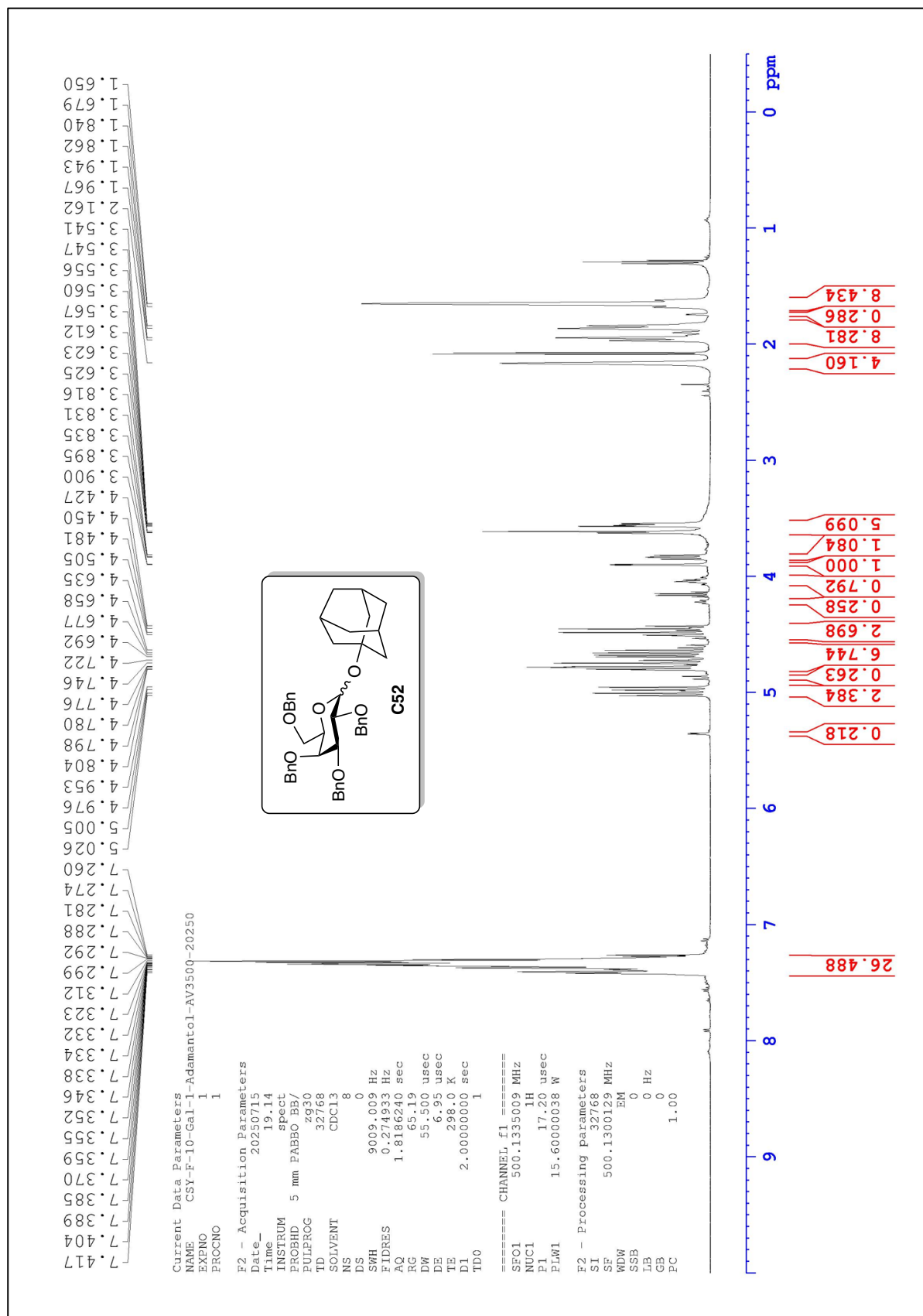
The ^{13}C Spectrum in CDCl_3 of Compound B54- β .



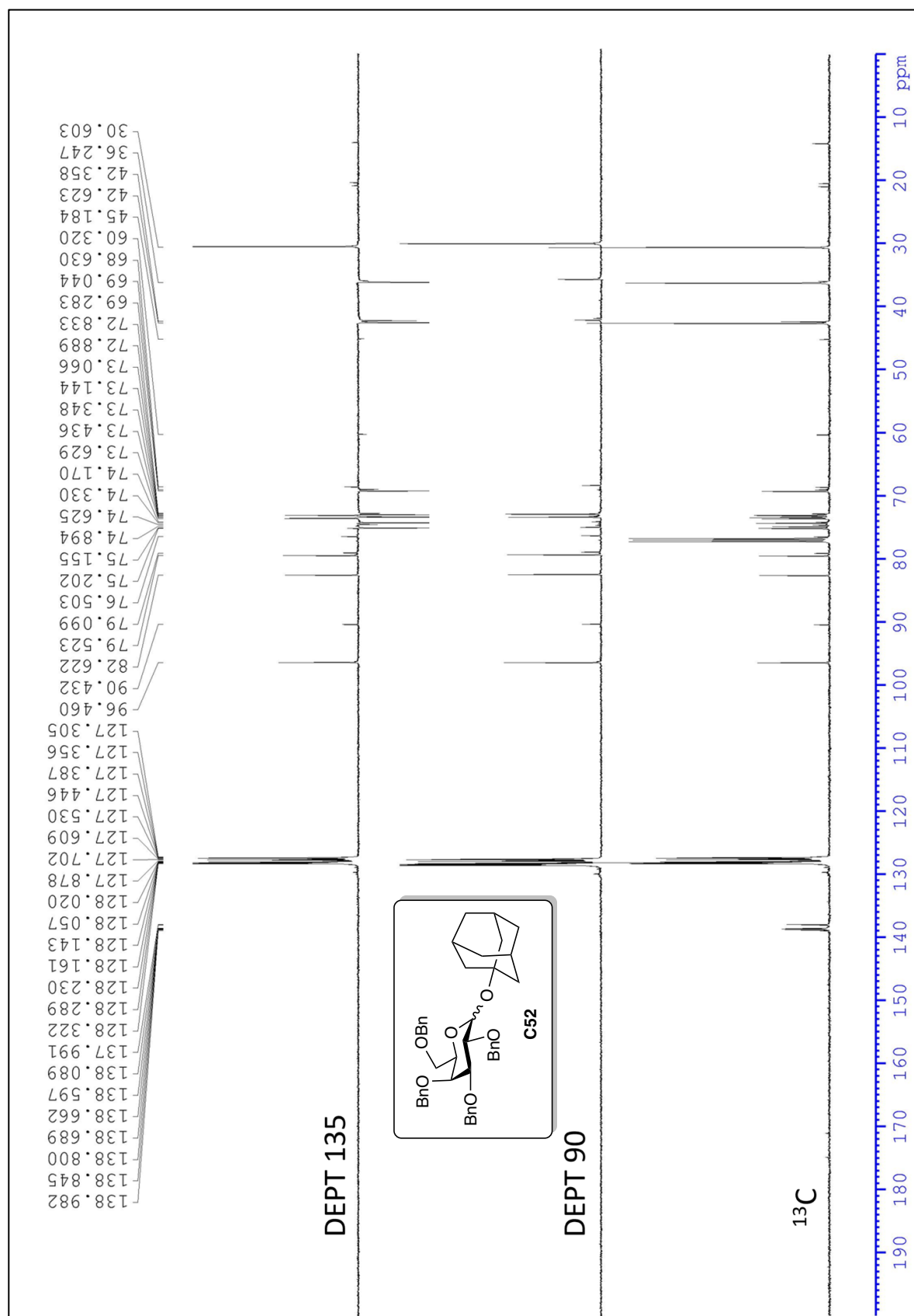
The ^1H Spectrum in CDCl_3 of Compound B56



The ¹³C Spectrum in CDCl₃ of Compound B56

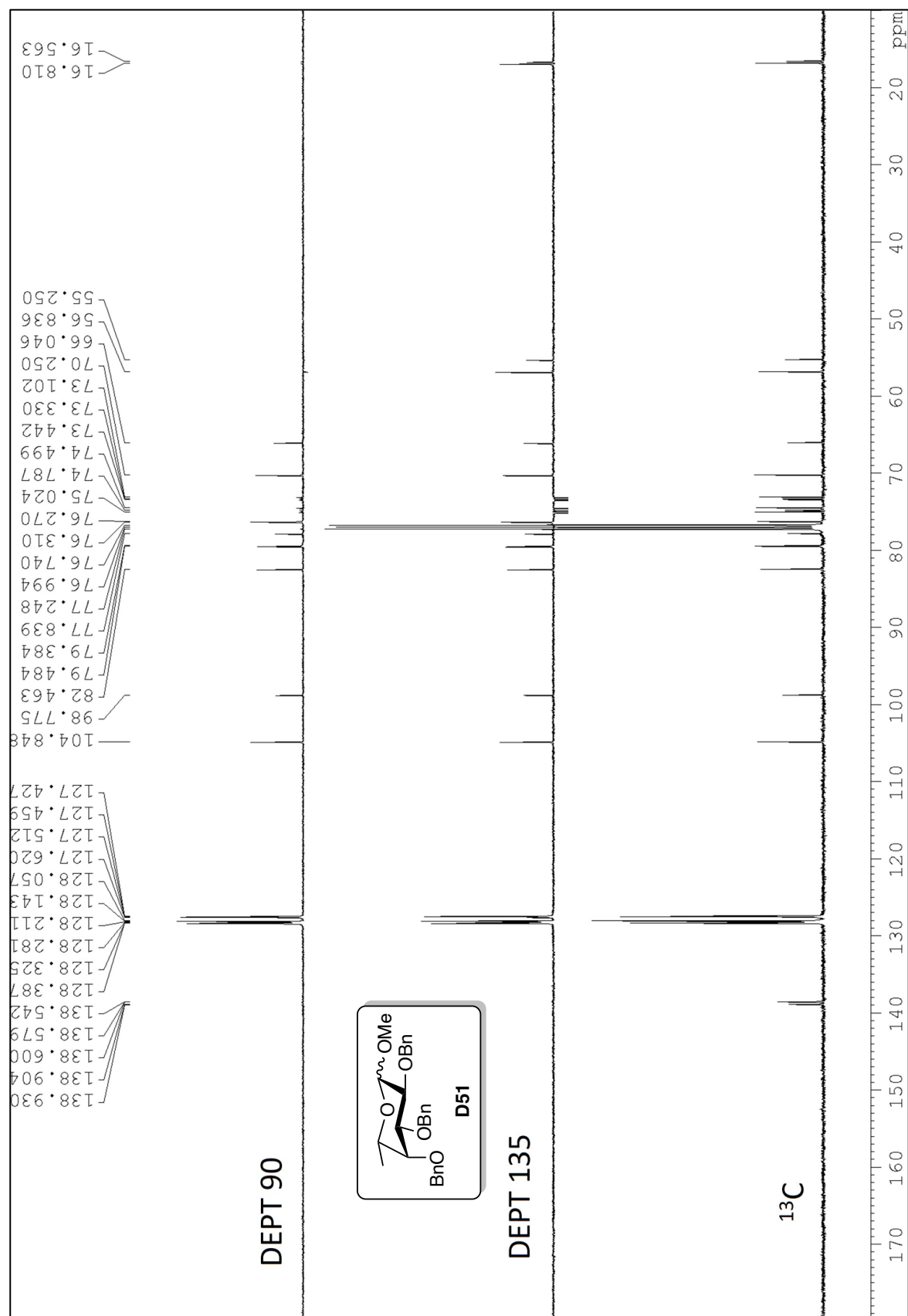


The ^1H Spectrum in CDCl_3 of Compound C52

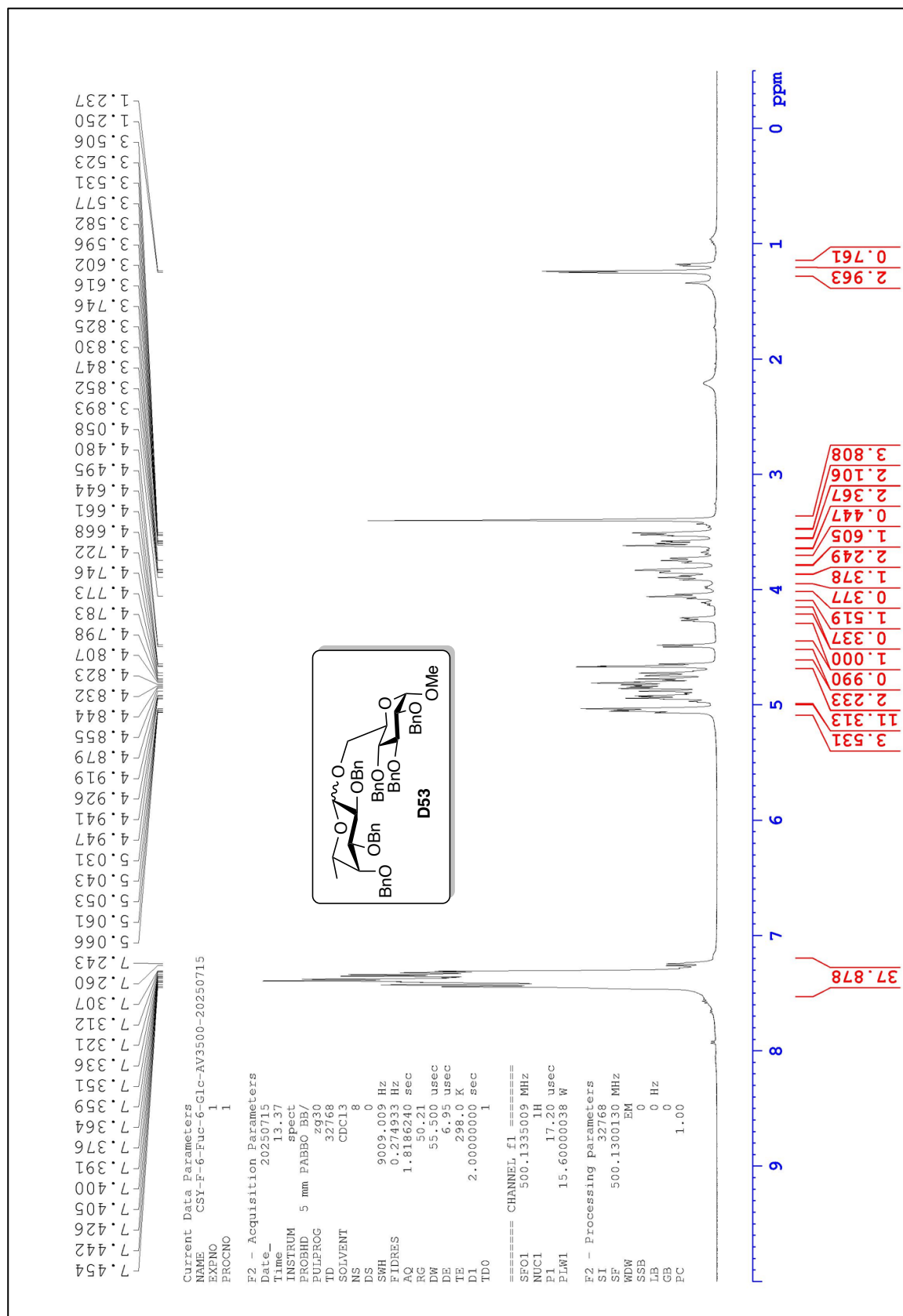




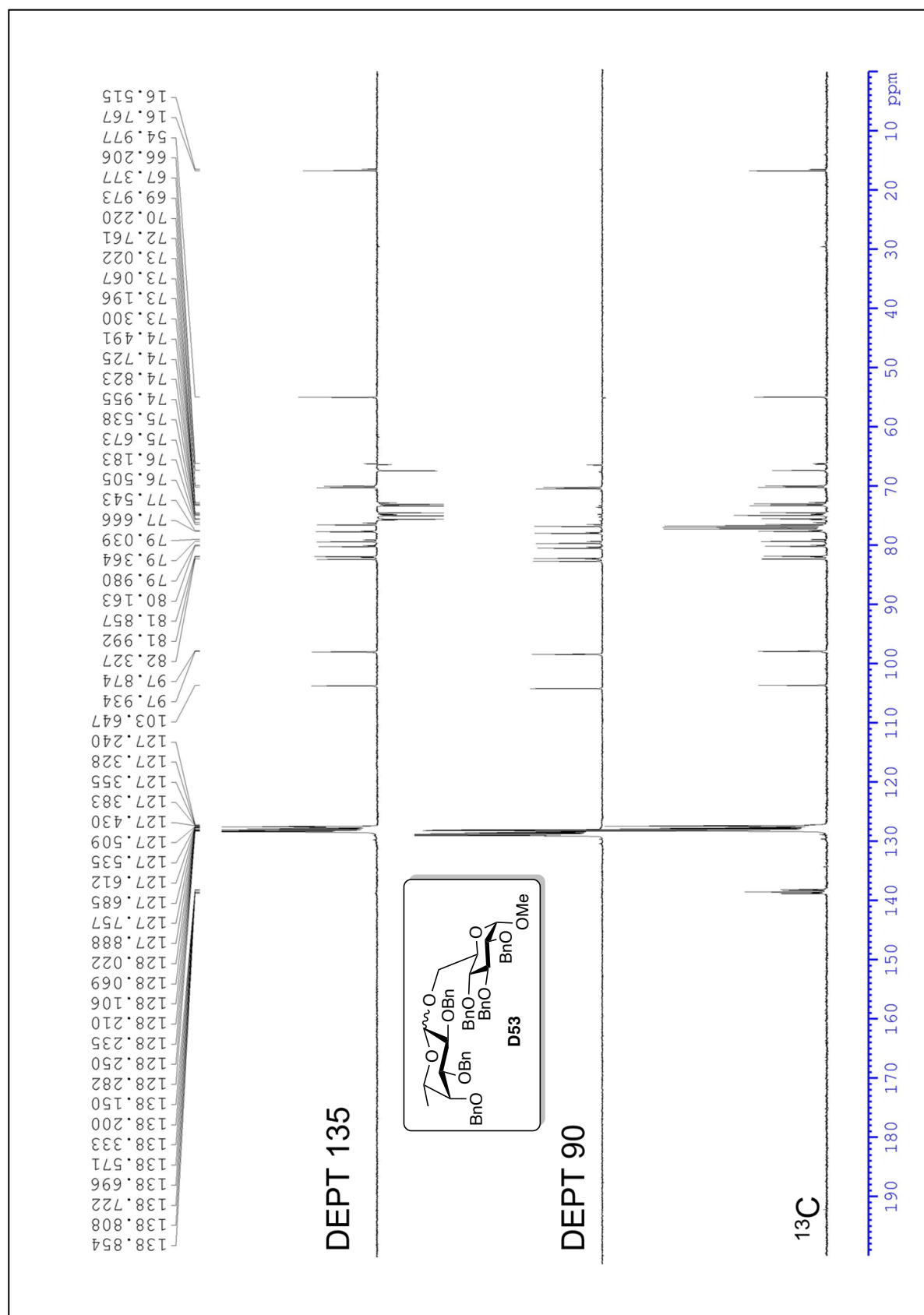
The ¹H Spectrum in CDCl₃ of Compound D51



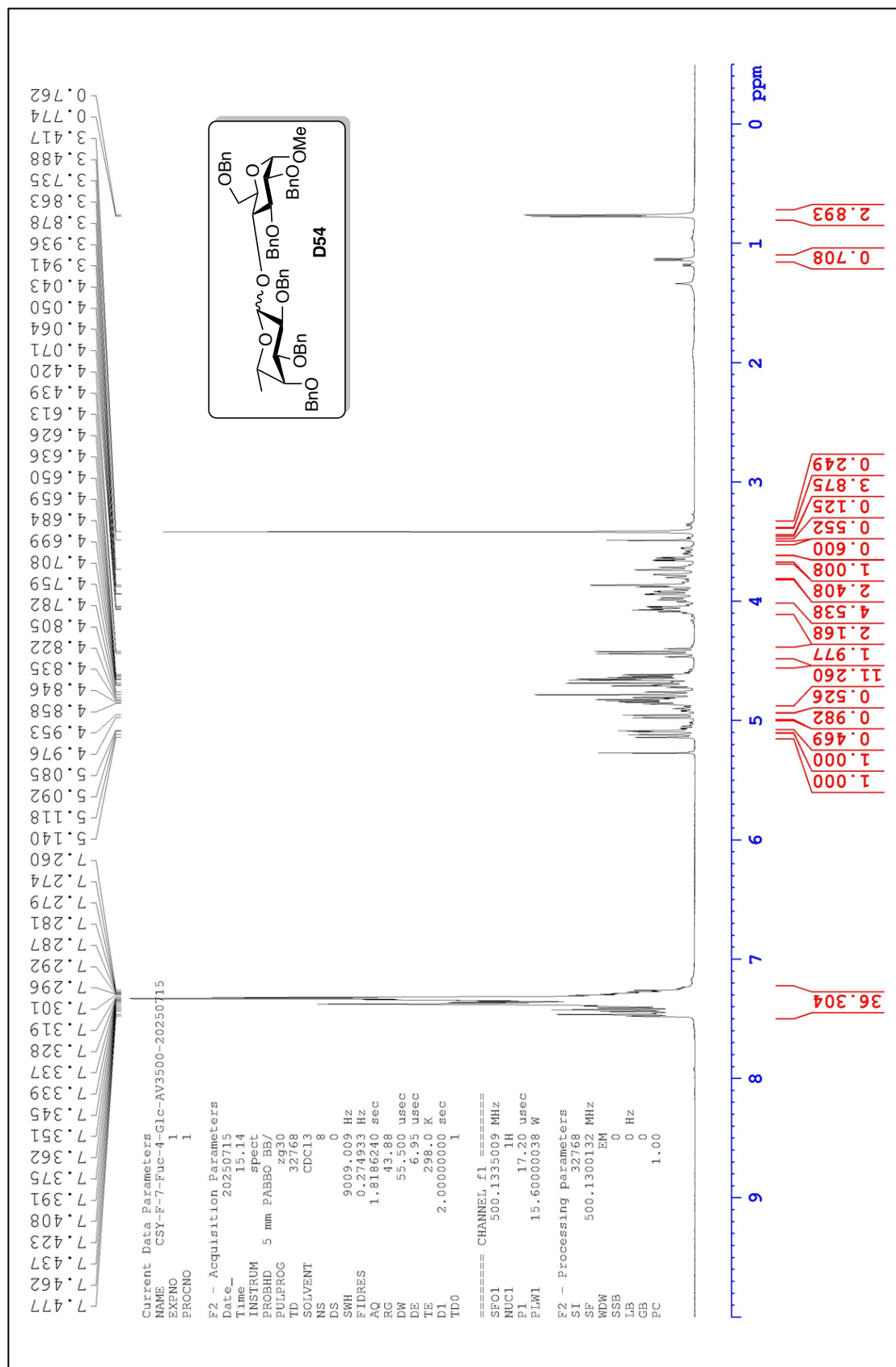
The ^{13}C Spectrum in CDCl_3 of Compound D51



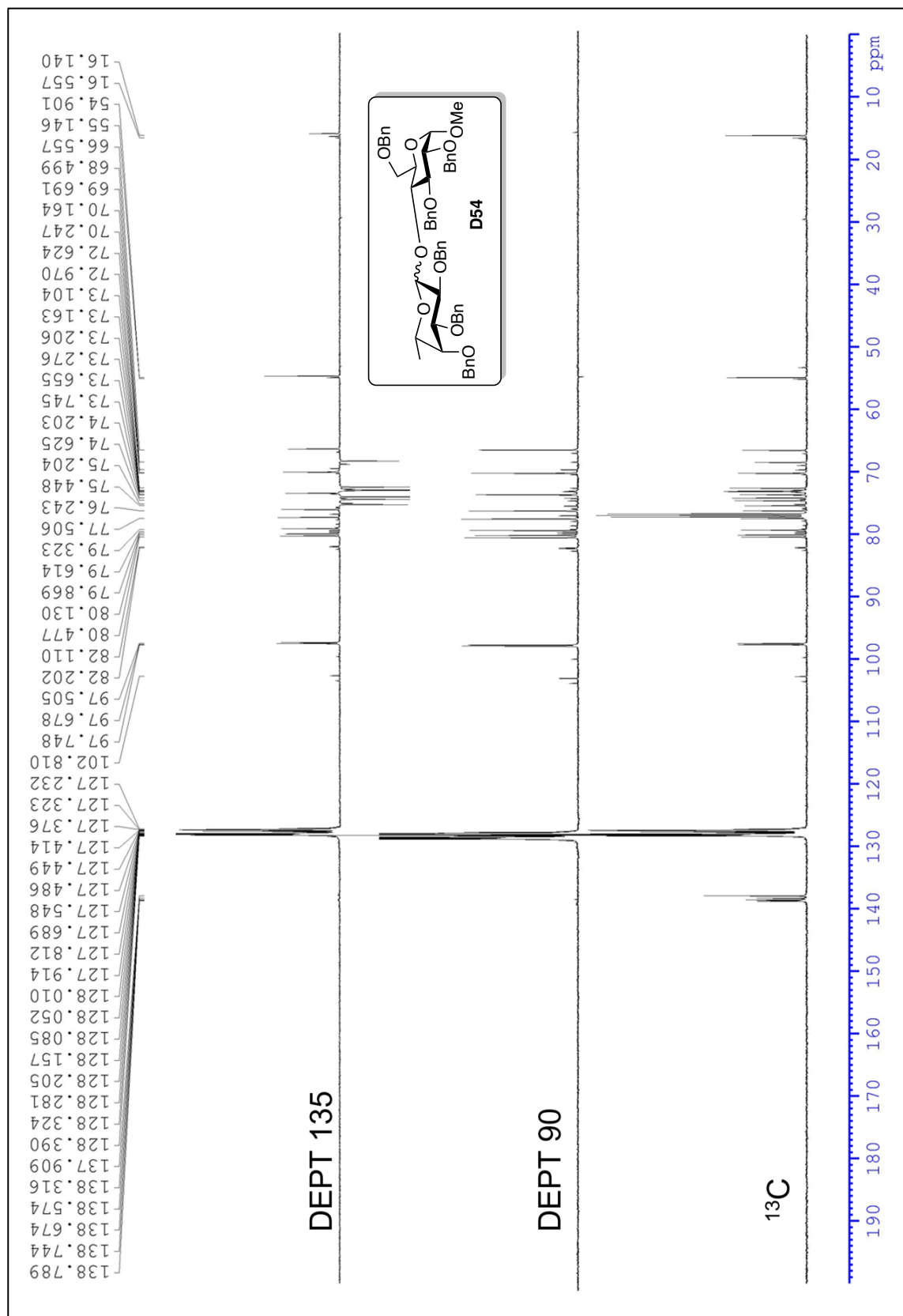
The ^1H Spectrum in CDCl_3 of Compound D53



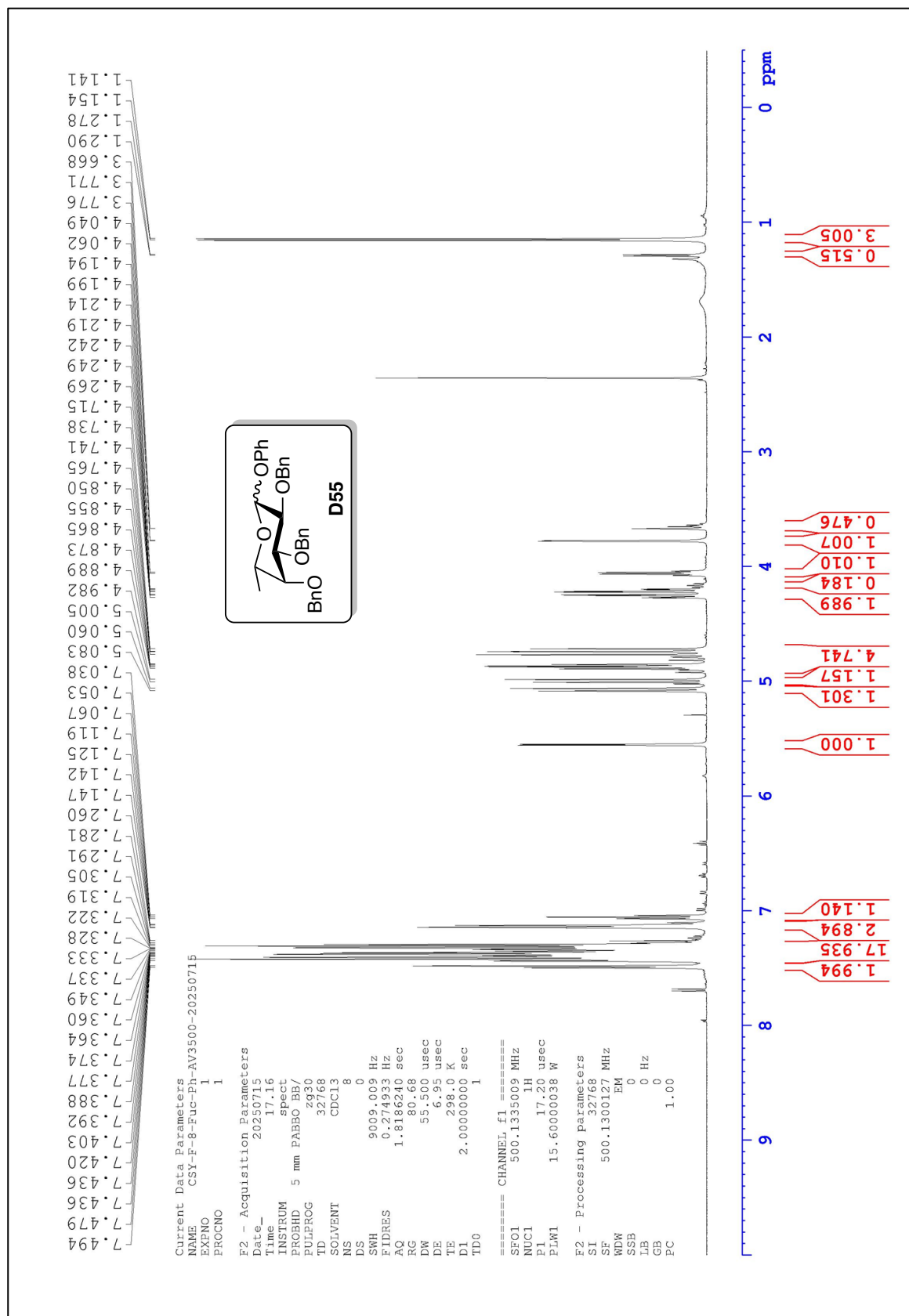
The ¹³C Spectrum in CDCl₃ of Compound D53



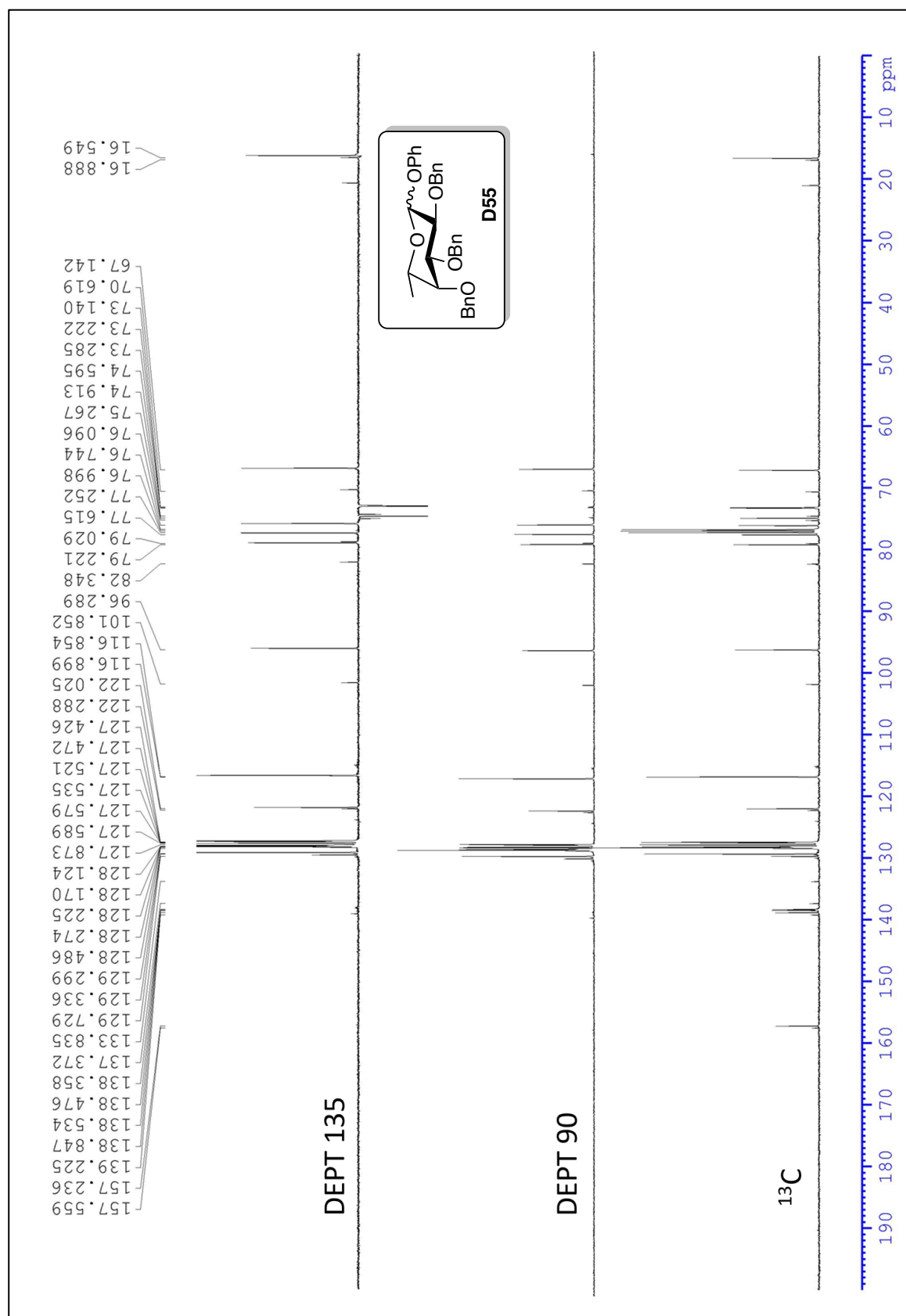
The ^1H Spectrum in CDCl_3 of Compound D54



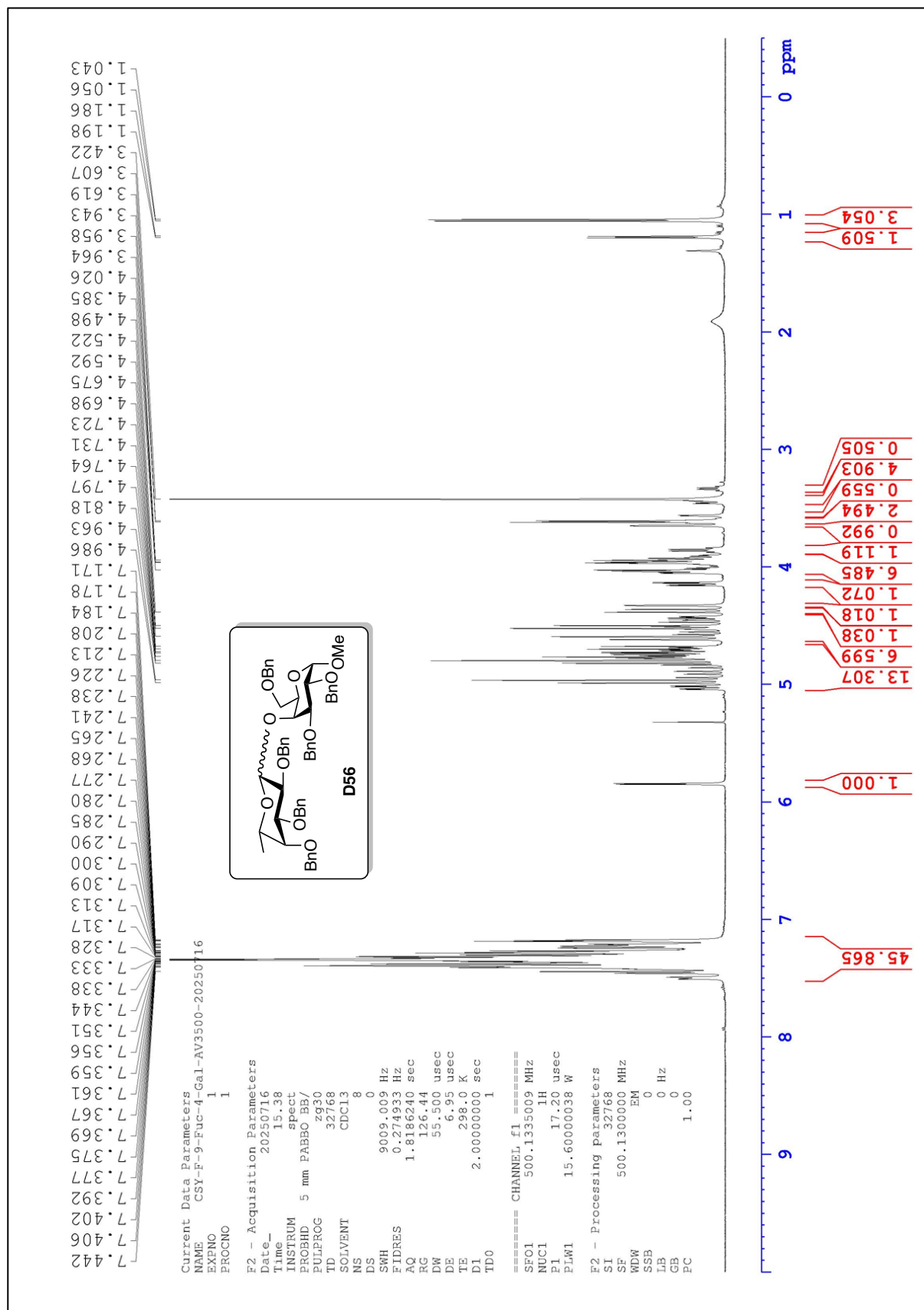
The ^{13}C Spectrum in CDCl_3 of Compound D54



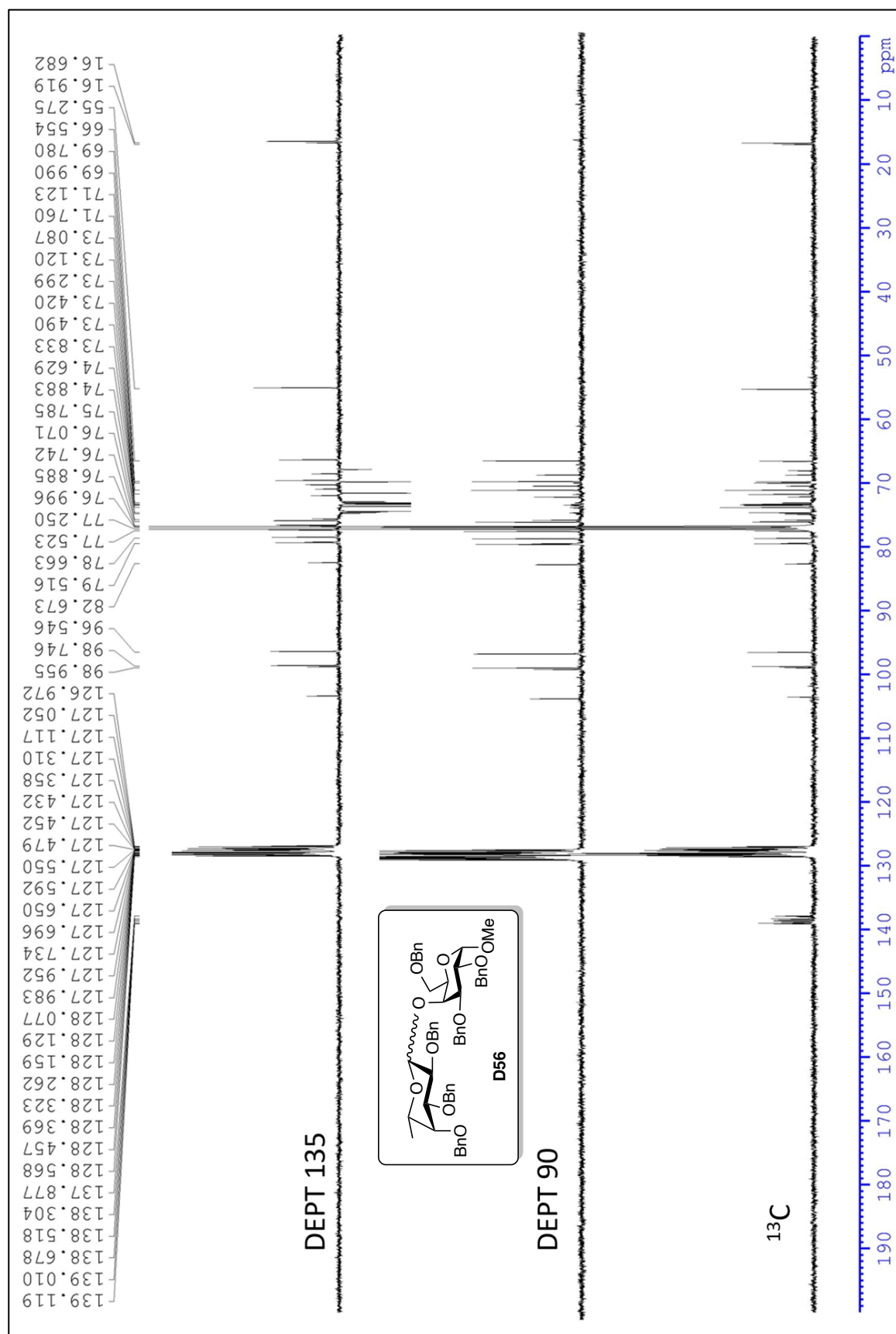
The ^1H Spectrum in CDCl_3 of Compound D55



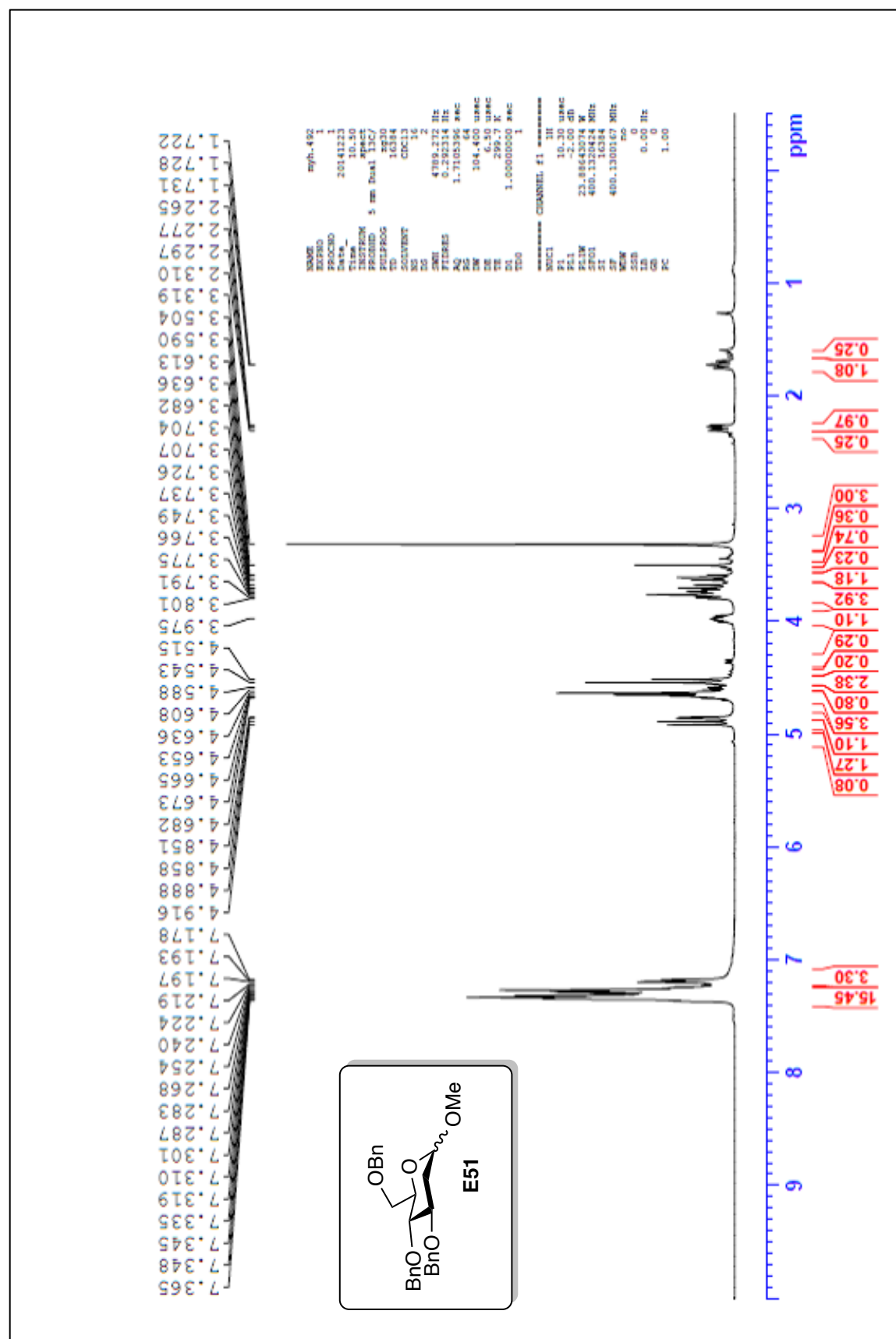
The ^{13}C Spectrum in CDCl_3 of Compound D55



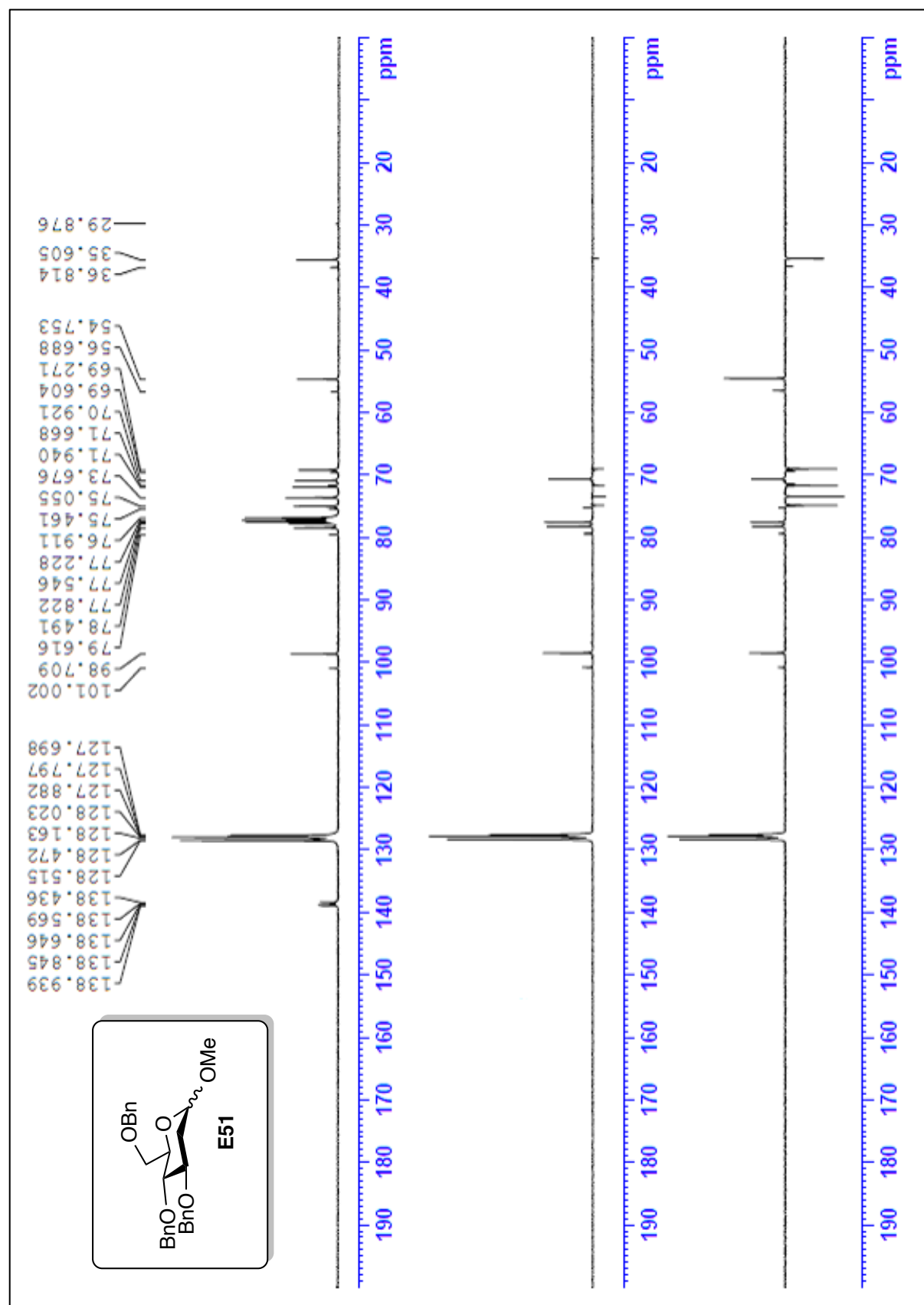
The ^1H Spectrum in CDCl_3 of Compound D56



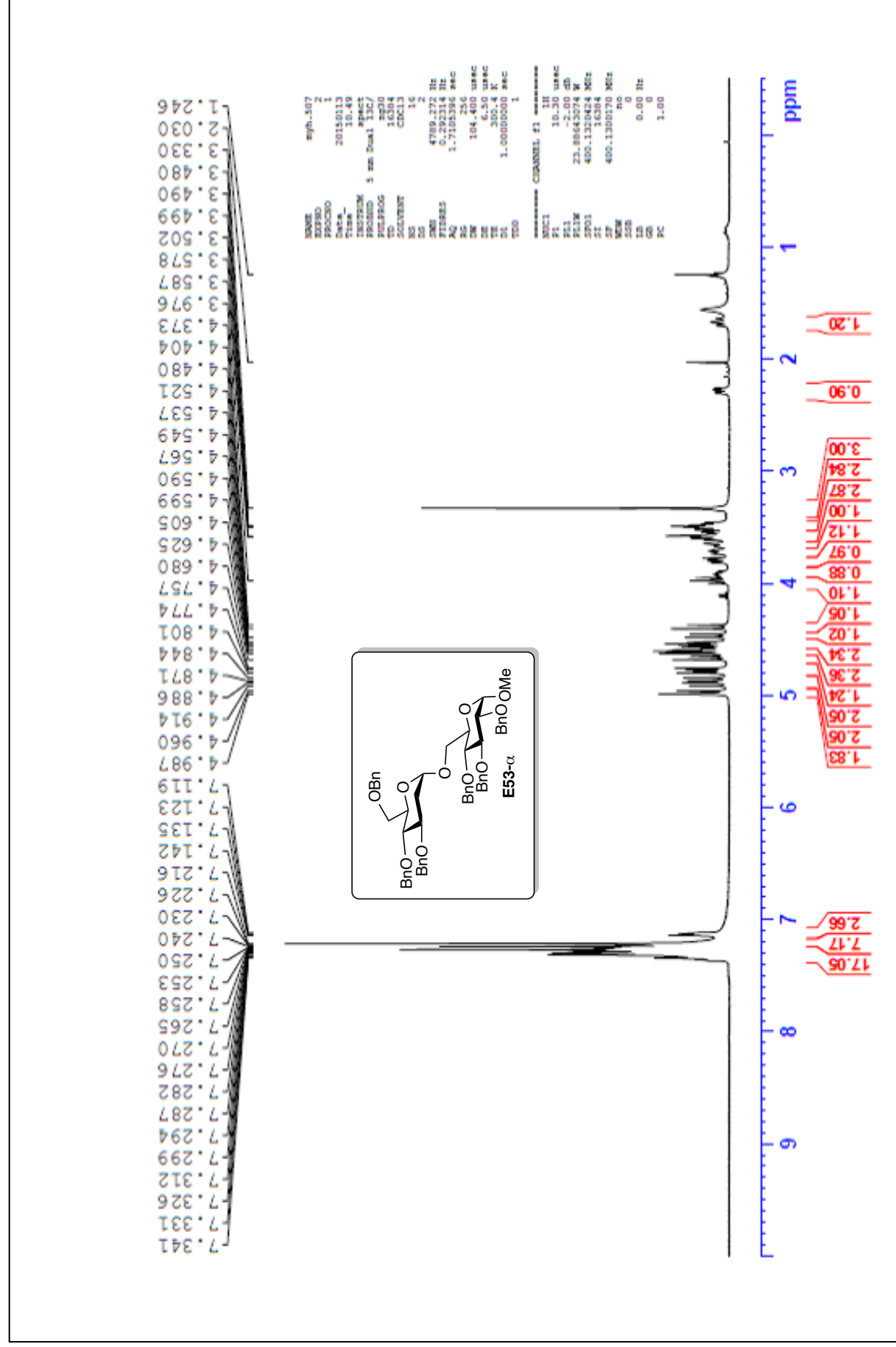
The ^{13}C Spectrum in CDCl_3 of Compound D56



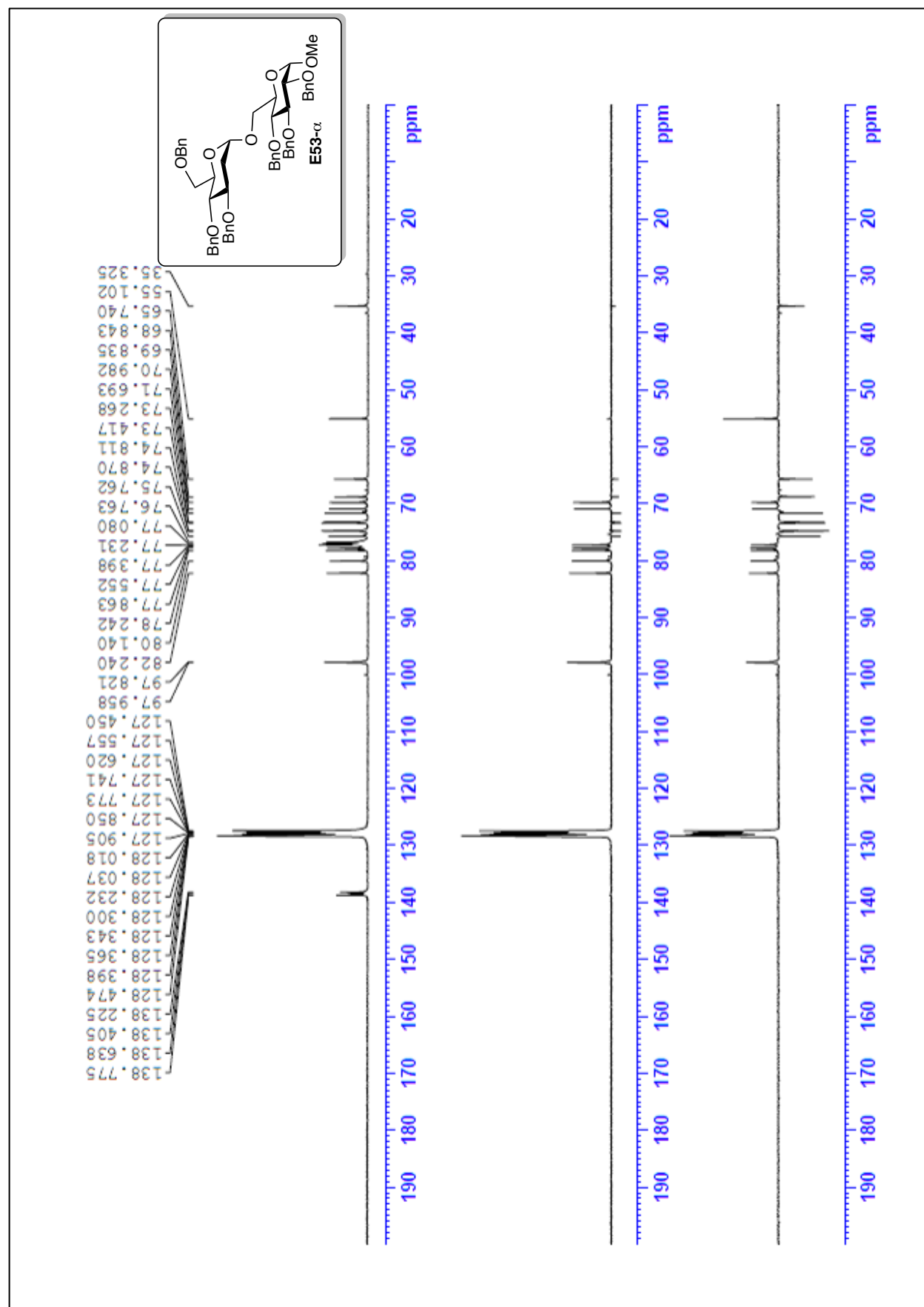
The ^1H Spectrum in CDCl_3 of Compound E51.



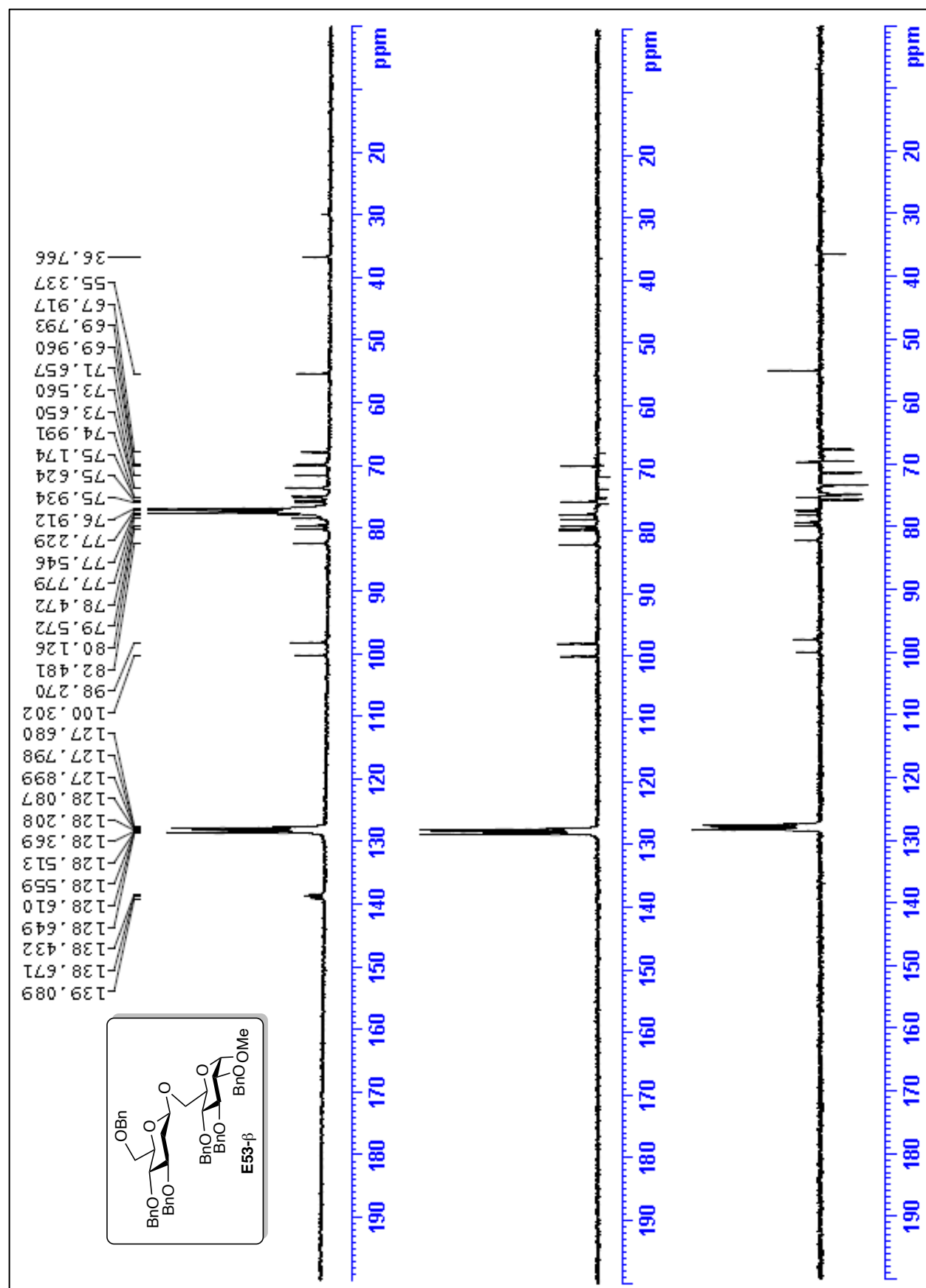
The ^{13}C Spectrum in CDCl₃ of Compound E51.



The ^1H Spectrum in CDCl_3 of Compound E53- α .

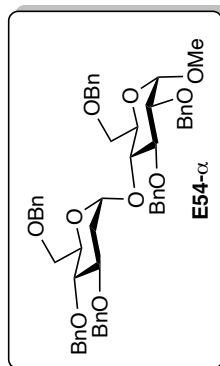


The ¹³C Spectrum in CDCl₃ of Compound E53-α.



The ¹³C Spectrum in CDCl₃ of Compound E53-β.

myh.510-1

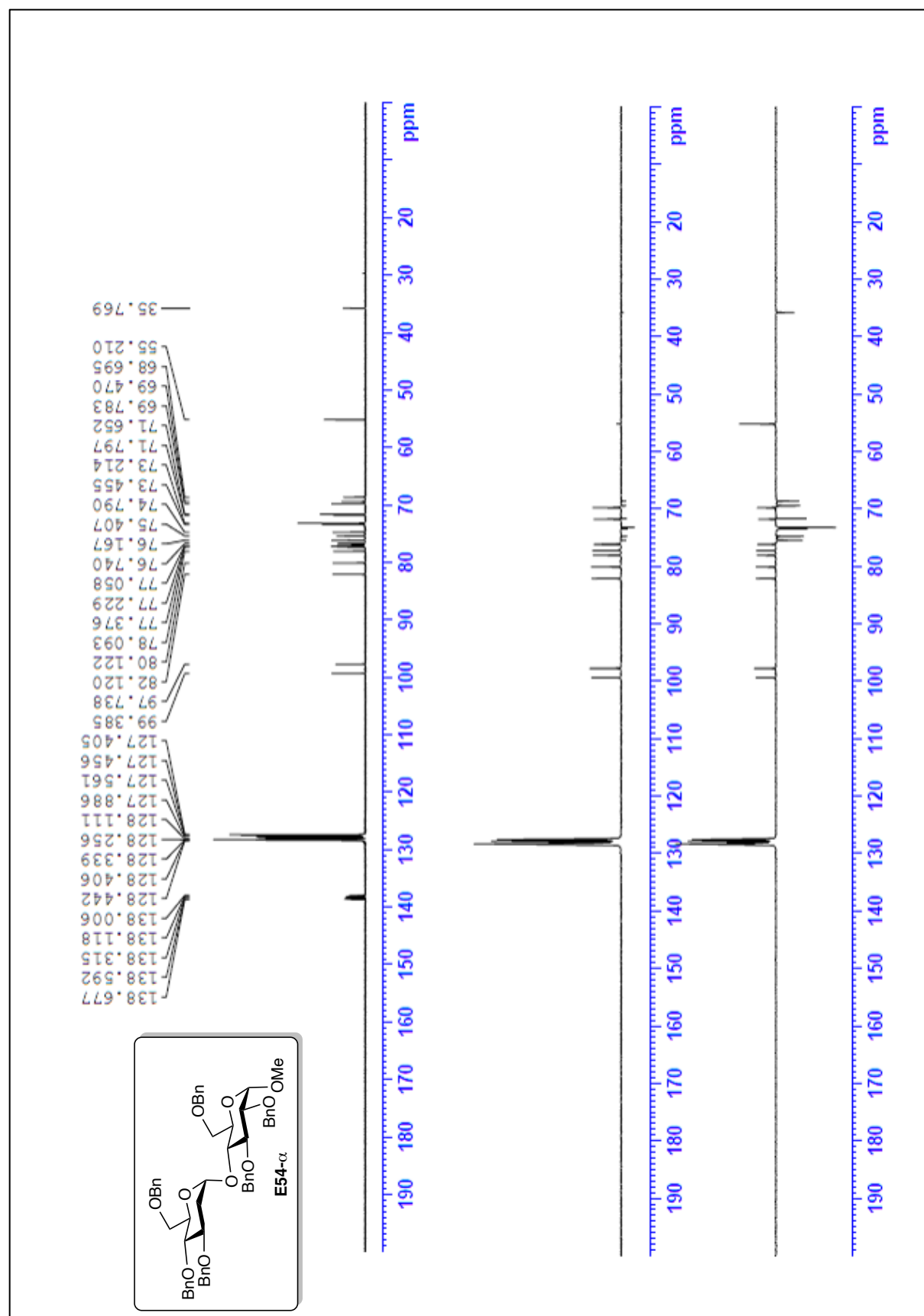


NAME myh.510
EXPNO 1
PROCNO 1
Date_ 20140110
Time 19:27
INSTRUM spect
PROBHD 5 mm PABBO BB-
PULPROG zgpg30
TD 65536
SOLVENT CDCl3
NS 16
DS 0
SWH 5597.015 Hz
FIDRES 0.341615 Hz
AQ 1.4626873 sec
RG 320
AQ 1.4626873 sec
RG 320
F2 89.313 MHz
F1 400.1300179 MHz
F2 89.313 MHz
F1 400.1300179 MHz
WDW 0
GB 0
PC 1.00

===== CHANNEL f1 =====
NUC1 13C
P1 13.40 usec
PL -2.00 dB
F1 101.6254061 MHz
SFO1 400.1300179 MHz
WDW 0
GB 0
PC 1.00



The ^1H Spectrum in CDCl_3 of Compound E54- α .



The ^{13}C Spectrum in CDCl_3 of Compound E54- α .